The nature of critical phenomena of the scaling theory of quantum Hall transitions in two-dimensional electron systems

Nii Amoo Dodoo-Amoo

Submitted in accordance with the requirements for the degree of Doctor of Philosophy.

The University of Leeds

School of Electronic and Electrical Engineering

May 2013

Abstract

The nature of the transitions that occur between the quantized plateaux observed in the quantum Hall effect (QHE) have been classified as second order quantum phase transitions. These transitions occur between the localized and the extended states found within a Landau level band of energies. The theory of the critical phenomena associated with these quantum Hall transitions (QHTs) predicts a universal behaviour irrespective of any microscopic detail of the two-dimensional system (2DES) within which they are observed such as carrier concentration or mobility. This proposed universality of QHTs can be verified by measuring the value of certain critical exponents governing the transitions. If valid, these critical exponents should be measured as a universal constant in all instances.

This thesis investigates the universality of QHTs using a finite-size scaling theory and attempts to address disagreements that exist in the literature on the critical exponents associated with QHTs. The scaling theory of QHTs presented here involves experimental studies based on varying either the temperature of the 2DES or the frequency of the applied electric field.

It was found that the critical exponents of QHTs are not universal across all systems investigated. It is shown that changing the nature of disorder within the system influences the value of the critical exponent measured. In general, it was found that the experimental observation of quantum criticality, as expected from the critical phenomena theory of QHTs, depends on the competition between three key length scales characterizing the 2DES; the size of system, the phase coherent length and the typical size of the electron clusters forming within the system.

A study on the limit of the observation of the QHE is also undertaken in the millimetre wave regime. It was found that localization within the 2DES, and as a result the QHE, is destroyed at frequencies below the millimetre wave regime for a GaAs based 2DES.

Acknowledgements

I would like thank my supervisors Professor Giles Davies, Professor Edmund Linfield and Professor John Cunningham for their support and guidance throughout the course of this project.

I would also like to thank the following colleagues, who have been of great assistance in the completion of this work. I would like to thank Divyang Mistry for valuable discussions and inspiration throughout our long collaboration together, I would like to thank Dr. Kashif Saeed for assistance with experimental setups and measurements, Dr. Matthew Byrne for his invaluable assistance and training during sample fabrication and Dr. Alexander Mayorov, Dr. Chris Wood, Dr. Andrew Burnett and Nicholas Hunter for reading through my thesis.

Finally, I would like to thank my parents for supporting me in all my endeavours all these years and my entire extended family for their encouragement and goodwill.

Contents

List of Figures

List of Tables

Abbreviations

2DES	Two-dimensional electron system
CPW	Coplanar waveguide
FRH	Fixed-range hopping
FWHM	Full width at half maximum
LL	Landau level
MBE	Molecular beam epitaxy
MIT	Metal-to-insulator transition
MMW	Millimetre wave
QHE	Quantum Hall effect
QHT	Quantum Hall transitions
RF	Radio Frequency
TE	Transverse electric
TEM	Transverse electromagnetic
UCF	Universal conductance fluctuations
VRH	Variable-range hopping

List of Principal Symbols

B	Magnetic field
ΔB	Full width at half maximum of Landau level peak
δ	Thouless number
e	Charge of an electron
E	Energy
E_F	Fermi energy
E_μ	Mobility edge
f	Frequency of the applied electric field
g	Conductance
h	Plank constant
I	Current
k_B	Boltzmann constant
κ	Composite critical scaling exponent
L	Length of system
L_{2D}	Length of two-dimensional electron system
L_{eff}	Effective length of the system
L_φ	Phase coherence length
l_0	Magnetic length
m	Mass of an electron
m^*	Effect mass of an electron

μ	Electron mobility
n	Carrier concentration
ν	Critical exponent of the localization length
N	Landau level index
p	Temperature exponent
σ	Conductivity
σ_{xx}	Diagonal component of conductivity
σ_{xy}	Hall component of conductivity
ξ	Localization length
ξ_p	Typical length of electron clusters
ρ	Resistivity
S_{21}	Transmission parameter of scattering matrix
T	Temperature
T_e	Electron temperature
T_L	Lattice temperature
τ_c	Classical or transport lifetime of an electron
τ_φ	Phase breaking time
τ_q	Quantum lifetime of an electron
r, R	Distance
$\bar{R}$	Mean hopping distance
V	Electric potential
w_c	Cyclotron frequency

Publications and conference proceedings

K. Saeed, **N. A. Dodoo-Amoo**, L. H. Li, S. P. Khanna, E. H. Linfield, A. G. Davies, J. E. Cunningham. “Impact of disorder on frequency scaling in the integer quantum Hall effect”, Physical Review B, 84, 155324 (2011).

N. A. Dodoo-Amoo, K. Saeed, L. Li, S. Khanna, E. H. Linfield, A. G. Davies and J. Cunningham, “Scaling Behaviour of the Integer Quantum Hall Effect in GaAs/AlGaAs Heterostructures”, Proceeding of the UK Semiconductor conference, Sheffield (UK) , 2011.

N. A. Dodoo-Amoo, K. Saeed, J. E. Cunningham, L. H. Li, S. P. Khanna, E. H. Linfield, A. G. Davies, “Role of Short-Range Interactions on Frequency Scaling of the Integer Quantum Hall Effect”, Proceedings of the 19th international conference on Electronic Properties of Two-Dimensional Systems (EP2DS19), Tallahassee (USA), 2011.

K. Saeed, **N. A. Dodoo-Amoo**, J. E. Cunningham, L. H. Li, S. P. Khanna, E. H. Linfield, A. G. Davies, “ Microwave frequency range scaling of the integer quantum Hall effect”, Proceedings of the 19th international conference on Electronic Properties of Two-Dimensional Systems (EP2DS19), Tallahassee (USA), 2011.

N. A. Dodoo-Amoo, K. Saeed, L. Li, S. Khanna, E. H. Linfield, A. G. Davies and J. Cunningham, "Universality in the scaling theory of the quantum Hall effect: a quantum percolation approach", Proceeding of the UK Semiconductor conference, Sheffield (UK) , 2012.

N. A. Dodoo-Amoo, K. Saeed, J. E. Cunningham, L. H. Li, S. P. Khanna, E. H. Linfield, A. G. Davies, "The quantum percolation model of the scaling theory", Proceedings of the 20th International Conference on High Magnetic Fields in Semiconductor Physics, Chamonix Mont-Blanc, (France), 2012

N. A. Dodoo-Amoo, K. Saeed, J. E. Cunningham, L. H. Li, S. P. Khanna, E. H. Linfield, A. G. Davies, "The quantum percolation model of the scaling theory: A unifying model for plateau-to-plateau transitions", Journal of Physics (accepted)

N. A. Dodoo-Amoo, K. Saeed, D. Mistry, L. H. Li, S. P. Khanna, E. H. Linfield, A. G. Davies, J. E. Cunningham. "Non-universality in scaling exponents in quantum Hall transitions", Physical Review B (submitted)

1. Introduction to the scaling theory of quantum Hall transitions

1.1 Introduction

The quantum Hall effect (QHE), discovered just after the centenary of the discovery of the original Hall effect by Edwin Hall [1] in 1879, has led to a large and varied field of research. First reported by von Klitzing, Dorda, and Pepper [2] in 1980, the QHE reveals a peculiar behaviour of a two-dimensional electron system (2DES) in the presence of a strong magnetic field. The most remarkable aspect of the effect is the precise quantization of the Hall conductivity σ_{xx} at integer multiples of e^2/h irrespective of the microscopic details of the 2DES.

The QHE is explained in terms of localized and delocalized states within the 2DES [3-5]. Electrons occupying localized states are restricted in their dissipation to a finite region of space which is very small compared with the size of the 2DES, while electrons occupying delocalized or extended states can freely propagate throughout the entire system.

The distinction between these two types of states originates from the disorder or the degree of randomness within the system, and this is generally studied as a theory of localization. The 2DES exhibits different transport properties depending on whether electron transport is due to the propagation of electrons occupying localized states or electrons occupying extended states.

By gradually changing a physical parameter of the 2DES like the magnetic field or carrier concentration, the states of the electrons contributing to transport can be changed from localized states to extended states or vice versa. This transition is known as a quantum phase transition (QPT) [6] and is observed in transitions between the quantized Hall conductivities in the QHE.

A QPT is a critical phenomenon [7] observed in systems where there is a sudden change of the properties of the system from one phase to another. Critical phenomena have been extensively studied long before the discovery of the QHE [8-10]. A familiar example is the transition of a fluid from a liquid to a gaseous state. Systems exhibiting critical phenomena can be divided into broad groups known as universality classes, such that all members belonging to a given class possess identical critical properties that can be defined by certain power or scaling laws.

Quantum Hall transitions (QHTs) are associated with the scaling law, $\xi(E) \sim |E - E_c|^{-\nu}$, which describes the divergence of the localization length $\xi(E)$ (i.e. the length defining the degree of spatial restriction of an electron at a given energy state E), as the critical energy separating localized states and extended states E_c, is approached. According to the theory of critical phenomena, the localization length exponent ν, is expected to be a constant value for all members belonging to this universality class. In other words, if all QHTs belong to the same university class, they will all possess the same value of ν irrespective of any microscopic detail of the 2DES.

The verification of the universality of QHTs, however, has yielded many contradictory results as summarised in a review by Huskestein *et al*. [11]. Even though it is accepted that some systems exhibit the expected universal behaviour [12-14], there is a growing body of experimental results that show a non-universal behaviour of QHTs [15-17]. In addition, it has recently been discovered that the nature of disorder within a 2DES plays an important role is determining universality [18].

The aim of this thesis is to investigate the nature of the critical phenomena observed within QHTs and to determine the factors influencing both the observation of universality and the lack of universality of QHTs within 2DESs.

In this thesis, the effects of temperature, the frequency of an applied electric field, the amount of electric current injected, and the nature of disorder on QHTs are studied within a wide range of 2DESs of varying characteristic properties.

The outline of the thesis is as follows. In Chapter 1, we review the formation of 2DES in semiconductor heterostructure. We also introduce aspects of the theory of localization that will be key to the analysis of results presented in this thesis. We then review the physics and features of the QHE and provided an in-depth discussion on QPTs and the critical phenomena observed in QHTs. Finally, we developed the analytic tools used in experimental determination of the universality or non-universality of QHTs and conclude with a discussion on previous experimental results present on the investigation of QHTs.

In Chapter 2, we investigate the effect of temperature on QHTs on four different samples. We also investigate the effect of a varying applied current on the nature of QHTs.

In Chapter 3, we develop a high resolution radio frequency (RF) technique that uses a varying frequency of an applied electric field to investigate QHTs. A frequency range between 100 MHz and 20 GHz is studied. In this chapter we also investigate the influence of disorder on the nature of QHTs using the frequency based technique.

In Chapter 4, a quantum percolation model is developed to interpret the various results presented in Chapters 2 and 3. The percolation model explains the occurrence of universality within QHTs, and crucially, it also explains the reason why universality is not observed in many experimental investigations.

In Chapter 5, a free space millimetre wave experimental technique is used to investigate QHTs between the frequency range of 70 GHz and 110 GHz in order to explore the high frequency limit of the QHE.

1.2 Two-dimensional electron systems (2DES)

In the classical degrees of freedom (3D Cartesian coordinates), a two-dimensional electron system (2DES) can be formed by restricting the movement of an electron gas in one direction while retaining freedom in the remaining two dimensions. All the work presented in this thesis is based on the transport properties and quantum effects observed in 2DESs. Studies of these systems have had a profound influence on our understanding of condensed matter systems and are also of practical importance in the development of high electron mobility transistors. Below, we discuss the formation of 2DES and briefly illustrate some of their properties and quantum nature.

1.2.1 Formation of a 2DES in a GaAs/AlGaAs heterostructure

Quasi two-dimensional electron systems were formed initially in oxide based structures such as Si-MOSFETs [19], where a voltage applied to a metal gate deposited on an insulating SiO_2 layer was used to create an inversion layer of carriers at the $Si - SiO_2$ interface. These devices provided the foundation for the development of modern electronics in the form of miniature, fast switching transistors. These structures, however, experience strong Coulomb scattering by charged impurities at the oxide-semiconductor interface [20-22] and as a result are largely unsuitable for the study of quantum mechanical effects in 2DESs. This led to advances in new growth techniques capable of an atomic scale control of the growth process, making it possible for the formation of high quality, low dimensional electron systems in semiconductor heterostructures.

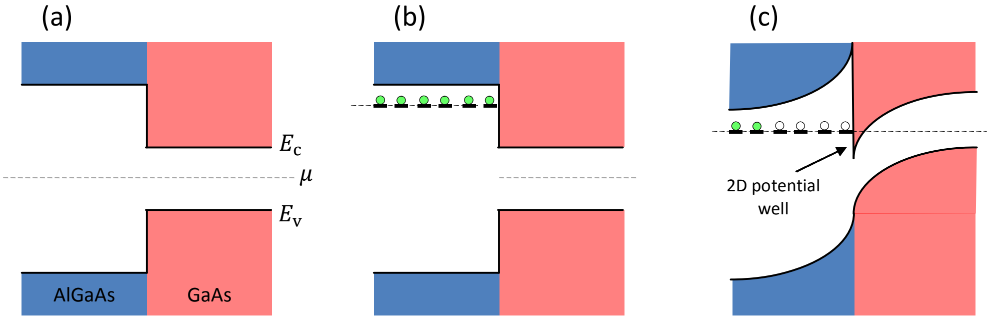

Figure 1.1. (a) The band structure of undoped AlGaAs and GaAs. (b) The band structure of the heterostructure with n-doped AlGaAs before equilibrium. (c) Band bending within the heterostructure at equilibrium where the dipping of the conduction band below the chemical potential produces a 2-dimensional potential well in the plane of the junction between the two materials.

We shall consider such a 2DES formed at the interface between two III-V compound semiconductors, GaAs and $Al_xGa_{1-x}As$, as this is the heterostructure used to fabricate all devices reported in this work. GaAs forms a cubic zinc blende structure where each Ga atom is surrounded by four As atoms and vice versa. In $Al_xGa_{1-x}As$, some Ga atoms in the crystal are substituted for Al, giving $Al_xGa_{1-x}As$ a very similar structure to GaAs but with a wider band gap (Fig. 1.1(a)) making it highly suitable to interface with GaAs. The $Al_xGa_{1-x}As$ layer is doped with Si donors while the GaAs remains undoped, and the structure is grown by a process known as molecular-beam epitaxy (MBE). At zero temperature, the chemical potential in the $Al_xGa_{1-x}As$ layer lies at the bound states of the donors, which is higher than the bottom of the conduction band of the GaAs layer. Fig. 1.1(b) illustrates the band structure of the two semiconductors before equilibrium is reached. Since the chemical potential must be constant throughout the structure at equilibrium, electrons bound to the donor states move into the GaAs conduction band in order to move the system towards equilibrium.

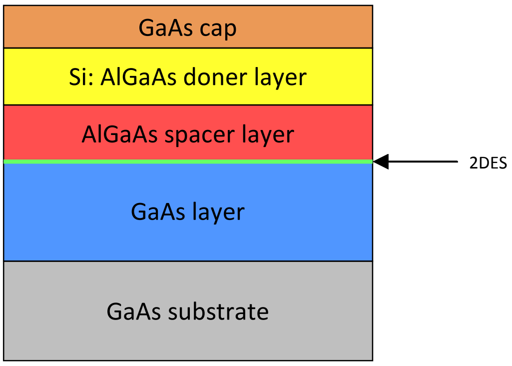

Figure 1.2. Schematic of a 2DES formed at the interface of the AlGaAs spacer layer and the GaAs layer in a GaAs/AlGaAs heterostructure.

This leaves the $Al_xGa_{1-x}As$ positively charged and the GaAs negatively charged and sets up an in-built electric field opposing further electron migration, resulting in equilibration of the chemical potential. The process causes the conduction bands of both layers to bend (as shown in Fig 1.1 (c)) to compensate for the movement of charge carriers. As the GaAs conduction band edge bends it dips below the chemical potential forming a quantum well with a typical width comparable to the wavelength of electrons at the chemical potential, $\lambda_\mu \sim$ 10 nm. The mobile electrons which are now in the GaAs well are trapped in the vicinity of the interface. Coulomb attraction prevents the electrons from moving away from the interface and into the GaAs, while the band edge discontinuity prevents electrons from moving back into the $Al_xGa_{1-x}As$ layer. The movement of the trapped electrons is therefore restricted to the plane of the interface and forbidden in the perpendicular direction.

2DESs of the form described above are subject to random potential scattering from the ionized donors left behind in the AlGaAs layer. The effect of the impurity potential can be reduced by placing a layer of undoped AlGaAs, commonly referred to as a spacer layer, between the doped AlGaAs and undoped GaAs layers to cut off the core of the random potential fluctuations originating from the ionized donors in the AlGaAs layer. This modification allows for very high electron mobilities to be achieved. Fig. 1.2 illustrates a typical GaAs/AlGaAs heterostructure. The growth process begins with the growth of a high quality layer of GaAs on top of a GaAs substrate in the chamber of an MBE machine, followed by the AlGaAs spacer layer. These two layers form the interface at which the 2DES is formed. The Si doped AlGaAs layer is then grown on top of the spacer layer and finally the heterostructure is capped with a thin layer of GaAs. The cap layer is important because the fabrication of these heterostructures into devices usually requires the deposition of some material on top of the sample surface and it is therefore necessary to have a layer separating the Si doped AlGaAs and these deposits. The cap layer prevents oxidation that would occur if AlGaAs is exposed to air.

The invention of MBE, beginning with the concept of modulation-doping introduced by Stormer [23], has allowed for significant progress in producing high quality 2DESs which have made possible a range of discoveries in condensed matter systems.

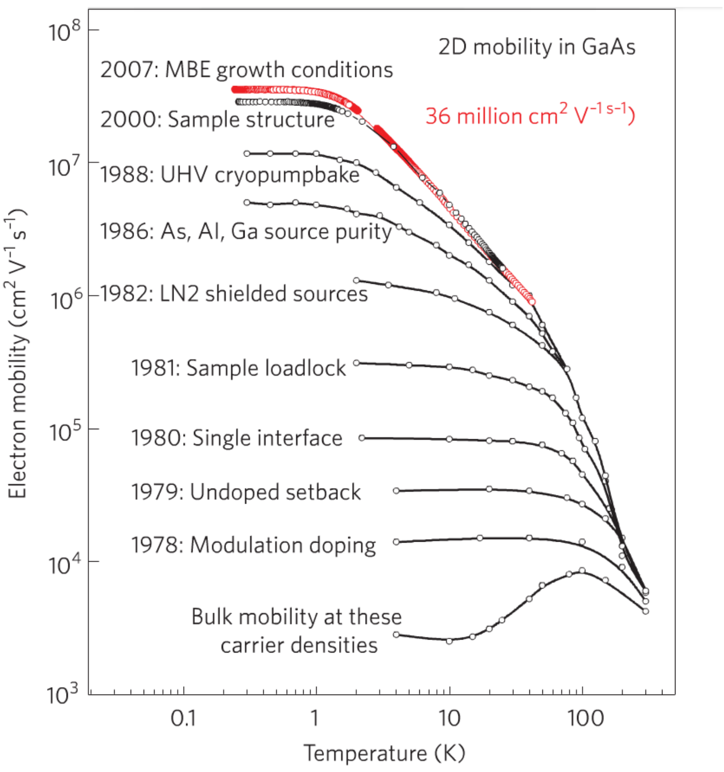

Figure 1.3. The history of improvements of electron mobility for GaAs based heterostructures over the last three decades taken from Ref. [24], and annotated with technical innovation responsible for the improvement.

Improvements in the MBE technique, which have largely been achieved by eliminating unwanted or unintended charged impurities in the MBE vacuum, have led to a significant increase in the low temperature bulk mobility of charged carriers from roughly $5 \times 10^3 \mathrm{cm}^2/\mathrm{Vs}$ in 1977 to $36 \times 10^6 \mathrm{cm}^2/\mathrm{Vs}$ by 2008 (see Fig. 1.3), a remarkable 7000 times increase in low temperature mobility. The great pace of progress is expected to continue with a possible $100 \times 10^6 \mathrm{cm}^2/\mathrm{Vs}$ mobility being achieved in the near future [25]. These improvements in mobility have been crucial to the study of condensed matter systems as they make it possible for quantum effects, previously hidden in low quality samples, to be observable in the cleaner and higher quality samples grown using the improved techniques.

1.2.2 Density of states

The band structure of the GaAs/AlGaAs heterostructure described above forms a triangular quantum well (Fig. 1.1(c)) at the interface which contains the 2DES. The width of this quantum well (i.e. the length in z or direction perpendicular to the interface) is extremely thin ($\leq$10 nm). For the purpose of analysing the distribution of states, the barrier or electric potential on the AlGaAs side of the interface forming the 2DES can be considered to be infinite. One may then approximate the electric potential on the GaAs side to be linear as one moves away from the interface. This oversimplified description is the basis for the triangular potential approximation [20] for the energy states of wavefunctions in the z direction caused by the confinement of the system.

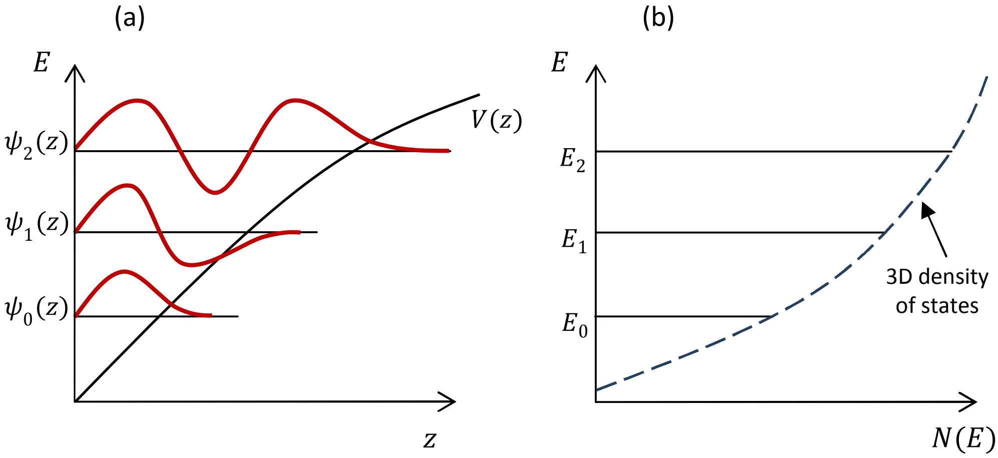

Figure 1.4. (a) A diagram of an approximation of the triangular quantum well that develops in GaAs/AlGaAs heterostructure where $V(z)$ describes the potential barrier moving away from the interface and in the GaAs layer. Only wavefunctions that satisfy the boundary conditions of the well can exist within the well. (b) Discrete density of states occurs at the corresponding energies found within the potential well.

The wavelengths of the carriers in the well must be comparable to the width of the well (as defined by the confining electric potential) and therefore carrier motion perpendicular to the interface cannot be viewed in a classical manner but must be quantized into discrete energy levels according to the Fermi wavelength, as illustrated in Fig. 1.4. It can be seen in Fig. 1.4(a) that only certain discrete energy levels that fulfil the wavelength and boundary condition in the z direction imposed by the well can exist within the well.

Without any excitation, motion in the z direction is impossible but carriers are still free to move in the plane of the interface, meaning that each discrete energy level in the z axis constitutes a subband of energies in the $x - y$ plane which exist due to the kinetic energy of carriers in that plane. Based on the description of an unconfined electron in free space by the Schrödinger equation, the energy spectrum of a single subband in a 2DES is shown to be,

$$E = \frac{\hbar^2 k^2}{2m} = \frac{\hbar^2}{2m}({k_x}^2 + {k_y}^2), \tag{1.1}$$

where k_x and k_y are the wave-vector components for motion parallel to the interface. In this two-dimensional plane, the number of states in the wave-vector space is given by $(2\pi)^{-2}$, and accounting for spin degeneracy the density of states is given as

$$D(\boldsymbol{k}) = \frac{2}{(2\pi)^2}. \tag{1.2}$$

Using polar coordinates, $d\boldsymbol{k} = k^2 sin\theta dk d\theta$, and from Eq. (1.1), the density of states is expressed in terms of energy as

$$D(E) = \frac{m}{\pi\hbar^2}. \tag{1.3}$$

Eq. (1.3) suggests that the density of states in a subband of a 2DES is constant and independent of energy. This is a fundamental feature of a 2DES which makes it extremely useful for studying quantum-mechanical effects.

As the triangular quantum well begins to fill up with carriers from ionized donors in the Si:AlGaAs layer, the states at the lowest subband E_0, are the first to be populated. If the carrier concentration is low enough, then only the first subband will be filled and the system behaves like a quasi 2DES. At higher numbers of carriers, however, more than one subband will be filled and this leads to parallel conduction of different planes within the 2DES and non-ideal two-dimensional conditions.

1.2.3 Disorder in 2DESs

Even though advancements in the growth of semiconductor heterostructures have produced some of the highest quality 2DESs formed to date, electron transport in 2DESs is still vulnerable to some amount of disorder which introduces random potential fluctuations into the system.

Disorder in 2DESs can be divided into Coulomb induced disorder and non-Coulomb disorder. The dominant source of disorder in 2DES formed from a GaAs/AlGaAs heterostructure originates from the remote ionized donors in the Si:AlGaAs layer [26]. The potential arising from these ionized donors can scatter electrons within the 2DES introducing disorder into the system. However, since these charged centres are separated from the 2DES by a spacer layer, the 2DES only experiences the tail end of a decaying $(1/r)$ potential. This is known as a long-range induced disorder. This disorder can be reduced by increasing the width of the spacer layer, though the donor layer must remain close enough to maintain a reasonable electron density. High electron density systems are more able to efficiently screen random potential fluctuations (the effects of screening on the potential landscape of a 2DES are discussed in more detail in Chapter 4). The doped silicon therefore plays the dual role of the source of both carriers and disorder.

An additional source of Coulomb disorder arise from the background ionized impurities in the GaAs layer itself. The prominence of this source of disorder depends on the purity of the GaAs layer which usually stems from the MBE chamber within which the growth takes place. In high quality 2DESs grown in modern MBE machines, this is usually negligible and is less of a concern.

Sources of non-Coulomb disorder include phonon induced deformations, surface roughness and alloy disorder. Phonons in the system originate from thermally induced vibrations which distort the lattice. This kind of disorder is greatly reduced (but still present) at low temperatures typically below 1 K.

Interface roughness is responsible for a small amount of scattering. Roughnesses at the interface arise owing to imperfect lattice matching between the GaAs and AlGaAs but are usually negligible in GaAs/AlGaAs systems.

In a typical GaAs/AlGaAs heterostructure, about 30% of Ga atoms are substituted by Al in the AlGaAs layer, but these replacements occur randomly. The resulting alloy therefore contains a non-periodic potential and thus introduces alloy disorder scattering. Random potentials of this form cause scattering on an atomic length scale. This type of disorder is therefore referred to as short-range disorder since it causes scattering to occur on a length scale comparable to length between atoms (as opposed to long-range disorder discussed above). The 2DES in GaAs/AlGaAs heterostructures almost entirely resides in the GaAs side of the interface, but the exponentially vanishing tails of the electron wavefunction in the 2DES penetrates into the AlGaAs alloy and produces a small amount of electron scattering. Once again, scattering from this form of disorder is usually irrelevant in a typical GaAs/AlGaAs heterostructure. In Chapter 3, however, alloy disorder is employed extensively in creating short-range systems. We shall see that increasing the short-range disorder within a typical GaAs/AlGaAs system has profound consequences on the nature of quantum Hall transitions in a 2DES.

1.2.4 Measurement of transport coefficients in a 2DES

Based on the effect of the simultaneous conditions of both an applied in-plane electric field $\boldsymbol{E}$ and a magnetic field $\boldsymbol{B}$ perpendicular to plane of the 2DES, we consider the conductivity and resistivity of a 2DES for the current component in the direction parallel to $\boldsymbol{E}$, the *diagonal component*, and the component in the direction perpendicular to $\boldsymbol{E}$, the *Hall component*.

Fig. 1.5. shows a schematic of a typical device, known as a Hall bar, used to perform these measurements. The 2DES is fabricated into the illustrated pattern (see section 2.1.1 for the detailed fabrication process) and a current (or an electric field) is applied from the S to D Ohmic terminals, while simultaneously measuring the voltage between either A and C or A and B.

When a magnetic field is applied to a 2DES, the motion of carriers in an electric field is no longer strictly parallel to $\boldsymbol{E}$ but exhibits an orbital motion as a result of the Lorentz force. The resistivity ρ and conductivity σ are no longer scalar but instead are tensors which describe the two dimensional nature of the motion of carriers. A current density $\boldsymbol{j}$ and the applied field $\boldsymbol{E}$ are related by, $\boldsymbol{j} = \boldsymbol{\sigma E}$ or where σ_{xx} represent the diagonal conductivity in the direction of $\boldsymbol{E}$ (terminals A-B), and σ_{xy} represents the Hall conductivity perpendicular to $\boldsymbol{E}$ (terminals A-C).

$$\begin{pmatrix} j_x \\ j_y \end{pmatrix} = \begin{pmatrix} \sigma_{xx} & \sigma_{xy} \\ \sigma_{yx} & \sigma_{yy} \end{pmatrix} \begin{pmatrix} E_x \\ E_y \end{pmatrix}, \tag{1.4}$$

If the 2DES is isotropic (a reasonable assumption) then from the symmetry of the kinetic coefficients, $\sigma_{xx} = \sigma_{yy}$ and $\sigma_{yx} = -\sigma_{xy}$.

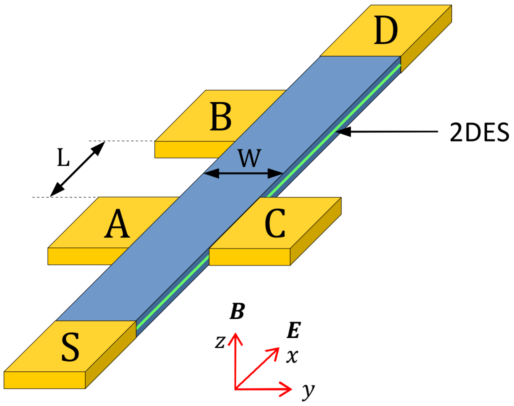

Figure 1.5. Diagram of a Hall bar made out of a 2DES (GaAs/AlGaAs heterostructure) used to measure transport coefficients. The x, y, z axes are shown including the direction of the electric field $\boldsymbol{E}$ and the magnetic field $\boldsymbol{B}$.

The resistivity tensor is an inverse matrix of $\boldsymbol{\sigma}$ and given as

$$\begin{pmatrix}\rho_{xx} & \rho_{xy}\\ \rho_{yx} & \rho_{yy}\end{pmatrix} = \begin{pmatrix}\sigma_{xx} & \sigma_{xy}\\ -\sigma_{xy} & \sigma_{xx}\end{pmatrix}^{-1} = \frac{1}{{\sigma_{xx}}^2+{\sigma_{xy}}^2}\begin{pmatrix}\sigma_{xx} & -\sigma_{xy}\\ \sigma_{xy} & \sigma_{xx}\end{pmatrix}, \tag{1.5}$$

Conversely, $\boldsymbol{\sigma}$ can be expressed in terms of $\boldsymbol{\rho}$ as

$$\begin{pmatrix}\sigma_{xx} & \sigma_{xy}\\ \sigma_{yx} & \sigma_{yy}\end{pmatrix} = \frac{1}{{\rho_{xx}}^2+{\rho_{xy}}^2}\begin{pmatrix}\rho_{xx} & -\rho_{xy}\\ \rho_{xy} & \rho_{xx}\end{pmatrix}. \tag{1.6}$$

The Hall and diagonal resistivity or conductivity can therefore we written as

$$\rho_{xy} = \frac{\sigma_{xy}}{{\sigma_{xx}}^2+{\sigma_{xy}}^2} \quad \text{or} \quad \sigma_{xy} = \frac{\rho_{xy}}{{\rho_{xx}}^2+{\rho_{xy}}^2}, \tag{1.7}$$

and

$$\rho_{xx} = \frac{\sigma_{xx}}{{\sigma_{xx}}^2+{\sigma_{xy}}^2} \quad \text{or} \quad \sigma_{xx} = \frac{\rho_{xx}}{{\rho_{xx}}^2+{\rho_{xy}}^2}. \tag{1.8}$$

In order to evaluate Eqs. (1.7) and (1.8), both the Hall and diagonal resistivity must be measured based on the physical dimensions of the Hall bar device illustrated in Fig. 1.5.

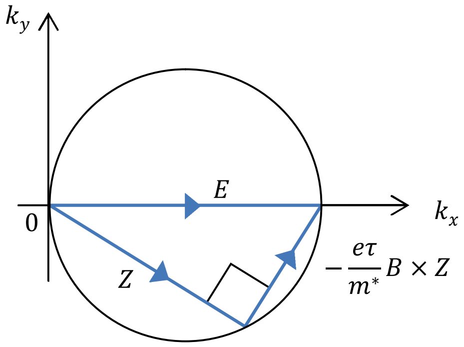

Figure 1.6. The locus of the Hall vector as a function of magnetic field (black circle)

The diagonal resistivity is determined using the applied electric field and current density in the diagonal direction, $\rho_{xx} = E_x/j_x$, where $E_x = V_{AB}/L$ (V_{AB} is voltage applied between terminals A and B) and $j_x = I_x/W$ (I_x is the current measured along S and D). The dimensions L and W are shown in Fig. 1.5. ρ_{xx} therefore can be calculated from

$$\rho_{xx} = \frac{V_{AB}\, W}{L\, I_x}. \tag{1.9}$$

Similarly, the Hall resistivity from $\rho_{xy} = E_y/j_x$ where $E_y = V_{AC}/W$ yields

$$\rho_{xy} = \frac{V_{AB}}{I_x} = R_{xy}. \tag{1.10}$$

We see from Eq. (1.10) an interesting characteristic of 2DESs, the Hall resistivity coincides with the Hall resistance, and in addition, they are both independent of any physical dimensions of the system.

A classical analysis of conductivity can be evaluated using the Drude formalism. First, we introduce a component known as the Hall vector $\boldsymbol{Z}$ which takes into account both the effects of the electric field and the magnetic field on the current density,

$$\boldsymbol{j} = \sigma_0 \boldsymbol{Z}, \tag{1.11}$$

where $\sigma_0 = n\frac{e^2\tau}{m^*}$, the Drude conductivity. The electric field can be described in terms of the Hall vector (see Fig. 1.6) as

$$\boldsymbol{E} = \boldsymbol{Z} - \frac{e\tau}{m^*}\boldsymbol{B} \times \mathbf{Z}. \tag{1.12}$$

Substituting Eq. (1.11) into (1.12) yields,

$$\boldsymbol{E} = \frac{\boldsymbol{j}}{\sigma_0} - \frac{e\tau}{m^*}\boldsymbol{B} \times \frac{\boldsymbol{j}}{\sigma_0}. \tag{1.13}$$

which can be expressed as the following tensor

$$\begin{pmatrix} E_x \\ E_y \end{pmatrix} = \begin{pmatrix} \frac{1}{\sigma_0} & \frac{e\tau}{m^*}\frac{1}{\sigma_0}B \\ -\frac{e\tau}{m^*}\frac{1}{\sigma_0}B & \frac{1}{\sigma_0} \end{pmatrix} \begin{pmatrix} j_x \\ j_y \end{pmatrix}. \tag{1.14}$$

It is observed that Eq. (1.14) contains the resistivity tensor ($\boldsymbol{E} = \boldsymbol{\rho j}$) where the diagonal resistivity is $\rho_{xx} = \frac{1}{\sigma_0}$ and the Hall resistivity is $\rho_{xy} = \frac{e\tau}{m^*}\frac{1}{\sigma_0}B = \frac{B}{en}$. This result predicts that the diagonal resistivity is independent of the magnetic field while the Hall resistivity is linearly dependent on the magnetic field.

This is the classical case of a 2DES under a magnetic field. We discuss the quantum-mechanical scenario in the next section.

1.3 Theory of Localization

Localization in charged particle systems is the concept that describes the spatial restriction imposed on single-particle wavefunctions in a disordered quantum mechanical system. The theory proposes that at the absolute zero of temperature the amplitude of a wavefunction of a charged particle can be exponentially localized or confined within a finite region of space given a sufficient amount of disorder. The consequence of this limitation on the displacement of charged particles within a system is manifested in a variety of physical phenomena that have profound effects on the transport properties of these charged particles. The work presented in this thesis is underpinned by various localization effects and in the sections below we explore the nature and theory of electron localization.

1.3.1 Localized and extended states

For a perfectly periodic crystal with no defects or impurities, it can be shown [27] that the solution of the one-electron Schrödinger equation results in a plane wave modulated by the periodicity of the lattice. This is known as Bloch's theorem. Due to the energy they possess, electrons found in such a crystal are arranged in *energy bands* separated by regions for which no wavelike electron orbitals exist [27]. These forbidden regions are known as energy gaps or band gaps. Electrons fill up states within the allowed regions of the energy spectrum, with electron possessing the lowest energies occupying states at the bottom of the band while those of the highest energy occupy states higher up the band. Each energy level within the energy band can be described by a wave vector. Electrons occupying the highest energy level (known as the Fermi level) of the energy band respond to an applied electric field as if they possess an effective mass m^* and are able to freely propagated within the system. Since electrons within this system are represented by plane wavefunctions with perfect periodicity, the probability of finding an electron within this system is the same for all locations. In this sense, electrons are considered to be delocalized and the energy states they occupy are referred to as *extended states* since their wavefunctions extend (with equal probability) throughout the entire system.

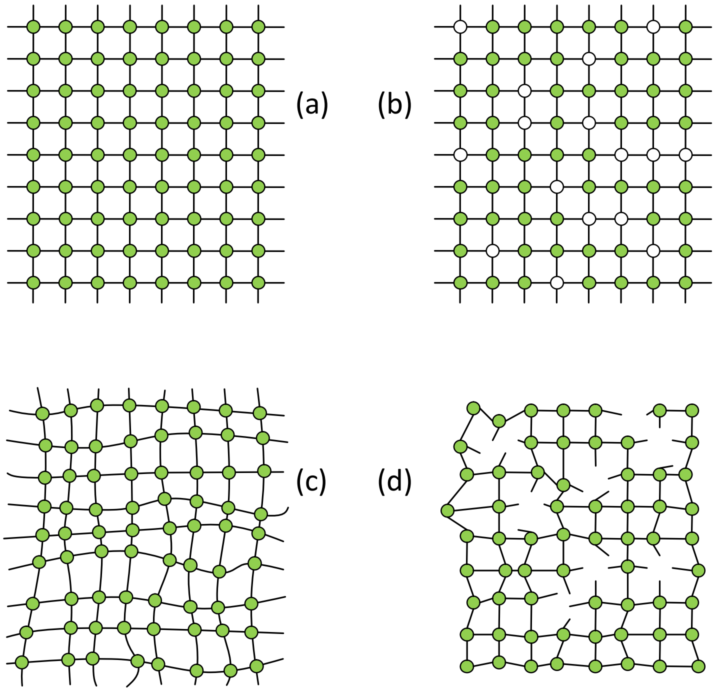

Figure 1.7: Possibly types of lattice disorder. (a) ordered lattice, (b) mixed-crystal formation of two different atoms in a lattice, (c) positional disorder through distortion of lattice, and (d) topological disorder with spontaneous formation of dangling bonds.

The Bloch formalism, which leads to extended states, applies to crystals with a period lattice and with little or no defects. However, in reality this crystalline state is the exception rather than the rule, particularly in semiconductors where impurities play an important role. Imperfection or disorder in crystalline materials exists in varying degrees and different forms. The most important crystalline imperfections are caused by chemical impurities, vacant sites, and interstitial atoms. Some of the effects of these imperfections on the lattice structure are described in Fig. 1.7. All these imperfections share a common feature of producing bound states that can bind to or release electrons [28]. If one considers a periodic lattice structure, the periodicity of this structure will be perturbed by defects in the lattice.

A single defect in an otherwise periodic potential will lead to a splitting off of one state from the band of extended (Bloch) states (see Fig. 1.8(a)). Electrons can be bound or repelled by this defect state and thus the state acts as a trap for electrons or holes. An electron occupying this isolated split-off state will be *localized* and its wavefunction vanishes rapidly as one moves away from the localized site. Since there is likely no correlation (periodic arrangement) between the defects that create these localized states, the spatial probability of find an electron occupying a localized state is not evenly distributed throughout the system, as with Bloch or extended states, but are resolved to a finite region of space. Localized states therefore cannot contribute towards dissipative conductivity at zero temperature. As the number of defects (disorder) increases, the density of states of the energy band takes on a Gaussian shape as shown in Fig. 1.8(b).

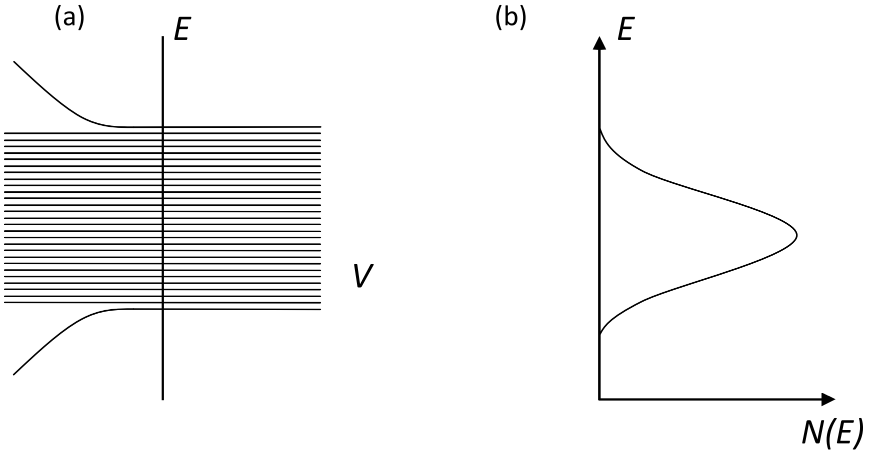

Figure 1.8: (a) The energy band of a simple periodic potential model as a function of the deviation V of the defect potential from the potential of an undisturbed lattice. The split off state is spatially localized to the vicinity of the defect. (b) The density of states of band of energy with many defects. The defects produce a Gaussian shaped band where all states are localized with the exception of states at the centre of the band.

States within the tail regions on the band are localized while only states at the centre of the band remain extended.

A convenient distinction between localized states and extended states arises when we consider the spatial extension of the wavefunctions of these states. As discussed above, for a perfect crystalline lattice the probability of finding an electron within the system is the same for all locations. An electron in such a system can propagate without being scattered throughout the entire system, in other words, the mean free path extends over the entire length of the system. Disorder can be introduced into this model through the distortion of the perfect lattice; phonon induced scattering, impurity scattering or other mechanisms that cause an electron wavefunction to lose its phase coherence. As the degree of disorder increases, the mean free path reduces. A sufficient increase in disorder however, can lead to localized states where an electrons occupying such a state is restricted to finite and small regions within the system. The extent of localization of wavefunctions can be described by a localization length ξ, which will be large as the system size for extended states and vanishingly small for localized states.

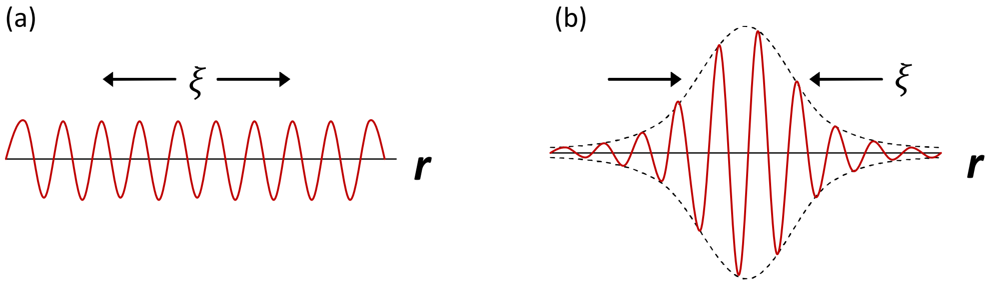

Figure 1.9: A description of localized and extended states. (a) Wavefunction of an extended state with a localization length that extends to infinity. (b) Wavefunction of a localized state, the amplitude if the wavefunction is maximum within a finite region of space but vanishes exponentially as *r* goes to infinity.

This provides a simple criterion for differentiating between the two types of wavefunctions. A description of the two types of wavefunction is shown in Fig. 1.9. A more detailed description of localization is discussed in the following section.

1.3.2 Anderson Localization

In 1958 Anderson [29] was the first to prove that a sufficient amount of disorder would result in a lattice with no diffusion of charge carriers and thus an absence of extended states. This was not at all apparent at the time as it was considered that an increase in disorder would simply lead to a reduction in the mean free path, but the states would remain extended and electrons will still diffuse to infinity given $t \to \infty$. The model used by Anderson also provided the first quantitative definition of localization.

He considered a perfect lattice with each site occupied by one atom, each with a single energy state E_n. Given the perfect periodicity of the lattice, a regular and periodic potential (as shown in Fig. 1.10(a)) will be felt by an electron moving through the lattice. This will result in a tight binding energy band of width B with extended states based on the Bloch formalism described above. Disorder in the form of a random potential was then introduced such that E_n at each site takes on a value statistically distributed over a range of potential of width V_0 as shown in Fig. 1.10(b). Anderson showed that if the value V_0/B is greater than a certain critical value $(V_0/B)_{crit}$, the solution for the Schrödinger equation for any energy in the band will no longer result in an extended Bloch state but will be localized in space. As a result, the probability of an electron remaining at its current location as $t \to \infty$ is very large value.

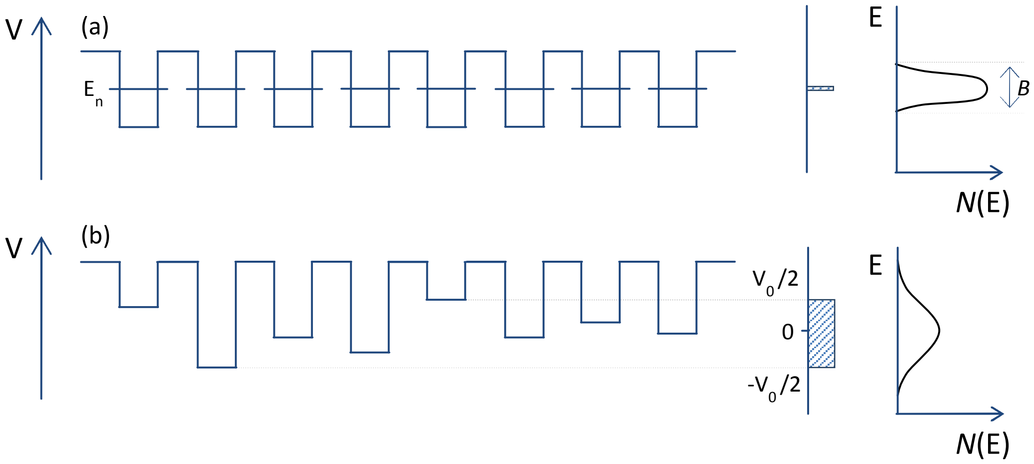

Figure 1.10. Anderson model: (a) Potential wells of equal depth in a near perfect lattice with a tight binding band of energy of width B. (b) Potential wells in a disordered lattice with potential fluctuation statistically distributed over a range of width V_0.

In other words, without any elementary excitation it becomes likely that an electron will never move from its current site. The localized wavefunction as described by Anderson has the following form [30];

$$|\psi(\boldsymbol{r})| \sim \exp\left(-\frac{|\boldsymbol{r}-\boldsymbol{r_0}|}{\xi}\right) \tag{1.15}$$

where ξ is the localization length (as described above) and $\boldsymbol{r}$ is some distance in space away from the location $\boldsymbol{r_0}$ of the localized state.

Mott [31] first pointed out that even if V_0/B lies below the critical value, localized states will nonetheless exist near the extremities (tail regions) of the energy band since any amount of disorder, however small, will create some localized states. Mott also showed that an energy E_μ, must mark the boundary between the localized states and extended states within the energy band. The critical energy E_μ, was later referred to as the mobility edge [32]. As shown in Fig. 1.11, a mobility edge can be found at both ends of the disorder energy band. As the range of distribution of the potential V_0, is increased (corresponding to increased disorder), $E_\mu$on both sides of the band approach each other until they merge at $(V_0/B)_{crit}$, at which point all states within the band are localized [31, 33]. Considering the left hand side of the energy band shown in Fig. 1.11, if the parameters of the system were to change such that the Fermi energy E_F, relative to the mobility edge moved from the regime in which $E_F < E_\mu$ to $E_F > E_\mu$, (i.e. E_F crosses over from the localized states into the extended states), we arrive at a metal-to-insulator transition (MIT) also known as the *Anderson transition* [33, 34]. If the Fermi energy lies in the extended regime, conductivity will be of a finite value as $T \to 0$. The system is therefore described as possessing metallic properties. If, however, E_F lies in the localized regime, the conductivity vanishes to zero as $T \to 0$.

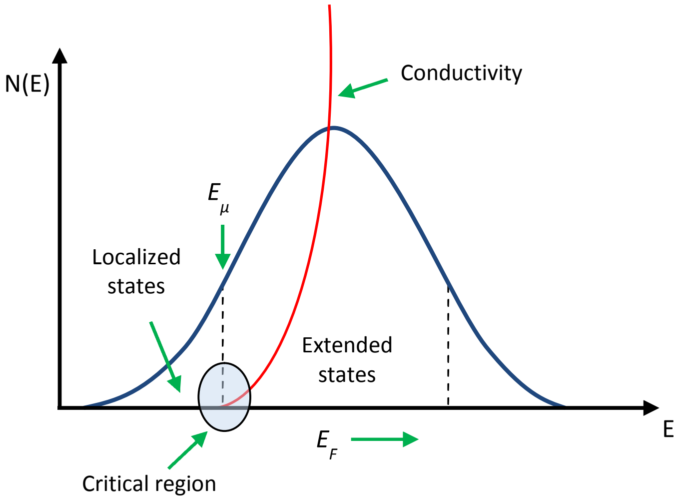

Figure 1.11. Density of states of a partially localized band where (on the left) all states are localized for $E_F < E_\mu$ and extended for $E_F > E_\mu$. Conductivity below E_μ is zero (at zero temperature) but of a finite value above E_μ. Increasing disorder will move the mobility edge on both sides towards each other until they merge at the centre of the band when the critical level of disorder is reached.

In this case, the system behaves as an insulator.

The position of E_F relative to E_μ can be changed by manipulating intrinsic properties of the system such as: compositional and impurity doping, changing the structural properties of the system, and by changing the carrier concentration. The transition can also be influenced by external factors such as the magnetic field, the temperature and the frequency of the applied electric field.

1.3.3 Transport in extended states of disordered systems

We begin the discussion on transport in disordered systems by first considering weakly disordered systems (such as the kind that can be approximated by unperturbed Bloch states) in which the majority of the electron states are extended. The electron transport theory of these systems, where the Fermi energy remains within the extended states, is based on the Boltzmann formalism whose condition applies if

$$\lambda \ll l, \tag{1.16}$$

where λ is the De Broglie wavelength and l is the mean free path. Boltzmann theory expresses the transport dynamics of a system in terms of acceleration and deceleration due to collisions with weakly scattering centres originating from a small degree of disorder. At finite temperatures the expression for conductivity from Boltzmann transport theory can be written [33] as,

$$\sigma = \int \sigma(E) \left(-\frac{\delta f(E)}{\delta E}\right) dE, \tag{1.17}$$

where $f(E)$ is the electron density function and $\sigma(E)$ is the energy dependent conductivity. The conductivity of the system is obtained by summing the expression in Eq.

(1.17) over all states in the energy band. In a weakly disordered system the Boltzmann formalism can be reduced [35] to Drude's expression for conductivity,

$$\sigma = \frac{e^2\tau}{m^*}n = e\mu n, \tag{1.18}$$

where e is the electric charge of the carrier, τ is the momentum relaxation time, m^* is the effective mass of the carrier, μ is the carrier mobility and n is the carrier density.

Contributions to conductivity from the extended states will be given by Eq. (1.18) but if the energy band includes localized states, at a sufficiently high temperature, carriers can be excited from localized states, across the mobility edge, and into extended states where the carrier will contribute towards the conductivity. This is known as activated conductivity and is given by the following expression [36],

$$\sigma_a \approx \sigma_0 \exp(-\frac{E_\mu - E_F}{k_b T}), \tag{1.19}$$

where σ_0 is the exponential prefactor which is determined by the conduction of states near the mobility edge. The term, $E_\mu - E_F$, is referred to as the mobility gap, and corresponds to the distance between the Fermi energy and the mobility edge.

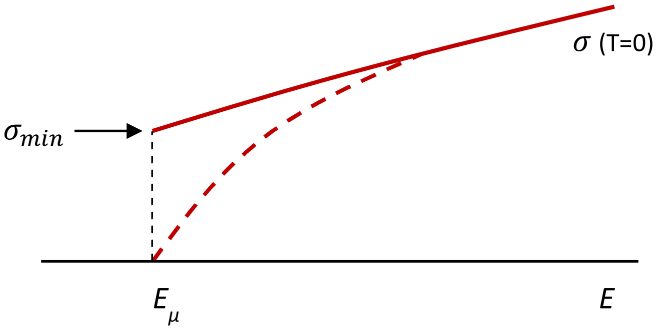

Figure 1.12. A schematic illustrating the mobility edge E_μ and its proposed relationship to conductivity. The solid line of conductivity describes an abrupt minimum conductivity as proposed by Mott, and the dashed line represents a continuous vanishing conductivity supported by scaling theory.

The mobility gap defines the minimum energy required for activated conductivity. It should be noted that this is a purely thermionic process and as a result σ_a tends to zero as $T \longrightarrow 0$.

An intriguing question emerges when, at $T = 0$, one considers what happens to conductivity as E_F crosses the mobility edge. Given that conductivity is expected to be zero in the localized regime and finite in the extended regime, will the transition be continuous or not? Based on the idea of Ioffe and Regel [37], Mott [38] argued that for an extended state, there is a minimum limit to metallic conductivity since the mean free path cannot be smaller than the interatomic spacing or k_F^{-1}. For a localized state on the other hand, the mean free path must be zero. Given that conductivity is zero on one side of the transition and of a non-zero value on the other side, Mott concludes that there must be a jump in conductivity at the mobility edge. This discontinuity in conductivity is depicted by the solid line in Fig. 1.12. This theory is, however, challenged by the one parameter scaling theory of localization which predicts a continuous transition as the Fermi energy approaches the mobility edge (dashed line in Fig. 1.12). The one parameter scaling theory will be discussed below in section 1.3.6.

1.3.4 Transport in localized states of disordered systems

The metallic conductivity described above for extended states is valid only if the mean free path is much larger than the De Broglie wavelength (Eq. (1.16)). It is clear that this condition is violated for localized states where electrons are restricted to finite regions in space. Conductivity in this regime is zero at zero temperature, but conductivity can be of a finite value at non-zero temperatures since transport maybe possible via phonon assisted hopping between localized states.

In the first instance we consider how an electron transition can occur between two neighbouring localized states, i and j at distances $\boldsymbol{R}_i$ and $\boldsymbol{R}_j$. From Eq. (1.15), the amplitude of the wavefunction of localized states decays exponentially from the centre. As a result there is a finite probability that a transition between these two states will occur by the tunnelling of an electron from one site to the other. The factor that determines the tunnelling probability is the integral of the overlap of the wavefunctions [28] of the two states (Fig. 1.13) and this probability increases as $R = |\boldsymbol{R}_i - \boldsymbol{R}_j|$ decreases. Assuming that the localization length is similar for both states, the tunnelling probability will have the form [30],

$$p_{ij} \propto \exp\left(-\frac{2R}{\xi}\right). \tag{1.20}$$

Though Eq. (1.20) describes a possible means of electron transport, without assistance from phonons it is unlikely that tunnelling alone would yield any conductivity as the nature of localization results in a statistical distribution of states over a relatively large range of energies, V_0/B.

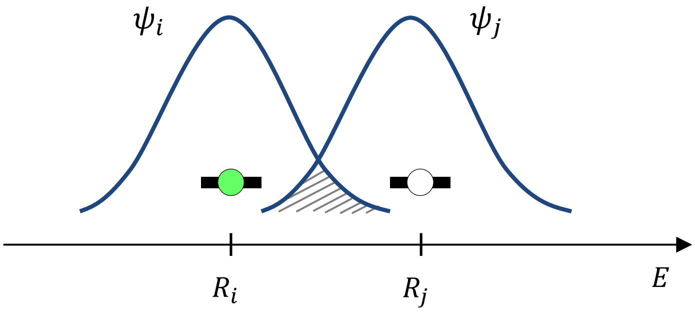

Figure 1.13. A diagram showing the overlapping wavefunctions of the neighbouring states i and j.

Distribution of states of this sort produces neighbouring states that may be close spatially but separated by comparatively large energies [30] as shown in Fig. 1.14(a). In the case of the transition between the localized states i and j, now accurately depicted in Fig. 1.14(b), the energy $W = W_j - W_i$ must be provided by a phonon. The hopping probability must therefore be modified to include the number of phonons of energy W available at thermal equilibrium. For sufficiently low temperatures ($k_b T \ll W$) this will be given by the Boltzmann factor, $\exp(-W/k_b T)$. The hopping probability can then be written as,

$$p_{ij} \propto \exp\left(-\frac{2R}{\xi} - \frac{W}{k_b T}\right). \tag{1.21}$$

Hops between localized states such as that described above, were first tackled by Miller and Abrahams [39]. In their seminal paper, Miller and Abrahams viewed the probability of each hop as a resistance, turning the problem into a random resistor network.

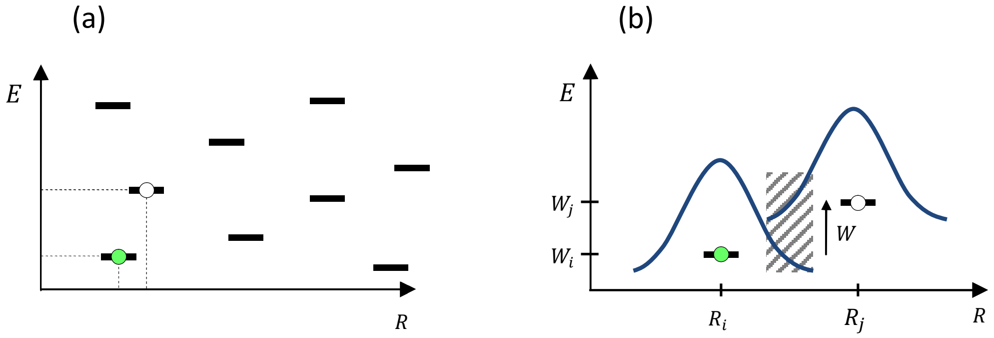

Figure 1.14. (a) The energetic and spatial distribution of states within a disordered system where states that are close in energy tend to be far in distance. (b) The overlap of wavefunctions displaying the required hopping energy.

They suggested that the overall resistance of the network was governed by certain one-dimensional critical resistor chains that connected one side of the network to the other. They assumed that hopping occurs between nearest-neighbour sites with the least resistance in the forward direction, and is determined solely by the spatial separation R, ignoring the energy separation W. However, as pointed out by various authors [40, 41], the paths produced by the Miller-Abrahams model leads to *hard hops*, or hops with distances much larger than the system's average hopping distance. In other word, the Miller-Abrahams model essentially leads an electron to dead ends.

Nonetheless, developing the nearest-neighbour idea of Miller and Abrahams further, if the spectrum of phonons available to the system allows for an average hopping distance of $\bar{R}$, some measure of electron transport can be achieved within the system. If $\bar{R}$ is very small (as compared with the mean nearest neighbour distance) it is clear that electron will still be effectively localized as at some point an electron would be confronted with a hard hop for which there are no phonons available with sufficient energy. However, if $\bar{R}$ should be gradually increased (by increasing the temperature of the system), a point is reached, $\bar{R} = R_c$, at which a set of localized states can be connected from one side of the system to the other. This forms a continuous path which enables some amount of dissipative conductivity. These two scenarios are described by Fig. 1.15. If the energy required for an averaging hopping distance of R_c to be achieved is W_c then conductivity of this nature can be described as [28],

$$\sigma = \sigma_f \exp(-\frac{W_c}{k_B T}). \tag{1.22}$$

This mechanism of electron transport within localized systems is known as *fixed range hopping* (FRH) [28] since it is based on jumps that are, on average, of fixed distances.

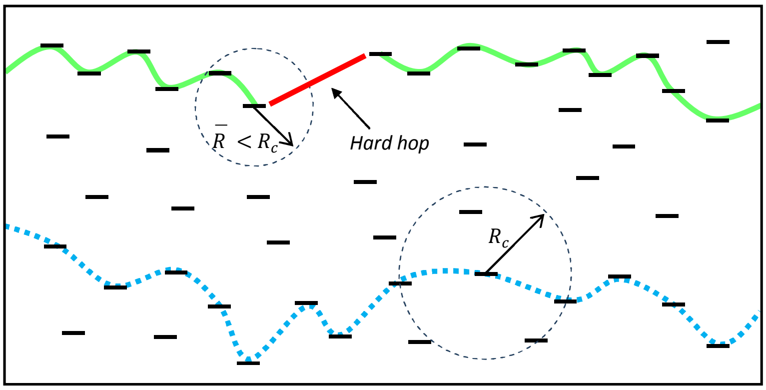

Figure 1.15. A diagram of nearest neighbour hopping showing two scenarios. The solid line demonstrates the case where $\bar{R} < R_c$. Electrons in this scenario encounter *hard hops* which inhibit dissipative conductivity. The dashed line illustrates the case for $\bar{R} > R_c$ where a continuous path across the entire system exists and dissipative conductivity is possible.

Mott [42] noted that as the temperature drops and phonons of energy W_c are no longer available, transport is still possible within a narrow band of energies near the Fermi level. However, unlike FRH, this kind of conductivity comprises hops of varying lengths, typically larger than the mean separation between nearest neighbour ($\bar{R} > R_c$).

Mott considered only energies around the Fermi level, as at very low temperature it is the likeliest location for filled and empty states to be in close energetic proximity of each other. At such low temperature, the available phonons only permit small changes in energy for each hop. As a result, conduction takes place over a very narrow range of energies around the Fermi level (see Fig. 1.16). The width of the band of energies within which hopping occurs, shown in Fig. 1.16 as $2\Delta E$, is determined by the temperature; the lower the temperature, the narrower the width and vice versa.

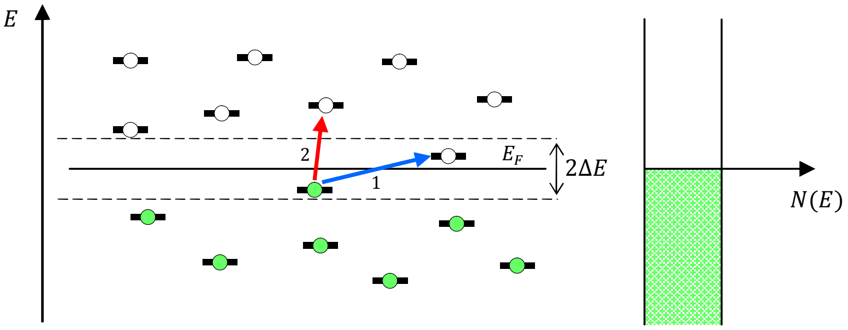

Figure 1.16. Conduction band containing states separated by the Fermi level. $2\Delta E$ represents the band of energies within which phonons are available to mediate hopping. Given such a narrow band, electrons will prefer to hop to longer and varying distances in order to find available site as shown by arrow 1, than to hop to nearer but energetically higher sites as illustrated by arrow 2.

If one assumes a constant density of states at the Fermi level, the conductivity in this low temperature regime is defined as [33],

$$\sigma = \sigma_0 \exp[-(T_0/\mathrm{T})^{1/(d+1)}], \qquad T_0 = \frac{C}{k_b N(\mu)\xi^3}, \tag{1.23}$$

where d is the dimensionality of the system, $N(\mu)$ is the density of states at the Fermi level and C is a numerical coefficient. It should be noted that the assumption of a constant density of states at the Fermi level is not always valid. The issue will be discussed further in the section 2.3.1. Since available states for hopping within this narrow band will be rare, the hopping distances will vary depending on the location of available empty states. Electrons will prefer to hop to empty states that further away in distance but require a smaller change in energy than to hop to states that close in distance but require a larger change in energy (see Fig. 1.16). This kind of conduction is known as *variable-range hopping* (VRH). Eq. (1.23) is more famously known as Mott's $T^{-1/4}$ law.

As has been discussed, there are various possible mechanisms responsible for conductivity within localized states. The dominant mechanism at any moment in time depends on the temperature of the system. At very high temperatures, electron are able to hop from one site to practically any other side, conductivity of this sort is more akin to metallic conductivity. As the temperature is reduced, FRH takes over as the dominant transport mechanism where the hopping distance is fixed. At even lower temperatures there is a crossover from FRH to VRH.

1.3.5 Weak localization and single parameter scaling

The presence of disorder in solids produces profound effects usually associated with randomness or non-periodic potential caused by disorder. A sufficiently small degree of randomness in a system can produces coherent quantum mechanical backscattering which gives rise to a rich variety of quantum transport phenomena such as the logarithmic increase of the resistances of thin metal films with decreasing temperatures [43], universal conductance fluctuations [44] and metal-insulator transitions [45].

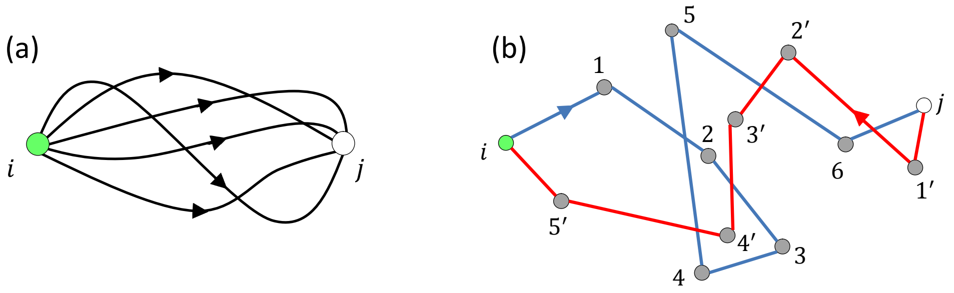

Figure 1.17. (a) Diagram showing an example of the quantum mechanically possible paths through which a transition between sites i and j can occur. (b) A graphical representation of backscattering of electron transport between sites i and j.

In the above discussions on electron transport, we indirectly adopted a particle view of transport for simplicity. In reality a transition between two sites would involve considering all the possible paths, however unlikely, a charged particle could use to achieve a transition from $\boldsymbol{R}_i$ to $\boldsymbol{R}_j$ as shown in Fig. 1.17(a). Coherent backscattering can then be understood as the interference of the different quantum mechanically allowed paths between $\boldsymbol{R}_i$ and $\boldsymbol{R}_j$. In particular, due to the multiple paths between two sites, an electron can be backscattered to its point of origin as illustrated in Fig. 1.17(b). The interference of waves travelling along time revered loops introduces a quantum correction to conductivity which is responsible for the quantum phenomena listed above. These effects occur in a regime where scattering events are predominately elastic and the phase coherence time is much larger than the elastic scattering time. This is known as the *weak localization* regime.

One of the most important works to emerge from the study of weak localization is the single parameter scaling theory [46]. It is based on the initial work of Thouless [47] who attempted to provide a practical description of localization in finite-size systems (as oppose to Anderson's mathematical definition). Thouless redefined the meaning of conductance of these systems in terms of Anderson localization and how it relates to Ohmic conductance.

Thouless imagined a system or solid made up of many blocks of size L^d (Fig. 1.18) where d is the dimension of system. If we consider the conductivity of just one of these blocks, a wave-packet moving from one end of the block to the other will exhibit a classical diffusive behaviour. In the first instance the packet will diffuse independent of the boundary conditions as if the block was of infinite length.

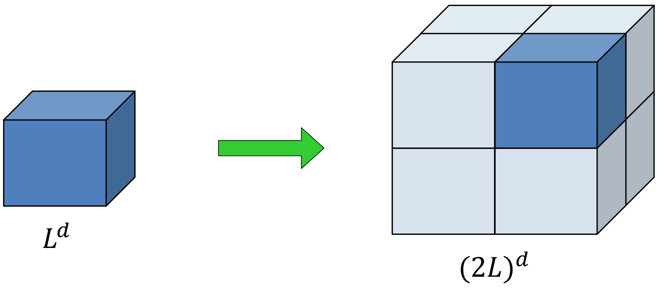

Figure 1.18. Thouless' concept of scaling where a system is made out of blocks of size L^d.

After a time t_D the wave-packet will arrive at the opposite boundary. The diffusion time is defined by,

$$t_D = L^2/D, \tag{1.24}$$

where D is the diffusion constant. According to the uncertainty principle, the energy level of the packet will be smeared or can be shifted by an amount of the order

$$\Delta E \approx \hbar/t_D, \tag{1.25}$$

after travelling for a time t_D. If two similar blocks $(2L^d)$ are joined end to end, the probability of the wave packet being transmitted (or reflected at the boundary) from the first block to the second block will depend on the typical spacing between energy levels within the block δW, and the coupling between energy levels in the two blocks, ΔE. If $\Delta E > \delta W$, the wave-packet will be in insensitive to the boundary [48] since the change in energy between the two blocks is within the energy the shift ΔE (uncertainty band-width of the level). The wave-packet will therefore be extended within the enlarged (two block) system. Conversely, if $\Delta E < \delta W$, the wave-packet will be reflected at the boundary and will remain localized within the first block.

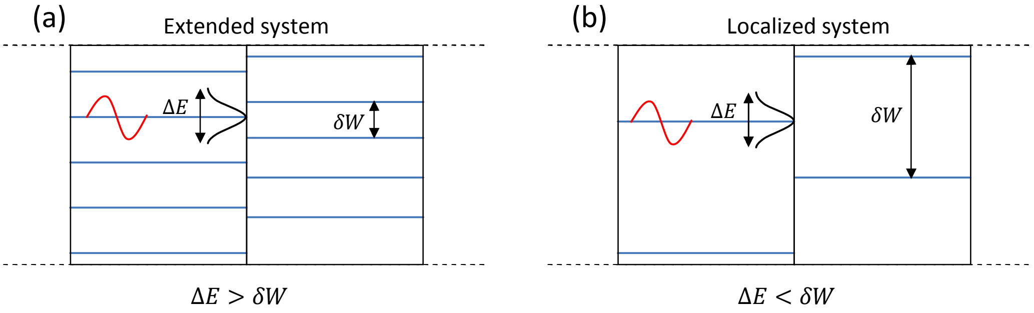

Figure 1.19.A schematic illustrating boundary conditions defining extended and localized systems. (a) In systems where $\Delta E > \delta W$, wavefunctions are able to transfer from one unit block to another making wavefunctions within the system extended. (b) In systems where $\Delta E < \delta W$, wavefunctions are reflected at the boundary and stay within the unit block. Such a system will be localized.

These two scenarios are described in Fig. 1.19. The scaling of the size of the system can be related to the conductivity of the system by considering the ratio,

$$\delta = \frac{\Delta E(L)}{\delta W(L)}. \tag{1.26}$$

If δ is exponentially small within a block, states will be localized in the larger system but if δ is large within a block, it will be extended in the larger system. Eq. (1.26) is known as Thouless' criterion or number. Sensitivity to boundary conditions appear to be a single parameter controlling the nature of transport within the system as its size is increased.

Combining Einstein's relation for conductivity, $\sigma = e^2 D \frac{dn}{dE}$, with Eq. (1.25), δ can be expressed in terms of electrical conductance G [49] by,

$$g = \frac{\hbar}{e^2} G \cong \delta, \text{ where } G = \sigma L^{d-2}. \tag{1.27}$$

The crucial point emphasized here is that the scaling behaviour of a system in terms of conductance is related to a physical measureable quantity (Eq. (1.27)) and is determined by a single parameter (Eq. (1.26)).

1.3.6 The scaling theory of localization

The scaling theory of localization tries to understand the localization problem by considering the behaviour of the conductance g as a function of system size L. The following analysis was first presented in the seminal paper by Abrahams, Anderson, Licciardello and Ramakrishnan [46]. This approach to localization provides a description of transitions between extended and localized states. Considering a block (L^d) of infinitesimal size, it is noted that all states will effectively be extended (this assumes that $\xi > L$ which is reasonable for a system of infinitesimal size). From the discussion on the Thouless criterion above, as the size of the system is increased, states in the block will emerge as either extended or localized in the larger system. Transitions between localized and extended states can therefore be examined by simply considering the effect of an increasing L on $g(L)$. This forms the basis of the scaling theory of localization.

If δ is very small, the system will be localized and from the previous discussion on localized transport (section 1.3.4), conductance in this regime will be defined by [50],

$$g(L) = g_c \exp\left(-\frac{L}{\xi}\right). \tag{1.28}$$

On the other hand, if δ is large g will be given by the Drude form of conductance which results in Ohm’s Law,

$$g(L) = \sigma L^{d-2}. \tag{1.29}$$

We note that there must exist a critical value δ_c which defines the mobility edge below which a system of increasing size will ultimately end up as a localized system and above which the increase in system size results in an extended system. g_c is the conductance associated with δ_c.

For the scaling analysis we must define a scaling function that allows conductance to be represented as a function of system size. Such a scaling function can be defined as the derivative of the logarithmic change of conductance with respect to size [50],

$$\beta(g) = \frac{d\ln g}{d\ln L}. \tag{1.30}$$

In this function a negative value of $\beta(g)$ (i.e. a negative derivative) means a decrease in g with size and as a result represents a localized system. Correspondingly, if $\beta(g)$ is positive then g increases with size and therefore the system is extended. In the localized regime, from Eq. (1.28) and (1.30), $\beta(g)$ will be given by [46]

$$\beta(g) = \ln(g/g_c). \tag{1.31}$$

Since $g \ll g_c$ in the localized regime, $\beta(g)$ will always be negative for Eq. (1.31). In the Ohmic regime ($g \gg g_c$) described by Eq. (1.29), $\beta(g)$ yields an asymptotic form

$$\beta(g) = d - 2. \tag{1.32}$$

The dependence on dimensionality d of the system in the Ohmic limit of the scaling function $\beta(g)$ therefore reveals an interesting result of these systems. For one dimensional systems ($d = 1$), the scaling function $\beta(g)$ is always negative. In other words, for $d = 1$ the system is always localized and therefore there is no metal-to-insulator like transition in such systems. All states are localized irrespective of disorder and g always tends towards zero with increasing L. This was a confirmation of a result that was already well known in disordered one-dimensional systems [51]. In two dimensions ($d = 2$), $\beta(g)$ tends to zero from Eq. (1.32). This is a marginal case which reflects the fact that there is a change from logarithmic localization to exponential localization. Nevertheless it is expected that $d = 2$ will always be localized. For $d = 3$, $\beta(g)$ is positive in the Ohmic limit and so one expects to find a metal-to-insulator transition in three-dimensional systems.

The analysis of the scaling function (Eq. (1.28 – 1.32)) is summarized in Fig. 1.20.

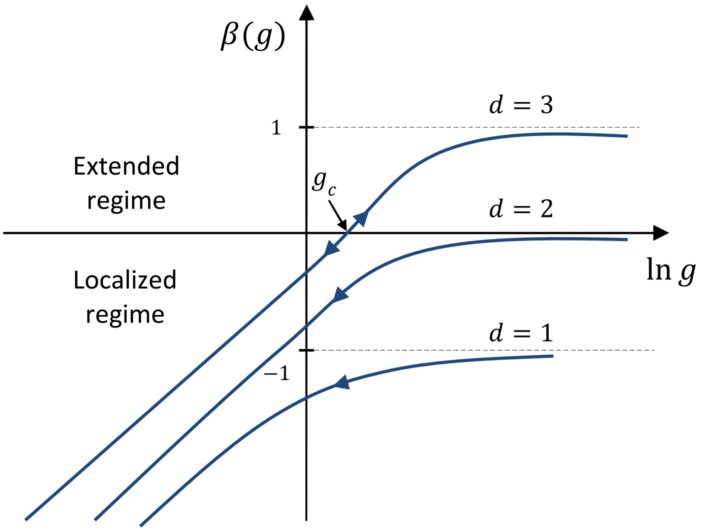

Figure 1.20. Dependence of $\beta(g)$ on $\ln g$ for d = 1, 2 and 3. The arrows show the movement of $\ln g$ as the size of the system is varied. d = 3 is the only case where bidirectional change is possible and thus a critical point g_c exists that separated the system from localized and extended behaviour. For all other cases, d = 1, 2, the system is always localized.

We see that the $d = 3$ curve must cross the $\beta(g) = 0$ line at some point as the size of the system increases, and thus g_c in the plot represents the metal-to-insulator transition point. Implicit in Fig. 1.20 is that $\beta(g)$ is continuous for all curves. This is in disagreement with the minimum metallic conductivity proposed by Mott [38] depicted in Fig. 1.12. The assumption that $\beta(g)$ is continuous is based on the fact that as g is a function of the size of the system and L evolves continuously, therefore $\beta(g)$ must also be continuous. Though this issue is still debated, it is widely accepted that metal-to-insulator transitions are continuous.

We will now discuss the $d = 3$ scenario, which involves a metal-to-insulator transition. Suppose a small block, with size L of the order of the mean free path, possess conductance g_0, where g_0 is considered to be the initial conductance of the system. If $g_0 > g_c$ then g_0 will be found somewhere in the positive half of the $\beta(g)$ plot in Fig. 1.20. On the other hand, g_0 will be found in the negative half of $\beta(g)$ if $g_0 < g_c$. Whether g_0 resides in the positive or negative half of $\beta(g)$ is determined by the Thouless number, in other words, by the microscopic disorder. If $\beta(g)$ is positive for the initial system, according to Eq. (1.30) an increase the size of the system will result in an increase in conductance. On the other hand if $\beta(g)$ is negative in the initial system, the natural consequence of the negative derivative is that an increase in size must result in a decrease in conductance. Therefore for a system with $g_0 > g_c$ an increase in size represents moving upwards along the $d = 3$ curve in Fig. 1.20 until at very large L the asymptotic limit of $\beta(g) = 1$ is reached, i.e. at very large L, the system possesses a characteristic Ohmic or metallic behaviour. Similarly, for a system with $g_0 < g_c$, the negative derivative demands that the system moves downwards along the $d = 3$ curve until at very large L, localized or insulating behaviour is dominant. These two types of movements along the $d = 3$ curve are illustrated by the arrows in Fig. 1.20 which depart in opposite directions from the critical point g_c. We also note that for $d = 1$ and 2, the movement along the curve with increasing size is always downwards since $\beta(g)$ is always negative.

It is therefore clear that for a fixed amount of disorder the characteristic behaviour of the system is determined by the initial conductance g_0 and its location relative to g_c. The $g = g_c$ point at $\beta(g) = 0$ is an unstable fixed point since any small deviation from this position will lead to one of two extremes, a metal or an insulator. The scaling theory of localization allows us to further investigate this critical point. As discussed previously, the initial conductance g_0 is determined by the Thouless number δ (i.e. disorder within the system), but we note that this can be changed simply by varying E_F of a weakly disordered energy band (Fig. 1.5), for example from the region of extended states towards the localized states. For a small change from the critical point, if $\beta(g)$ has a slope of ν^{-1} so that [50]

$$\beta(g) = \frac{1}{\nu}\delta g, \qquad (1.33)$$

then as E_F approaches the critical point g_c (mobility edge) from extended region towards the localized region the conductivity (which is Ohmic in the extended region) must quickly vanish and tend towards zero with an exponent ν according to

$$\sigma \propto (\delta g)^{\nu}. \qquad (1.34)$$

If the conductivity is written as $\sigma \propto 1/\xi$ [50], it is found that the localization length must diverge as at the critical point is approached

$$\xi \propto (\delta g)^{-\nu}. \tag{1.35}$$

Since this is a description of a phase transition from an extended system towards a localized system, the exponent ν is expected to be a universal constant, as in any critical phenomenon involving a single correlation length (ξ). Critical phenomena are discussed in more detail below in a section 1.4.2.

Eq. (1.35) is one of the most important predictions of the scaling theory of localization and the centre piece of this thesis. In the following chapters we shall investigate the nature of this critical phenomenon in two-dimensional systems, where scaling will be achieved by varying the effective length of the system, and disorder will be controlled by the varying position of E_F in the energy band.

1.4 The quantum Hall effect (QHE)

The quantum Hall effect (QHE) is one of the most remarkable features of a 2DES. It is characterized by the formation of plateaux in the Hall resistivity and the formation of oscillations and peaks in the diagonal conductivity. Key to the understanding of QHE was the concept of localization which was reasonably developed at the time of the discovery of the QHE. In this section we describe the QHE using concepts already developed above on the theory of localization and two-dimensional systems. Of great interest to this thesis is the transition between adjacent plateaus in the QHE. The central aim of most of the work presented in this thesis is to investigate the nature of these plateau-to-plateau transitions.

1.4.1 Introduction to the QHE

The discovery of the QHE, including the initial discoveries that led to it, were largely unexpected since the classical analysis of the effect of magnetic field on a 2DES (as described in section 1.2.4) does not predict the QHE. The QHE, illustrated in Fig. 1.21, has the pronounce features of a Hall resistivity plateauing at precisely quantized values of h/ie^2, where i is an integer, and a diagonal resistivity that vanishes to zero where these quantized levels appear. The resistivity tensor which takes the form,

$$\rho = \begin{bmatrix} 0 & \frac{h}{ie^2} \\ -\frac{h}{ie^2} & 0 \end{bmatrix}, \tag{1.36}$$

is clearly in opposition to the classical form shown in Eq. (1.14).

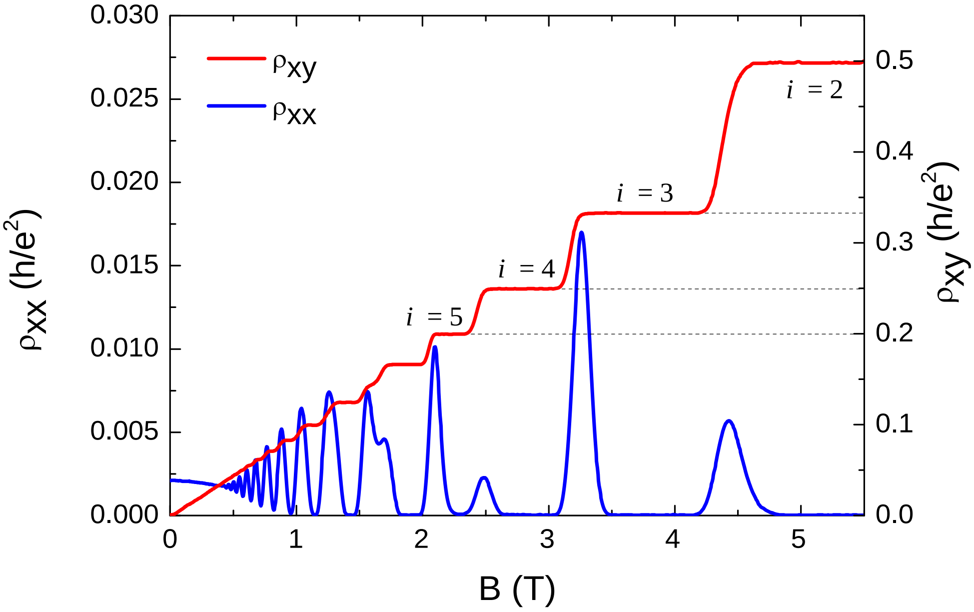

Figure 1.21. The Hall resistivity ρ_{xy} and diagonal resistivity ρ_{xx} of the quantum Hall effect measured from a Hall bar. ρ_{xy} is quantized at values of h/ie^2 where i is an integer.

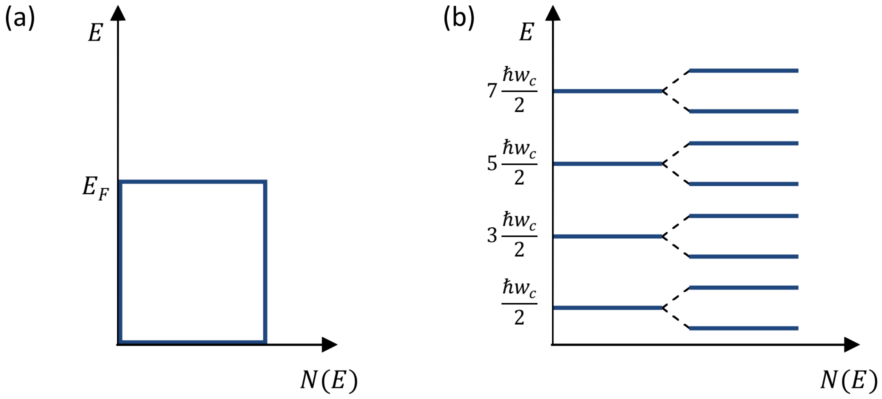

Figure 1.22. Density of states of 2DES, (a) at zero magnetic field, (b) and in the presence of a magnetic field. In strong fields, each Landau level splits into two spin resolved levels.

Although largely unexpected, a theoretical prediction suggesting the existence of the QHE was made by Ando, Matsumoto and Uemura [52]. Initial experiments hinting of the existence of the QHE were carried out by Wakabayshi and Kawaji [53, 54] on silicon MOSFETs but they were unable to discover the full extent of the QHE features mainly due to the low quality of semiconductor devices at that time. The observation of quantized Hall plateaus was first observed by von Klitzing, Dorda and Pepper in 1980 [2]. The observation was most profound because of its quantised nature and the realization that the quantized Hall resistances are dependent only on fundamental constants of nature, h/e^2.

Under an applied perpendicular magnetic field electrons in a 2DES move in an orbital manner with a frequency $w_c = eB/m^*$, known as the cyclotron frequency. Solving the Schrödinger equation for these electrons in a magnetic field, it can be shown that the eigenvalues of a two-dimensional system lie on odd integer multiples of $\hbar w_c/2$,

$$E_n = \hbar w_c\left(n + \frac{1}{2}\right) = \hbar\frac{eB}{m^*}\left(n + \frac{1}{2}\right), \tag{1.37}$$

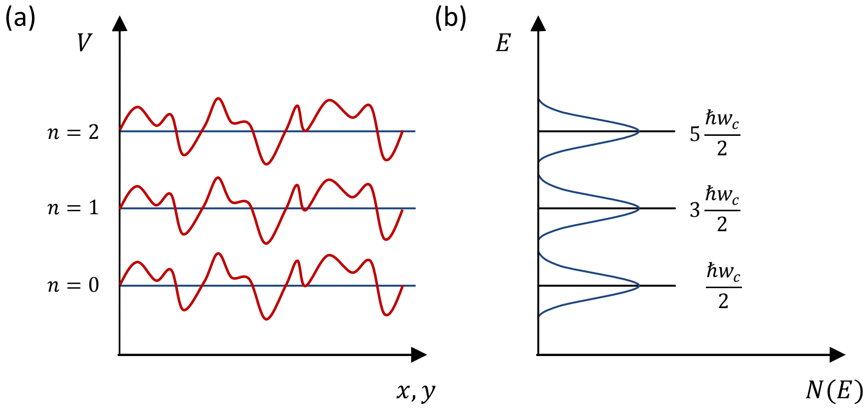

Figure 1.23. Random potential fluctuations experienced by the 2DES shown in (a) cause a smearing of LLs forming a narrow band of energies centred about the LL, shown in (b). This is known as disorder broadening.

where n is an odd positive integer and E_N denotes the Nth energy level. The sub-band or energy spectrum of a 2DES under a magnetic field is therefore no longer a seemingly continuous band of energies but is divided into discrete energy levels known as Landau levels (LLs). Fig. 1.22 shows the separation of the sub-band into LLs. Each of these LLs, due to the spin degeneracy, further splits into two separate energy levels, spin up and spin down, at high magnetic fields.

Disorder within the 2DES, discussed above, has the effect of smearing out or broadening the LL into Gaussian-like peaks due to the random potential introduced by various sources of disorder (see discussion of disorder in 2DESs above). Eq. (1.37) is therefore rewritten as

$$E_n = \hbar w_c \left(n + \frac{1}{2}\right) + V_{0(x,y)}, \tag{1.38}$$

where $V_{0(x,y)}$ represents the random potential experienced by carriers within the systems.

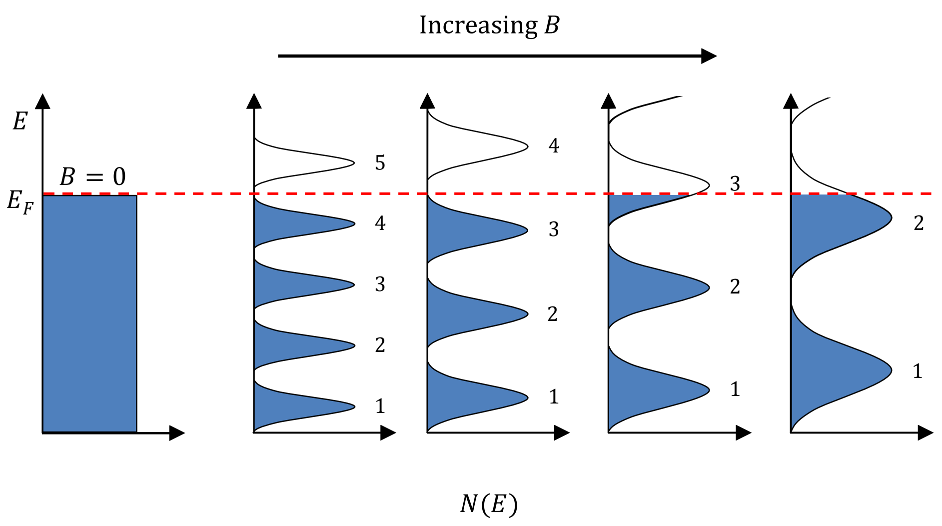

Figure 1.24. An illustration of the Fermi level passing through successive LLs as the magnetic field is increase.

The broadened LLs are no longer discrete energy levels but take the form of Gaussian bands of energies as shown in Fig. 1.23. The amount of broadening will be determined by the strength of the random potential.

The degeneracy of each LL is equal to the number of flux quanta within a given area and this is given by,

$$n_L = \frac{eB}{h}. \tag{1.39}$$

The carrier density of the entire 2DES is thus made up of the sum of all filled (and partially filled) Landau levels,

$$n_{2D} = \nu \frac{eB}{h}, \tag{1.40}$$

where ν, known as the filling factor, is the number of filled Landau levels.

Under a finite applied magnetic field, states accommodate electrons which will fill up from the lowest state in the lowest LL up to the Fermi energy. The number of filled LL will be determined by the carrier concentration and will be indicated by the filling factor ν (Eq. (1.40)). As the magnetic field is increased, the degeneracy of each LL will increase according to Eq. (1.39), and electrons at the Fermi energy will therefore drop down to fill up the empty states below and as a result the Fermi energy will adjust accordingly. Increasing the field therefore has the effect of moving the Fermi energy through successive LLs. This process is illustrated in Fig. 1.24.

In a weakly disordered 2DES where some degree of LL broadening occurs, the density of states will be greatest at the centre of the LL. From the discussion on extended and localized states in the previous sections above, it would be expected that states in the tails of the band will be localized while those close to the centre will remain extended throughout the system [5] as shown in Fig 1.25. When the Fermi energy coincides with the centre of the LL (half filling factors) where states are extended, electrons will be scattered in the diagonal direction under an applied electric field. σ_{xx} is greatest in this region due to the availability of extended states. On the other hand, electrons are able to scatter in the Hall direction (i.e. the direction perpendicular to the electric field) due to the applied magnetic field. The change in σ_{xy} with magnetic field is linear in this region as described by the classical case presented in Eq. (1.14).

When the Fermi energy is in between LLs, however, the density of states is vanishingly small. Electrons in this region are less able to screen random disorder potentials and therefore states in this region are localized. Electrons are no longer able to scatter in the diagonal direction and σ_{xx} goes to zero. Similarly, electron are unable to drift any further in the Hall direction and σ_{xy} is held at a constant value which is an integer multiple of $e^2/\hbar$. The result of the preceding analysis is the plot shown in Fig. 1.21.

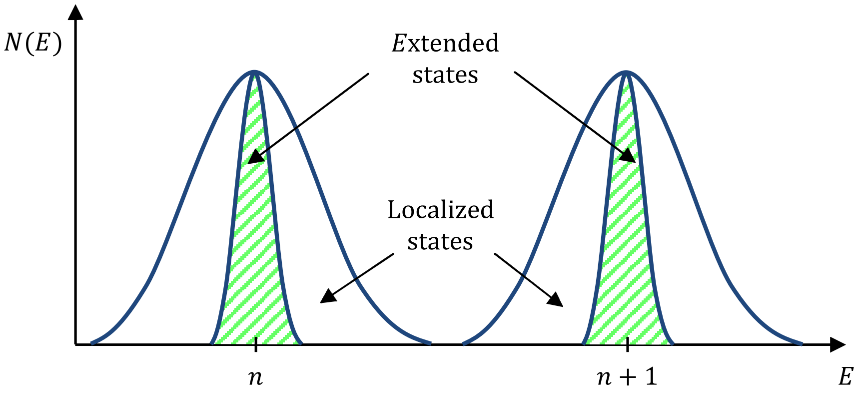

Figure 1.25. The diagram shows the extended and localized regions with of two consecutive Landau levels.

1.4.2 Quantum phase transitions in the QHE and critical universal singularities

A broadened Landau level band contains both extended states (at its centre) and localized states (in the tail regions). It is therefore expected that an Anderson like metal-to-insulator transition occurs within the QHE as the Fermi level moves through a LL band at high magnetic fields. It has been shown by many authors [55-58] that in the limit of a system of infinite size and temperature of absolute zero, states are extended only at a single unique energy which corresponds to the discrete non-broadened energy of a Landau level, this is known as the critical energy E_c. Anderson transitions in the QHE, or quantum Hall transitions (QHTs), are therefore insulator-to-insulator transitions with a metallic or extended state at E_c. Critical transitions in the QHE are also known as plateau-to-plateau transitions since they occur in the region that joins adjacent Hall plateaus. We also recall from the scaling theory of localization discussed in section 1.3.6

that, as the transition boundary is approached (in this case E_c) the localization length ξ diverges. This is the hallmark of a critical phenomenon.

Critical phenomena in physics are one of the most striking aspects of the macroscopic physical world. They describe seemingly abrupt changes between different phases of matter which occur at a certain critical point in some parameter of the Hamiltonian (a parameter that changes the quantum state) of the system. These phase transitions are characterized by the divergence of a measurable quantity of the system, known as the order parameter [59], to infinity as the critical point is approached. The order parameter is a physical characteristic quantity of a system which is a numeric measure of both the type and amount of ordering in a system close to the critical point. For example, in a liquid-to-gas phase transition the appropriate order parameter is related to density which describes the ordering of particles within the system [7, 10]. The Hamiltonian parameter, of which the critical point is a function, is usually some externally applied parameter that causes a change in the order parameter, for example, temperature, pressure, magnetic field or electric field. Critical phenomena include observations such as phase transitions in classical fluids (water), opalescence of carbon, superconductor-to-insulator transitions, transitions in superfluids (Helium: He^3 and He^4), ferroelectrics and ferromagnetism [7, 9, 10].

Criticality of the type observed in the QHE are known as *continuous quantum phase transitions* (QPTs) [6] or second order phase transitions. These transitions can take place with zero latent heat. QPTs are referred to as continuous transitions, because the order parameter changes continuously as the critical point is approached unlike, for example, the thermal (first order) transition from liquid to a gaseous state where there is an abrupt and discontinuous change in the order parameter (the density, or in other words the volume) of system on either side of the critical point.

Based on either empirical or heuristic arguments, it has been observed that there are similarities between these apparently very different phase transitions [59], and in a vast number of cases these different system have demonstrated similar behaviours in the region close to the critical point. These similarities can be summarized in certain asymptotic laws, known as scaling laws [8], that define the nature of transitions as the critical point is approached.

In the case of the QPT in the QHE, the appropriate order parameter is observed to be the localization length, which serves as the correlation length of a wavefunction within the 2DES. The localization length contains information relating to the order within the system (ξ is dependent on, and a numeric measure of, disorder). Thus, the divergence of the order parameter as the critical point is approached can be related to the scaling law [11]

$$\xi \sim |E - E_c|^{-\nu}, \tag{1.41}$$

where ν is the critical exponent that describes the nature of the divergence of ξ. Eq. (1.41) describes the observed singularity (divergence to infinity) in QHTs. It is noted that Eq. (1.41) which in this context refers to QHTs is the equivalent of Eq. (1.35) which was formulated for metal-to-insulator transition. Both equations describe the same critical transition. The order parameter in both equations is the same but in the case of QHTs, the critical point occurs in the energy spectrum whereas in the case of metal-to-insulator transitions discussed in Eq. (1.35), criticality occurs in the conductance of the system.

Within systems that exhibit critical phenomena the correlation length ξ of the system represents the distance over which the system maintains some amount of order or coherence. In other words, the divergence of ξ signifies a divergence of the length over which order is maintained. In the context of localized systems, the length over which the wavefunction of an electron behaves like a Bloch-like extended state (the length of coherence) diverges as the critical point is approached. Microscopic disorder on length scales much smaller than ξ are insignificant to the behaviour of the system, as an electron will remain extended over the entire length of correlation regardless. As the critical point E_c is approached, ξ is extended over larger and larger regions of space. The system therefore begins to look more homogenous, or independent of disorder, since electron transport will not be characterized by the specific microscopic details on length scales smaller than ξ. One realises that various individual systems of different characteristics will become similar and indistinguishable near the critical point. It therefore follows that systems exhibiting criticality can be divided in to broad groups, known as *universal* classes [7, 60], that are only defined by very general characteristics such as symmetry or dimensionality [6]. These universal classes possess identical critical properties, and in particular can be identified by the value of the critical exponent related to the divergent correlation length. For QHTs occurring in any 2DES, the value of ν in Eq. (1.41) is expected to be universal for all 2DES [6, 11] in accordance with the theory of critical phenomena [7] and independent of microscopic details of the system such as mobility and carrier concentration.

In the following section we discuss the value of the universal critical exponent ν of the correlation length and how it can be experimentally determined using a finite-size scaling analysis.

1.4.3 Finite-size scaling of quantum Hall transitions

Strictly speaking, the theory of critical phenomena of QPTs requires a divergence of the order parameter to infinity, i.e. a singularity, in a system of infinite size and at the absolute zero of temperature. In reality, these transitions occur at non-zero temperatures and in systems of finite size. In finite-size systems, long distance correlation is cut-off by the restriction imposed by the physical boundaries of the system, but in the simultaneous limit of the temperature approaching zero and the system size tending to infinity, the scaling laws of infinite systems can be approximated in finite systems. This forms the essence of finite-size scaling.

Using various numerical methods and after considerable theoretical efforts (review in Ref. [11]), a vast amount of data have been obtained on the estimated value of ν based on finite-size scaling arguments. These results have been summarized in Table 1.1. It is observed from Table 1.1 that the estimated value of ν is expected to be between 2.0 and 2.5, however most values appear to centre around $\nu \sim 2.3$. The most accurate numerical value obtained so far [11, 61] is $\nu = 2.35 \pm 0.03$ reported by Huckestein and Kramer [56] is based on a random Landau matrix model.

On the experimental front, the physical scaling of the size of a 2DES was initially considered somewhat impractical for experimental investigation as it would involve fabricating numerous samples with only small variations in size. It was also not apparent that such an approach would yield results that could be combined to describe the nature of a single system. A better approach would involve somehow expanding or contracting the size of a single system.

Table 1.1 Critical exponent of the localization length ν of quantum Hall transition obtained by various theoretical methods taken from Kramer *et al* [61].

ν	Model	Method	Reference
∞	Short-range impurities	Self-consistent perturbation	[62]
≈ 2	Peierls tight binding	Transfer matrix scaling	[63]
≈ 2.0	Short-range impurities	Recursive green function	[64, 65]
2.35 ± 0.03	Random Landau matrix	Recursive green function	[11, 56]
2.3 ± 0.1	Random Landau matrix	Recursive green function	[66]
2.4 ± 0.2	Random Landau matrix	Recursive green function	[67]
2.4 ± 0.1	Finite range impurities	Chern number scaling	[55]
≈ 2.3	Spin-orbit scattering	Thouless number scaling	[68]
≈ 2	Double layer system	Thouless number scaling	[69]
≈ 2	Random matrix model	Scaling of level statistics	[70]
2.5 ± 0.5	Chalker-Coddington	Transfer matrix scaling	[71]
2.4 ± 0.2	Random saddle points	Transfer matrix scaling	[72]
2.5 ± 0.5	Chalker-Coddington type	Real space renormalization	[73]
2.39 ± 0.01	Chalker-Coddington type	Real space renormalization	[74-76]
2.5 ± 0.4	Super spin chain	Density matrix renormalization	[77]
2.33 ± 0.03	Counter-propagating chiral Fermions	Monte Carlo	[78]

Inspired by the work of Thouless and the single parameter scaling theory of localization, Pruisken [79] observed that if the phase coherence length L_φ of the 2DES is less than the physical dimensions of the system, then the 2DES can be considered to contain within it many subsystems, where the size of a subsystem is defined by the length L_φ such that adjacent lengths of L_φ can be considered as two separate systems. Defined in this manner, electrons in a system possess an effective size L_{eff} and will experience the same boundary conditions as described by the Thouless number. We note that in this case $L_{eff} = L_{\varphi}$. Similar to the Thouless block described above in section 1.3.5, if $L_{eff} \ll \xi$ in 2DES, an electron will defuse for a time τ_{φ} defined by the phase coherence time after which it is scattered, analogous to the scattering at the boundary of a Thouless block. As described by Thouless, as the size of the system increases the conductivity in the system will resolve into one of two asymptotic extremes. Similarly, as the effective L_{eff} (the phase coherence length) is increased, an electron is allowed to coherently explore more and more of the system, revealing the intrinsic nature of disorder within the system. If the condition $L_{eff} \ll \xi$ still remains after L_{eff} is equal to the physical size of the system L, the system will have metallic behaviour. Conversely, as L_{eff} is increased, if $L_{eff} \gg \xi$ occurs before $L_{eff} = L$, then the system will exhibit localized behaviour. For a temperature dependent phase coherent length

$$L_{\varphi} = \sqrt{D\tau_{\varphi}} \text{ where } \tau_{\varphi} \propto T^{-p}, \tag{1.42}$$

the effective size can therefore be expressed as

$$L_{eff} \propto T^{-p/2}, \tag{1.43}$$

where p is the temperature exponent of the inelastic scattering length. It is noted that Eqs. (1.42) and (1.43) are the same as the Thouless argument in Eq. (1.24), and as a result L_{eff} is also known as the Thouless length. In light of the above scaling argument, it can be seen that the conductivity of the system is dependent on the ratio of L_{eff} and ξ. From Eq. (1.41) and (1.43) it is observed that the scaling (or power) law of conductivity as the critical point is approached will depend on the critical exponent $\kappa = p/2\nu$. We define a natural scale $\mu = (L_{eff}/\xi)^{1/\nu}$ such that [79]

$$\mu = |E - E_c|T^{-\kappa}, \tag{1.44}$$

so that $\mu \leq 1$ describes metallic behaviour while $\mu > 1$ describes localized behaviour. The conductivity tensor near the critical point will be dependent on μ and reflect its power law behaviour in the following scaling law [11, 79],

$$\sigma_{\alpha\beta}(T, E) = S_{\alpha\beta}[|E - E_c|T^{-\kappa}], \tag{1.45}$$

where $\sigma_{\alpha\beta}$ represent the various coefficients of the conductivity tensor and $S_{\alpha\beta}$ is the corresponding constant of the scaling function. The derivative of the scaling function in Eq. (1.45) near the critical point therefore provides direct experimental access to the critical exponent κ as follows:

$$\frac{d\sigma_{\alpha\beta}(E_c)}{dE} \propto T^{-\kappa}. \tag{1.46}$$

Substituting a changing Fermi energy with its analogous change in magnetic field and noting that the above expression only applies close to the critical point, for the Hall conductivity σ_{xy}, Eq. (1.46) represents a temperature dependence of the slope of σ_{xy} near the critical point (as shown in Fig. 1.26)

$$\frac{d\sigma_{xy}(B_c)}{dB} \propto T^{-\kappa}. \tag{1.47}$$

κ can be measured as the gradient of Eq. (1.47) on a double log scale. On the other hand, it is observed that the derivative in Eq. (1.46) near the critical point for the diagonal conductivity σ_{xx}, is a measure of the width of the conductivity peak in magnetic field

$$\Delta B_{\sigma_{xx}} \propto T^{\kappa}, \tag{1.48}$$

such that κ is obtained as the gradient of the double log plot of Eq. (1.48). Equivalents of Eq. (1.47) and (1.48) exist for the resistivity coefficients as $d\rho_{xy}/dB \propto T^{-\kappa}$ and $\Delta B_{\rho_{xx}} \propto T^{\kappa}$ respectively.

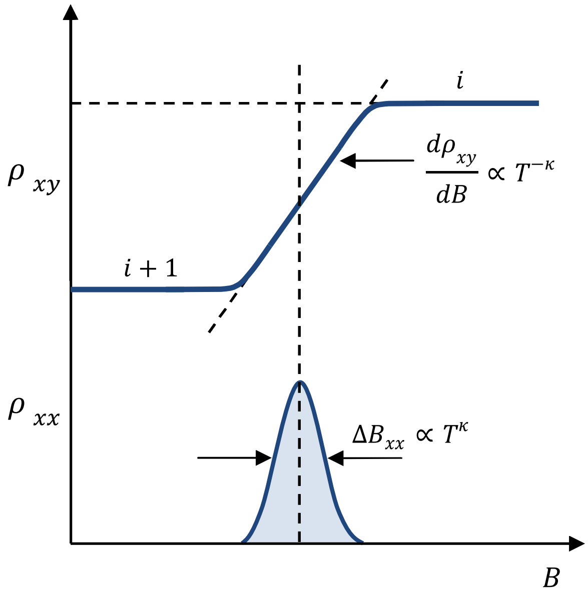

Figure 1.26. A schematic showing the relation between the scaling exponent κ and measured resistivities of a Landau level.

If the value of the inelastic scattering exponent is taken to be $p = 2$ as predicted by Fermi liquid theory [56], and giving the theoretical calculated value of $\nu \approx 2.35$, $\kappa \approx 0.42$. The first experimental investigation of the critical exponents based on the Eq. (1.47) and (1.48) was reported by Wei *et al*. [12] where remarkably κ was measured to be $\kappa \approx 0.42$ in both the Hall and diagonal component for a 2DES formed in a In-GaAs/InP heterostructure, and as would be expected with critical phenomena, this value was independent of LL index. It was therefore declared that the highly anticipated critical phenomena of QHTs did in fact exist and that these QHTs are indeed continuous second order quantum phase transition.

1.5 Experimental results on the scaling of QHTs

The result reported by Wei e*t al*. [12] on the criticality of QHTs was truly remarkable, owing largely to its precise agreement with the general consensus on the theoretical value of ν. However, subsequent results on the criticality QHTs have been contradictory at best and chaotic at worse [11]. As described above, the criticality ν is determined based on a composite exponent $\kappa = p/2\nu$, where p is assumed to be 2. Therefore, in order for κ to be a universal critical exponent, the inelastic scattering exponent p has to be universal, a point on which some disagree [80]. In addition it is not clear why the value of the clean limit of a Fermi liquid, $p = 2$, is used rather than the disordered (or dirty) value of $p = 1$ [81].

The Wei *et al*. experiment on InGaAs/InP systems was quickly followed by similar investigations in GaAs/AlGaAs heterostructures, where it was found that the value of κ was not universal as previously reported and was dependent on the strength of impurity scattering [15]. Wei *et al*. consequently performed their own experiments on GaAs/AlGaAs devices where they found that κ was only universal (with the expected value of $\sim$0.42) for temperatures below 200 mK [82]. Systematic studies on Si metal-oxide-semiconductor 2DESs also found κ to be non-universal and dependent on Landau level [83, 84]. With the universality of p in question, investigations based solely on determining p in InGaAs/InP 2DESs using current dependent measurements (current scaling) reported the inelastic scattering exponent to be universal and Landau level dependent with $p = 2$ [14], but this contradicted experiments on GaAs/AlGaAs structures that found p to vary between a value of $p = 2.7$ and $p = 3.4$ [17, 85].

In general, universality of critical exponents (of either κ or p) was observed in InGaAs/InP systems but it was almost always absent in GaAa/AlGaAs systems. It was therefore suggested that that the difference in criticality reported by various experiments depended on the nature of disorder potentials within a 2DES, as this was the fundamental difference between a InGaAs/InP system and a GaAs/AlGaAs system. In InGaAs/InP systems, the electron gas is formed in an alloy with disorder originating from short-range alloy scattering (as discussed in section 1.2.3) and therefore random potentials within this system vary on an atomic length scale. The electron gas in GaAs/AlGaAs systems on the other hand are situated in the high quality GaAs layer, and the dominant mechanism of disorder in these systems stems from random *long-range* potentials of ionized impurities remote from the electron gas. This short-range/long-range argument based on disorder potential was given some standing from the experimental results of Li *et al*. [18], who showed that by changing the nature of disorder with the system from long-range to short-range, the value of κ will crossover from the non-universality to universal criticality demonstrating the importance of disorder potentials. It still, however, remains unclear why this is the case and thus this thesis will propose a theory for this discrepancy.

It is noted that though κ was the value being determined in these early experiments on scaling theory, the exponent of interest is the localization length exponent ν, which is the determinant of the critical phenomenon. While efforts to measure ν indirectly through κ have been fraught with contradictions, the determination of ν via the more direct means of estimating the localization length ξ have yielded better success though these results are not completely free of controversy. By sampling the conductivity in localized regions around the critical point and at different temperatures ξ can be estimated in proportion to the approaching critical point, $\xi \propto |B - B_c|^{-\nu}$, and thus ν can be determined. Using this method it was reported [86] that ν was found to be $\nu \approx 2.35$ and universal across all samples investigated.

Another method that has been used to estimate ξ is the measurement of QHTs at very low temperatures in samples of different physical size. As the temperature is lowered it is possible for the phase coherence length to exceed the physical dimensions L of the system. This scenario is characterized by the saturation in conductivity as a function of temperature, since further reduction in temperature no longer has an effect on electron transport. As the critical point is approached, the divergence of ξ (now no longer determined by L_φ) will be cut off by the physical dimensions of the system such that at or below the saturation temperature, $\xi = L$. ξ in Eq. (1.41) can therefore be replaced by L and the critical exponent can be determined from a double log plot of $L \propto \Delta B^{-\nu}$. Using this physical scaling argument, the critical exponent was consistently found to be $\nu \approx$ 2.3 [85, 87] and independent of Landau level. However, in this $L_\phi > L$ regime the system is non-self-averaging [30] due to coherent backscattering (section 1.35 and Fig. 1.17(b)). One therefore expects pronounced manifestations of quantum interference induced conductance fluctuations [30, 88-90] which appear to be absent in the data provided by size scaling investigations.

It is possible to vary the phase coherence length by varying the frequency of the applied current (or electric field). This technique is discussed in greater detail in Chapter 3. It was observed, through dynamic scaling, that the width of the conductivity peaks follow the scaling power law of Eq. (1.48) where κ was found to be universal [13] in one report but non-universal in others [16, 91].

The main focus of this thesis is therefore the verification of criticality within QHTs and in particular there is a focus on why there are numerous discrepancies within the field. Universal criticality will be investigated using a broad range of techniques that require the application of various aspects of low temperature electron transport. We shall individually and independently investigate each of the critical scaling exponents discussed above. The critical phenomena will be investigated as function of temperature, frequency and current. We will also investigate the effect of disorder on the criticality of phase transitions within the QHE. In dynamic or finite-frequency scaling, we extended the frequency range of scaling beyond that reported in the literature and present the highest data resolution ever reported. We then propose a unifying model for of the scaling theory of QHTs which attempts to explain most of the discrepancies observed within the literature.

2. The temperature dependent scaling of quantum criticality in quantum Hall transitions

2.1 Introduction

In this chapter, we investigate the nature of quantum Hall transitions (QHTs) using temperature dependent processes. As discussed in Chapter 1, all QHTs are expected to belong to the same universality class of phase transitions [6]. As a result, the critical exponent of these transitions will possess the same value of $\nu \sim 2.3$ [56], though not all experimental investigations agree with this statement [11]. In section 1.4.3, it was shown that the temperature dependent analysis of the critical phenomenon of QHTs results in a composite scaling exponent $\kappa = p/2\nu$, which has also been suggested to be a universal constant [12, 79]. In this chapter we investigate all three exponents independently in order to verify their universality and the relationship between them.

ν is determined using a variable range hopping analysis which takes into account the temperature dependent conductivity of the 2DES as the critical point at the centre of a LL band is approached. κ is determined using the finite-size analysis developed in section 1.4.3, where the width of the LL conductivity peaks and the slope of plateau-to-plateau transitions are considered. And p is determined using a current scaling analysis which examines the electron inelastic scattering rate by increasing the electron temperature through the applied electric current.

2.2 Samples and experimental techniques

The characteristic details of all the various samples used in this chapter are provided below, along with a description of the experimental setup used for the results presented in this chapter.

2.2.1 Sample characteristics

All the samples used in the chapter were fabricated from GaAs/AlGaAs wafers grown by molecular beam epitaxy. Four different wafers with the structure shown in Fig. 2.1(a) were grown. Beginning with a GaAs substrates, the growth sequence is as follows: an undoped 1-μm-thick high quality GaAs layer, an undoped $Al_{0.33}Ga_{0.67}As$ spacer layer (which is either 20 nm or 40 nm thick), a 40 nm Si-doped $Al_{0.33}Ga_{0.67}As$ layer with dopant concentration of 2×10^{18} cm^{-3}, and a thin 10 nm GaAs cap layer.

A Hall bars with a channel width of 100 μm and length of 300 μm between voltage probe arms was patterned onto each sample using optical lithography. Low resistance ohmic contacts were prepared by evaporating 170 nm of a Au/Ge/Ni eutectic onto the ends of the probe arms of the Hall bar, which was then annealed at 430 °C for 80 seconds under an atmosphere of nitrogen. The Hall bar pattern with ohmic contacts is shown in Fig. 2.1(b). The device contains of ten ohmic contacts. The two ohmic contacts at the left and right ends of the device (as shown in Fig. 2.1(b)) are used to inject current into the device while the other eight contacts on either side of the channel are used as voltage probe arms. The fabricated Hall bar device is attached to a chip package and wire bonded as shown in Fig. 2.2.

For each sample (one from each of the four wafers investigated) the electron density n_{2D} and mobility μ are obtained from low field measurements of the Hall and the zero-field diagonal resistivities (see measurement calculations in section 1.2.4). The sample characteristics are summarized in Table 2.1. The table includes two different electron scattering times, the transport or classical lifetime of an electron τ_c, and the quantum lifetime of an electron τ_q. We briefly discuss these two lifetimes as they convey a lot about the characteristics of the samples being investigated. In addition, distinguishing between them will be become important in analysing the results presented in this thesis.

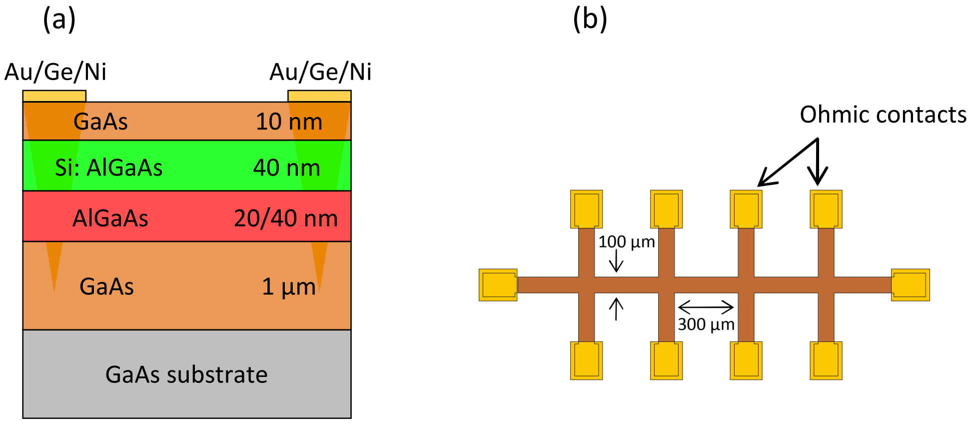

Figure 2.1. (a) Device structure of the 2DES GaAs/AlGaAs heterostructure with Au/Ge/Ni, which form the ohmic contacts, annealed into the heterostructure. (b) Top view of the Hall bar device with length between probe arms of L = 300 µm and with a channel width of W = 100 µm

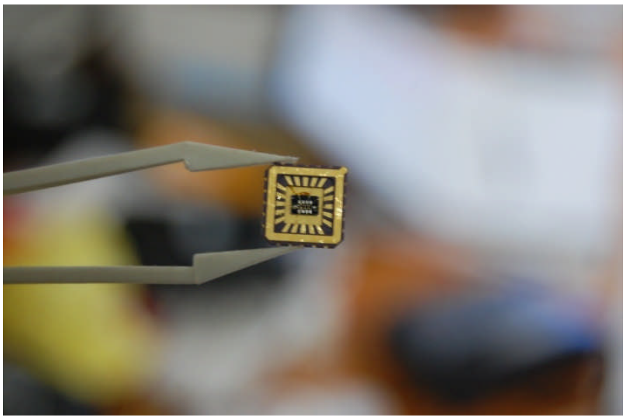

Figure 2.2. A picture of the finished Hall bar device attached and wire bonded to a chip package. The device itself is the dark square sample in the middle of the package. The ohmic contacts can be seen as the tiny gold coloured squares on the sample.

When the relaxation time of a system is determined from a simplified Boltzmann equation, the mean time between collisions is weighted by a factor of $1 - \cos\theta$

$$\frac{1}{\tau_c} = \int_0^{\pi} Q(\theta)(1 - \cos\theta)d\theta, \qquad (2.1)$$

where $Q(\theta)$ is proportional to the probability of scattering an electron through an angle θ. At zero magnetic field, the transport mobility as determined from the Drude formalism, $\mu = e\tau_c/m^*$, relies on the expression in Eq. (2.1). The classical lifetime therefore includes only a fraction of actual collisions since small angle collisions are effectively ignored due to the weighted factor. At zero magnetic field, the Drude mobility is an accurate reflection of scattering events occurring in the system since the majority of dephasing events will consist of short-range scattering off impurities within the vicinity of the 2DES. These short-range collisions produce large scattering angles that are less supressed in Eq. (2.1).

TABLE 2.1. Heterostructure and transport characteristics measured at 100 mK

Sample	AlGaAs spacer (nm)	n_e (×10^{11} cm^2)	μ_e (×10^5 cm^2 V^{-1}s^{-1})	τ_c (ps)	τ_q (ps)
L1	20	2.99	3.8	14.78	0.92
L2	40	1.55	1.09	4.15	1.25
L3	20	2.45	0.51	1.94	0.53
L4	40	1.92	8.68	33.07	1.47

At high magnetic fields, however, small perturbations can result in the dephasing of cyclotron orbits making small angle scattering events significant. The quantum life time τ_q expressed as,

$$\frac{1}{\tau_q} = \int_0^{\pi} Q(\theta)d\theta, \tag{2.2}$$

is therefore a measure of all collisions within the system, irrespective of scattering angle, and a better measure of dephasing events at high fields. The phase sensitivity of cyclotron orbits is evident in the collision broadening of Landau levels which is related to the quantum lifetime through $\Gamma = \hbar/2\tau_q$. The quantum lifetime can be measured from the envelope of the amplitude of Shubnikov-de Haas (SdH) oscillations (i.e. the low field oscillations of the QHE) [92]. The amplitude of the SdH oscillation $\Delta\rho$ is given by the Dingle formula [93] as

$$\Delta\rho = 4\rho_0 X(T)\exp(-\frac{\pi}{\omega_c\tau_q}), \tag{2.3}$$

where ρ_0 is the zero field resistivity and $X(T)$ is a thermal damping factor given as

$$X(T) = (2\,\pi^2 kT/\hbar\omega_c)/\sinh(2\,\pi^2 kT/\hbar\omega_c). \tag{2.4}$$

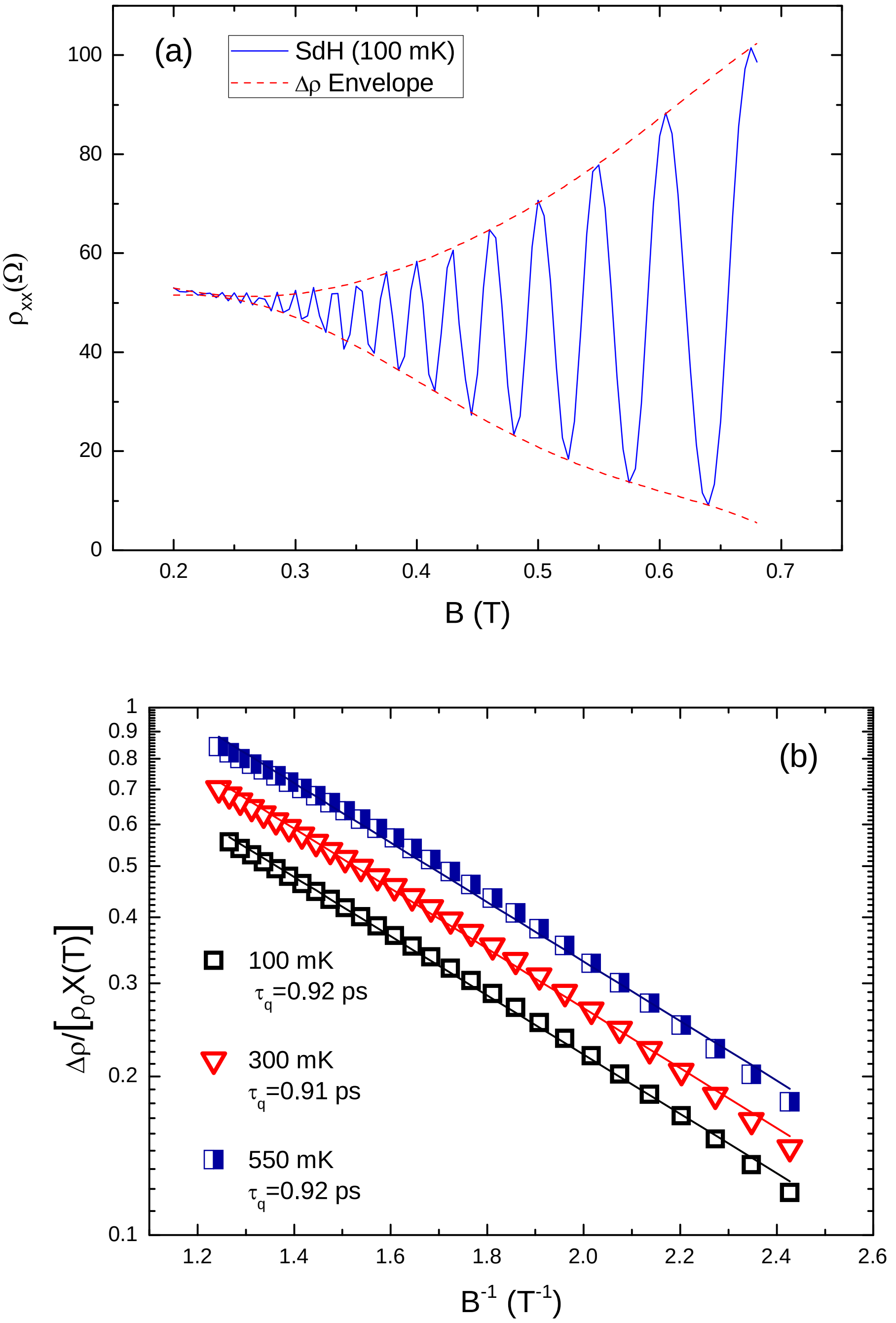

Figure 2.3. (a) A plot of the SdH oscillation of sample L1 at 100 mK. The dashed line is a least squared fit of the amplitude of the oscillations. (b) τ_q determined from the Dingle plot of L1 at three different temperatures which have been slightly offset on the y-axis for clarity.

Eq. (2.3) was originally derived by Ando [94] for oscillations in σ_{xx}. From Eq (2.3) and (2.4), $1/\tau_q$ can be determined from the slope of a logarithmic plot of the SdH amplitude divided by $X(T)$ to correct for thermal damping, against $1/B$. Fig. 2.3(a) shows the SdH oscillations of sample L1 at 100 mK and the fitted envelope of the amplitudes. In Fig. 2.3(b) τ_q is found to be approximately 0.92 ps at three different temperatures for the sample. The agreement between different temperatures indicates that the temperature dependence is correctly accounted for by the damping factor [93].

The quantum lifetimes for all four samples are listed above in Table 2.1. The first thing one notices it that τ_q is consistently smaller than τ_c, and this is because τ_q counts both large and small angle scattering events. Secondly, the effect of the spacer width is observed in the measured value of τ_q; the 20 nm spacer samples have quantum lifetimes that are smaller than the 40 nm spacer samples. This is not observed for the classical lifetimes. Varying the spacer width affects the Coulomb scattering from remote ionized impurities in the donor layer (Section 1.2.3), which are predominantly small angle scattering events. The smaller the spacer width, the greater the effect of this long-range ionized impurity scattering. This is reflected in Table 2.1. The difference in τ_q for samples with the same spacer width (and comparable electron densities) will therefore be determined by short-range scattering mechanisms within the samples. It is observed in Table 2.1 that between samples with the same spacer widths, the sample with the larger τ_c is also the sample with the larger τ_q. The ratio τ_c/τ_q is a measure of whether scattering events are dominated by short-range interaction (large angle scattering) or long-range interaction (small angle scattering). If the predominant scattering mechanism is short-range (i.e. large angle scattering occurs on much shorter times scales than the small angle scattering time), τ_c/τ_q will tend towards unity. This is because large angle scattering events are equally accounted for by both lifetimes. But if the dominant scattering mechanism is long-range (small angle) scattering there will be a greater difference between τ_c and τ_q since τ_c suppresses the contribution of smaller angle scattering events. For high quality samples which are mainly limited by long-range scattering from ionized impurities τ_c/τ_q is expected to be between 10 and 100 [26, 93, 95].

Finally, we note the importance of carrier density in these GaAa/AlGaAs samples. At high carrier concentration, long-range potential fluctuations are more effectively screened by the 2DES and therefore small angle scattering is reduced (increasing τ_q). Using this simplified argument we note that for samples with the same spacer widths in Table. 2.1, τ_q increases as a function of carrier density. At high density the majority of small angle scattering is screened and $\tau_c/\tau_q \sim 1$, and the sample tends towards the short-range scattering regime. The effect of carrier densities and screening will be discussed in more detail in Chapter 4.

As observed in Table 2.1, a wide range of sample characteristics are used in this work in order to verify the universal critical phenomena, which should be independent of sample details such as those described in Table 2.1.

2.2.2 Experimental setup

The samples are attached to the base plate of a ^{3}He/^{4}He dilution refrigerator with a base temperature of less than 14 mK as measured by a ruthenium oxide (RuO_2) senor attached to the base plate. The diagonal and Hall resistivities (or voltages) are measured from the probe arms of the Hall bar using two lock-in amplifiers. A low frequency current (usually between 7 Hz and 215 Hz) is injected into the device and along the longitudinal channel of the Hall bar.

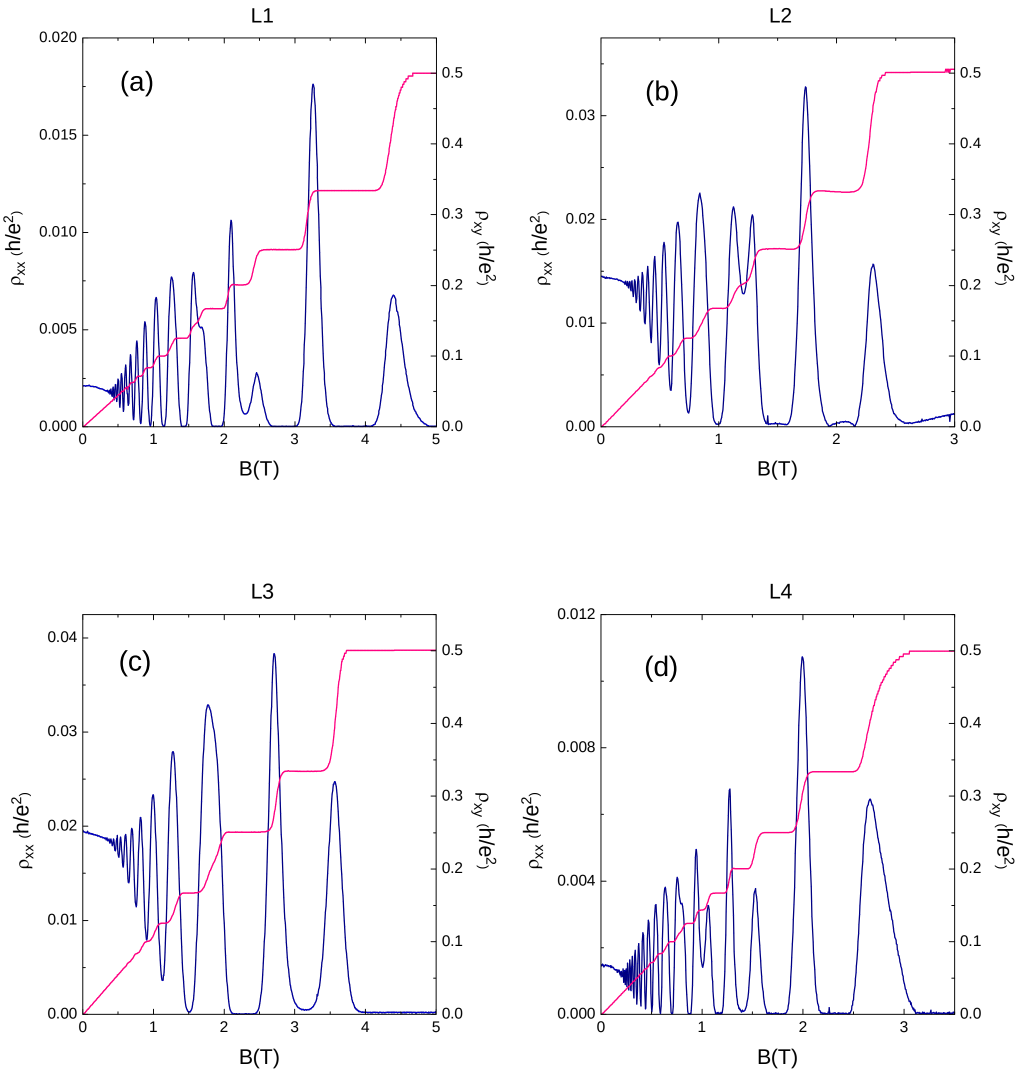

Figure 2.4. Plots of the ρ_{xx} and ρ_{xy} taken at a temperature of 100 mK for all four samples investigated.

The Hall resistivity is determined from the voltage measured from opposite probe arms while the diagonal resistivity is measured from adjacent probes arms as described in section 1.2.4. It was found that excitation currents below 50 nA did not cause heating within the samples; this was determined by varying the excitation current by small increments and observing the effect of temperature on the SdH oscillations. Unless otherwise stated a fixed current of 10 nA was used for all the temperature scaling measurements below.

Fig. 2.4 shows the 100 mK plot of ρ_{xx} and ρ_{xy} for all sample. Our analysis would mainly be centred on both spins of the $N = 1$ Landau level since these are the only ones with spin resolved energy levels available.

2.3 Direct determination of the critical exponent of the localization length, ν

We now begin with the investigation of critical phenomena in quantum Hall transitions by attempting to directly determine ν, which is expected to be ~ 2.35, from the localization length in the tail regions of a Landau level conductivity peak. At low temperatures the transport mechanism in this region is well understood to allow the localization length to be calculated.

2.3.1 Adaptation of localized hopping

Transport between strongly localized states (as found in the tail regions of a disorder broadened Landau level) is only possible through hopping between localized states. As discussed previously (Section 1.3.4), in the low temperature limit variable range hopping (VRH) is the predominant transport mechanism and is defined by Mott's $T^{1/4}$ law [33] as

$$\sigma_{xx}(T) \propto \exp[(-T_0/T)^{1/d+1}], \tag{2.5}$$

where d is the dimensionality of the system. For $d = 2$, the exponential temperature dependent term is reduced to $T^{-1/3}$.

Mott's law, however, is based on the assumption that the density of states near the Fermi level is constant. This is valid when a wide range of energies around the Fermi level are involved in the hopping process, but in the low temperature limit, only a very narrow range of energies around the Fermi level contribute towards the hopping conductivity. In this regime it was pointed out that electron-electron interaction should reduce the density of states near the Fermi level. Efros and Shklovskii [96] demonstrated that Coulomb interaction in this regime does in fact reduce the density of states and creates a Coulomb gap such that Mott's VRH conductivity is redefined as

$$\sigma_{xx}(T) = \sigma_0 \exp[(-T_0/T)^{1/2}], \tag{2.6}$$

where

$$k_B T_0 = C \frac{e^2}{4\pi\epsilon_r\epsilon_0\xi}. \tag{2.7}$$

The prefactor of the exponential in Eq. (2.6) has been observed to be temperature dependent, $\sigma_0 \propto 1/T$ [97-99]. The dimensionless constant C is expected to be of the order of unity and is believed to be $C \approx 6$ [100].

Therefore at very low temperatures where a Coulomb gap is expected, the localization length can be determined from a double log plot of Eq. (2.6) where T_0 will be the gradient of a linear fit to the plot. From Eq. (2.7) we note that, $\xi \propto 1/T_0$. The divergence of ξ as the critical field is approached $\xi \propto |B - B_c|^{-\nu}$, can then be rewritten as

$$T_0 \propto |B - B_c|^{\nu}. \tag{2.8}$$

The critical exponent ν can therefore be determined as the gradient of the double log plot of Eq. (2.8).

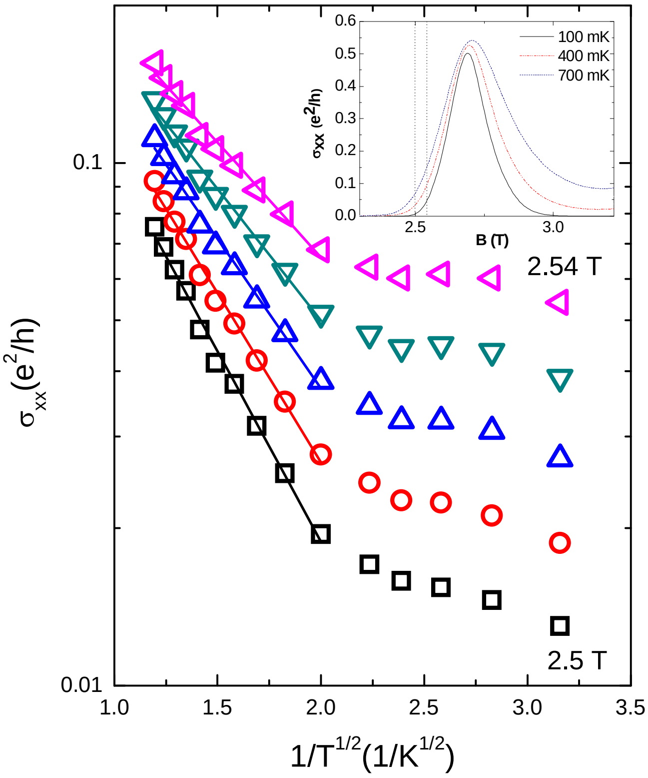

Figure 2.5. Analysis of VRH conductivity in the tail regions of the $N = 1 \downarrow$ LL of sample L3 between 2.5 T and 2.54 T. The solid lines are linear fits to Eq. (2.6). The inset shows the LL analysed and the two vertical dotted lines indicate the range sampled.

Fig. 2.5 shows the Efros–Shklovskii VRH equation applied to the localized region of the $N = 1 \downarrow$ LL of sample L3. We notice a weak temperature dependence of conductivity at very low temperatures (< 200 mK). We do, however, find good agreement with Eq. (2.6) at temperatures above 200 mK indicated by the linear fit of the solid lines in Fig. 2.5. The gradient of each linear fit represents a field dependent value of T_0 which is inversely proportional to $\xi(B)$. We notice that the gradient of the linear fit becomes gentler as the centre of the LL is approached. This indicates a growing or diverging ξ on approaching the critical field. We also notice that the linear fits appear to converge towards some finite conductivity when extrapolated to high temperatures. The convergence point is argued to be the minimum metallic conductivity proposed by Mott (see section 1.3.3).

A tendency for the conductivity to saturate at lower temperatures is observed in all the four samples investigated, with all samples possessing the same saturation temperature of $\sim$200 mK. In addition, the saturation region is independent of magnetic field (or energy within the LL). These two observations suggest that the saturation is due to a finite-size effect. Similar saturation regions are commonly observed in transport measurements of samples of small sizes [82, 85, 87, 101]. It has been previously shown that changing the size of the sample does indeed change the cut off saturation temperature [85]. We therefore neglect the saturation region in the remainder of our analysis.

2.3.2 ν in spin resolved Landau levels

It is important to discuss briefly how the critical field of the data presented below is determined. We recall that the critical point is important because it is the point at which the localization length diverges to infinity (the point of singularity) and this coincidence with the location of a LL. According to the theory of the QHE, within a two-dimensional system LLs are found at discrete energy values corresponding to the integer values, n, of $\hbar w_c(n+1/2)$, (see section 1.4.1). In the presence of disorder, however, a LL is no longer a single or discrete point but rather a band of energies consisting of both localized and extended states. The singularity of the localization length occurs within the extended states, and strictly speaking, at thermodynamic limit. However, since the data presented below are of systems of finite-size, the critical point, according to finite-size scaling theory, is approximated by the peak in the density of extended states. This is roughly located at the centre of a LL conductivity peak of σ_{xx}, but may not necessarily coincide with the geometric centre of the peak due to contributions of localized states transport to σ_{xx}. On the other hand, any measurement of σ_{xy} about a specific LL must pass through a critical value ${\sigma_{xy}}^*$, which corresponds to the Hall conductivity at the critical energy or field. Experimentally, it is well known that ${\sigma_{xy}}^*$ is not affected by disorder mechanisms such as temperature, unlike its equivalent in the diagonal conductivity ${\sigma_{xx}}^* = 0.5e^2/h$. The existence of ${\sigma_{xy}}^*$ is confirmed in Fig. 2.6 below where it can be seen that all traces within the plot passes through a single point independent of temperature. It can be seen from the figure that as the temperature is reduced, though the plateau-to-plateau transition becomes steeper, it passes through the ${\sigma_{xy}}^*$ point. It is obvious that the critical point must be within this transition region. In the limit of the absolute zero of temperature the transition will be a step function of infinitesimal width but, as shown in Fig. 2.6, must still pass through ${\sigma_{xy}}^*$ and since the critical point must be within the plateau-to-plateau transition width, ${\sigma_{xy}}^*$ must be the critical point.

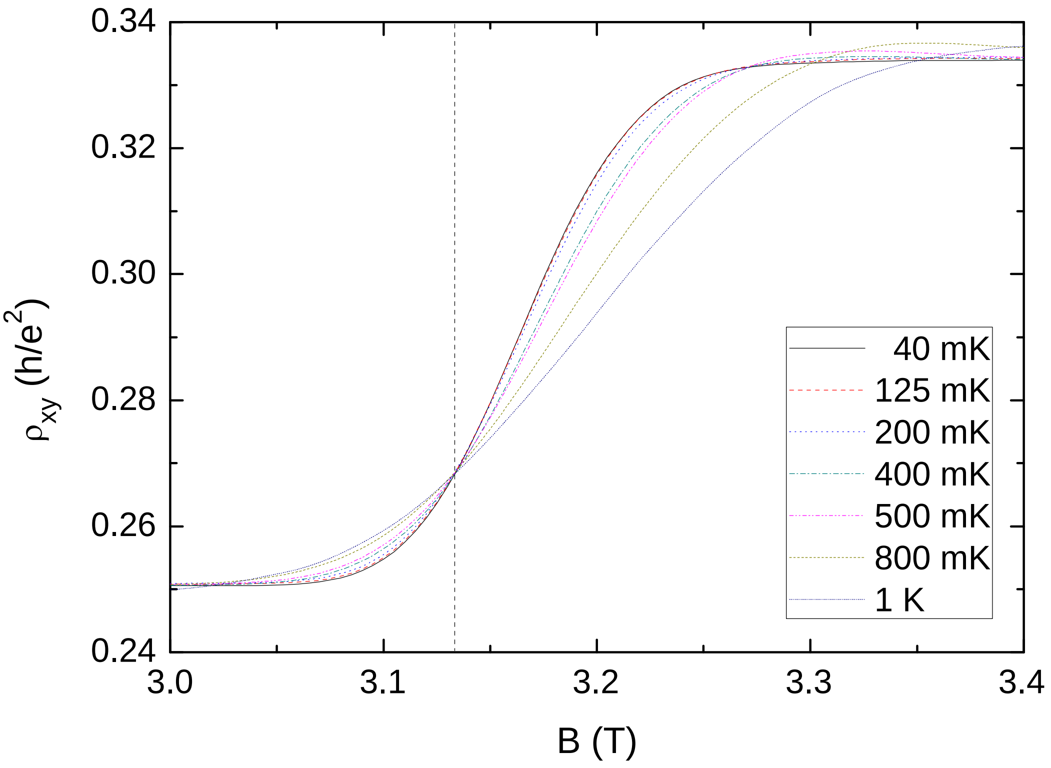

Figure 2.6. The Hall resistivity for the $N = 1 \downarrow$ LL for sample L1. It is observed that all temperature traces pass through and intersect at a single point which coincides with the critical field at the centre of the LL.

Having dealt with the issue of the location of the critical field, we apply the VRH analysis to all four samples under investigation in order to determine the critical exponent ν. Fig. 2.7 shows a similar plot to Fig. 2.5. The plot in Fig. 2.7(b) is obtained according Eq. (2.6) for the low field side of the LL shown in Fig. 2.7 (a). It is observed from the plot that VRH is in good agreement with the data and extends deep into the tails of the broadened LL. From the field dependent values of T_0 obtained for each sample, ν is determined from Eq. (2.8). Applying this analysis to all samples, the plots in Fig. 2.8 are obtained. For each sample, T_0 is plotted against $\delta B = |B - B_c|$. This can be plotted twice for each sample, one from approaching the B_c from the high field side of the LL and another from the low field side approach. The critical exponent ν is therefore determined twice for each sample. The values are summarized in Table 2.2.

It is noted that in determining the range of data included in Fig. 2.8, the critical point it determined using the Hall conductivity as discussed above, and far away from the critical point, the data is limited by the zeroing of the conductivity of the lowest temperature.

In Table 2.2, it is observed that the data is in remarkable agreement with the theoretically predicted value of $\nu \approx 2.35$ [11] for all sample.

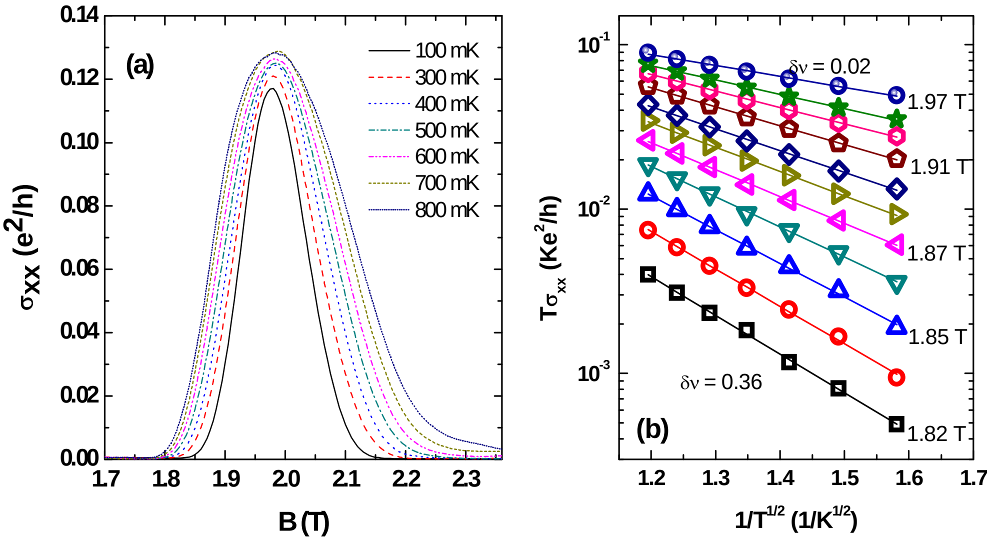

Figure 2.7. (a) Temperature dependence of the $N = 1 \downarrow$ LL transition peak for sample L4. The peak width increases with temperature. (b) Semi-log plot of the temperature dependence of σ_{xx} taken from the data in (a), using Eq. (2.6).

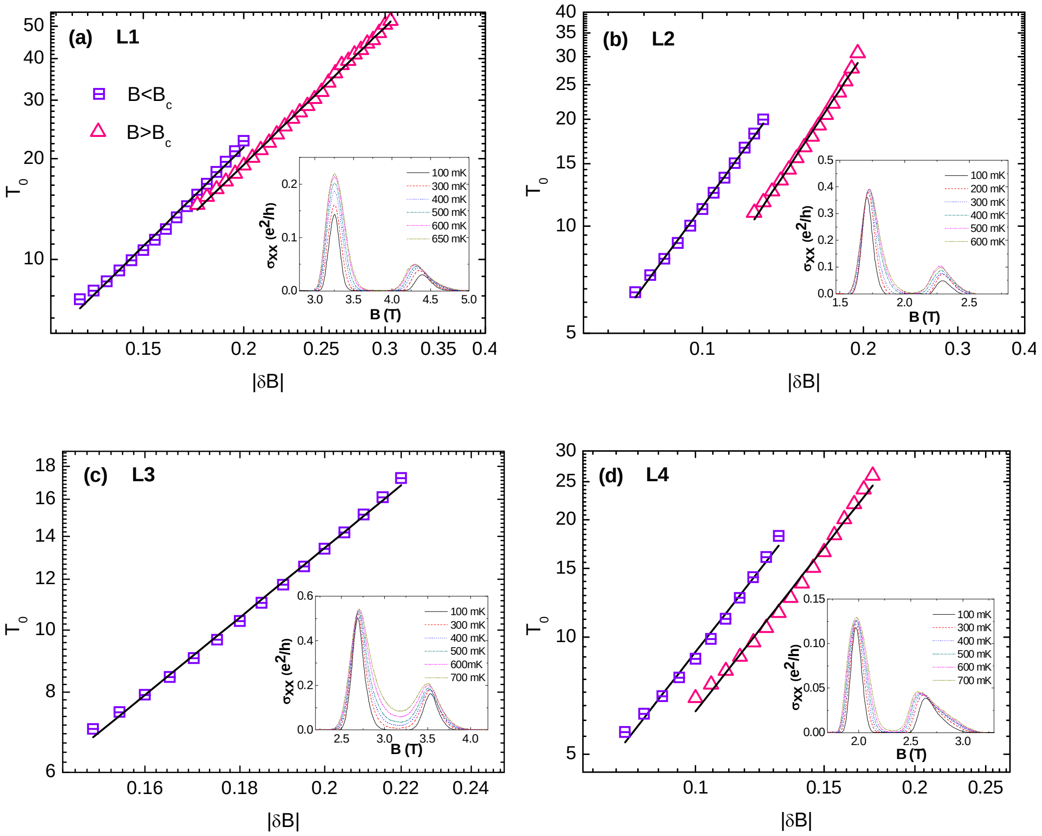

Figure 2.8. Logarithmic plot of T_0 as a function of distance in magnetic field away from the critical point, δB, for the $N = 1 \downarrow$ LL. ν is measured as the gradient of the linear fit to $\ln(T_0) = \nu \ln(\delta B)$. ν is determined for all four samples investigated, ■ shows measurements taken on the low-B side of the critical point, while ▲ show measurements on the high-B side. The values determined are in good agreement with the expected value of $\nu \approx 2.3$. The insets show $\sigma_{xx}(B)$ as a function of temperature for all samples; strong temperature dependent LL coupling is observed in sample L3 preventing the determination of ν for the high-B sided of the LL. The values of ν obtained are summarized in Table 2.2.

TABLE 2.2. The localization length exponent ν, measured for the N = 1↓ Landau level. Each sample has two measured values of ν, one from the low field side of the LL and the other from the high field side.

Sample	$N = 1\downarrow$	
	$B < B_c$	$B > B_c$
L1	2.37 ± 0.05	2.34 ± 0.02
L2	2.05 ± 0.03	2.28 ± 0.05
L3	2.36 ± 0.03	1.79 ± 0.01
L4	2.39 ± 0.08	2.39 ± 0.06

It should be noted that the range of error in the determination of ν presented in the table represent the error incurred in fitting a linear line to the data in Fig. 2.8. Both the high field and low field values of ν in all samples are in good agreement with the exception of sample L3 where the high field value obtained was $\nu = 1.79 \pm 0.01$. This discrepancy is attributed to the strong onset of LL coupling between the $N = 1 \downarrow$ and $N = 1 \uparrow$ LLs with increasing temperature evident in the inset of Fig. 2.8(c). This is caused by the relatively high level of disorder broadening in this particular heterostructure. As discussed above, the broadening of a LL is related to the quantum life time by $\Gamma = \hbar/2\tau_q$, and from Table 2.1 it is observed that sample L3 has the smallest quantum life time, $\tau_q = 0.53$, making it the sample with the most disordered LL broadening. It is observed from the insets of Fig. 2.8 that spin coupling in the other samples is negligible.

Assuming $C \approx 6$ [100, 102] and using $\epsilon_r \approx 12.6$ for GaAs, the localization length calculated from Eq. (2.7) is consistently found to grow to $\xi \approx 3\ \mu m$ as the critical point of the LL is approached and $\xi \approx 200\ nm$ as the Fermi energy enters the tail region.

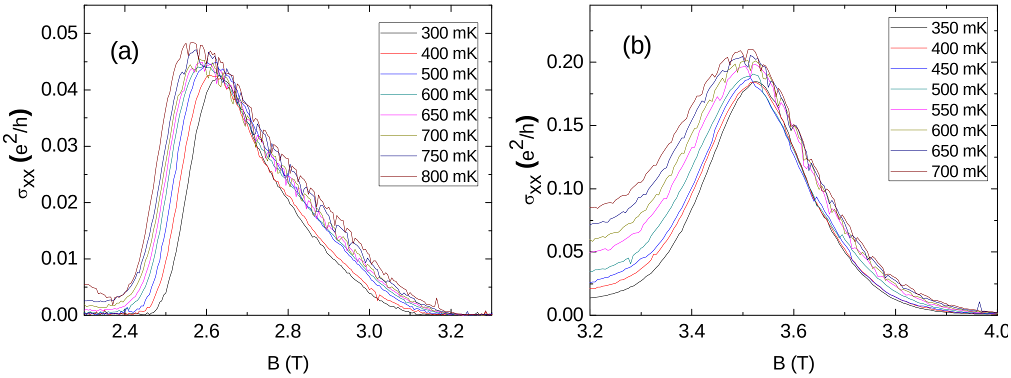

Figure 2.9. Plot (a) and (b) show pronounced conductance fluctuations in the $N = 1 \uparrow$ LL of samples L1 and L3 respectively. These fluctuations make it impossible to determine ν to any reasonable accuracy.

These values are consistent with measurements on devices of comparable heterostructures of similar sizes [100, 103].

It is noted that ν was only determined for one of the spin resolved LLs. Data from the $N = 1 \uparrow$ LL could not be used as the conductivity peaks exhibited pronounced conductance fluctuations as shown in Fig. 2.9. These fluctuations show strong correlation between various independent temperature traces, it therefore possible that these are universal conductance fluctuations (UCFs) [30, 104]. UCFs are irregular but nevertheless reproducible fluctuations of conductance in mesoscopic samples and can occur when the phase coherence length is comparable to the size of sample. The conductance fluctuations are also observed in the spin up peaks of higher LL indices but never on the spin down LLs.

From the results obtained in Table 2.2, it can be concluded that critical phenomena (as determined from measurements of ν) in QHTs are indeed universal, independent of any microscopic sample detail, and in accordance with continuous quantum phase transition as proposed by the theory [6]. In the following section we measure the composite critical exponent κ and investigate its universal criticality.

2.4 Determination of the composite critical exponent, κ

We determine κ using the Pruisken formalism [79] discussed in section 1.4.3 where it was proposed that the composite exponent κ can be measured from the temperature dependence of the width of the diagonal conductivity or resistivity peak,

$$\Delta B_{\rho_{xx}} \propto T^{\kappa}, \tag{2.9}$$

or the gradient of the Hall transition between the insulating phases of the QHE,

$$d\rho_{xy}/dB \propto T^{-\kappa}, \tag{2.10}$$

where κ is related to ν by $\kappa = p/2\nu$. κ can be experimentally determined as the gradient of a linear fit of the double log plot of either Eq. (2.9) or (2.10). We note that the exponent of interest is ν, which is the critical exponent of the divergent localization length.

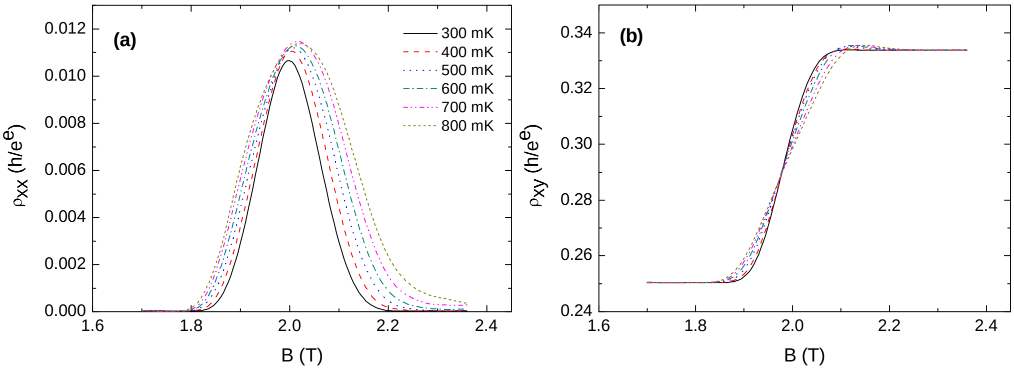

Figure 2.10. The temperature dependence of (a) ρ_{xx} and (b) ρ_{xy} as a function of magnetic field for N = 1↓ for sample L4.

ν is expected to possess a universal value independent of the microscopic details of the system. If it is assumed (for the time being) that $p = 2$ according to Fermi liquid theory [105], then κ is simply the reciprocal of ν, $\kappa = 1/\nu$. Thus a universal value of $\kappa \approx 0.43$ will confirm the universality of $\nu \approx 2.35$. This is the approach that has been use by previous investigations [12, 15, 18].

Unlike the previous section, results are presented for both spins of $N = 1$ since the observed fluctuations do not introduce any significant error in the data when the parameter under consideration is the width of the peak. The fluctuation only affect the diagonal resistivity data and are completely absent from the Hall resistivity data. Fig. 2.10 shows an example of the data consider in determining κ, taken from one of the samples.

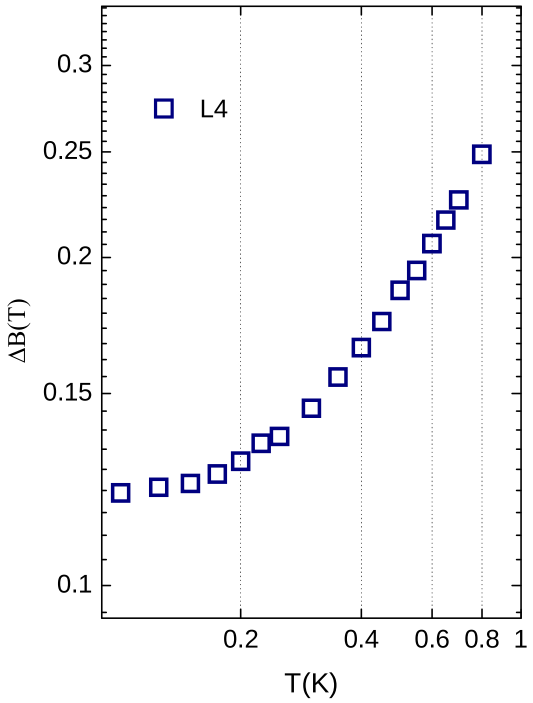

Figure 2.11. Finite-size effects are also evident in resistivity data. The plot shows a saturation of the width of the resistivity peak at very low temperature for sample L4.

For each sample, ρ_{xx} and ρ_{xy} are measured at many different temperatures between 100 mK and 1 K. From Fig. 2.10, it is clear that as the temperature is increased the width of the peaks also increases and the gradient of the transition slope decreases according to Eqs. (2.9) and (2.10).

The finite-size effects observed in the previous section are also evident in the resistivity data. Fig. 2.11 shows the saturation of the width of ρ_{xx} at low temperatures. The width ΔB, is determined as the full-width-at-half-maximum (FWHM) of the peak. Once again the saturation region is not considered in the analysis. The cause of the saturation region will be discussed in more detail in Chapter 4.

Table 2.3 show the results for κ for both spins of the $N = 1$ LL as determined from both the FWHM of the resistivity peaks and the maximum gradient of the Hall transitions (see Fig. 2.12). Once again, the error shown in Table 2.3 originates from the linear fit to the data. In general the results obtained from Eq. (2.9) and (2.10) agree well with each other.

TABLE 2.3. The exponent κ measured for Landau levels $N = 1\downarrow$ and $N = 1\uparrow$ using both the width of the transition peaks, $\Delta B_{\rho_{xx}}$, and the maximum gradient of quantum Hall transitions, $d\rho_{xy}/dB$.

	$N = 1\downarrow$		$N = 1\uparrow$	
Sample	$\Delta B_{\rho_{xx}}$	$d\rho_{xy}/dB$	$\Delta B_{\rho_{xx}}$	$d\rho_{xy}/dB$
L1	0.42 ± 0.01	0.23 ± 0.02	0.41 ± 0.01	0.44 ± 0.02
L2	0.67 ± 0.02	0.66 ± 0.03	0.44 ± 0.02	0.42 ± 0.03
L3	0.55 ± 0.04	0.60 ± 0.02	0.46 ± 0.02	0.43 ± 0.03
L4	0.54 ± 0.02	0.54 ± 0.02	0.34 ± 0.01	0.16 ± 0.02

The results however do not depict a universal behaviour of the critical exponent. Even though the value of κ for the $N = 1 \uparrow$ LL is closely distributed about the predicted value of $\kappa \approx 0.43$ (i.e. $\nu \approx 2.35$), the value of κ for the $N = 1 \downarrow$ LL in not. This is especially surprising since, for the same samples, ν was found conclusively to be universal for the $N = 1 \downarrow$ LL when universal criticality was determined using the hopping conductivity analysis above.

The results presented in Table 2.3 are consistent with previous investigations on the critical phenomena of QHTs in GaAs/AlGaAs heterostructures where universality of the critical exponent was not conclusive [15]. The results on κ present an interesting picture where, for the same sample, ν is found to possess the theoretically expected universal value but κ does not. The discrepancy between the ν and κ results could be due to a non-universal behaviour of the third exponent p. We therefore complete the investigations of the critical phenomena using temperature dependent methods to study the temperature exponent p.

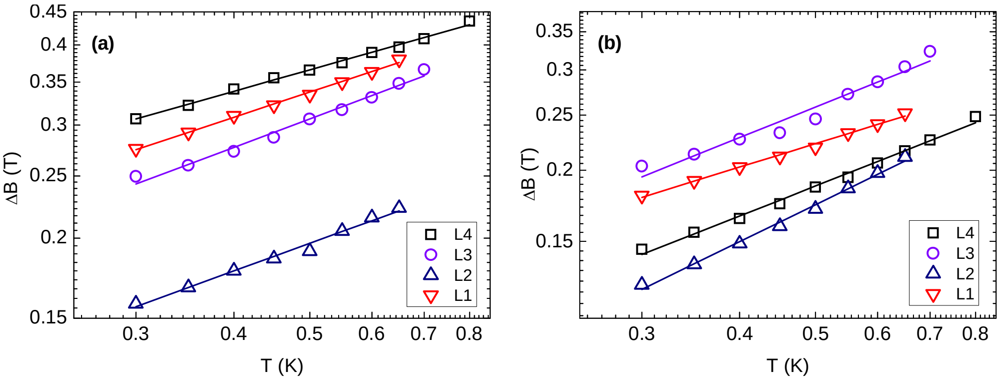

Figure 2.12. Double log plots of ΔB vs. T for (a) $N = 1 \downarrow$ and (b) $N = 1 \uparrow$ for sample L4. κ is measured as the gradient of the linear fits and presented in Table 2.3.

2.5 Current scaling of the QHE

The scaling exponent p is the least studied exponent involved in the temperature dependent analysis of the critical phenomena of QHTs. The value of p is always assumed to be $p = 2$, but this value is derived from the Fermi liquid theory of clean metallic films [106]. This is especially questionable since there appears to be no obvious justification of using the clean limit result of a 2DES instead of the disordered result of $p = 1$ [105], since 2DES in any practical sense are generally disordered systems. It is also not obvious that p should be universal as it is dependent on disorder according to Fermi liquid theory. Even more important is whether p is due to electron-electron scattering or electron-phonon scattering or a combination of both. In addition, the theoretical values of p stated above are based on zero magnetic field conditions of a 2DES, it is not clear whether they apply at high magnetic fields. Results on p are presented below and it is shown that this scaling exponent depends on both disorder and magnetic field.

2.5.1 Thermal coupling and the inelastic scattering exponent of two-dimensional Fermi liquids

The origins of the exponent p in the scaling argument of QHTs (discussed in section 1.4.3), stems from its influence on the effective size of the system. From our discussion on the Thouless length [48] in Chapter 1, it was noted that the size of system L acts as the cut-off of coherence electron transport such that states with $\xi(E) < L$ appear localized while states with $\xi(E) > L$ behave as extended states. If one realises that it is not simply the size of system that determines this cut-off but rather the loss of phase coherence on arrival at the boundary of the system, then a coherent system is defined by an effective length based on the phase coherent length L_{φ}. It is therefore noted that L_{φ}, among other things, can be determined by the physical boundaries of the system. Within a system with any degree of disorder, the phase coherent length can be defined as [50]

$$L_{\varphi} = (D\tau_{\varphi})^{1/2}, \tag{2.11}$$

where D is the diffusion constant for an electron within the system and τ_{φ} is the phase breaking time or inelastic scattering time. At sufficiently high temperatures, the phase coherence length is determined by a temperature dependent inelastic scattering time, $\tau_{\varphi}(T)$. It is therefore intuitive to assume that $\tau_{\varphi} = \alpha T^{-p}$ [105] such that,

$$L_{\varphi} \propto T^{-p/2}. \tag{2.12}$$

where α is the constant of proportionality and p is the inelastic scattering exponent.

We attempt to measure p in our samples by using an electron heating model proposed by Anderson *et al*. [107]. In an experimental investigation of electron transport in thin metallic films, it was observed that at low temperatures a sufficiently high applied electric field E has a similar dependence of conductivity as an increase in temperature [108]. Based on this observation, Anderson *et al*. [107] noted that at very low temperatures where the inelastic scattering length is long, electrons are almost out of thermal contact with phonons and therefore under an applied electric field these electrons will heat up, absorbing the power being delivered to the sample through the acceleration of charge under the electric field. Thermal energy being absorbed by electrons from the electric field increases until this excess energy can be transferred to the lattice through a collision. During this time interval the electron temperature T_e will be out of equilibrium with the lattice temperature T_L. These hot electrons will therefore maintain their temperature (or energy) for a distance L_φ or time τ_φ such that T_e can be defined as [107]

$$k_B T_e \sim eEL_\varphi. \tag{2.13}$$

where E here represents the applied electric field. From Eq. (2.12) and (2.13) the coefficient of the ratio of $\ln(T_e)$ to $\ln(E)$ is $\eta = 1/(1 + p/2)$ such that

$$T_e \propto E^\eta. \tag{2.14}$$

Eq. (2.14) can also be expressed in terms of the applied current I (or voltage) as $T_e \propto I^\eta$. By bringing T_e out of equilibrium with T_L by applying a high electric field (or current), the temperature exponent p can be measured (this is discussed in the next section). This is only possible at low temperatures where thermal coupling between the electron gas and the lattice is weak. At higher temperatures however, energy will be efficiently transferred between the lattice and the electron gas (i.e. τ_φ is very small) which makes causing an imbalance in the equilibrium difficult.

2.5.2 Determination of the temperature exponent p, at the critical field

The experiments yielding the results presented above (sections 2.3 and 2.4) were conducted in the strong thermal couple regime, where $T_L = T_e$, by using a very low current. We also note that due to effective thermal sinking, the ambient temperature or bath temperature T_b of the sample chamber of the dilution refrigerator was in good equilibrium with T_L of the sample. The sample is placed in good thermal contact with the mixing chamber plate which is also the location of the temperature sensor used to control the bath temperature. In the strong thermal coupling regime therefore, a steady state is established between all relevant temperatures ($T_b = T_L = T_e$) by the transfer of energy through phonon emissions. In all experiments discussed in this thesis a sufficient time delay always follows a manual change in the T_b setting of the fridge to allow this equilibrium to be established. Thus moving forward, we will always assume that $T_b = T_L$.

Transport coefficients measured in the strong coupling regime reflect T_L which in this regime is equal to T_e. At high applied currents (or electric fields) T_e will come out of equilibrium with T_L such that $T_e > T_L$. The transport coefficients measured in this regime hence reflect T_e rather than T_L. By calibrating T_e with transport measurements in the strong coupling regime where the value of T_e is known (since $T_e = T_L$), the relationship between the applied current I and T_e can be established.

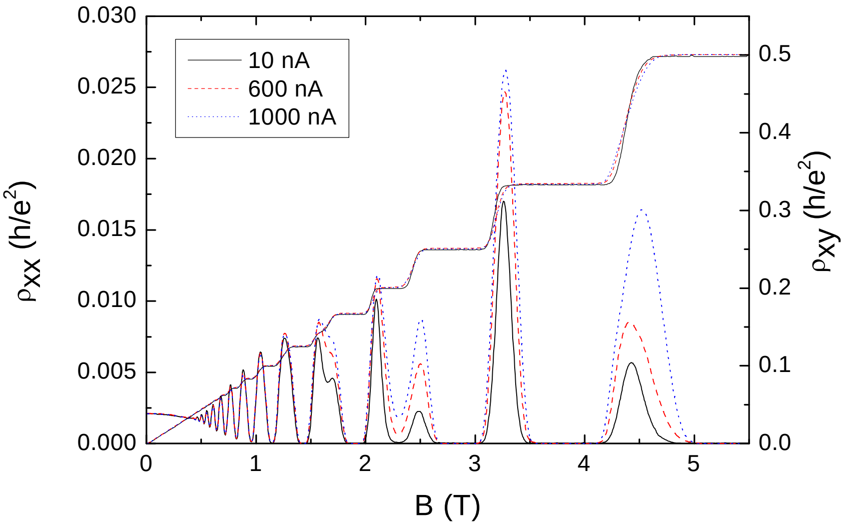

Figure 2.13. Transport coefficients measured at three different applied d.c. currents. Electron heating is evident in the broadening of peaks and the reduction in transition slopes between plateaus.

This is achieved by comparing the transport measurements taken in the weak coupling regime ($T_e > T_L$) with those taken in the strong coupling regime ($T_e = T_L$). To determine p, we compare the resistivity at the critical field (at the centre of each LL) within the two regimes in order to establish the relationship between I and T_e. It is noted that the applied current representation of Eq. (2.14) is simply

$$T_e \propto I^{\eta}. \tag{2.15}$$

Since the 2DES most resembles metallic behaviour at the critical field within a LL, it is the most appropriate place to apply Anderson's electron heating model (originally used to study metallic films) [107].

The effect of increasing the sample current is shown in Fig. 2.13. It is clearly observed that the increase in the d.c. current has a similar effect on transport coefficients as an increase in temperature. The only difference here is that the relevant temperature of the system is being controlled by the electric field rather than the bath temperature of the dilution fridge. As mentioned above, the relation in Eq. (2.15) will be determined by taking measurements at the critical field, in particular, the maximum slope observed between plateau-to-plateau transitions will be the calibrating thermometer used in measuring T_e. The maximum slope $d\rho_{xy}/dB_{max}$, occurs at or very close to the critical field. Fig. 2.14 shows ρ_{xy}, determined for both a varying temperature and a varying current, for the transition about the $N = 1 \downarrow$ LL in sample L1. All the curves in Fig. 2.14 intersect at the critical field which is also the $d\rho_{xy}/dB_{max}$ point. The similarities between the two plots are evident. The effects are similar because the underlining mechanism is a temperature dependent scaling phenomenon.

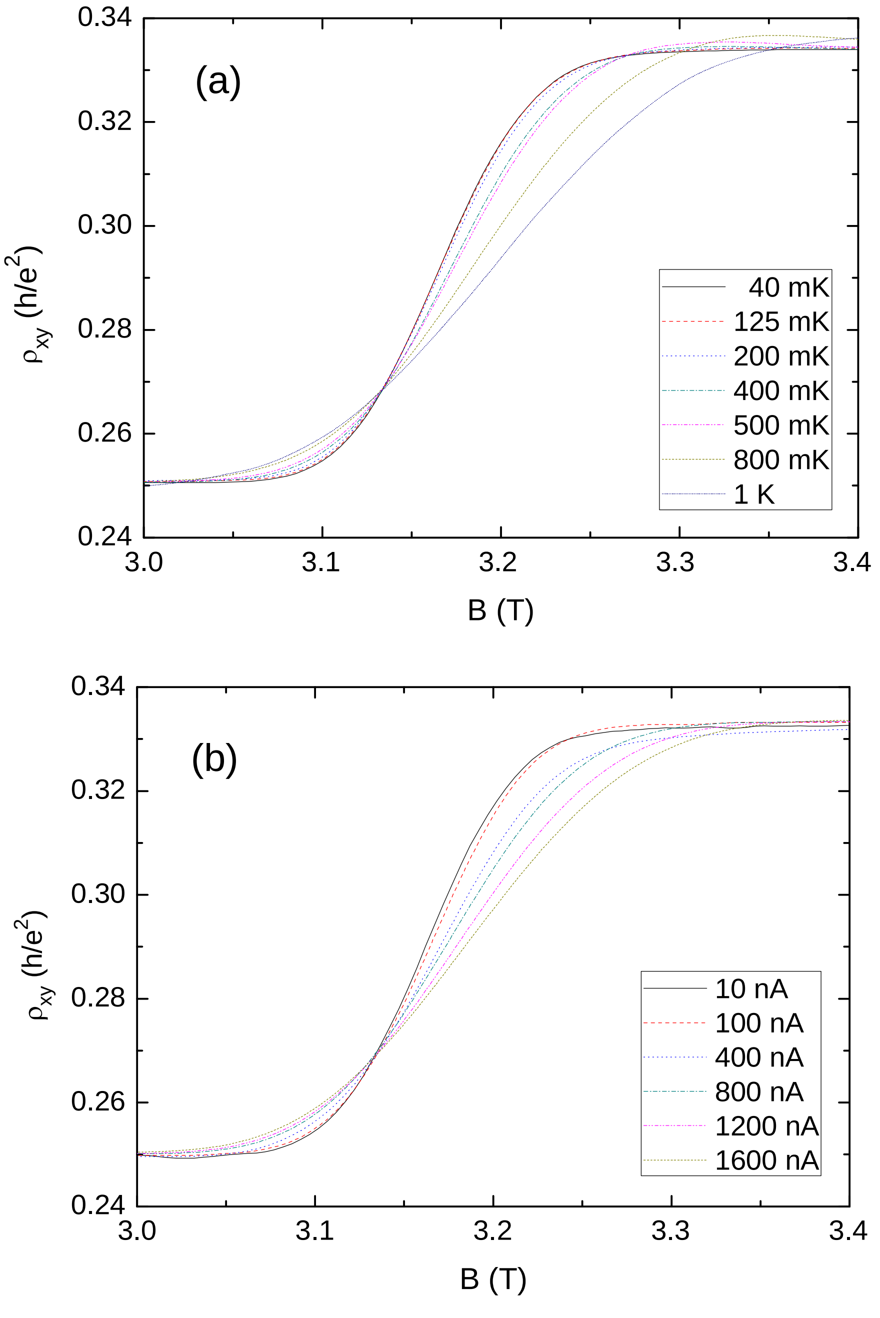

Figure 2.14. The transition slope between adjacent plateaus is shown (a) as a function of varying temperature at 10 nA and (b) as a function of the applied current at 40 mK. The effect in both cases is observed to be similar.

In the case of Fig. 2.14(a), scaling (of the phase coherent length) is controlled by the lattice temperature while in Fig. 2.14(a), scaling is controlled by the electron temperature. Fig. 2.15 is a plot of $d\rho_{xy}/dB_{max}$ using the data in Fig. 2.14(b). It shows the two coupling regimes. At low currents, electron heating is negligible, the lattice is easily able to soak up the excess heat due to T_e and therefore continually maintains the equilibrium. $d\rho_{xy}/dB_{max}$ does not change with increasing current in this regime. At high currents, however, we observe a logarithmic dependence on transport coefficients due to the weak thermal coupling between electrons and the lattice. Scaling is observed within this regime as T_e takes over as the relevant or operative temperature.

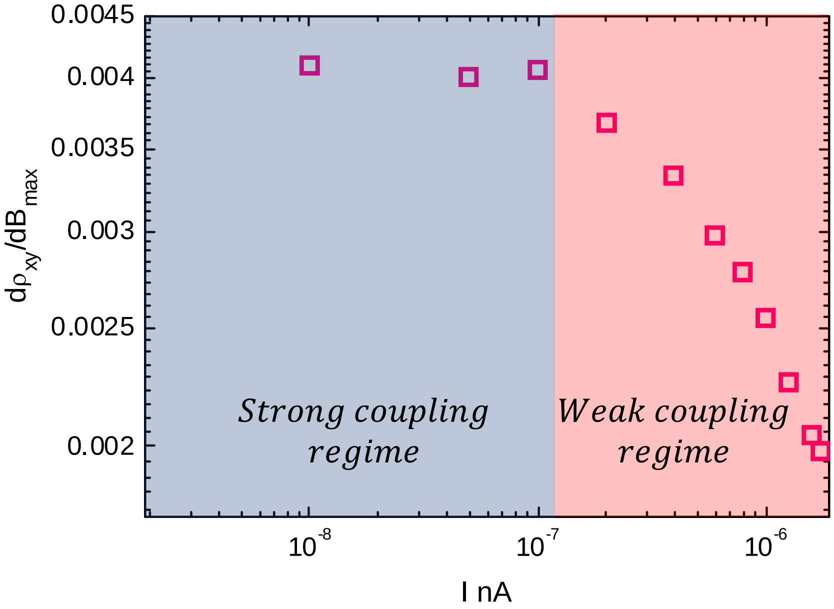

Figure 2.15. Dependence of the $d\rho_{xy}/dB_{max}$ on current. In the strong coupling regime, increasing the current has negligible effect on the slope of the plateau-to-plateau transition. At higher currents however, there is weak coupling between T_e and T_L. The significantly higher T_e is able to influence the transport coefficients of the system.

We now proceed to the experimental determination of p using Eq. (2.15). Fig. 2.16 describes how T_e is calibrated using $d\rho_{xy}/dB_{max}$. It is noted that the underlining scaling mechanism is the same irrespective of whether T_e or T_L is the relevant temperature. The aim of the plots in Fig. 2.16 is to discern what the electron temperature is at a given current in order to apply Eq. (2.15). To do this, we first measure the value of $d\rho_{xy}/dB_{max}$ at various temperatures in the weak coupling regime. This is shown in Fig. 2.16(a). Though the temperature is changed by varying T_L, we recall that in this regime $T_e = T_L$. Fig. 2.16(a) therefore presents the relationship between T_e and $d\rho_{xy}/dB_{max}$.

In Fig. 2.16(b), $d\rho_{xy}/dB_{max}$ is measured again, but this time as a function of the applied current. Having already calibrated T_e using $d\rho_{xy}/dB_{max}$, the electron temperature corresponding to a given current is simply the temperature that produces the equivalent value of $d\rho_{xy}/dB_{max}$ in the weak coupling regime. Therefore from Fig. 2.16, the current I_1 corresponds to the temperature T_1.

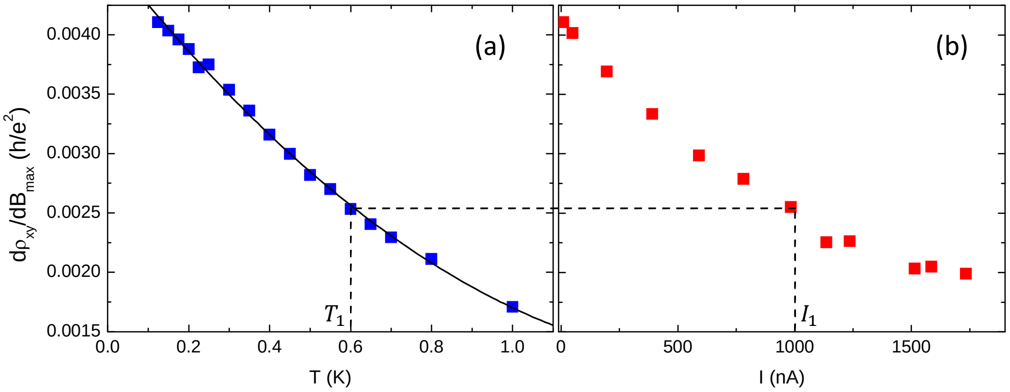

Figure 2.16. $d\rho_{xy}/dB_{max}$ for the $N = 1\downarrow$ of sample L4 measured both as function of temperature and current. The dashed line indicates, for example, that T_e at $I_1 = 1000$ nA is equivalent to $T_1 = 600$ mK.

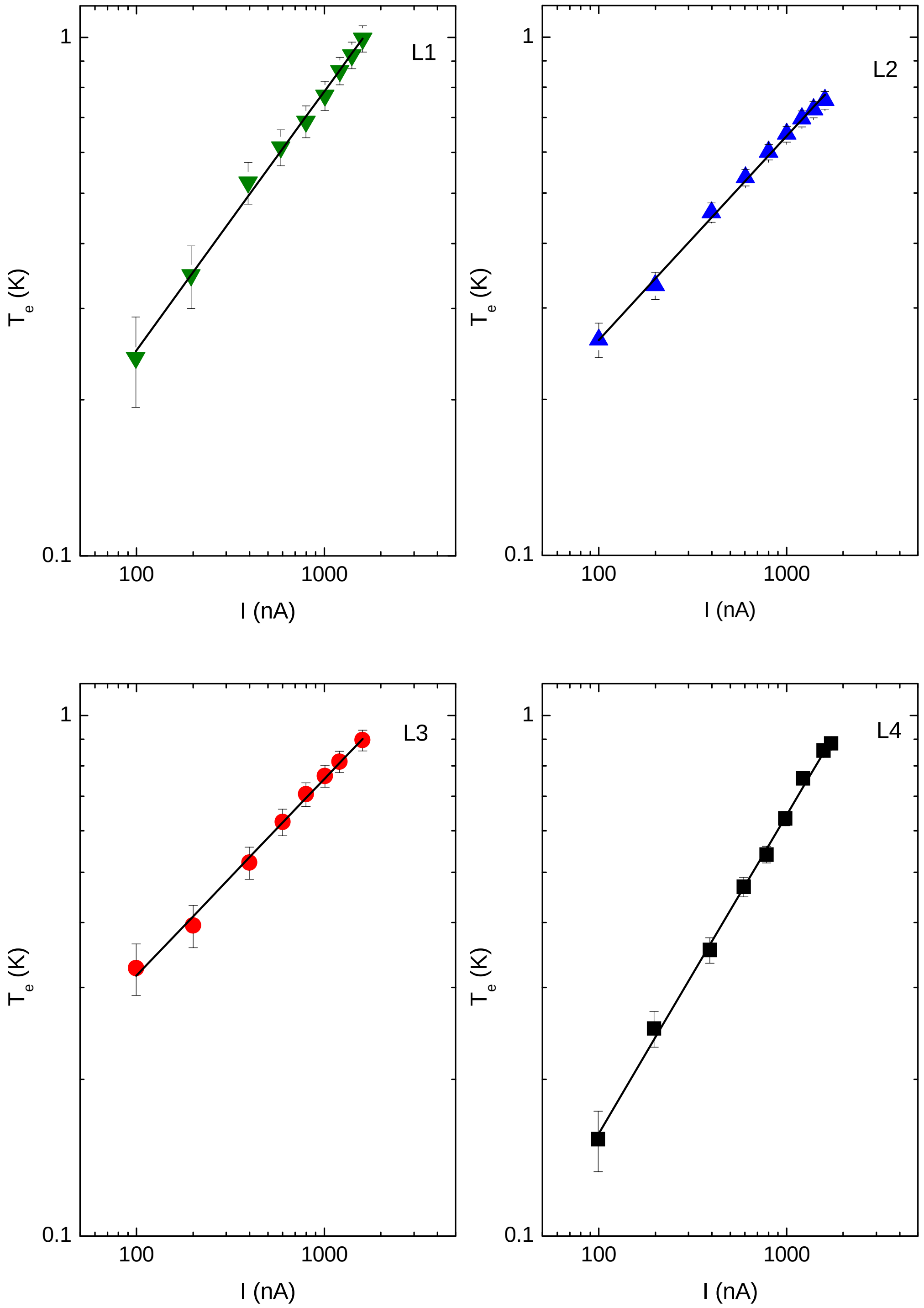

Figure 2.17. A double log plot of T_e vs. I for $N = 1 \downarrow$ LL for all four samples. p is determined from the gradient of the least-squared linear fit to the data.

TABLE 2.4. The temperature exponent p determined for various transitions in all four samples.

Sample	Plateau to plateau transition		
	$N = 1 \downarrow$	$N = 2 \uparrow$	$N = 2 \downarrow$
L1	2.01 ± 0.04	2.02 ± 0.08	2.06 ± 0.05
L2	3.09 ± 0.06	3.11 ± 0.13	3.23 ± 0.26
L3	3.29 ± 0.09	-	-
L4	1.27 ± 0.02	1.55 ± 0.09	1.64 ± 0.09

Using the Anderson electron heating model, p is determined in all samples for the $N = 1 \downarrow$, $N = 2 \uparrow$ and $N = 2 \downarrow$ LLs. We recall that the gradient of the linear fit of the double log plot of Eq. (2.15) is $\eta = 1/(1 + p/2)$. Fig. 2.17 shows p determined for the $N = 1 \downarrow$ LL for all four samples. It is noted that all plots show a good linear fit to the heating model, where the solid lines in Fig. 2.17 represents a least-square fit to the data. The results are summarized in Table 2.4.

The value of p is not found to be universal between the samples investigated. The value of the exponent, however, is similar amongst LLs of the same sample with slight increases at higher LL indices (mostly likely due to the increasing degeneracy at higher LLs, see Fig. 2.4). Due to the strong disorder broadening in sample L3, all but one LL were completely spin degenerate and thus p was only obtainable for one LL. However, a striking dependence of p on mobility is observed in the results, this is plotted in Fig. 2.18. p is consistently found to increase with decreasing mobility. The results suggest that the rate of phonon emission is different for each sample, and in particular, depends on the nature of disorder within the sample. The more disordered the sample the greater the rate of phonon emissions, and therefore, the greater the value of p.

Initial scaling investigations of QHTs assumed the value $p = 2$, taken from the Fermi liquid theory value for a metallic film in the clean limit. This proved necessary for a good agreement with the universally expected value of $\kappa \sim 0.43$ [12] to be obtained given that $\kappa = p/2\nu$. This seemly fortuitous coincidence, however, has lead to confusion in the literature regarding the temperature dependence of the critical phenomena of QHTs. The temperature exponent p ($\tau_\varphi \propto T^{-p}$), is mainly determined by electron-electron (e-e) scattering and electron-phonon (e-ph) scattering. At very low temperatures e-e scattering is the dominant dephasing process in thin metallic films [109]. The dephasing process occurs through multiple scattering events involving small energy transfers $\Delta\varepsilon$, between electrons (where $\Delta\varepsilon \ll k_B T$).

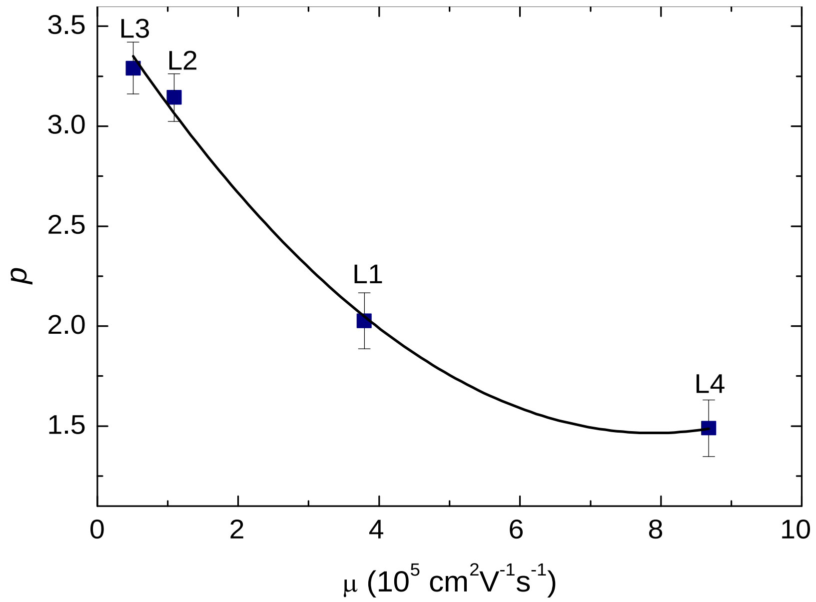

Figure 2.18. Figure showing the dependence of p on the mobility of the samples investigated. The valve of p are averaged over each sample a clear increase with decreasing mobility is observed. The solid line is a guide for the eye.

These scattering events arise from fluctuations in background potential generated by the ensemble of electrons and other Coulomb sources (remote ionized impurities). In this e-e scattering regime, an electron can lose phase coherence without relaxing its excess energy (through numerous $\Delta\varepsilon$ transfers), this is known as Nyquist dephasing [106]. In the presence of disorder, the scattering time in a 2DES is expected to favour a linear dependence on temperature, $p = 1$, [105, 109-111] at zero magnetic field but, in the clean limit, $p = 2$ [109, 110, 112] is predicted.

At higher temperatures however, the loss of phase coherence is dominated by e-ph scattering with electron relaxation occuring through inelastic collisions where $\Delta\varepsilon$ is of the order of $k_B T$. Unlike the case for e-e scattering, the temperature dependence of τ_φ is not expected to have a universal behaviour in either the clean or dirty limit [109].

It is therefore of great interest to the work presented here to determine whether the dephasing mechanism occurring close to the centre of the LL is dominated by e-e scattering or e-ph scattering as this will confirm the validity of the assumption of $p = 2$ and by extension the scaling relationship $\kappa = p/2\nu$. The temperature at which the transition between e-e and e-ph scattering occurs is somewhat disputed; some studies favour a transition to e-e scattering below $\sim$10 K [109] while others suggest a temperature of $\sim$0.2 K [113]. The results presented here, however, favour an e-ph scattering mechanism near the centre of the LL for the temperature range investigated. This is indicated by the non-universality of p typical of e-ph scattering and the dependence of p on mobility. These results confirm the theoretical studies of τ_φ in the integer QHE regime where p was found to be dominated by e-ph interaction and depend on electron mobility [114, 115]. Our results are also in agreement with the experimental investigation of

Koch *et al*. [85]. Even though the method for determining p was different from that used by Koch *et al*., the results are similar as p was also found to be non-universal and dependent on mobility. The values of p and the corresponding mobilities obtained from Koch *et al*. are in good agreement with the curve in Fig. 2.18.

The results favouring the universality of p and e-e scattering obtained by Wei *et al*. [14, 116, 117] therefore appear inconsistent. First, according to the theory of e-e and e-ph scattering, one expects $p = 1$ for disordered films if e-e scattering is the operative mechanism [109]. This would invalidate the assumption of $p = 2$ used by Wei *et al*. [12]. It is therefore unexpected that $p = 2$ was obtained in the low mobility short-range alloy disordered InGaAs/InP systems used by Wei *et al* [14].

If p is not universal, then one does not expect the proposed universal relationship $\kappa = p/2\nu$ to be valid. This describes the results presented here, no correlation is found between values of p in table 2.4 and the corresponding values of κ in table 2.3 even though ν was found to be universal in all samples in table 2.2. It is also important to note that the variation in p observed in the results presented above does not show any correlation with carrier concentration, spacer width or quantum life time, quantities that are related to e-e scattering. Instead, the results presented here show that p depends on the zero field classical mobility of the samples measured, the quantity that is least related to e-e interaction and more representative of microscopic disorder.

The collection of the results present here therefore suggests that p is not crucial to the critical phenomena observed in QHTs.

2.6 Conclusion

In the study of critical phenomena of QHTs presented in this chapter, we have attempted to verify the expected divergence of ξ as the critical point within a LL is approached. A universal critical exponent of value $\nu \approx 2.3$ is expected. The results presented here have independently investigated all three scaling exponents in the scaling relationship $\kappa = p/2\nu$ using temperature dependent methods. It was found that ν, determined from the localized hopping regime, is in good agreement with theoretical predictions and is observed to be universal and independent of sample characteristics. κ, however, was found to non-universal in our experiments. Further, investigations of the temperature exponent p based on electron heating also did not yield universal values. The results on p suggest that the dephasing process near the critical point is dominated by e-ph scattering and therefore the assumption of $p = 2$ is not justified. The results presented here do not confirm the relationship $\kappa = p/2\nu$, especially since p cannot be universal and must be dependent on disorder. These investigations therefore support universality in ν but does not support the case for $\kappa = p/2\nu$.

Even though it is argued here that p must not be crucial to the critical phenomena of QHTs, the role of κ is less obvious. As discussed above, the assumption $p = 2$ appears to be only a fortuitous coincidence which is required to explain the initial experimental results obtain on κ [12]. One cannot, however, dismiss the result of $\kappa \approx 0.43$ which is so widely observed that it cannot be coincidence. It has been suggested [102, 118] that the correct dependence of κ on ν is simply an inverse relationship, $\kappa = 1/\nu$, without any dependence on p. Given the results presented here, this seems to be more likely since an (incorrect) assumption of $p = 2$ will result in the same relation. This still does not explain why the reciprocal relation was not observed in our results on κ. The explanation for this will be left for Chapter 4 after further results on κ have been presented in Chapter 3.

The work presented in this chapter represents the first and only attempt to investigate all scaling exponents independently within the same sample in order to provide a coherent picture of the nature of criticality in QHTs and study the relationships between the proposed critical exponents. All previous investigation have only looked at a subset of exponents and rely on various assumptions for non-measured exponents. A summarized version of this chapter has been published in Refs. [119, 120].

3. Finite-frequency scaling of quantum Hall transitions

3.1 The effect of frequency on critical phenomena and localized systems

So far, we have investigated the quantum criticality of quantum Hall transitions (QHTs) in localized systems using techniques that involved changing the temperature of the system. In this chapter we look at how a similar analysis can be made using a high resolution frequency technique which has many advantages over a temperature based method. In this section we describe the effect of a varying electric field on the transport properties of interest in the finite-size scaling of QHTs.

3.1.1 Dynamic scaling

We introduce the concept of dynamic scaling in order to explain how the scaling analysis of the critical phenomena observed in QHTs can be studied by varying the frequency of an externally applied electric potential. It should be noted that any mention of frequency henceforth will exclusively refer to the frequency of the applied electric field.

In the foregoing analysis, critical phenomena were discussed in terms of the thermodynamic or static properties of the system [7], in particular the correlation in position of electron transport. We considered a divergent correlation length, which acted as the order parameter, as the critical point was approached (see section 1.4.2). It was shown that fluctuations on length scales smaller than the correlation length were insignificant to the behaviour of the system. At the critical point where the correlation length diverges to infinity (or the boundary of the system), the system becomes homogenous. As a result, individual systems of different characteristics are indistinguishable near the critical point, forming a universality class possessing identical behaviours. Discussed in the context of zero temperature, this view of the criticality represents the static description of the critical phenomena where the correlation in the spatial dimension is the only parameter considered. It was implicitly assumed that fluctuations that affected the temporal component of the system were infinitely long. In other words, it was assumed that the system remained correlated over time throughout the entire process.

At non-zero temperatures however, this time invariance assumption is violated and fluctuations in the temporal dimension are introduced in the form of time dependent correlation functions such as relaxation rates, spin-diffusion constants, thermal induced conductivities and other time dependent perturbations [8, 9]. The order parameter therefore now includes a temporal dimension over which order must be maintained. As the critical point is approached, fluctuations in both the spatial dimension and the temporal dimension must diverge towards infinity for quantum criticality to be realised. In the context of QHTs, an electron wavefunction must maintain correlation (i.e. maintain its eigenstate of energy) in space as determined by its localization length and also in time as determined by its phase coherence time as dictated by its relaxation rate. It is noted that the relevant relaxation rate will be determined by the relaxation mechanism that has the shortest time period as this will be the limiting factor on correlation. The conditions for universality are still maintained if both the temporal correlation and spatial correlation simultaneously diverge on approaching the critical point such that the systems appear homogenous at the critical point. If on the other hand the spatial correlation diverges without a divergence in temporal correlation then the properties of the system as the critical point is approached will be defined temporal fluctuations which are dependent on the specific characteristics of the system such as the relaxation mechanism. In other words, universality will not be observed as electron transport will retain sample specific properties.

The spatial and temporal dimensions can be combined into a single dimensional space by introducing a *dynamic exponent* z [6, 11]. z relates the spatial correlation length ξ (in distance) to the temporal correlations length ξ_τ (in time) as [6],

$$\xi_\tau \sim \xi^z. \tag{3.1}$$

The exponent z is therefore a measure of how skewed time is relative to space near the critical point. In the temperature dependent investigations discussed in Chapter 2, even though it was not explicitly mentioned, the temporal correlation length was converted to the spatial dimension using the Thouless boundary argument or the Thouless length, first introduced in section 1.3.5. We now define the general form of this conversion which will be applicable to all temporal perturbations (both temperature and frequency).

ξ_τ is manifested in the spatial dimension as a dephasing or coherence length L_φ which acts as the order parameter controlled by temporal events. In other words, order in this case refers to the length L_φ, over which an electron maintains its eigenstate of energy or remains unperturbed, where L_φ is related to the phase braking time τ_φ. The relationship between ξ_τ and L_φ will depend on the specific form of the temporal perturbation. Similar to the finite size scaling argument developed in Eq. (1.42) to (1.45), the conductivity of the system will depend on both L_φ and $\xi(B)$ through the finite-size scaling form

$$\sigma_{\alpha\beta}\left(L_\varphi, B\right) = F_{\alpha\beta}[\xi(B)/{L_\varphi}^{1/\nu}], \tag{3.2}$$

where $F_{\alpha\beta}$ is a universal scaling function. The width of the conductivity peak is related to the dephasing length through (see section 1.4.3 for full derivation),

$$\Delta B \sim {L_\varphi}^{1/\nu}. \tag{3.3}$$

Temporal perturbations introduced by temperature and frequency can be defined in terms of the dephasing length as

$$L_\varphi \sim T^{-1/z_T}, \tag{3.4}$$

and

$$L_\varphi \sim f^{-1/z_\omega}, \tag{3.5}$$

where z_T and z_ω are dynamic scaling exponents for T and f, respectively. From Eq. (3.3) the width of the conductivity peak as a function of T and f is given as

$$\Delta B \sim T^{1/\nu z_T}, \tag{3.6}$$

and

$$\Delta B \sim f^{1/\nu z_\omega}. \tag{3.7}$$

If we recall from the temperature dependent investigations in Chapter 2, that $L_\varphi \sim T^{-p/2}$, then the temperature scaling function used in the Chapter 2 is recovered from Eq. (3.4) and (3.6) if dynamic exponent is taken to be $z_T = 2/p$.

From experimental observations [12-14, 116], it is suggested that close to the critical point the value the dynamic exponent is $z_T = z_\omega = 1$ [6]. This is in accordance with the theory of critical phenomena since close to the critical point the system becomes homogenous and is independent of spatial and temporal perturbations. Therefore the method of temporal perturbation, be it temperature dependent or frequency dependent, should not matter.

Bearing in mind that finite-size scaling is an approximation of critical phenomena which occurs at $T, f = 0$, both the temperature and frequency must be made to tend towards zero in the critical region in order for there to be an approximate divergence of ξ_τ (or L_φ) or else universality between equivalent systems will not be observed. This could be a possible explanation for the dependence of z_T on the disorder of the system as observed in the current scaling results reported in the previous chapter. It is possible that the temperature was not low enough to allow an adequate divergence of ξ_τ near the critical point. This argument is discussed in greater detail in Chapter 4 (section 4.5.1).

Finally, we note that the relevant parameter controlling the dynamic scaling depends on the ratio hf/k_BT. For $k_BT \gg hf$, due to its higher dephasing rate, the temperature is the relevant parameter that determines ξ_τ. Conversely, if $k_BT \ll hf$, the frequency becomes the relevant parameter. A crossover between the two parameters is therefore expected at $k_BT = hf$. In the scaling regime where the frequency is the dominant phase breaking mechanism, $L_\varphi(f)$ represents the distance an electron diffuses within the disordered medium during one cycle, $1/f$, of the applied alternating electric field [121].

3.1.2 A.C. hopping in localized systems

The non-zero frequency of the applied electric field imposes a phase breaking mechanism $L_\varphi(f)$, where the system is coherent on a time scale proportional to the period of the field, $1/f$. In this section we describe the phenomenological process underpining decoherence through the application of a high frequency field to a disordered system. We consider the process of conduction in the localized regime of a disordered 2DES.

In the d.c. conduction of disordered systems, a continuous flow of current is setup between two electrodes where the direction of electron transport is determined by the direction of the applied field. Losses due to conduction therefore stem from electrons moving from one electrode towards the other. In a.c. conduction, the direction of electron transport is revered after each half cycle of the applied electric field. At very high frequencies, electron may only be able to hop to one state (or a few states) before the electric field is revered. In the high frequency limit therefore, losses in disordered systems can be occur through the back and forth transfer of electrons between pairs of states. A.C. losses can be accounted for by resonant transitions between pairs of states. This is generally known as the pair approximation [122, 123].

Consider a pair of sites i and j within a localized system and let the transition rate between the two states be τ_{ij}^{-1} such that transitions between i and j will only occur if $\tau_{ij} < 1/f$, where f is the frequency of the applied electric field. The frequency, or period of the alternating field, acts as a cut off limit on the transfer of electrons between states, restricting transitions that take too long to occur. It is reasonable to assume that the coupling of wavefunctions between states decreases with increasing separation, hence for a random distribution of states of the kind describe by Anderson localization, pairs of states which lie close together will have shorter transition times or higher transition rates than pairs of states that are further apart. At very high frequencies of the applied field, the cut-off for transitions will be so restrictive that only the closest pairs of states will have a transition time quick enough to contribute towards a.c. losses. Fig. 3.1

demonstrates such a scenario, where two such pairs of states are shown, $i \leftrightarrow j$ and $k \leftrightarrow l$. From the discussion on the distribution of states in Anderson localization in Chapter 1, we recall that the occurrence of these closest pairs of states, that are both close in energy and space, within a disordered system will be rare. Pairs of this kind will therefore be widely separated as shown in Fig. 3.1. In other words, $\tau_{ij} \ll \tau_{il}, \tau_{ik}$. Charge transfer occurring within pairs can therefore be considered to be independent and decoupled from their surroundings. A.C. conduction is then due to pair-hopping between resonant pairs of states which are determined by the frequency of the applied field.

Of interest to the scaling problem being discussed is the frequency dependent effective length of the system which in this high frequency regime will be determined by the average distance ΔR between the states of a resonant pair. The pairs i, j and k, l in the scaling sense, can be considered as two separate systems since they are effectively decoupled.

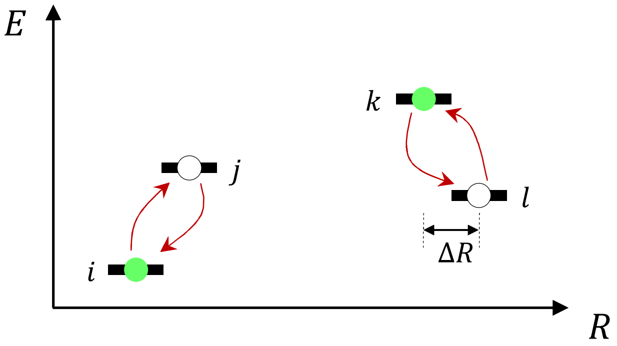

Figure 3.1. A diagram showing resonant pairs i, j and k, l. In the high frequency limit coupling to states that are far apart is cut off such that electron transfer is restricted to only states that are closest. Adjacent pairs of resonating states are therefore effectively decoupled from the rest of the system.

This is very similar to the Thouless argument that has been used throughout this work where a dephasing length defines the size of independent subsystems within a disordered system. It is clear from the discussion above that ΔR acts as the length of coherence, $L_{\varphi}(f) \sim \Delta R$, since coupling to sites larger than ΔR cannot occur.

As the frequency is reduced, the time within which coherent transitions occur increases and an electron is able to travel further within a half cycle of the applied field. Thus reducing the frequency increases ΔR, allowing an electron to interact with more of its surroundings. This is depicted in Fig. 3.2(a), which is a modification to Fig. 3.1. As the frequency is lowered, $1/f$ becomes large enough to include transitions over larger distances. In Fig 3.2(a), $\tau_{jk} < 1/f$ and as a result ΔR increases. Reducing the frequency therefore introduces variable range hopping within the system, which enables the coupling of previously isolated pairs.

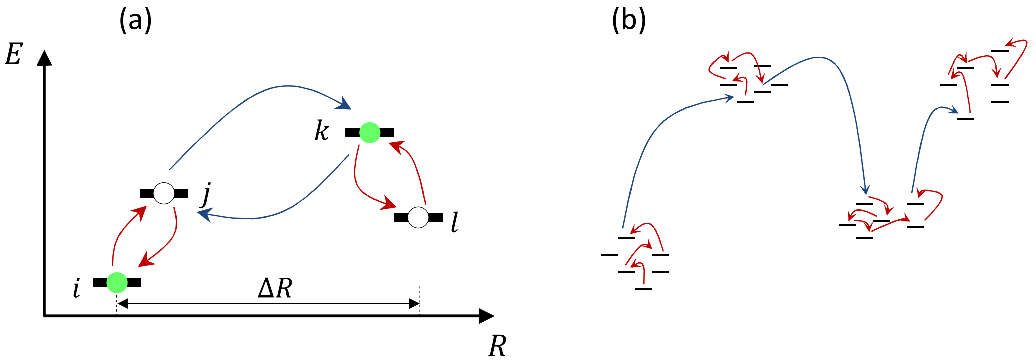

Figure 3.2. As the frequency is decreased, longer distance transitions begin to occur. (a) shows coupling between two resonant pairs, the blue arrow shows the introduction of longer distance VRH into the system. (b) As the frequency is further decreased, allowing multiple hops, conduction occurs between previously isolated clusters of states.

In this multiple hopping regime [124, 125] electron transport occurs between clusters of pairs [126] as shown in Fig. 3.2(b). Further decreasing the frequency ($f \rightarrow 0$) progressively increases the effective area of conduction until the entire system is included or until the dephasing mechanism, hitherto controlled by frequency, is taken over by temperature. Further decreases in frequency cannot increase $L_{\varphi}(f)$ beyond the temperature dependent dephasing length $L_{\varphi}(T)$ since beyond this point the dephasing length will be determined by temperature dependent events.

Changing the measurement frequency, in a similar way to changing the measurement temperature, varies the effective size of the system and allows the scaling analysis to be extended into the frequency regime through the temporal perturbation of the system. Therefore in the simultaneous limit of decreasing frequency (diverging $L_{\varphi}(f)$) and the divergence of ξ as the critical point is approached, universal criticality of QHTs can be observed within a 2DES as described by Eq. (3.7). It is noted that this statement assumes that the temperature dependent dephasing length is already larger than the sample size otherwise it would place a restriction on the divergence of L_{φ}.

Using this hopping approach it has been shown that the real part of the high frequency conductivity has the following logarithmic dependence on frequency [125]

$$\sigma(f) \propto f^{s}, \tag{3.8}$$

Where the exponent s is usually found in the interval $0.5 < s < 1$ [123, 126].

In the following sections, the frequency scaling analysis will be used to investigate the universality of QHTs within systems of varying degrees of disorder.

3.1.3 Previous experimental result on finite-frequency scaling

As discussed in the previous section, the dynamic scaling exponent relates the correlation time to the correlation length ($\xi_\tau \sim \xi^z$) and L_φ is the spatial equivalent of the correlation time as determined by temporal events. In the frequency regime L_φ is related to the dynamic exponent through $L_f \sim f^{-1/z}$ (Eq. (3.5)). For non-interacting electrons it can be shown [127, 128] that $L_f = 1/\sqrt{\rho_0 hf}$ where ρ_0 is the density of states at the critical point. Comparing this with the frequency dependent relation for L_f yields a value of $z = 2$. The result $z = 2$ is realised if the frequency dependent length is defined by a density-density correlation function $L_f = [D(f)/f]^{1/2}$ [121] where $D(f)$ is the frequency dependent diffusion coefficient.

The first experimental results on the dynamic exponent as measured from frequency by Engel *et al.* [13] reported a value of $z \approx 1$ but this disagreed with the preceding non-interaction theory. Shortly after the publication of this result, numerical calculations reported that a value of $z = 1$ ought to be found if Coulomb interaction between electrons near the QHT is considered [128-130]. To be consistent with $\nu \approx 2.3$, which hitherto had also been based on non-interacting single-particle analysis (but unlike z, proven correct by experimental results), numerical analysis was used to show that even though the value of z is modified under Coulomb interaction, ν still maintains its value of $\nu \approx 2.3$ [129]. It has also been predicted that the range of interaction (short or long-range) affects the value of z [131]. The result reported by Engel *et al.* of $z \approx 1$ was confirmed by Hohls *et al.* [132] but other results do not agree [16].

Experimentally, the most thorough high frequency investigation of critical exponent still remains the work of Engel *et al.* [13] where frequencies between 0.2 – 14

GHz was considered, the largest bandwidth hitherto reported in the literature. Most investigations following Engel *et al*. were carried out at lower frequencies, 0.1 – 6 GHz [133] and 0.7 – 7 GHz [16]. Two other studies exist at higher frequencies although the results presented appear to be somewhat controversial. A range between 35 – 52 GHz was investigated by Kuchar *et al*. [91], and although a value of $\kappa \approx 0.4$ was reported, the robustness of this study is not at all clear as no plots of the frequency range or even the fit are shown. The result is even more questionable when presented again in Ref. [132], since the plot shown is obscure and appears to shows little evidence of scaling. Investigations of QHTs at even higher frequencies have reported the observation of Hall plateaus in the terahertz frequency regime; but this result has to be treated with caution, as it is likely that quantum Hall plateaus are destroyed in the terahertz regime in much the same way they are destroyed at high temperatures. The unlikelihood of these high frequency results being correct will be discussed further in Chapter 5.

Experimental techniques that have been employed in finite-frequency scaling investigations include coplanar waveguide (CPW) techniques [13], coaxial cables [133], rectangular waveguides [91, 134] and free-space systems (though not finite-frequency) [135]. In the studies reported below, a high resolution CPW technique is used. Both the bandwidth and the frequency range investigated are extended beyond that report by Engel *et al*. Scaling is observed from close to d.c. up to 30 GHz, and the critical exponent is determined within a 20 GHz bandwidth. This work replaces the work of Engel *et al*. as the most extensive frequency dependent investigation conducted on scaling exponents.

3.2 High frequency devices and experimental techniques

Details about sample fabrication, the CPW device used, and the experimental setup for measuring the high frequency devices are discussed below. The device used in this work consists of a CPW with a dielectric that contains a 2DES. The operating, design and significant features of the device are discussed below. The fabrication and mounting of the device is also discussed, followed by the experiment arrangement used to measure ultra-low temperature losses in the device.

3.2.1 Coplanar waveguide devices

The high frequency excitation of the 2DES is performed using metallic conductors, that form a CPW, and are deposited on the surface of a sample containing the 2DES. A CPW [136] is a structure in which all conductors supporting the propagation of a wave are found within the same plane. The CPW structure consists of central conducting line which is separated from two ground planes on either side by narrow gaps or slots as shown in Fig. 3.3. These three conducting planes are placed on a dielectric slab with an electric and a magnetic permittivity of ε_r and μ_r, respectively. An ideal CPW requires ground planes of infinite width but in practice a width many times the wavelength of the propagating wave is sufficient for a good CPW approximation. The electromagnetic wave that propagates along the CPW consists of an electric field and a magnetic field that oscillate in planes orthogonal to the direction of propagation, this is known as a transverse electromagnetic mode or TEM mode.

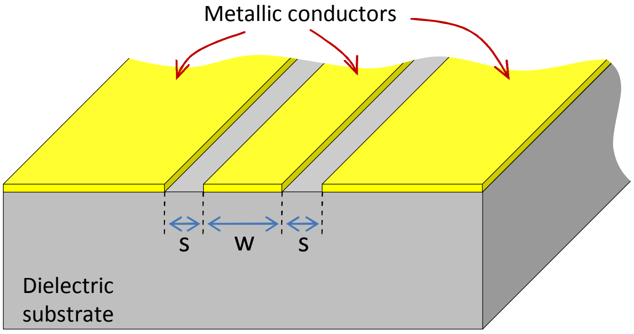

Figure 3.3. A structure of a conventional CPW which consists of three metallic conductors separated by a distance *s* and placed on top of dielectric substrate. The conducting planes on either side of the centre conductor are known as ground planes.

Though in practice a CPW transmission supports a quasi-TEM mode, the error made in evaluating propagation as a pure TEM is negligible for microwave and lower millimetre wave frequencies.

The structure of a conventional CPW permits the propagation of two fundamental modes; an even mode and an odd mode. The even mode is excited when the two ground planes have the same electric potential but differ from that of the centre conductor. The odd mode, on the other hand, is excited when the potentials of the ground planes have different signs but the same magnitude. The distribution lines of electric and magnetic fields for these two modes are shown in Fig.3.4. The even mode is often described as the symmetric mode while the odd mode is referred to as the anti-symmetric mode; this originates from the symmetry in field lines evident in Fig. 3.4(a) and the lack of it in Fig. 3.4(b). The field lines distribution in the even mode causes low dispersion (or signal loss) of the propagating wave over a large range of frequencies making it suitable for very broadband application and circuit designs.

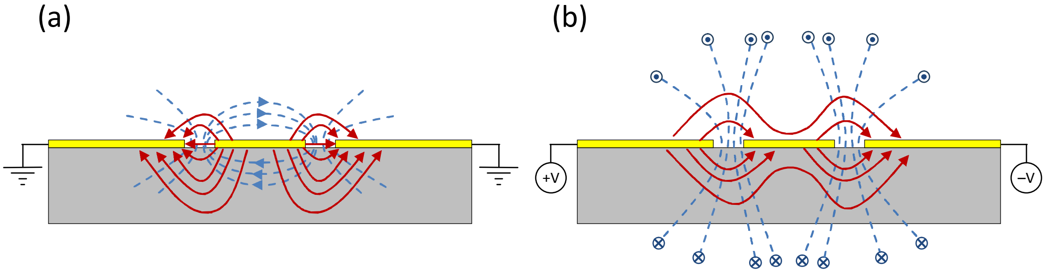

Figure 3.4. Electric (solid red) and magnetic (dashed blue line) field distribution of (a) the even mode and (b) the odd mode of a CPW. The even mode is known as the symmetric mode and the odd mode, the anti-symmetric mode. The mode excited depends on the relative potential of the conducting planes.

This is the mode excited in the work presented below thus we shall henceforth only concern ourselves with even mode propagation. We note that the quasi TEM nature of propagation attributed to the CPW stems from the existence of dispersion (even if minimal) inherent in CPW transmission. Dispersion, however, can be reduced by using a substrate with a high dielectric constant thereby confining most of the field lines within the substrate or having slot lines of very small widths.

In the devices presented here, the conducting planes constituting the CPW are deposited on top of a GaAs substrate containing a 2DES. The 2DES itself lies about 70 nm below the surface. The propagating wave on top of the sample is therefore capacitively coupled to the 2DES below as shown in Fig. 3.5(a). The real part of the conductivity of the 2DES Re[σ_{xx}] can therefore be modelled as a shunt resistance to ground as shown in Fig. 3.5(b) where the 2DES absorbs some amount of power from the propagating signal. This acts as an additional loss incurred by the signal.

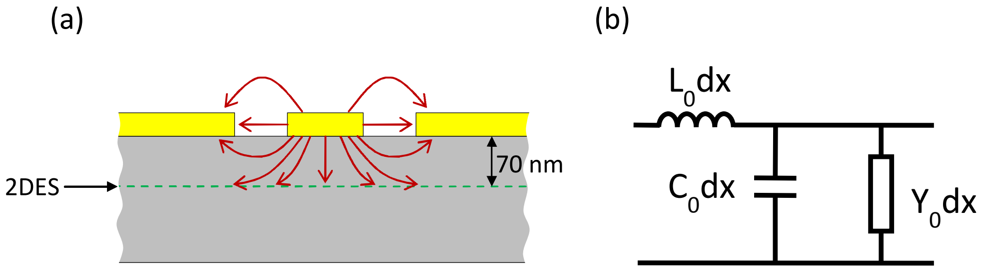

Figure 3.5. (a) A cross-section view of the electric field lines of the propagating wave coupling with the 2DES system below. (b) A model of the circuit formed by the 2DES-CPW, where L_0, C_0, and Y_0 are the inductance, the capacitance and the admittance per unit length of the 2DES-CPW, respectively. Y_0 represent losses of the CPW due to the 2DES or power absorbed by the 2DES from the CPW.

Measuring the magnitude of this loss allows Re[σ_{xx}] of the 2DES to be calculated and since σ_{xx} is dependent on magnetic field, Re[σ_{xx}] determined at different magnetic fields will provide the magneto-conductivity data of the embedded 2DES.

The high magnetic field characteristics of the 2DES-CPW device are as follows. In the plateau region of the QHE, σ_{xx} of the 2DES vanishes to zero (as expected in the QHE) and therefore the 2DES is effectively invisible or transparent to the propagating wave above. In this region the 2DES is non-dissipative and thus losses in the propagating signal due to the 2DES are extremely small and, as we shall see below, negligible. As the centre of the LL is approached the 2DES becomes highly conductive and dissipative, akin to a metallic sheet. At this point, the losses in the propagating signal due to the presence of the 2DES become relatively more pronounce and significant.

The characteristic impedance of the CPW is designed to be 50 Ω in the plateau region. This is achieved by considering the ratio between the width of the centre conductor w and the width of the slot or gap s in the CPW design (see Fig. 3.3).

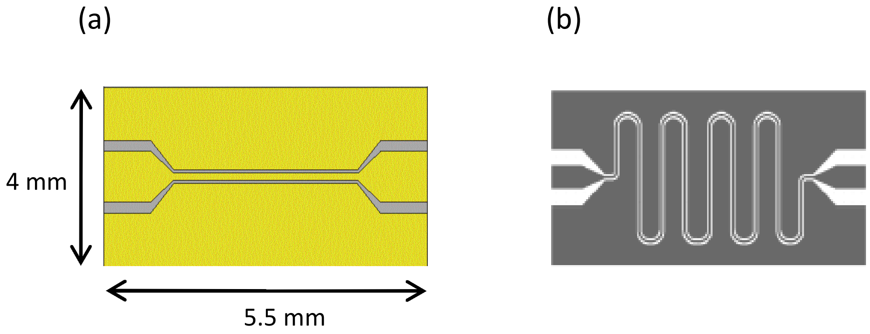

Figure 3.6. Schematic of the two designs used for the 2DES-CPW, they include (a) a straight centre conductor of length 5.5 mm and (b) a meandering centre conductor of length 20 mm. In both designs $s = 30$ μm and $w = 50$ μm and the pattern has whole dimensions 3 mm by 5.5 mm.

Matching the CPW to 50 Ω is done to suppress reflections at boundary between the CPW and the external transmission lines, which is also matched at 50 Ω.

The CPW designs used in this work, consists of two patterns; a CPW with a straight centre conductor (Fig. 3.6(a)) and a CPW with a meandering centre conductor (Fig. 3.6(b)). The width and length of both devices are the same; 3 mm by 5.5 mm. The width of the centre conductor, $w = 50$ μm, and the width of the slot, $s = 30$ μm, are the same in both designs. The main difference between the two patterns is the length of the centre conductor which determines the area of the 2DES excited. The straight CPW has a centre conductor of length $l = 5.5$ mm while the meandering line has $l = 20$ mm. The meandering line therefore probes an area just over 3.5 times greater than the straight CPW. A longer meandering line increases the signal-to-noise ratio by increasing the sensitivity of the signal to losses occurring in the 2DES. The disadvantages of a meandering line include a pattern which is more difficult to fabricate and a complex geometry that is susceptible to resonances and cross coupling (cross talk) between parallel lengths of the meandering line.

Finally, we discuss the issue of the active or excited region of the 2DES. Although the CPW sits on top of a large surface area covering the 2DES, the active region under excitation is the region between the centre conductor and the ground plane, i.e, the gap or slot width s. All other areas are under zero or very weak excitation. The effective physical length of the 2DES is therefore ~ 30 μm (the width of the gap). Charge carriers within the 2DES move between the ground plane and centre conductor line. Charge transport within the 2DES therefore occurs in the direction perpendicular to the direction of the propagating wave and along the electric field lines. Fig. 3.7(a) indicates the active length of the 2DES, which is largely located within the slot regions of the CPW. Fig. 3.7(b) shows a top view of the active region excited beneath the CPW.

A look at the time varying electric field within the active region shows a field which alternates with the frequency of the propagating wave (Fig. 3.8).

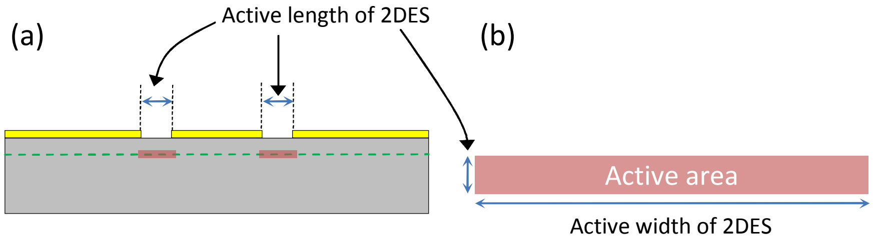

Figure 3.7. The schematic in (a) shows the active region of the 2DES below the surface. The highlighted region of the 2DES shows the active length of the 2DES excited. The figure in (b) shows a top view of the active area excited by the CPW. The active width shown in (b) corresponds to the length of the centre conductor. It is noted that the direction of electron transport in the 2DES is along the active length (and not the active width) shown in both (a) and (b).

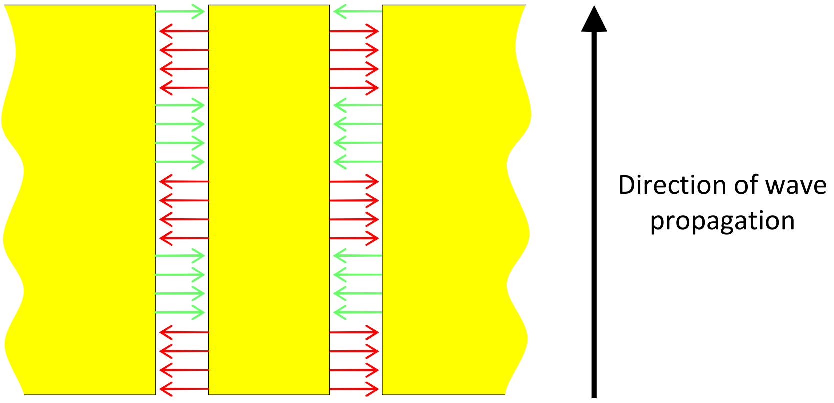

Figure 3.8. The time varying electric field of the even mode as the wave propagates along the CPW.

In the context of a.c. hopping discussed in section 3.1.2, for a low frequency signal where the period of the electric fields is much greater than the time required for charge carriers to move between the centre conductor and the ground plane, electron transport will possess d.c. characteristics. In other words, if the half cycle period of the applied electric field is greater than the time it takes for an electron to move across the gap, the 2DES will behave as if it is being excited by a d.c. signal.

3.2.2 Device and sample fabrication

As discussed in the previous section, the devices used for high frequency excitation of the 2DES consists of conducting planes deposited on top of a dielectric where the dielectric in this case refers to the 2DES sample or the GaAs/AlGaAs heterostructure. In addition to the CPW pattern shown in Fig. 3.6, the devices used in this work also include ohmic contacts placed on the edges of an etched mesa which defines the borders of the 2DES. The complete design of the device pattern is shown in Fig. 3.9. The ohmic contacts allow for simultaneous d.c measurements to be obtained while a.c. measurements are taken using the CPW. The d.c. measurements are important as they verify the a.c. results and also to identify the location of LLs observed in the a.c measurements.

The process involved in fabricating the devices is as follows. The surface of the 2DES sample is chemically etched to a depth of about 200 nm to reveal a square mesa (raised surface) containing the 2DES as shown by the dashed line in Fig. 3.9. Ohmic contacts formed from an alloy of Au/Ge/Ni are deposited (through thermal evaporation) across the edge of the etched mesa after the contact regions have been lithographically defined. The contacts are then annealed at 430 °C for 80 seconds in an atmosphere of nitrogen. The pattern of the conducting planes of the CPW is lithographically defined and then formed from a 30/350 nm layer of Ti/Au evaporated onto the surface of the sample.

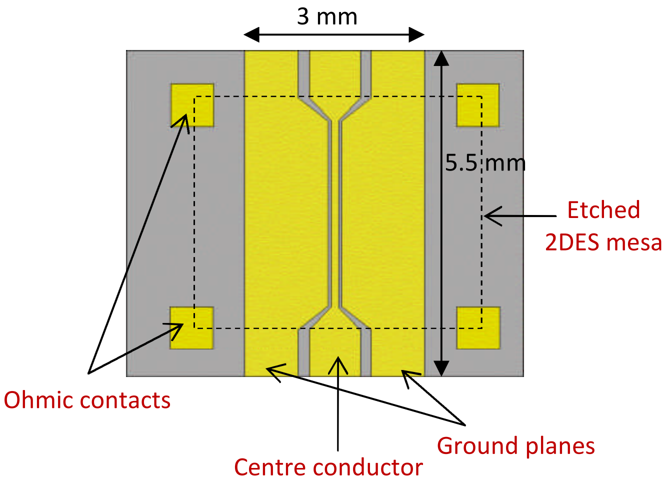

Figure 3.9. Complete design of 2DES-CPW devices showing the ohmic contacts and the conducting plane of the CPW.

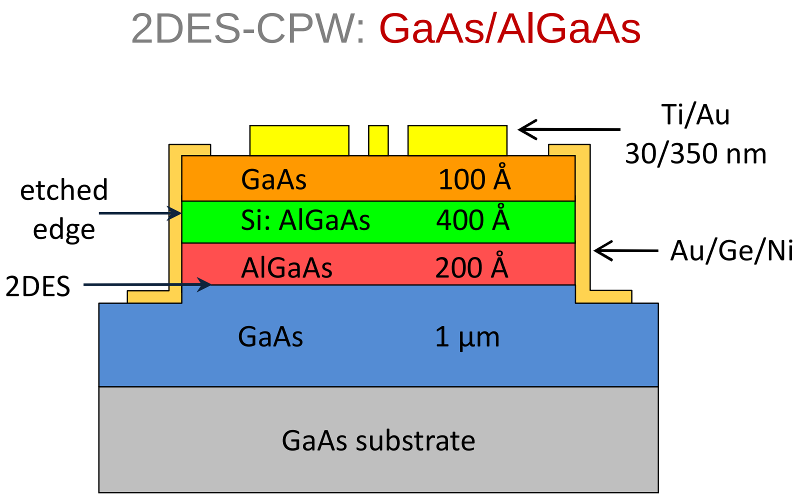

Figure 3.10. A schematic showing a cross-section of the 2DES-CPW device. The diagram depicts the various layers of the GaAs/AlGaAs heterostructure, the Ti/Au deposits that form the conducting planes of the CPW, and the ohmic contacts formed from annealed Au/Ge/Ni deposits on the edge of the etched mesa.

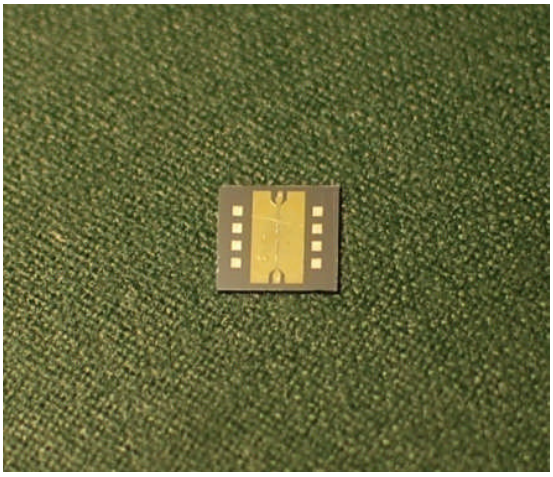

Figure 3.11. A photograph of the fabricated device which shows the CPW with ohmic contacts on either side.

Fig. 3.10 shows a cross-section of the sample after completion of the fabrication process. The figure depicts all elements of the device including the various layers of the GaAs/AlGaAs heterostructure. A photograph of the fabricated device is shown in Fig. 3.11.

The device is mounted into a sample holder which consists of two coaxial connectors attached to both sides of the device by copper strips as shown in Fig. 3.12. These copper strips connect the grounding and centre conductor of the coaxial connectors to the ground planes and centre conductor of the CPW using silver epoxy. This was found to be the most effective method of delivering the high frequency signal to the device.

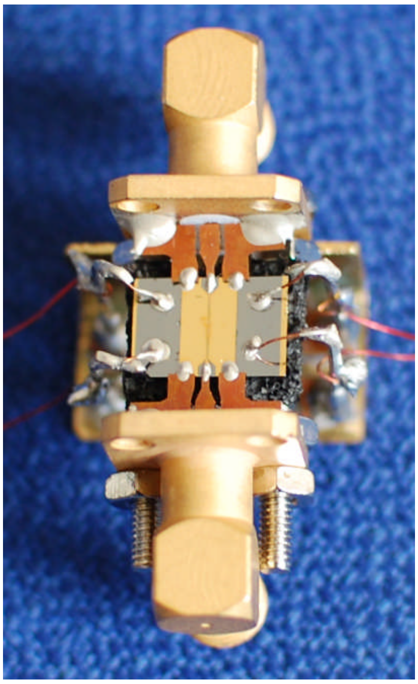

Figure 3.12. Sample mounted in a sample holder which consists of coaxial connectors attached to the CPW via copper strips.

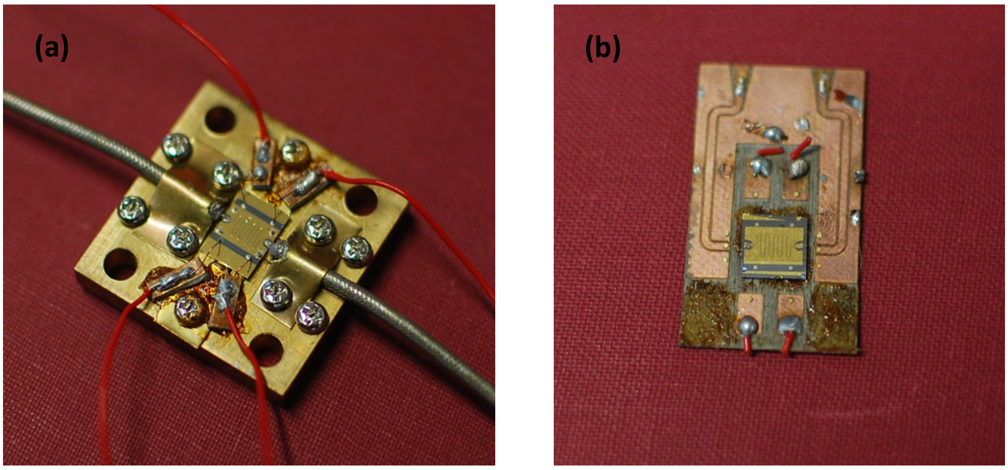

Figure 3.13. Pictures showing previous versions of 2DES-CPW mounts. (a) A coaxial cable directly attached the device with silver epoxy. (b) An attempt to connect the 2DES-CPW device with a microstrip transmission line.

The most significant difficulty encountered in mounting the device originated from establishing electrical contact with the external transmission line. The high frequency signal was delivered to the device through coaxial cables and establishing a good coaxial to CPW transition was problematic; when cold, the electrical contact, which was made using a conductive silver epoxy, tended to shrink and break contact with the device. Fig. 3.13 shows two previous version of the device mount that were ultimately unsuitable due to the breaking of electrical contact when cooled down.

3.2.3 Experimental setup

The experimental setup is centred around a dilution fridge as the 2DES-CPW device has to be cooled down to very low temperatures in order to observe the high frequency response of the QHE. The devices in the following experiments are inserted into a

^{3}He/^{4}He dilution fridge with a base temperature of < 14 mK and a 12 T superconducting magnet. The 2DES-CPW is thermally attached to the base plate of the fridge by a copper rod that screws into the button of the device mount shown in Fig. 3.12. The device is connected to the external circuit through coaxial cables. The cables come down from the top of the dilution fridge and extend to the base plate where they are connected to the device via the coaxial connectors seen in Fig. 3.12.

Outside the fridge, the input of the 2DES-CPW is connected to a vector network analyser (via coaxial cables) which is capable of generating very low noise and high frequency signals up to 40 GHz. The output of the 2DES-CPW is first connected to a 20 dB amplifier which in turn is connected back to the network analyser which doubles both as the signal generator and detector.

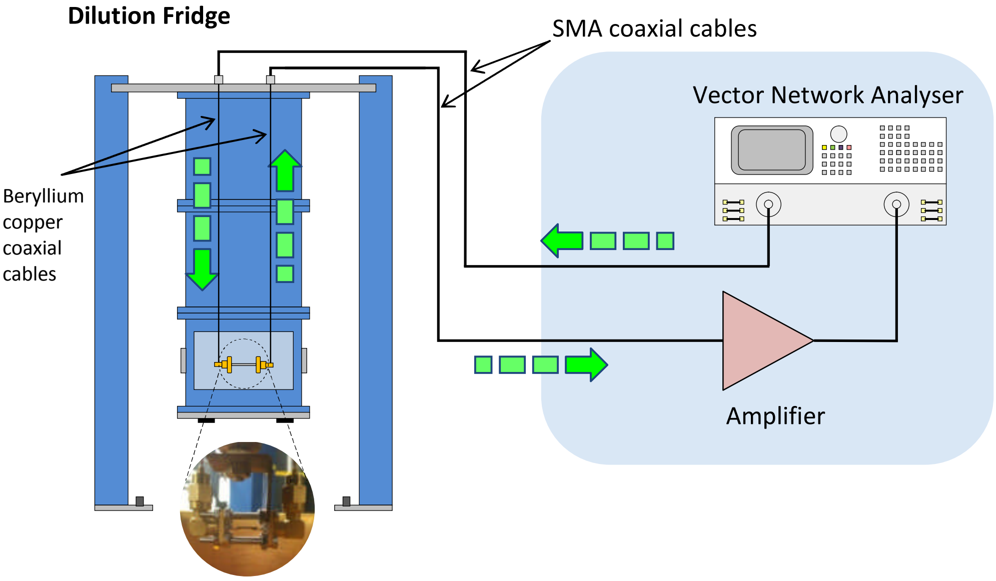

Figure 3.14. A schematic showing the experimental setup for the high frequency measurement of 2DES-CPW devices.

The schematic of the setup is shown in Fig. 3.14.The view of the internal structure of the dilution fridge is shown in Fig. 3.15. The coaxial cables from the network analyser are connected to coaxial inputs found on top of the dilution fridge. Beryllium copper coaxial cables then carry the signal all the way down to the base plate, beneath which the sample holder is mounted. The mounted device is shown in see Fig. 3.14.

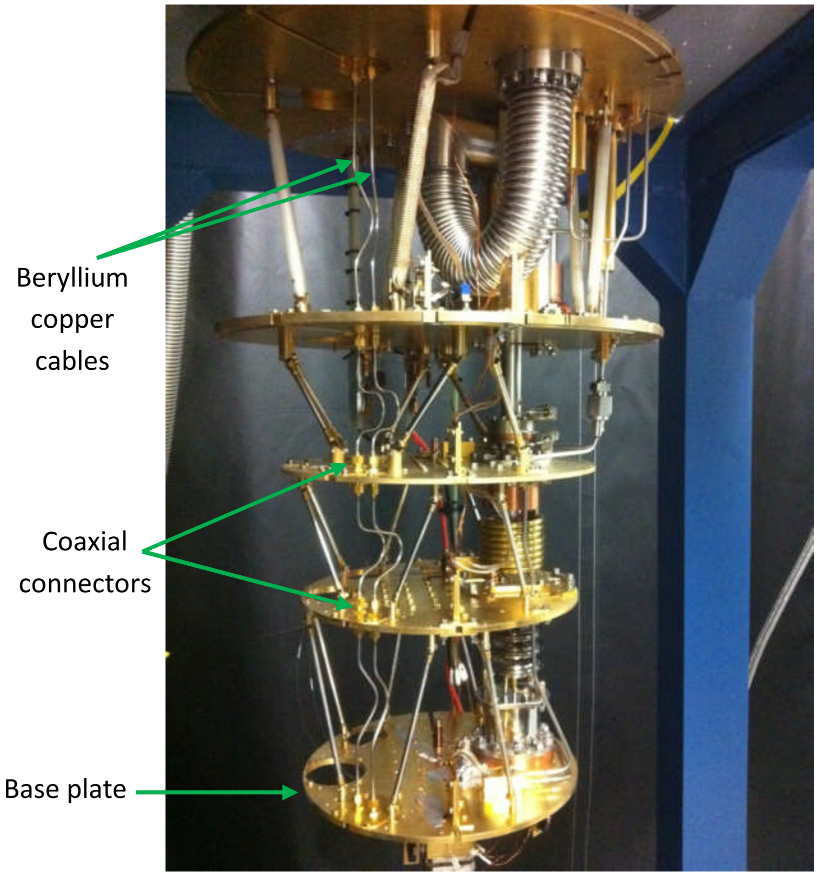

Figure 3.15. A picture showing the internal structure of the dilution refrigerator. The beryllium copper coaxial cables, coming from the top of the fridge, are connected between successive temperature plates by coaxial connectors.

The plates shown in Fig. 3.15 act as dividers for different temperature regions within the dilution fridge. The beryllium copper cables are connected to successive temperature regions by coaxial connectors.

In operational mode, high frequency or microwave signals are sent from the network analyser, down the dilution fridge, and launched into the 2DES-CPW. During CPW transmission, the signal interacts with and simultaneously probes the 2DES. The output signal from the 2DES-CPW devices is then passed through a 20 dB amplifier to amplify the output since the input or injected signal must be of very low power (more on this below). The magnitude and the phase of the amplified signal are then measured by the network analyser, and contain information on the conductivity of the 2DES. This process is carried out over several frequencies per magnetic field point in order to generate a high frequency and magnetic field dependent response of the 2DES. The results obtained are presented in the following section.

3.3 Frequency dependent measurements on 2DES-CPW devices

Measurements taken on a standard GaAs/AlGaAs-based 2DES-CPW are reported below. Results on microwave measurements carried out are presented and similarities between d.c. and a.c. measurements discussed. This is then followed by determination of the scaling exponent κ in the high frequency regime. Features of the high frequency response of QHTs in the 2DES are also discussed.

3.3.1 Microwave measurements

The results presented in this section are taken from a 2DES-CPW device fabricated from a GaAs/AlGaAs heterostructure with a carrier density of $n = 2.89 \times 10^{11}\ \mathrm{cm}^{-2}$ and a mobility of $\mu = 380{,}000\ \mathrm{cm}^2\mathrm{V}^{-1}\mathrm{s}^{-1}$ (measured at 100 mK). The device is incorporated into the setup described above (Fig. 3.14), where the 2DES-CPW is excited with microwave frequencies of very low power. The power ratio of the received signal to the transmitted signal, or the S_{21} parameter, is measured as a logarithmic scalar (in decibels or dB)

$$\mathrm{S}_{21}\ (\mathrm{dB}) = 10\log_{10}(|P_t/P_0|), \tag{3.9}$$

where P_0 is the power of the signal leaving the network analyser and P_t is the power of the transmitted signal received by the analyser. It should be noted from Eq. (3.9) that we

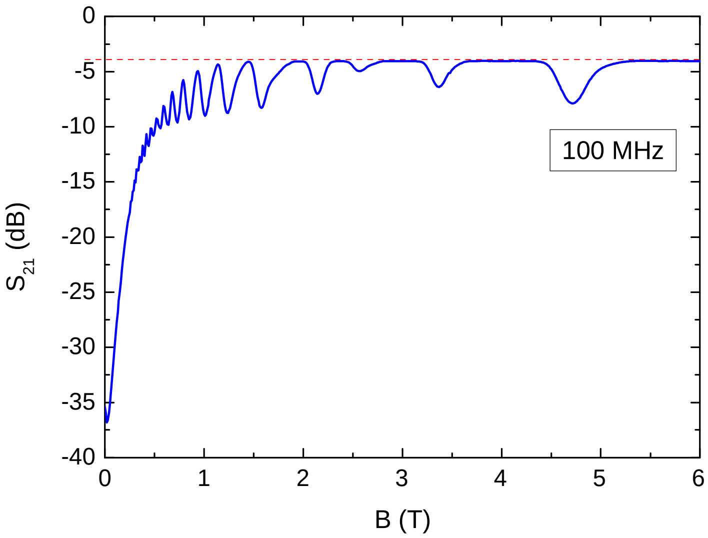

Figure 3.16. A plot showing the transmission characteristics of the 2DES-CPW at 100 MHz as a function of magnetic field. The S_{21} appears to follow an inverted trace of the diagonal conductivity.

are only interested in the magnitude of the S_{21} parameter.

Fig. 3.16 shows a plot of the magnetic field dependence of the S_{21} parameter measured from the 2DES-CPW device excited with a signal of frequency 100 MHz. The most striking observation from Fig. 3.16 is that it is of remarkable resemblance to an inverted diagonal magneto-conductivity (σ_{xx}) trace of the QHE. It is also noticed that the trace hits an asymptotic value (illustrated by the dashed line in Fig. 3.16) which appears to be the zero conductivity value of the S_{21} parameter.

Transmission is most impeded close to the zero field (0 T) where the S_{21} parameter is observed to possess its lowest value. This means that the 2DES, which has been integrated into the transmission circuit, is most conductive at these field causing significant losses to the power of the transmitted signal since (as shown in Fig. 3.5(b)) the 2DES acts as a shunt resistance or short circuit to ground. At higher fields however, the 2DES becomes highly resistive and essentially acts as an open circuit allowing more of the signal to be transmitted. At very high fields (from 2 T onwards in Fig. 3.16) the 2DES is found to oscillate between states of zero conductivity, where the S_{21} parameter hits the dashed line, and a small finite conductivity observed as dips in the S_{21}. $S_{21} = -4$ dB therefore represents transmission losses due to all other parts of the circuit except the 2DES since within this zero conductivity region the 2DES is effectively invisible to the circuit.

It is clear from Fig. 3.16 and the discussion above that the high frequency plot reflects the QHE of the 2DES. In order to confirm this however, it is essential to compare the high frequency responses to the conventional d.c. measurements of the 2DES. This is done using the Ohmic contacts (see Fig. 3.9) on the same device.

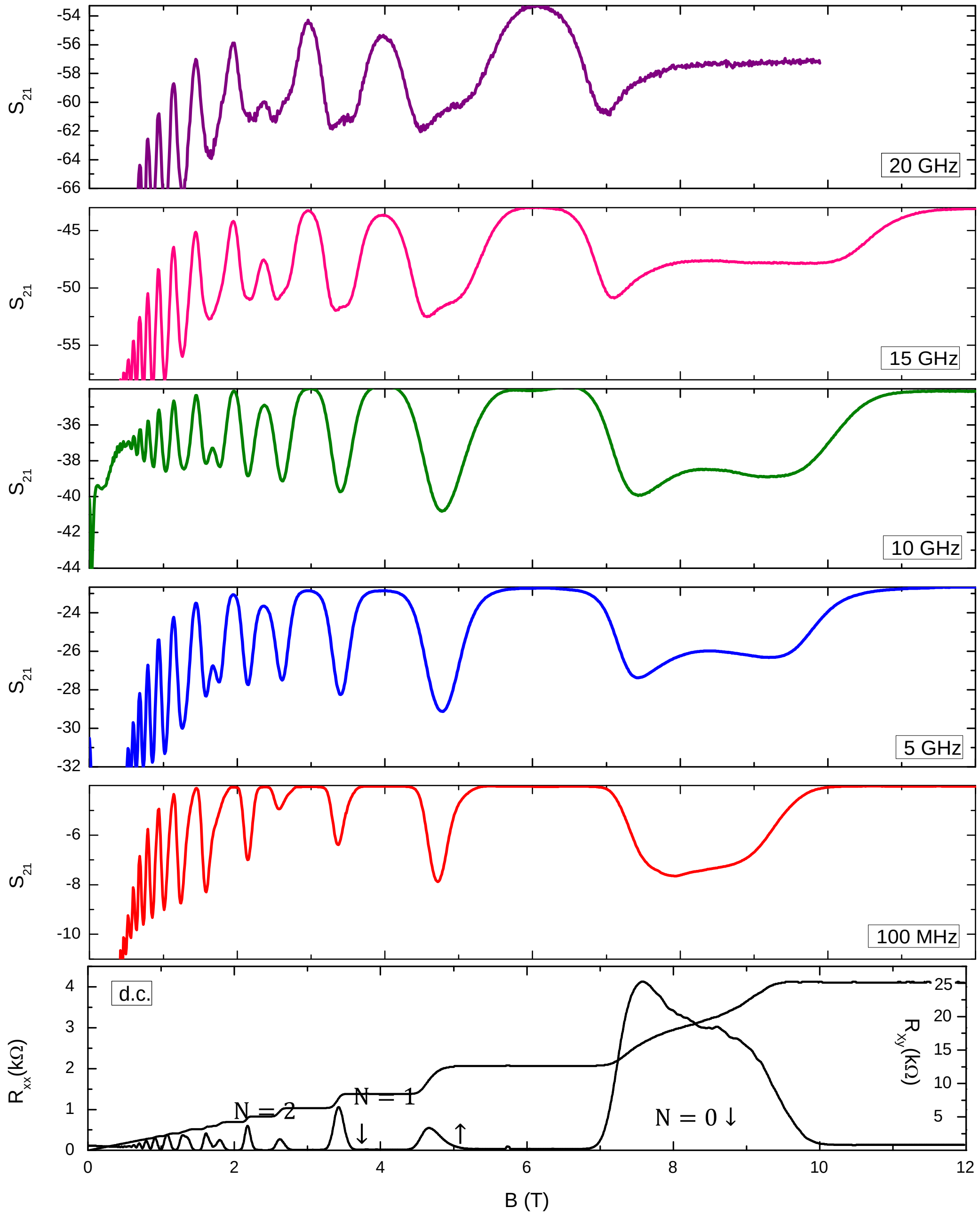

Figure 3.17. This figure shows a set of magnetic field dependent plots of the resistance of the 2DES at d.c. and the S_{21} measurements at high frequency. Good agreement is found between LL peaks observed at d.c. and the dips observed at high frequency. A broadening of the LL dips in S_{21} measurements is observed as the frequency is increased.

Fig. 3.17 presents such a measurement. It is observed in this figure that LL peaks occurring in the d.c. trace correspond to dips in the S_{21} measurements at high frequencies. The dips in the S_{21} parameter can therefore be conveniently matched with their corresponding LL. Due to the nature of the excitation of the 2DES, only σ_{xx} can be obtained from the transmission measurements. The Hall data cannot be measured with this high frequency setup. As explained in section 3.2.1, losses in the transmitted signal are due to the movement of charged particles along the electric field lines (see Fig. 3.8), therefore S_{21} measurements reflect the diagonal conductivity. The use of Ohmic contacts, which enable Hall data to be taken from the 2DES-CPW device, are therefore essential in verifying the LLs observed in the transmission measurements.

The S_{21} value at the zero conductivity regions (i.e. the regions with the maximum value of S_{21}) is frequency dependent. It can be seen from Fig. 3.17 that the zero conductivity value of the S_{21} for these regions decreases with increasing frequency, starting at $\mathrm{S}_{21} \sim -4$ dB at 100 MHz to $\mathrm{S}_{21} \sim -54$ dB at 20 GHz. This behaviour simply reflects the frequency dependent lossy nature of the transmission lines, and especially losses due to the coaxial connectors that connect the beryllium copper coaxial cables between the successive temperature plates within the dilution fridge (see Fig.3.15).

The plot in Fig. 3.18(a) shows the magnetic field response of the S_{21} parameter covering the $\mathrm{N} = 1 \downarrow$ and $\mathrm{N} = 1 \uparrow$ LLs of the 2DES-CPW. It is observed from this plot that the transmission loss become significantly worse as the frequency is increased, offsetting the zero conductivity asymptote accordingly. The frequency response of the setup is measured at three different magnetic fields in the plot presented in Fig. 3.18(b). The three fields considered in this plot are taken from the centre of the $\mathrm{N} = 1 \downarrow$ LL and the two insulating zero conductivity regions on either side of the LL.

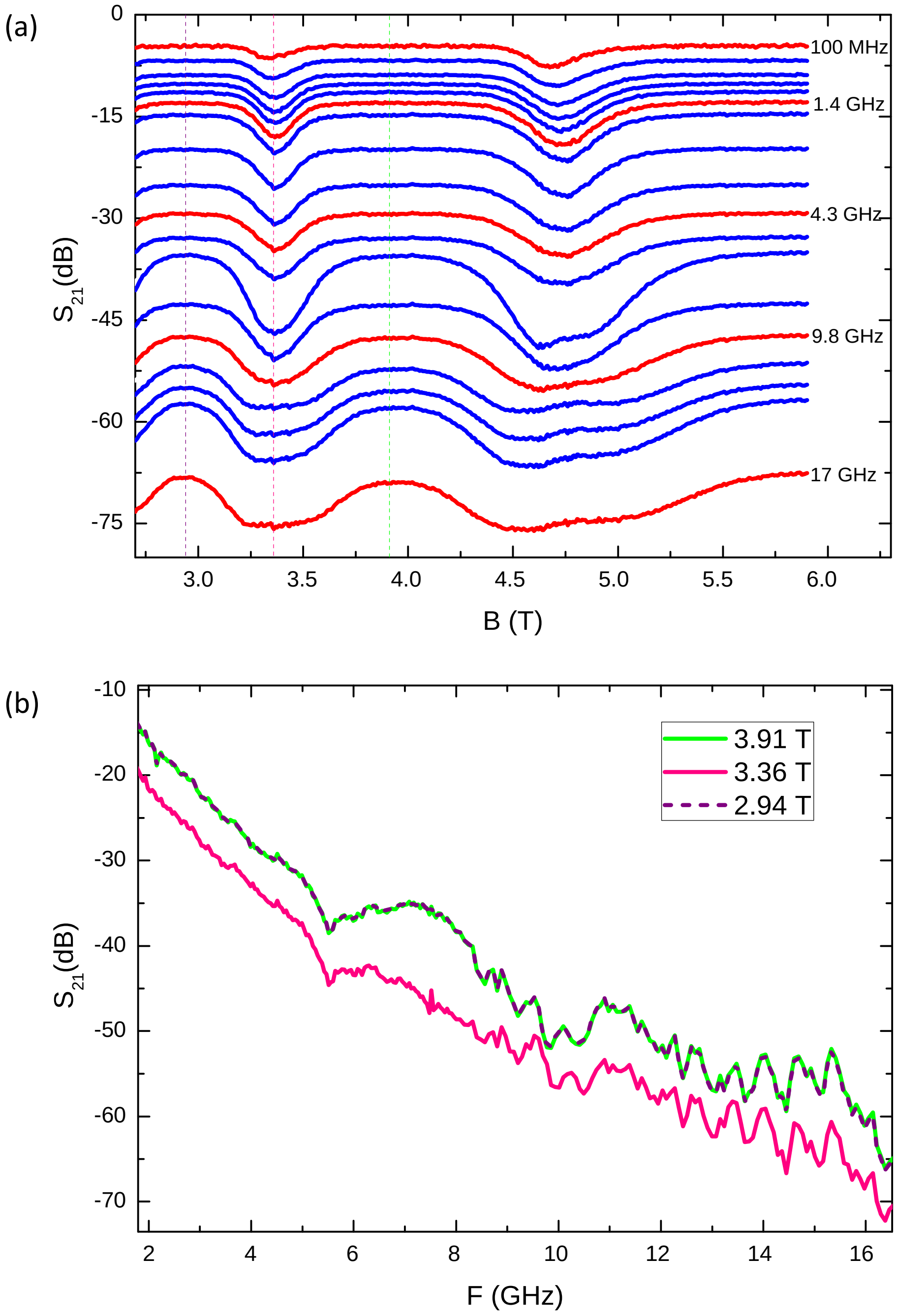

Figure 3.18. (a) The magnetic field dependence of S_{21} covering the $\mathrm{N} = 1\downarrow$ and $\mathrm{N} = 1\uparrow$ LLs shown at different frequencies, where greater offsets are observed at higher frequencies. The frequency responses of fields indicated by the dashed lines in (a) are plotted in (b).

The precise field points considered in Fig. 3.18(b) are represented by the dashed lines seen in Fig. 3.18(a). It is even clearer from Fig. 3.18(b) that the setup becomes increasingly lossy as the frequency is increased. It is important to appreciate, however, that the majority of these losses are not due to the 2DES but other parts of the circuit. It is observed in Fig. 3.18(b) that the frequency response is exactly the same for both of the zero conductivity regions located on either side of the LL. In these zero conductivity regions the 2DES is effectively invisible to the circuit. At the centre of the LL where the conductivity is greatest, however, we notice both an offset and change in the frequency response that do not match the zero conductivity responses.

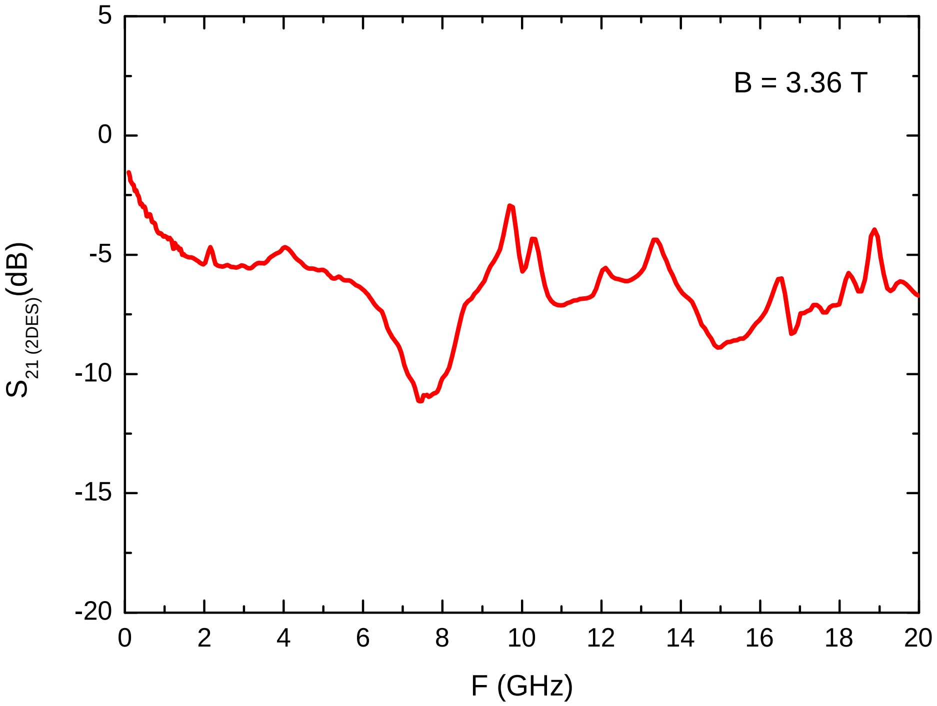

Figure 3.19. The frequency response of the 2DES at the centre of the N = 1 ↓ LL minus the zero conductivity response. This plot represents the intrinsic response of the 2DES at its most conductive.

The losses intrinsic to the 2DES alone therefore are the differences between the two curves. This difference is plotted in Fig. 3.19. This plot, which describes the frequency response at the centre of the $\mathrm{N} = 1\downarrow$ LL (at B = 3.36 T), is obtained by subtracting the zero conductivity response from the response at the centre of the LL. The S_{21} values in this plot represent losses intrinsic only to the 2DES. Although the response in Fig. 3.19 applied only to the centre of the LL, the intrinsic 2DES responses for all fields are obtained by the same method; subtracting the zero conductivity response from the raw S_{21} response.

We now consider the nature of the response in Fig. 3.19. According to Eq. (3.8), one expects the 2DES to become increasingly lossy at higher frequencies (with a linear dependence on a double log scale). Such a general trend is observed in Fig. 3.19 but we also note the observation of several resonances of different magnitudes within the spectrum. These resonances are believed to originate from frequency dependent interactions between the 2DES and its environment. This includes the characteristic and physical features of the substrate (such as physical size and permittivity) within which the 2DES is located and the characteristic of the CPW above the 2DES. The two strongest resonances in the frequency response appear to be related, through a fundamental frequency that occurs at 7.5 GHz and a first harmonic at 15 GHz. It is found that the fundamental frequency occurs when the length of the sample coincides with

$$\frac{\lambda_{eff}}{2} = \frac{c}{2f\sqrt{\varepsilon_r}}, \tag{3.10}$$

where λ_{eff} is the effective wavelength in the GaAs substrate with a dielectric constant of $\varepsilon_r = 12.9$ and c is the speed of light. For a sample of length 5.5 mm, a resonant frequency is expected at ~7.5 GHz according to Eq. (3.10). This is in good agreement with

Fig. 3.19. Though Eq. (3.10) appears to account for the strongest resonances, the particular origins of the other resonance are difficult to pinpoint, it is however possible that they must stem from some characteristic of the 2DES-CPW device and not due to intrinsic electron transport of the 2DES.

3.3.2 Conductivity of a 2DES in a high frequency network

As touched on above, the setup containing the 2DES-CPW device can be modelled by an equivalent circuit to represent a two-port network with characteristic impedance $Z_0 = \sqrt{L_0/C_0}$. The 2DES beneath the CPW appears as a load in the network with admittance Y as shown in Fig. 3.20. The two-port network shown in Fig. 3.20 represents a transmission or *ABCD* matrix [137]. The relation between Y and S_{21} from transmission line theory is given as [137]

$$S_{21} = \frac{2}{2+Z_0 Y}\ . \tag{3.11}$$

The conductance of the 2DES, which is the real part of admittance ($Re[Y] = G$) is given as $G = 2Re[\sigma_{xx}]\frac{l}{w}$ where the factor 2 is due to existence of two slots lines in the CPW, each of width w and length l, within which the 2DES is excited.

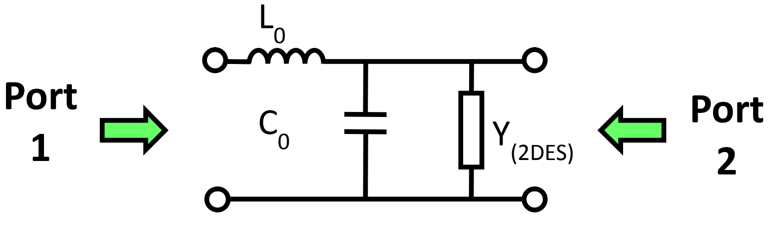

Figure 3.20. A two-port network model of 2DES-CPW circuit with a characteristic impedance $Z_0 = \sqrt{L_0/C_0}$. The 2DES appears as admittance Y in the model.

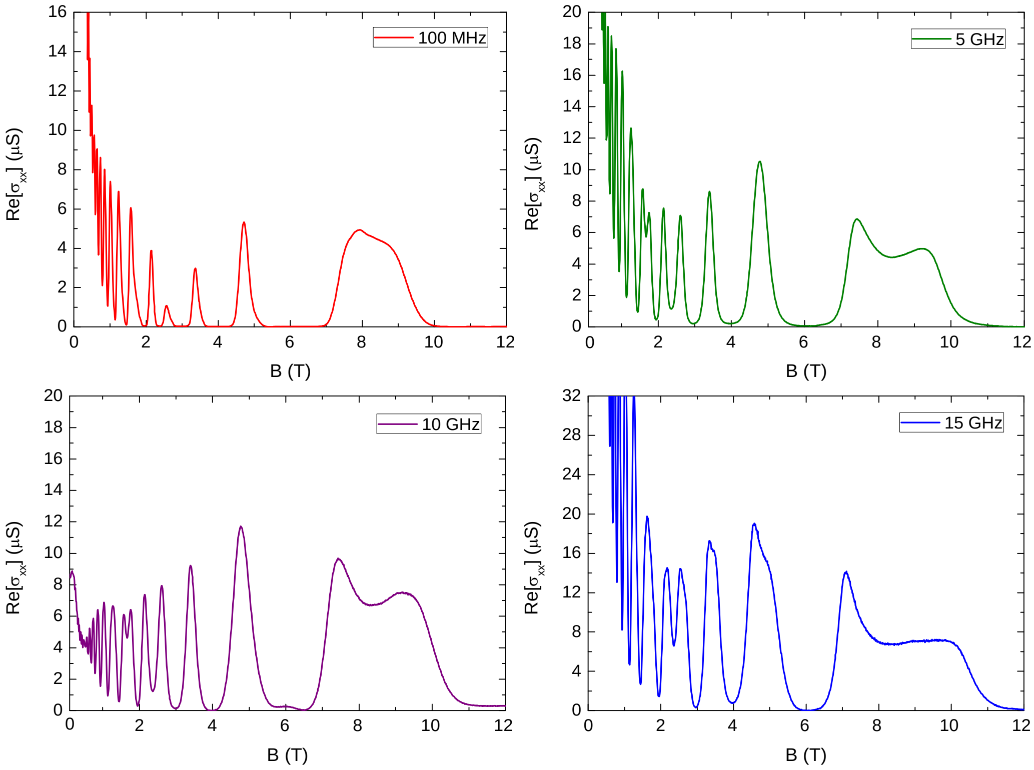

Figure 3.21. Conductivity measured from the (intrinsic) $S_{21\,(2DES)}$ of the 2DES-CPW device at four different frequencies

Eq. (3.11) can then be rewritten as

$$S_{21} = \frac{w}{w + Z_0 Re[\sigma_{xx}] l} \, . \tag{3.12}$$

In order to take into account the effect of frequency and the separation g between the conducting planes of the CPW and the 2DES below, two correction factors, $A(f)$ and $B(g, Re[\sigma_{xx}])$, are introduced such that

$$S_{21} = \frac{w + B}{w + B + (A + Z_0) Re[\sigma_{xx}] l} \, . \tag{3.13}$$

These correction factors are computed through simulations carried out on a finite-element electromagnetic field solver (HFSS).

From Eq. (3.13), the conductivity of the 2DES can be calculated from the magnetic field response of the S_{21} parameter after the zero conductivity response has been subtracted (the method described in Fig. 3.19). The results obtained from applying Eq. (3.13) are shown in Fig 3.21 for four different frequencies. It can be observed from Fig. 3.21 that Eq. (3.13) has the visual effect of inverting the S_{21} response. The values obtained from Fig. 3.21 are in good agreement with d.c. values obtained from the sample investigated.

3.3.3 High resolution frequency measurements

From the measurement techniques and analysis described in the sections above, a high resolution description of the QHE can be obtained by combining the magnetic field response of $Re[\sigma_{xx}]$ with small increments in frequency. In practice, the data is taken as follows: at a given magnetic field, frequencies between 10 MHz and 20 GHz are transmitted through the 2DES-CPW circuit. The frequencies are sent one after the other (finite-frequency transmission) separated by a small time delay that takes into account the distance travelled by the signal and the relaxation time of the interacting 2DES. The interval in frequency between successive signals is $\sim$ 40 MHz. The ratio between the incident and transited signal is then measured by the analyser after which the data is converted into conductivity using Eq. (3.13). All measurements are carried out at a temperature below 100 mK where small deviations in the temperature of the system ($\pm$ 50 mK) have no significant effect on measured values and the QHE. This technique yields a very high resolution description of the frequency dependent evolution of the QHE that can be used in the investigation of the scaling of QHTs.

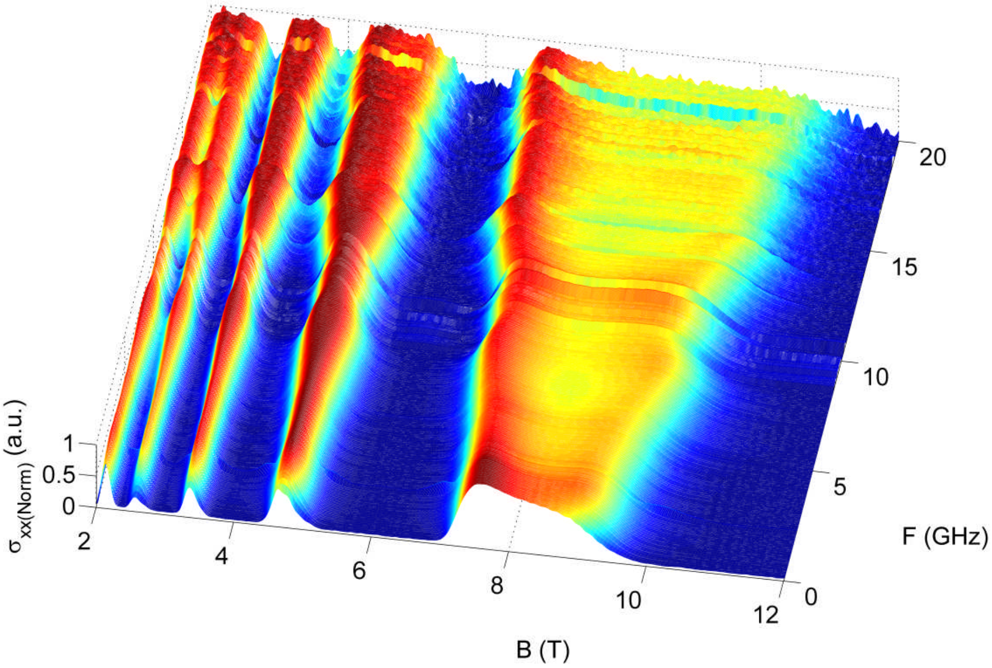

Figure 3.22. High resolution plot of the (normalized) diagonal conductivity of the QHE taken from 2 T to 12 T and from 10 MHz to 20 GHz, at intervals of 40 MHz.

The result of this measurement is shown in Fig. 3.22. The familiar outline of σ_{xx} of the QHE can be seen from the cross-section of the data. It is also very clear that there is a broadening of the widths of the LL conductivity peaks, a central feature of the scaling theory of QHTs. Fig. 3.22 also shows both abrupt discontinuities, these features originate from the resonances discussed in Fig. 3.19. The measurement range presented in Fig. 3.22 is limited to 20 GHz because of the onset of a significant drop in the signal-to-noise ratio at higher frequencies. The noise at frequencies close to 20 GHz observed in Fig. 3.22 is predominantly due to a limitation in the coaxial connectors in the dilution fridge (shown in Fig. 3.15) and also due to the deviation from the quasi-TEM approximation of the CPW at higher frequencies.

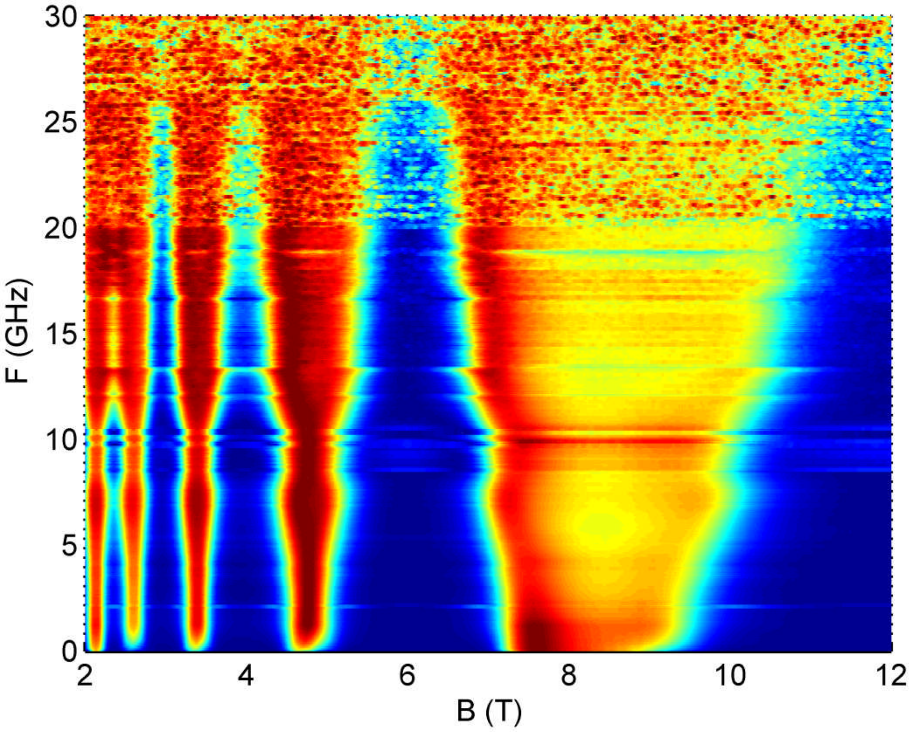

Figure 3.23. A top view (in the frequency-field plane) of the frequency dependence of the QHE up to 30 GHz. Though the data between 20 GHz to 30 GHz contains a significant amount of noise, the broadening of the LL conductivity peaks is observed within the entire frequency range.

Nevertheless, Fig. 3.23 presents measurements taken up to 30 GHz where the noise within the system is extremely high. These results, however, prove that the broadening of LL peaks are observable up to 30 GHz. Fig. 3.23 represents the largest scaling bandwidth reported to date, a significant improvement on the 14 GHz bandwidth results reported previously by Engel *et al*. [13].

Another peculiar feature of these high resolution measurements is the observation of a shoulder on the high field side of the $N = 0 \downarrow$ LL (between 6 T and 12 T) prominent in Fig. 3.22.

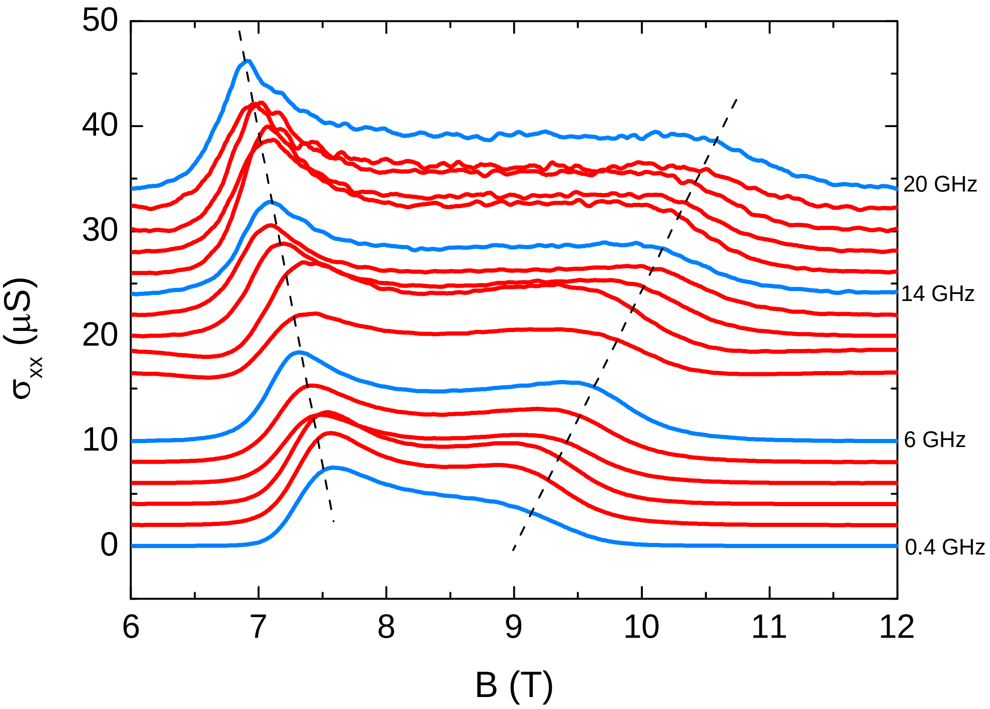

Figure 3.24. A plot illustrating the shoulder effect on the N = 0 ↓ LL. The traces have been offset for clarity.

Though the observation of this shouldering effect is first recognized in the results presented in Figs. 3.17 and 3.21, it is briefly discussed below.

The emergence of a strong shoulder at lower filling factors (or high fields), clearly observed in the N = 0 ↓ LL, represents an asymmetry in the density of states. This asymmetry originates from the formation of an impurity band in the energy spectrum due to the attractive scattering centres close to the 2DES [138]. Fig. 3.24, which shows the N = 0 ↓ LL conductivity peak for various frequencies, provides clearer evidence of the shouldering effect. The shape of the density of states is influenced by the polarity and the amount of the scatterers present in the system.

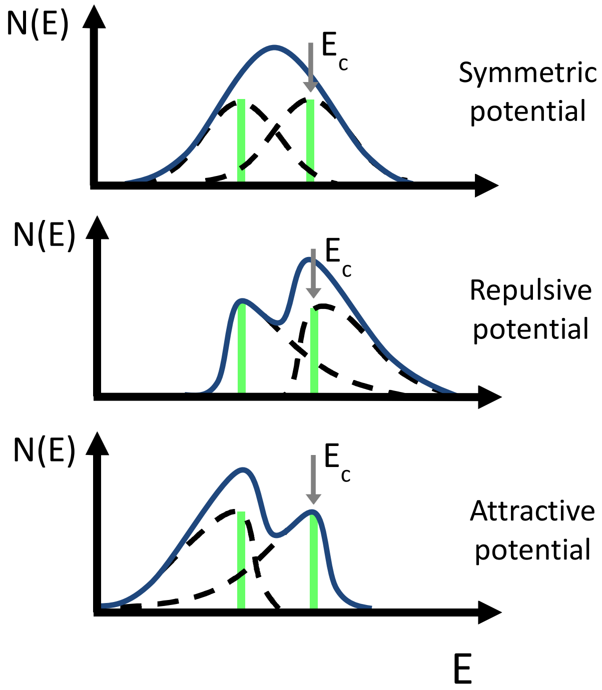

Figure 3.25. The asymmetry of a LL which depends on the nature of the scatterers within the system. Systems dominated by either attractive scatterers or repulsive scatterers will have opposite features in their asymmetry, while systems with equal amount of repulsive and attractive scatterers maintain a symmetric density of states.

In the case of the scatterers being repulsive only, the asymmetry will be reversed, while a symmetric density of states will exists if there are equal amounts of attractive and repulsive scatterers [138]. The schematic representation of these three scenarios is shown in Fig. 3.25 based on numerical solutions presented by Wegner [139] and discussed by Aoki [138]. The conductivity measured from the system therefore is the result of the overlap in states between the 2DES and the impurity band. As the frequency (or temperature) is increased, the broadening of the LL peak, as well as the impurity band peak, reveals the asymmetry in the density of states. This effect has been previously observed by several authors in both temperature and frequency dependent measurements of the

QHE [91, 133, 140]. The asymmetry of the LL peaks is only pronounced at low filing factors and almost non-existent at higher filling factors (low fields), and as a result, LLs at higher filling factors (higher than $\mathrm{N} = 0 \downarrow$ LL) can be investigated without effects from the impurity band being a significant concern.

3.4 Finite-frequency scaling of QHTs in GaAs/AlGaAs systems

We now return to the central focus of this work, the investigation of the criticality of transitions between the insulating states of the QHE, or QHTs, by evaluating the scaling exponents of these transitions. In particular, we have concerned ourselves with a central question of whether these transitions belong to the same universality class and whether universality is contingent on any condition. In the previous chapter, the temperature dependence of the QHTs was investigated. In this section, we perform a similar analysis based on the frequency dependent measurements discussed above.

3.4.1 Power scaling of QHTs

The critical exponent κ is measured from the full-width-at-half maximum (FWHM) of the LL conductivity peak according to Eq. (3.7) restated below

$$\Delta B \sim f^{\kappa}. \tag{3.14}$$

As discussed in section 3.1.1, the frequency regime is dominant when $hf \gg k_B T$. In this regime, frequency controls the phase breaking mechanism and therefore the scaling process. The application of microwave signals to the 2DES-CPW device requires the injection of some amount of power. It is therefore important to stay within a regime where the microwave power does not heat up the 2DES and reduce the dominance of frequency within the system (i.e bring the systems out of the $hf \gg k_B T$ regime). This is achieved by measuring the effect of varying powers of the microwave signal on the conductivity of the 2DES. Since the width ΔB of the LL conductivity peak is the essential characteristic being measured, this width is determined for different powers. The results are shown below in Fig. 3.26. The figure shows the dependence of ΔB on the power of the applied signal at three different frequencies. An increase in the power of the applied signal is accompanied an increase in the temperature of the system. We notice in Fig. 3.26 that initially there is no effect on the ΔB (i.e. the conductivity) of the 2DES at lower powers. Within this saturated region, frequency will be the dominant parameter of scaling. This is clearly observed in Fig. 3.26 by comparing ΔB for different frequencies, it is noticed that ΔB increases with frequency within this regime as expected from Eq. (3.14). This indicates that hf is dominant in this regime. As the power (and as a result, the temperature) is increased, however, a power scaling effect does occur, ΔB begins to increase with power and it is observed that the curves of the discrete frequencies shown begin to merge at higher signal power levels. This signifies a transition from a frequency dominated regime towards a temperature dominated regime ($hf \rightarrow k_B T$). At even higher powers, all frequency curves will merge onto the same line (observed by extrapolating the curves shown in Fig. 3.26). At this point a varying frequency no longer has any influence on the 2DES and conductivity is predominantly determined by the temperature parameter ($k_B T$ dominated regime).

In determining the scaling exponent κ, it is important to keep the system within the saturated regime.

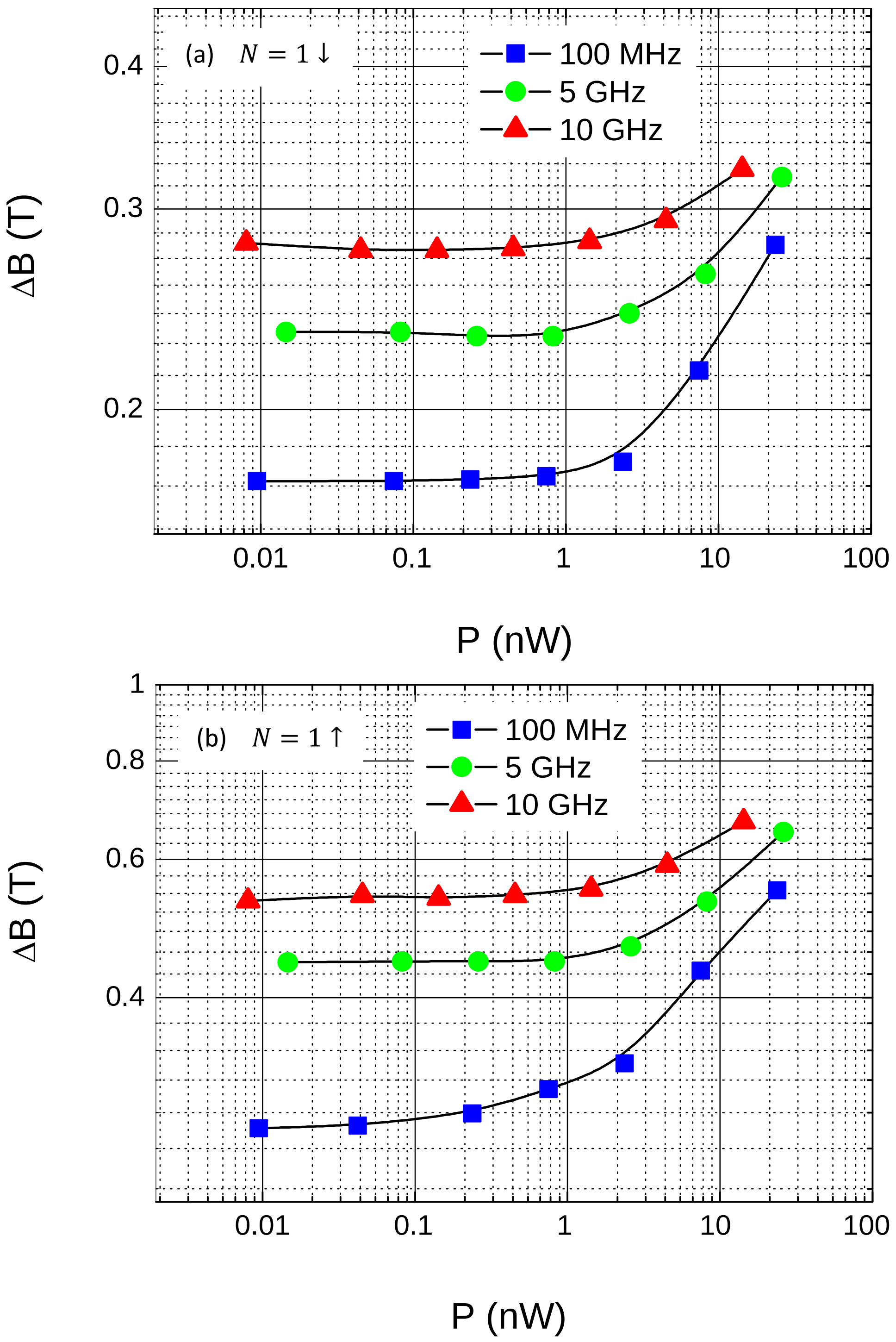

Figure 3.26. Plots showing the dependence of ΔB on microwave power at three different frequencies for two LLs. The saturated regions (< 1nW) represent the frequency dependent regime while the non-saturated region (>1nW) signify a transition to the temperature dependent regime.

All results presented in this section are therefore carried out at $P < 0.01$ nW, well within the frequency dominated regime. In performing the frequency scaling experiments presented below, the temperature of the dilution fridge is initially set to its base temperature $<$ 14 mK and the signal power kept within the saturated region. As the experiment is carried out the temperature of the fridge increased slightly but remains below 35 mK. The slight increase is due to a small and unavoidable amount of heat originating from dissipation in the current carrying cables and thermal dissipation from the 2DES-CPW device itself (even within the saturated region). As discussed above (from Fig. 3.26), however, this is not sufficiently high to influence the measurements being taken.

3.4.2 Frequency dependent determination of the scaling exponent κ

In measuring κ we will only consider the $N = 1 \downarrow$ and $N = 1 \uparrow$ LLs. The $N = 0 \downarrow$ LL is not considered due to significant contribution to conductivity of the impurity band at higher fields. Higher LLs are also not considered in this analysis due to spin degeneracy. Fig. 3.27 shows a contour plot of the normalized conductivity of the $N = 1$ and $N = 2$ LLs, it illustrates the extent of spin resolution and spin degeneracy of the LLs. The $N = 1$ LLs are found to be spin resolved for the frequency range considered while the $N = 2$ LLs are largely degenerate.

The dependence of the ΔB on frequency is more clearly presented in Fig. 3.28 which shows the normalized conductivity of the $N = 1 \downarrow$ LL. The dashed line in the figure denotes the FWHM.

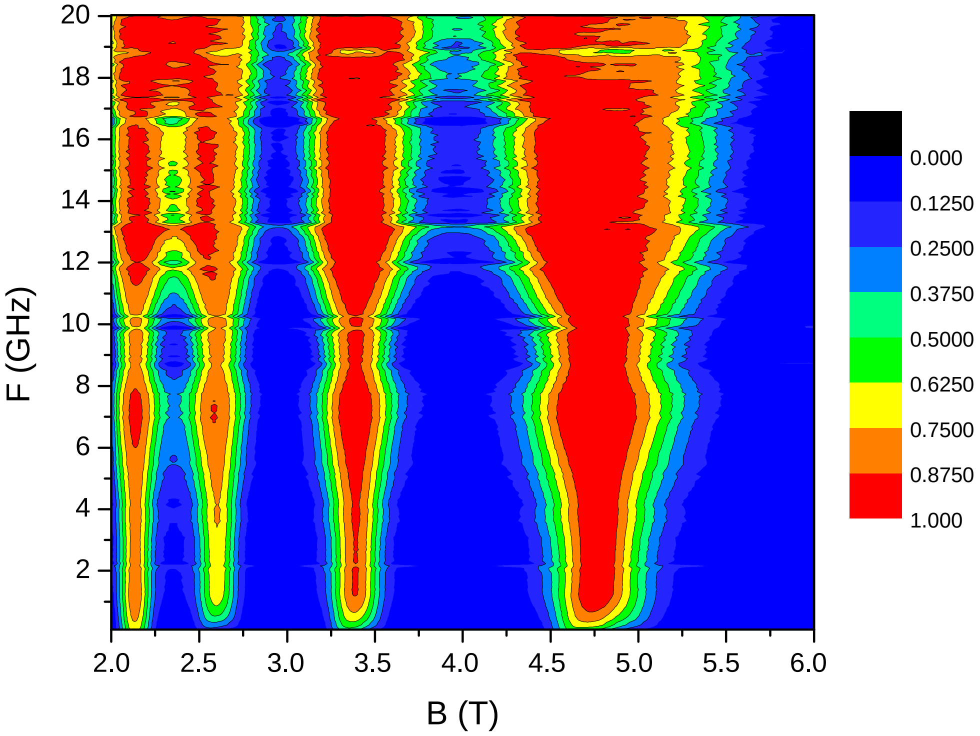

Figure 3.27. A contour plot of the frequency response of the 2DES illustrating the degree of spin degeneracy of the $N = 1$ and $N = 2$ LLs.

The plots of ΔB vs. f for both $N = 1 \downarrow$ and $N = 1 \uparrow$ LLs are shown in Fig. 3.29. The plots largely consist of two regions, a frequency insensitive region and a frequency dependent region. The insensitive region, which is found at $f < 2$ GHz, represents a saturated region where increases in frequency have negligible effect on the width of the conductivity peak. It is noted that this saturated region also observed in all higher LLs not considered below (for $f < 2$ GHz). Similar to the saturation regions observed in the temperature dependent measurements discussed in Chapter 2 (Fig. 2.5), the origins of the saturated region observed here originate from the effect of the finite-size of the device.

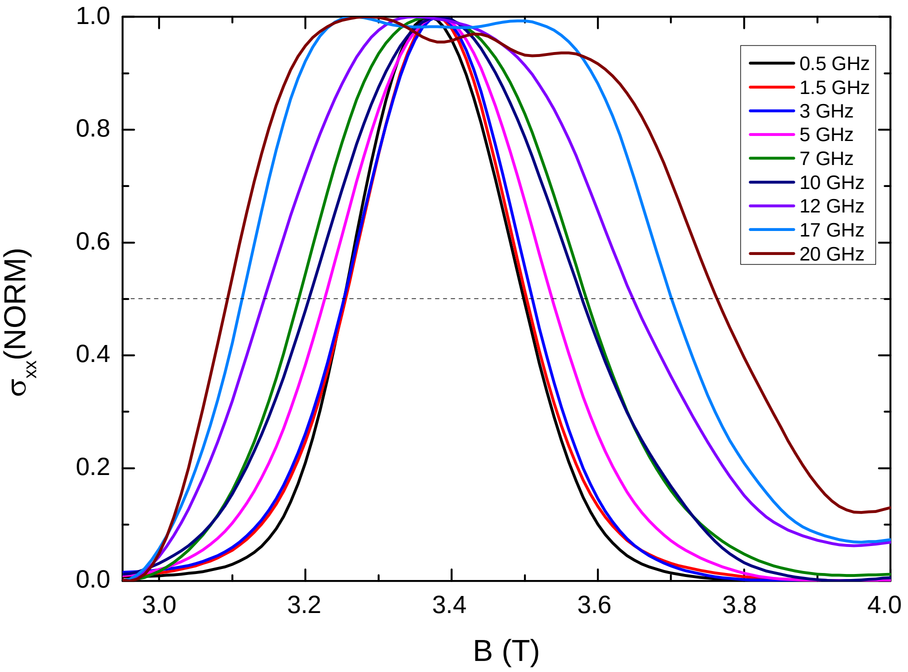

Figure 3.28. A plot showing the dependence of ΔB on frequency for the $N = 1 \downarrow$ LL. The dashed line represents the FWHM.

It is important to note that the transition between the saturation region and the frequency dependent region in Fig. 3.29 is not a transition between $k_B T$ and hf dominated regions as observed in Fig. 3.26 since we are sure that the temperature plays no role for the microwave powers used in these measurements. The transition is therefore due to a size effect of the device. The size effect is discussed in detail in Chapter 4.

Within the frequency dependent region we notice a somewhat abrupt dip representing a sudden constriction in the width of the conductivity peak. This constriction stems from resonances within the frequency response discussed in section 3.3.1. The scaling exponent κ is determined from the linear fit of the frequency dependent region according to Eq. (3.14).

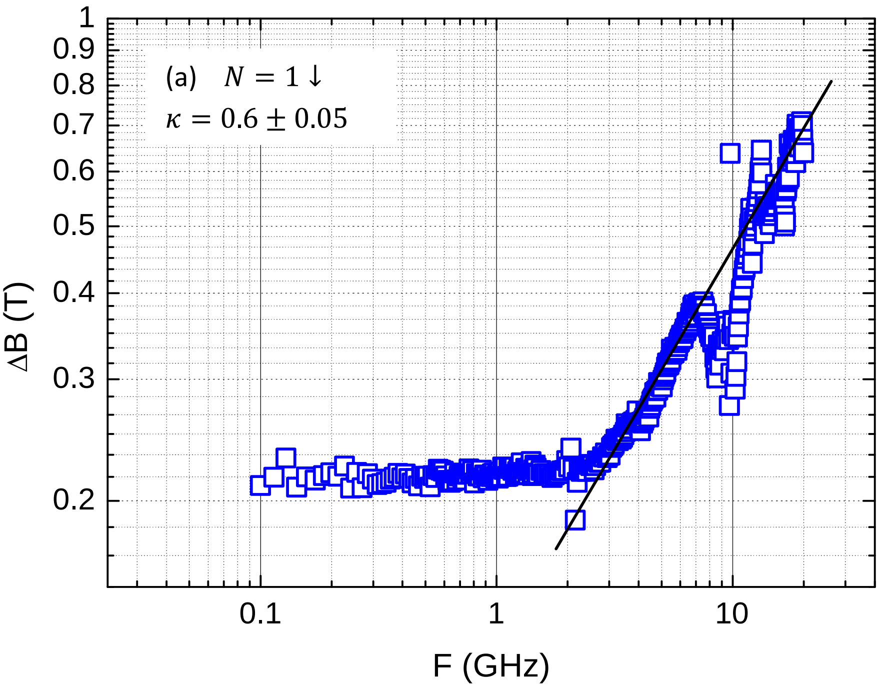

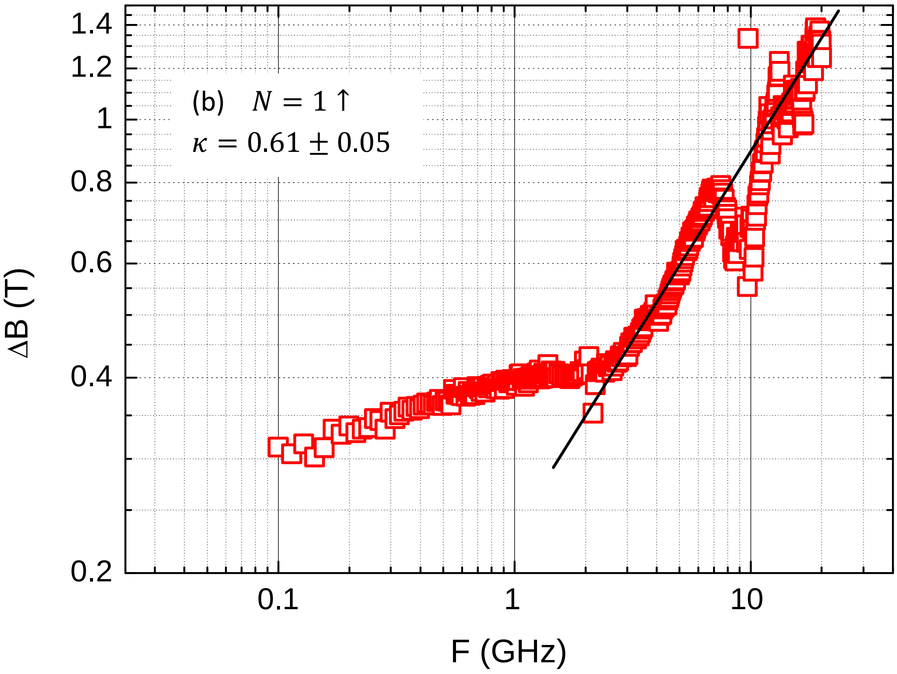

Figure 3.29. Frequency dependence of ΔB for the (a) $N = 1\downarrow$ and (b) $N = 1\uparrow$ LL. The solid line is a fit to the data where the scaling exponent κ is the gradient of the fit.

In determining the fit the resonance dip is excluded. It is noted that the data excluded does little to change the value of κ which is measured to be $\kappa = 0.6 \pm 0.05$ and $\kappa = 0.61 \pm 0.05$ for $N = 1 \downarrow$ and $N = 1 \uparrow$ LLs, respectively.

From previous discussions on the universal criticality of QHTs, we recall that the critical value of κ is expected to be ≈ 0.42. The value of κ measured here, however, is more consistent with the non-universal values obtained from the temperature scaling results presented in Chapter 2 where value of κ tended to be higher than 0.42. Universal transitions (as determined by the value of the scaling exponent) are not observed within these frequency dependent measurements. These results further call into question the universality theory of QHTs.

3.5 Short-range disorder in finite-frequency scaling of QHTs

A commonly suggested reason for the non-universality of critical exponents has been the nature of the disorder experienced by the 2DES. Universal criticality of the phase transitions occurring in the QHE was initially investigated in 2DESs formed in InGaAs/InP heterostructures. The major source of disorder within these systems originates from the alloy scattering inherent in the InGaAs, which occur on an atomic length scale. This makes InGaAs/InP 2DESs systems dominated by short-range scattering in contrast to GaAs/AlGaAs systems discussed so far in this work in which long-range scattering dominates. Below, we discuss the formation of a short-range 2DES in a GaAs based heterostructure and determine the nature of criticality within this system by measuring the scaling exponent κ.

3.5.1 Induction of short-range disorder in GaAs based heterostructures

In the sample considered so far in this chapter, the 2DES is formed from a standard GaAs/AlGaAs heterostructure where the disorder with the system is predominantly caused by random potentials fluctuations from ionized impurities in the donor layer. The 2DES system is separated from these charged centres by a spacer layer, and this cuts off the core of the Coulomb potential leaving the 2DES to experience only the slow varying tails of the potential. In addition, part of the potential is screened by the electrons in the 2DES. This makes the nature of disorder within GaAs/AlGaAs systems weak and long-ranged. This long-range nature of the potential fluctuations greatly reduces scattering within the 2DES.

In order to change the nature of disorder in GaAs based heterostructures from long-range to short-range, Al impurities were introduced into the GaAs layer during the growth of the heterostructure to induce alloy scattering within the vicinity of the 2DES. This causes electrons to scatter on much shorter length scales than in a long-range system (similar to the scattering in InGaAs systems). The result is a $Al_xGa_{1-x}As/Al_{0.33}Ga_{0.67}As$ heterostructure where x is the concentration of impurity as a ratio of Al to Ga atoms. The alloy scattering centres are randomly distributed within the GaAs layer to produce scattering events that are independent and uncorrelated creating the type of disorder described by Anderson [29].

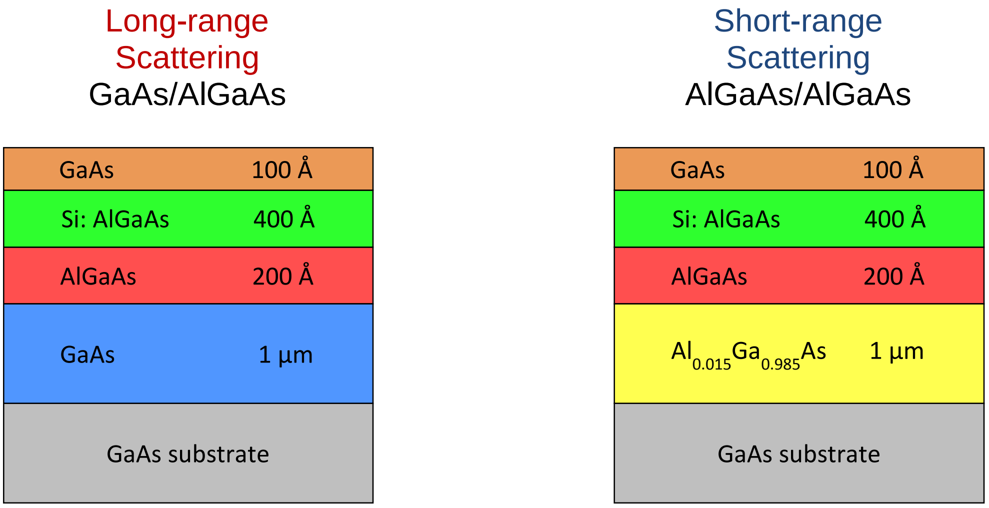

Figure 3.30. A schematic of the heterostructures of the long-range disorder and short-range disorder wafers. Both wafers are grown with similar characteristics with the exception the Al doping of the GaAs layer in the short-range wafer (and no such doping the long-range wafer).

In our samples the Al concentration was chosen to be x = 0.015 (or 1.5%) based on previous studies reported by Li *et al*. [141] where it was found that the amplitude of the alloy potential fluctuations of such a ratio was significantly larger than the background potential fluctuations ensuring that scattering events are dominated by short-range disorder.

The schematic of both the long-range and short-ranged GaAs based heterostructures are shown in Fig. 3.30. Using the long-range disorder wafer as a reference, the short-range disorder wafer was grown in a similar manner with the exception of the Al doping of the GaAs layer. The sample characteristics of the heterostructures are summarized in Table 3.1. Both samples were grown with the same Si doping, spacer layer and had comparable carrier concentration.

TABLE 3.1. Characteristics for long-range (L-range) and short-range (S-range) samples.

Sample	Si δ ($\times 10^{18}$ cm^{-3})	spacer (nm)	Al x (%)	n_e ($\times 10^{11}$ cm^{2})	μ_e ($\times 10^{5}$ cm^{2} V^{-1}s^{-1})	τ_c (ps)	τ_q (ps)	τ_c/τ_q
L-range	2	20	0	2.89	3.8	14.78	1.14	13.0
S-range	2	20	1.5	2.57	1.09	4.15	0.76	5.5

Included in Table 3.1 are the classical lifetimes τ_c and the quantum lifetimes τ_q of both heterostructures. As discussed in Chapter 2 (section 2.1.1), the classical lifetime is predominantly a reflection of large angle scattering events, typical of short-range scattering, occurring within the 2DES. The quantum life time on the other hand is equally sensitive to all scattering events including small angle scattering events, typical of long-range scattering systems. The Dingle plots used to evaluate the quantum lifetime determined from the amplitude of the SdH oscillations of the samples are shown in Fig. 3.31 (see Chapter 2 for details on the Dingle method).

The ratio τ_c/τ_q is a parameter that indicates the dominant scattering type; τ_c/τ_q tends towards unity for a system dominated by short-range (large angle) scattering, while τ_c/τ_q is typically between 10 and 100 for systems dominated by long-range (small angle) scattering [26, 93, 95]. It is observed from Table 3.1 that Al impurity significantly reduces the lifetime ratio towards unity suggesting a change in the nature of disorder of the 2DES towards short-range scattering.

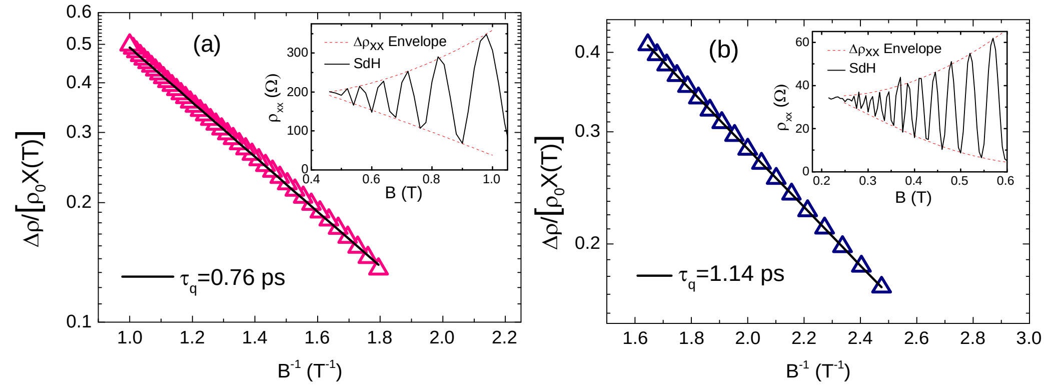

Figure 3.31. Dingle plots for (a) the short-range sample and (b) the long-range sample, determined from the SdH oscillations (shown as insets).

3.5.2 Microwave characteristics of short-range 2DES

Similar to the characteristics shown above for the long-range sample, the microwave frequency characteristics of the short-range sample are briefly discussed.

Fig. 3.32 shows the magnetic field response of the S_{21} parameter measured at different frequencies for the short range 2DES-CPW device. The figure also includes the d.c. magnetoresistance taken from the Ohmic contacts which is used to identify the LL peaks in the high frequency response. It is evident from the figure that the LL peaks are in alignment with the dips in the S_{21} response confirming the location of the various LLs. Similar to the long-range device measured above, we notice that the S_{21} response rises to an asymptotic limit which determines the zero conductivity point of the short-range system.

Fig. 3.33(a) shows the response of the short-range 2DES-CPW device at zero magnetic field.

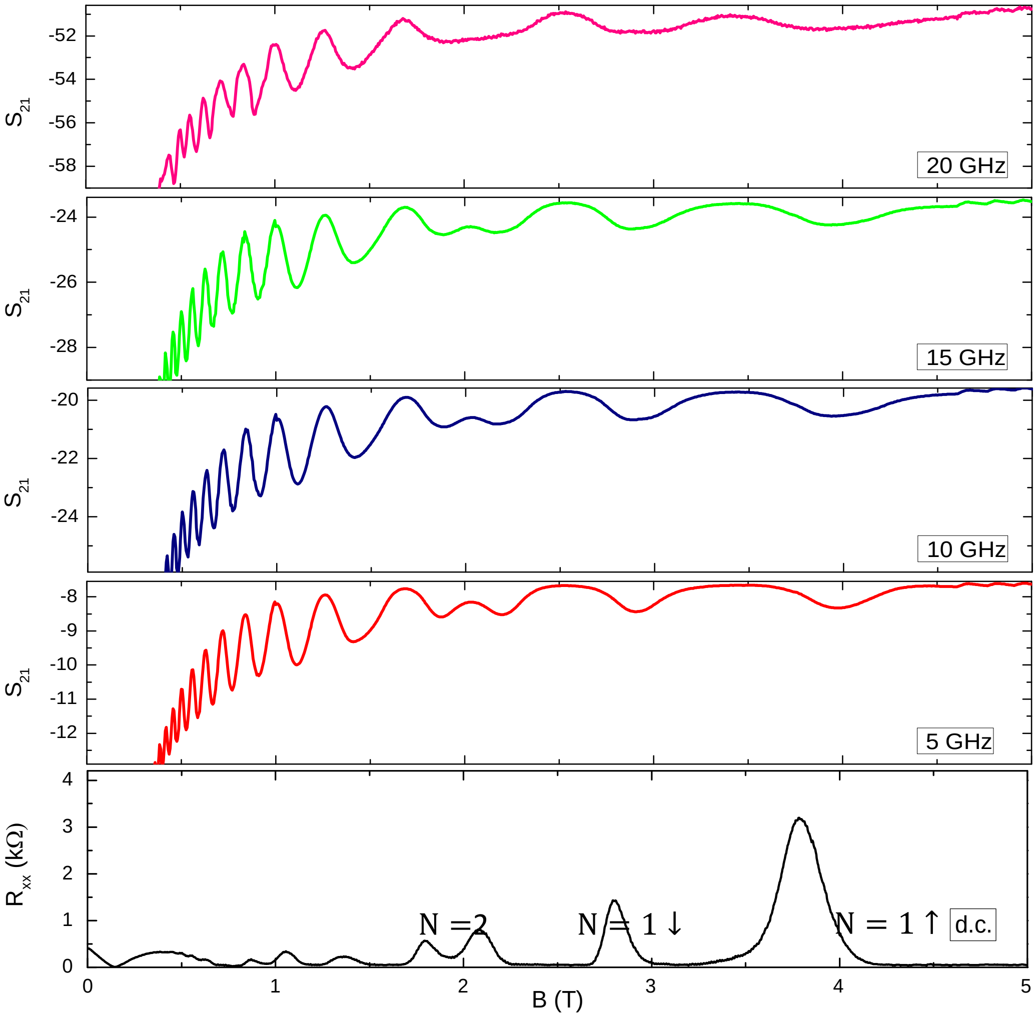

Figure 3.32. The magnetic field response of the S_{21} parameter at different frequencies compared with the d.c. magnetoresistance for the short-range sample.

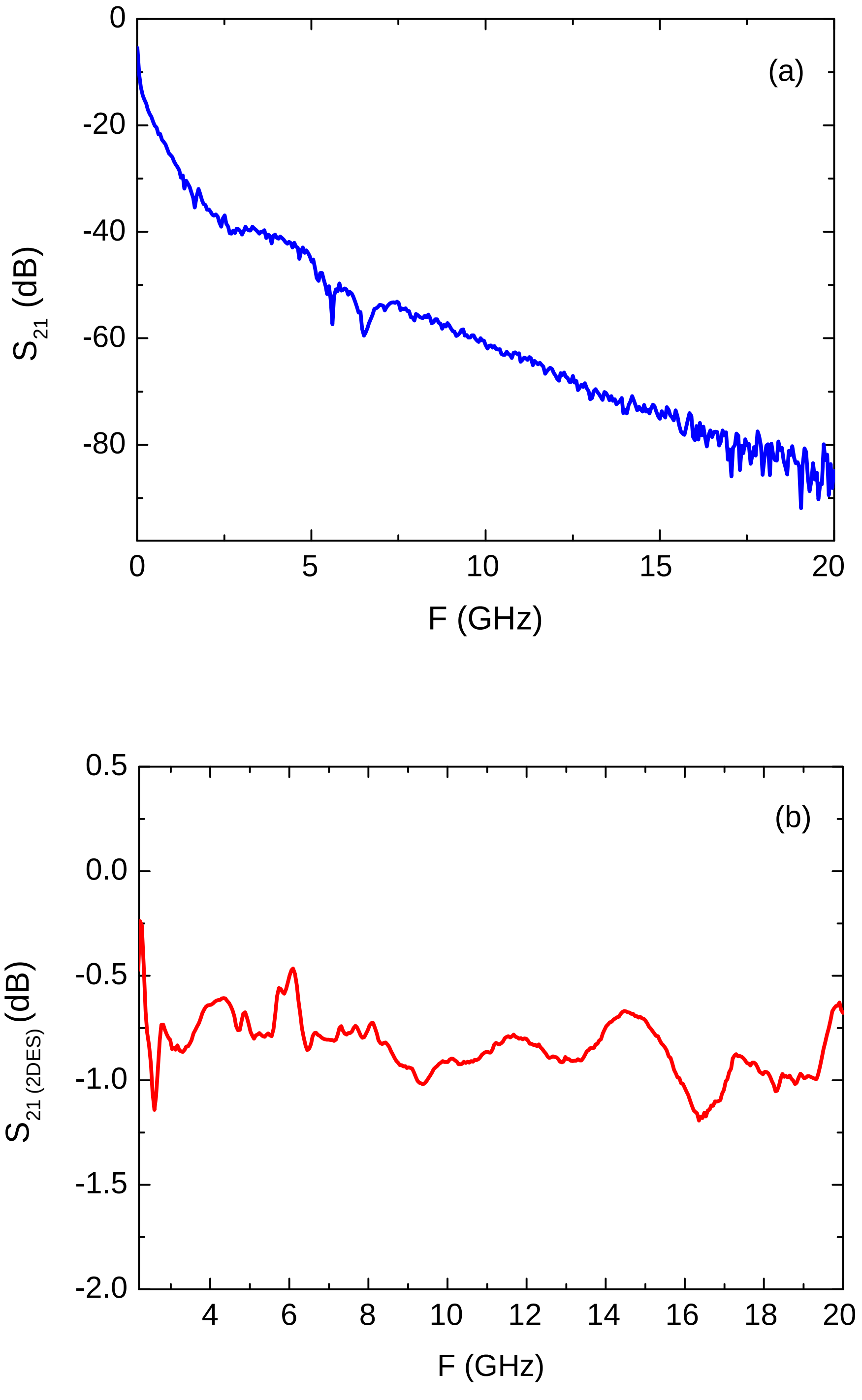

Figure 3.33. (a) The zero field frequency response of the short range 2DES-CPW device and (b) the intrinsic 2DES frequency response take from the maximum of the $N = 1 \downarrow$ LL.

Subtracting the frequency response at the zero conductivity point from the entire data set yields the intrinsic S_{21} response of the 2DES shown in Fig. 3.33(b). In Fig. 3.33(a), as expected, the response is more lossy at high frequencies due to the frequency dependent losses of the transmission line. Fig. 3.33(b) on the other hand shows the intrinsic S_{21} response determined at the peak of the $N = 1 \downarrow$ LL, and just like in the long-range equivalent, we observed a moderately flat response which is only slightly lossy at higher frequencies. A difference between the devices, however, is that the magnitude of the resonances observed in the short-range device is smaller compared with that of the long-range device.

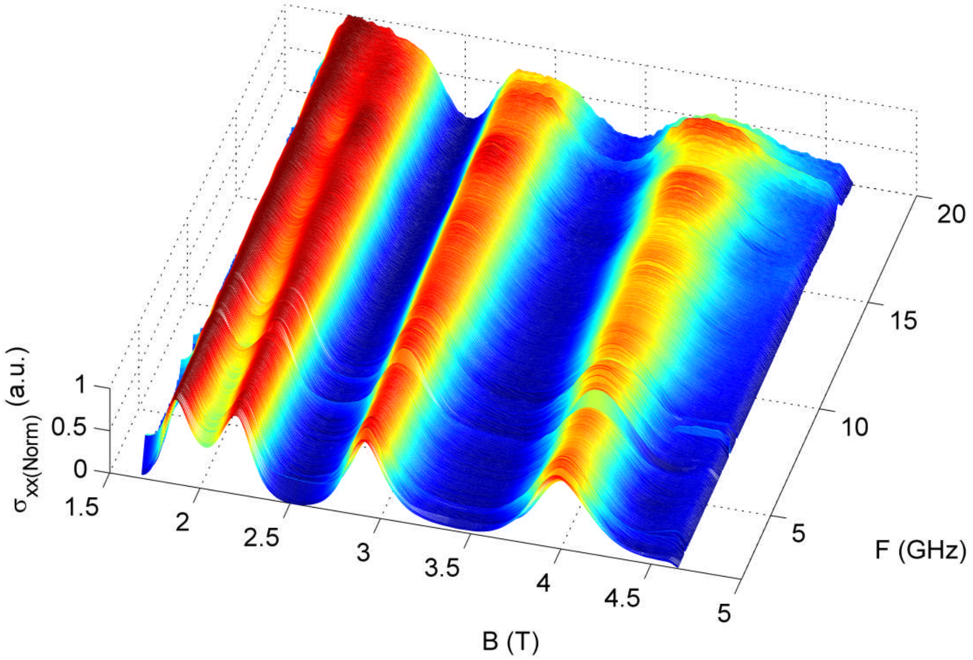

Figure 3.34. High resolution frequency measurements of the short-range 2DES-CPW device showing spin resolved $N = 1$ LLs and spin degenerate $N = 2$ LLs.

The results of high resolution frequency measurement of the short-range device is shown in Fig.3.34 where four LLs can be observed, two from the degenerate LLs of $N = 2$ LLs and two spin resolved LLs from the $N = 1$ LLs. Just as before, we shall only consider the spin resolved LLs of the $N = 1$ LL. The $N = 0 \downarrow$ LL is not considered here due to the same high field effect of the impurity band discussed above. We notice from Fig. 3.34 that the LLs broaden with increasing frequency as expected and required by the scaling theory analysis. We will now consider the nature of scaling within the short-range device.

3.5.3 Determination of κ of short-range sample

The scaling exponent is determined for a frequency range between 2 GHz to 20 GHz, which excludes the size effects which occur below 2 GHz. As confirmation of the insignificance of the temperature increase introduced from the microwave power, Fig. 3.35 shows the power scaling plot at 5 GHz for both $N = 1$ LLs considered. Measurements are carried out at microwave powers of $P <\ 0.01$ nW and from Fig. 3.35 it is observed that this region lies in the temperature independent part of the curve.

As has been employed in the previous analysis, the scaling exponent κ is determined from the width of the LL conductivity peaks. Fig. 3.36 illustrates the evolution of the peak width throughout the frequency range investigated. The double log plots from which κ is determined for the $N = 1$ LLs are shown in Fig. 3.37. The critical exponent determined in the short-range device appears to be in good agreement with the expected universal value of $\kappa \sim 0.42$, where the solid line in the figure represents a guide to the eye for $\kappa = 0.42$.

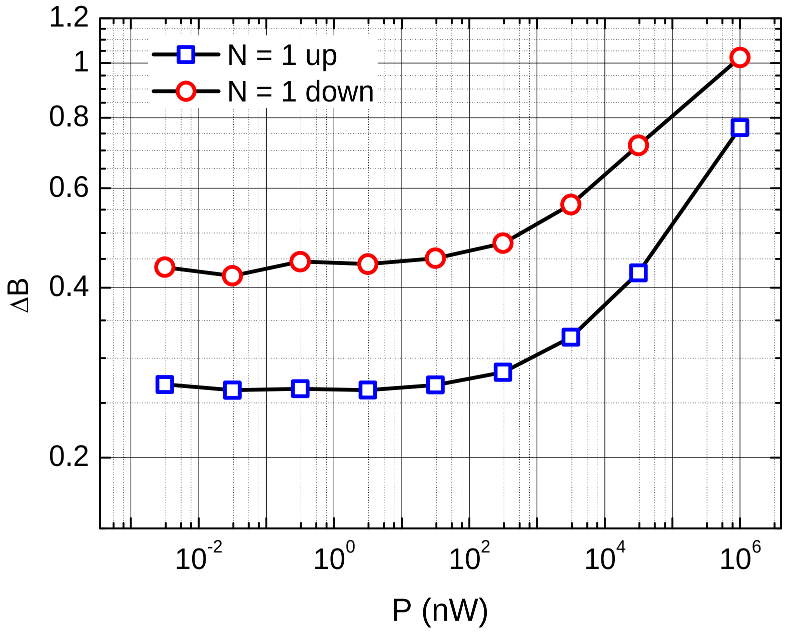

Figure 3.35. Power scaling of the $N = 1$ LLs at 5 GHz in the short-range 2DES-CPW device. It is observed that at powers below 100 nW the influence of electron heating is insignificant.

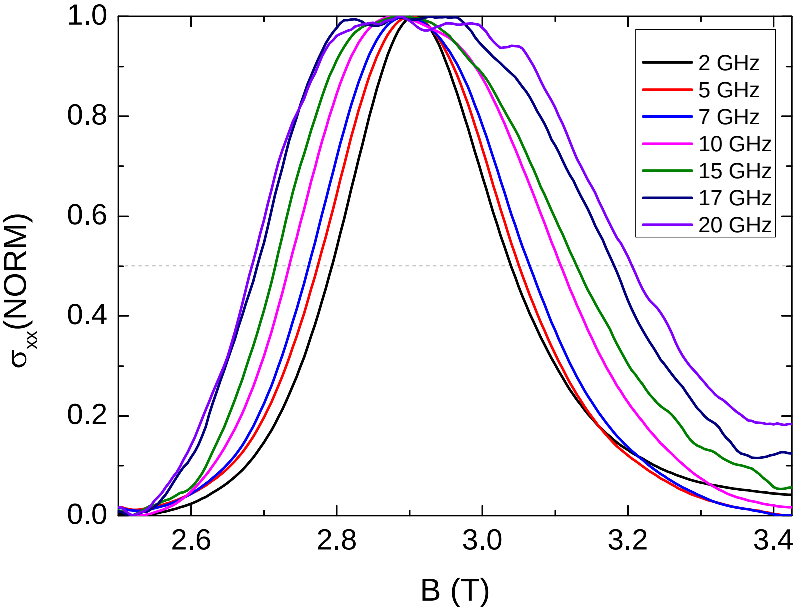

Figure 3.36. Normalized conductivity peaks of the $N = 1 \downarrow$ LL sampled at different frequencies throughout the range investigated.

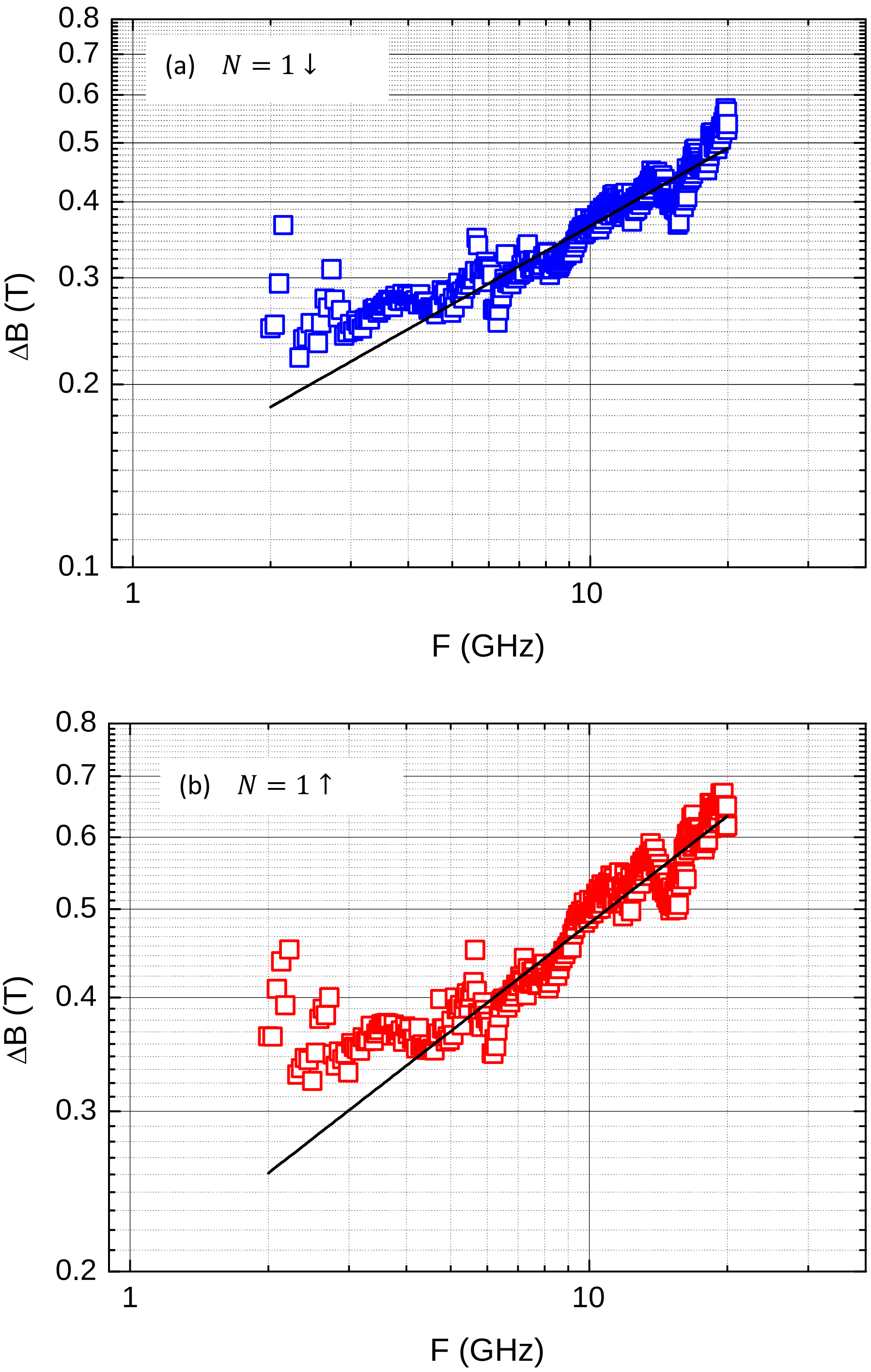

Figure 3.37. Frequency dependence of ΔB for the (a) $N = 1 \downarrow$ LL and (b) $N = 1 \uparrow$ LL. The solid line represents $\kappa = 0.42$. We observe that in the short-range device κ is in good agreement with the expected value of $\kappa \sim 0.42$.

This is a considerable change in the gradient as compared to that obtained for the long-range device of $\kappa \sim 0.6$. These results strongly suggest a correlation between the nature of criticality of QHTs and the nature of disorder in the 2DES, a relationship that will be further developed in the next chapter. Just as with the temperature scaling results presented in the previous chapter, these results do not conclusively support the unconditional universality of QHTs. The discrepancies between the results presented here and the theory are tackled in the next chapter.

3.6 Conclusion

In this chapter we have discussed the effect of frequency on electron transport within a 2DES and how it can be used to investigate QHTs through the concept of dynamic scaling. These investigations on the criticality of QHTs have been performed using high frequency measurement techniques applied to 2DES-CPW devices.

The measurements have been carried out on two different heterostructures that are differentiated by the nature of disorder. In the GaAs/AlGaAs system, disorder originates from remote ionized impurities that are remnants of Si doping in the spacer layer. Random fluctuations from these remote point charge sources only weakly perturb the 2DES and are classified as long-range disorder potentials. The other heterostructure investigated was an AlGaAs/AlGaAs heterostructure which included Al impurities in the GaAs layers, changing the nature of disorder from long-range scattering to short-range alloy scattering. Frequency dependent scaling analysis carried out on these heterostructures revealed a universal nature in the short-range device and a non-universal behaviour in the long-range device judged by the value of the scaling exponent expected from the scaling theory of QHTs. The result strongly supports the view that the nature of disorder within the system plays an integral part in the critical behaviour of QHTs.

In the following chapter the discrepancies in the criticality of QHTs observed so far, in both temperature and frequency, are explained using a quantum percolation model which offers insightful answers to the seemly indecipherable collection of results presented so far on the scaling theory QHTs.

Parts of this of this chapter has been published in Refs [142, 143].

4. The quantum percolation model of the scaling theory of QHTs

4.1. Introduction

In this chapter, the critical behaviour of QHTs occurring at the centre of LLs is explored in the context of a quantum percolation theory. The scaling theory of the QHE is perhaps the one of the most misunderstood aspect of plateau-to-plateau transitions but remains crucial to the understanding of the QHE. The bulk of the confusion, apparent from our discussion on the topic so far, revolves around the nature the universal criticality of scaling exponents associated with QHTs.

The experimental results presented so far are summarized below. We are reminded that the main objective of this work is to investigate the nature of the critical behaviour of the localization length exponent ν as the centre of the LL is approached. It is hypothesized by the scaling theory [6] that all QHTs experienced in 2DESs are universal processes that belong to the same universality classes and as such ν is a constant value of $\nu \sim 2.35$ [11] in all QHTs. In the temperature dependent scaling analysis presented in Chapter 2, the universal criticality of ν is measured through a composite exponent $\kappa = p/2\nu \approx 0.42$ [79] which is determined close to the centre of the LL. The temperature dependent results on κ do not confirm the expected universal behaviour. In an alternative approach where ν is determined directly within the tail regions of the same LL and away from the centre, ν is conclusively found to be in good agreement with the universal theory. In addition, the relationship between κ and the temperature exponent p is not found to hold. The results presented for p suggests that the assumption that $p = 2$ does not hold and it is proposed in section 2.4.2 that κ may not have any dependence on p, a result that still maintains the value of $\kappa \approx 0.42$ (i.e if $\kappa = 1/\nu$). The questions to be answered in the temperature dependent investigations are threefold, (a) why is universality conclusively found within the tail regions of the LL but inconclusive around the centre of the same LL (an ambiguity backed by previous results [86]), (b) though universality is not found in κ (i.e. around the centre of the LL) why do some studies observe universality in this exponent [12] while others do not [15], and (c) what is the correct relationship between κ, p and ν.

As regards to the frequency dependent investigates, the major question that arises from the results presented is the question of the role of disorder in the universal criticality of QHTs as it was observed that increasing the amount of disorder within a 2DES changes the nature of QHTs from a non-universal critical constant (in a long-range system) towards the expected universal critical constant (in a short-range system).

In an attempt to answer these questions a percolation model is employed which allows for various features and seemingly contradictory results obtained from the experimental investigations of QHTs to be explained in a physically transparent and visually intuitive manner, providing a unifying model of plateau-to-plateau transitions. The model presented here is founded on the quantum mechanical interpretation of the classical theory of percolation. The model is based on interactions between clusters of electrons that form within the bulk of the 2DES and how these interactions relate to temporal perturbations experienced by the system as the Femi level approaches the centre of the LL.

Three crucial crossovers between the quantum and classical percolation are identified that government the nature of criticality within QHTs, and associated with these crossover are three different length scales. These crucial length scales dictate the quantum-classical nature of plateau-to-plateau transitions which are manifested in the various results discussed above.

The model presented below is the first attempt made in the literature to explain the various seemingly contradictory features observed in the experimental determination of the universal criticality of QHTs using crossovers of various length scales to provide a unified picture of plateau-to-plateau transitions.

4.2. The effect of Coulomb interaction and screening in 2DESs

The two main sources of disorder within the 2DES, we recall, are both associated with charged impurities; the remote ionized impurities (or donors) which are separated from the 2DES by the spacer layer, and the residual ion impurities located within the vicinity of the 2DES (i.e. unintentional charged impurities present in the MBE vacuum during the growth process). Residual ions are important in determining the zero field or Drude mobility of the system. The classical or Drude mobility is less dependent on the remote ions [144] but the long-range fluctuations from these remote ionized impurities however have profound effects on the 2DES at high magnetic fields. These high field effects influenced by long-range fluctuations will be the focus of our present interest.

Due to the separation imposed by the spacer layer, the potential fluctuations from the remote ions felt by electrons in the 2DES tend to be smooth and slow varying [145]. The long-range potential fluctuations are random fluctuation as they arise from the randomly (uncorrelated) positioned impurities in the donor layer. The statistical properties of the long-range potential can be easily evaluated in the two limiting cases of the effective potential; at high densities of the 2DES and at the bare potential or low density limit of the 2DES. At a high electron density, the 2DES is able to effectively screen the potential fluctuations by small redistributions in the electron density [146] which suppresses or flattens out the external long-range fluctuations of the bare potential. This is known as linear screening [20] and the 2DES takes the form of a homogenous electron fluid. At low electron densities however, non-linear screening [147] occurs where the electron density becomes strongly non-homogenous. In the non-linear regime, due to the low density, the degree of electron redistribution available is not sufficient to compensate for potential fluctuations and therefore the electron liquid is torn apart into isolated clusters of electrons by the random potential [147, 148].

In a strong magnetic field a regime of inhomogeneity and non-linear screening exists within the tail regions of the LL. Within the tails of the LL, the Fermi energy lies in a region where the electron density is low. Fig. 4.1(a) shows the bare potential experience along a cross-section of the 2DES. Initially electrons start filling up from the bottoms of the potential wells formed by the bare potential up to the Fermi level. A top view of Fig. 4.1(a) translates into a landscape covered with pools or clusters of electrons corresponding to the locations of the potential wells as shown in Fig. 4.1(b), everywhere else represents regions of high potential corresponding to hills illustrated in Fig. 4.1(a).

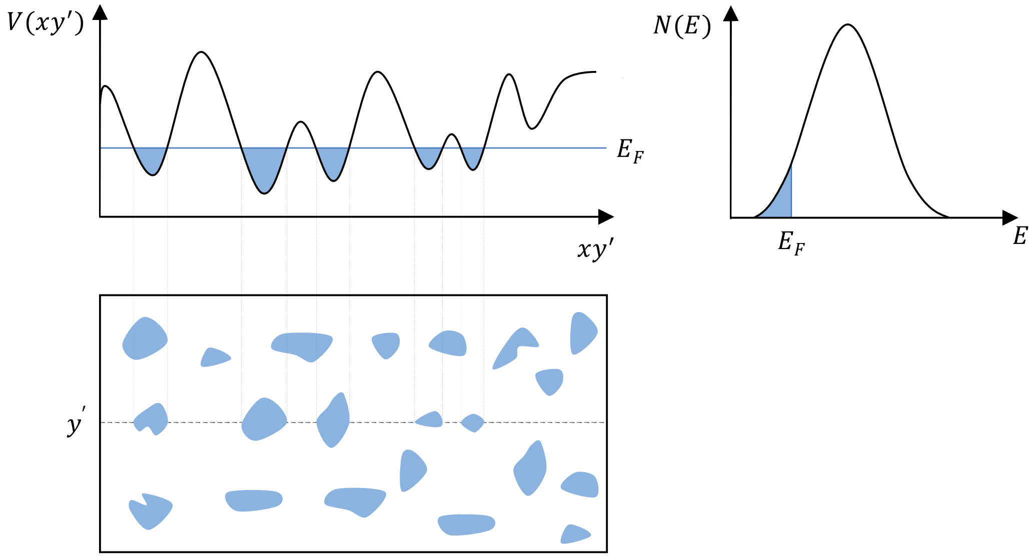

Figure 4.1. A schematic representing non-linear screening within the tail regions of the LL band. (a) shows the bare potential generated by the remote impurities in the donor layer along a line xy' in the plane of the 2DES. Electrons fill up from the bottom of the wells up to the Fermi level. (b) illustrates the view of the 2DES at the current Fermi level. Filled wells appear as electron clusters in the 2DES surface. (c) shows the position of the Fermi level within the LL band.

The average concentration of electrons in the system is determined by the position of the Fermi level within the density of states of the LL band illustrated in Fig. 4.1(c). This scenario is descriptive of a non-linear screening regime. It clear that due to their low density, electrons are only able to partially screened by the bare potential, so that the 2DES exists in an inhomogeneous state where the electron liquid is separated into isolated electron clusters by regions of high potential caused by the long-range potential fluctuations. As the filling factor is increased (by varying the magnetic field for example), the LL band increasingly fills up with electrons. Consequently, the wells in the bare potential are increasingly filled with electrons at higher electron densities.

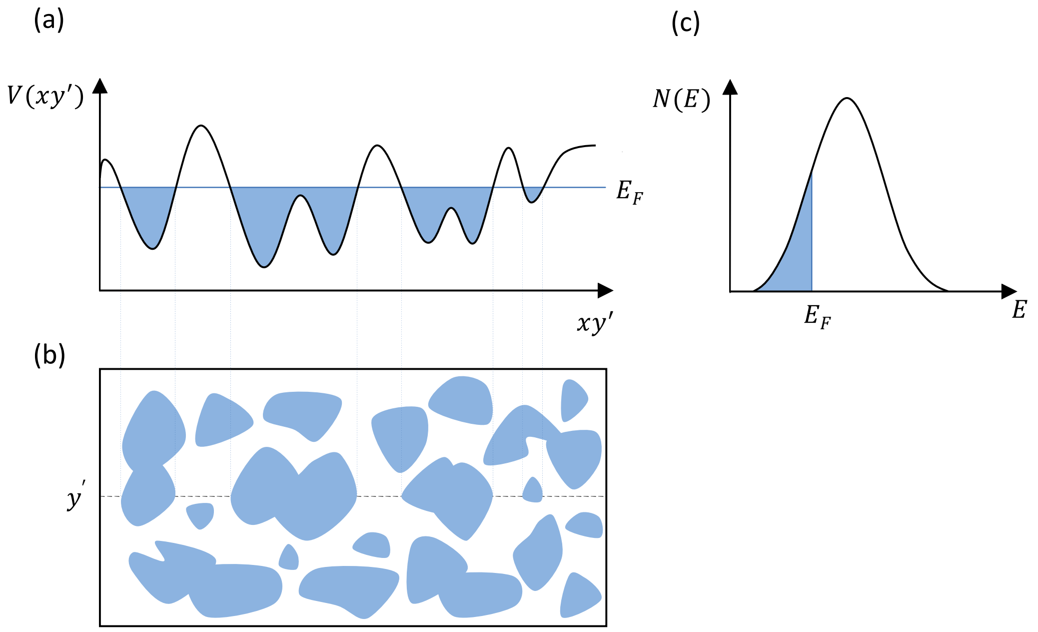

Figure 4.2. As the carrier density increases local potentials well become filled with electrons, and electron clusters merge to form clusters of larger sizes.

Adjacent wells begin to merge forming larger and larger clusters of electrons. The Fermi liquid begins to cover larger surface areas screening more of the bare potential. The progression from the previous scenario is illustrated in Fig. 4.2.

As this processes progresses, a point is reached where the electron density is sufficiently high to compensate for the entirety of the bare potential. At this point we have perfect screening and the system enters a linear screening regime. The effective potential is completely flat. In this linear screening regime, which is illustrated in Fig. 4.3, the Femi level lies at the centre of the LL band where the electron density is the highest.

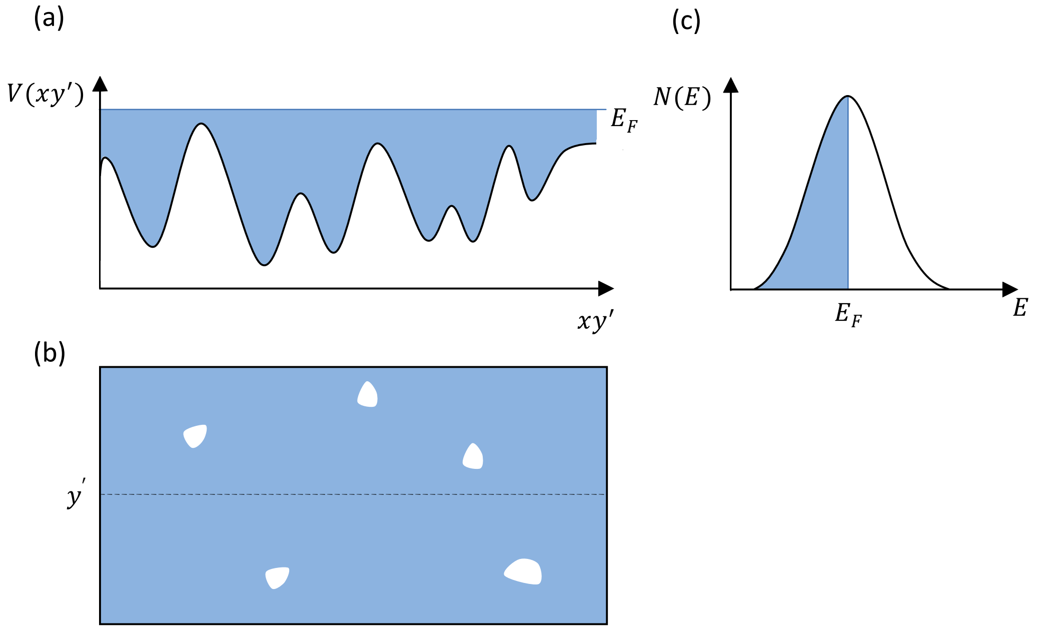

Figure 4.3. When the Fermi level is close to the centre of the LL, the 2DES acquires a density modulation that compensates for bare potential, leading to a linear regime where the effect of small fluctuations in the potential is irrelevant.

From the above descriptions, we notice that when the filling factor is close to a half integer value (centre of the LL band), the system is in a linear screening regime and the long-range potential fluctuations experienced in the plane of the 2DES is greatly reduced. On the other hand, when the filling factor is close to an integer value, the system enters a non-linear screening regime and potential fluctuations will be large.

Even though the system as a whole may be within the non-linear regime, due to electron-electron interaction small regions within the 2DES exist where the screening is *locally* linear. From the present description of the Fermi liquid in the non-linear regime, two regions are easily identified: regions of high electron density where the electron density is close to the bulk value $n_0 = eB/h$ of the LL, and regions of depletion in which no electrons are found. The former is located at the bottom of a partially filled potential well, where the carrier concentration approaches the bulk value, $n(\boldsymbol{r}) \approx n_0$, and the latter region represents the depleted high potential hills which are without any concentration of electrons, $n(\boldsymbol{r}) = 0$. This picture describes a non-interacting view of the 2DES at high fields where a sharp boundary (with respect to $n(\boldsymbol{r})$) will exist between the bulk and depleted regions. These two regions are sometimes referred to as incompressible fluids [149], since they are completely filled to capacity with either electrons or holes. An incompressible fluid (electrons or holes) describes as a fluid for which all states within the bulk are occupied such that no adjustment or redistribution in the density is possible to compensate for an external potential [150]. These regions are naturally completely incapable of screening the bare potential.

The presence of electron-electron interaction however introduces a third region which is found between the incompressible bulk region and the incompressible depleted regions. In the case of interaction, Coulomb repulsion between electrons at the edge of the incompressible fluid smears outs the sharp boundary. As one moves from the zero density in the depleted region towards n_0 in the bulk, $n(\boldsymbol{r})$ will gradually grow from 0 to n_0 [151]. There therefore exists an intermediate region where the density varies between 0 and n_0 and not completely full. The intermediate region contains unoccupied states such that compressibility is possible. When exposed to an external potential, electrons within this compressible region are able to arrange themselves (redistribute) in a manner which screens the bare potential [150], just as in a metal. The effective potential within the compressible (or metallic) region is therefore flat and screening within this region is linear (local linear screening).

Fig. 4.4 illustrates the properties of the various regions discussed for a single potential well found within the potential landscape of a 2DES.

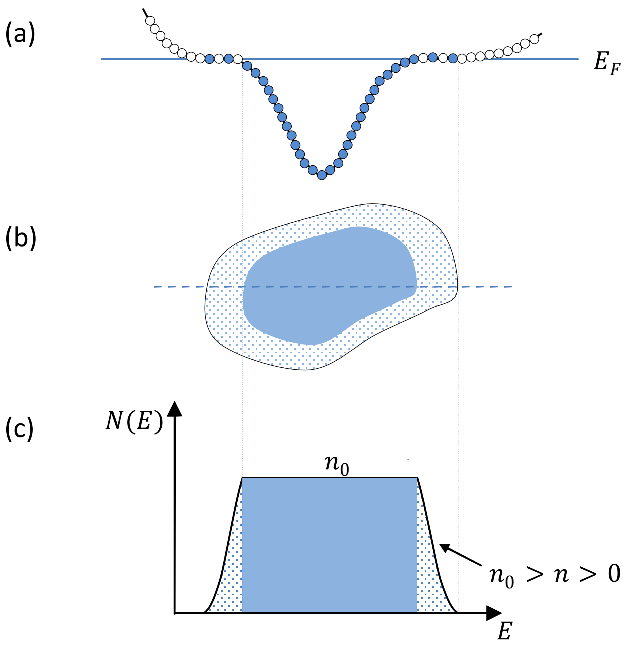

Figure 4.4. A schematic showing areas of local linear screening and non-linear screening. (a) shows electrons in a potential where the local redistribution of electron density close to the Fermi level is sufficient to attain linear screening, metallic region therefore is found at the Fermi level. The bulk of the cluster remains non-linear. (b) shows a top view the electron cluster. (c) shows the profile of the carrier density across the cluster.

It is seen in Fig. 4.4(a) that states in the middle of the well are all occupied, representing the incompressible electron fluid. Screening is absent from in this region and the electron states bend according to the bare potential. At the boundary of the well however, a compressible or metallic region exists with unoccupied states in its interior. Strong linear screening in this region flattens out the bare potential by small redistributions of the local electron density. As one moves further away from the centre of the well, a higher potential or depleted region is found, this region represents an incompressible hole fluid which also bends in accordance with the bare potential [150].

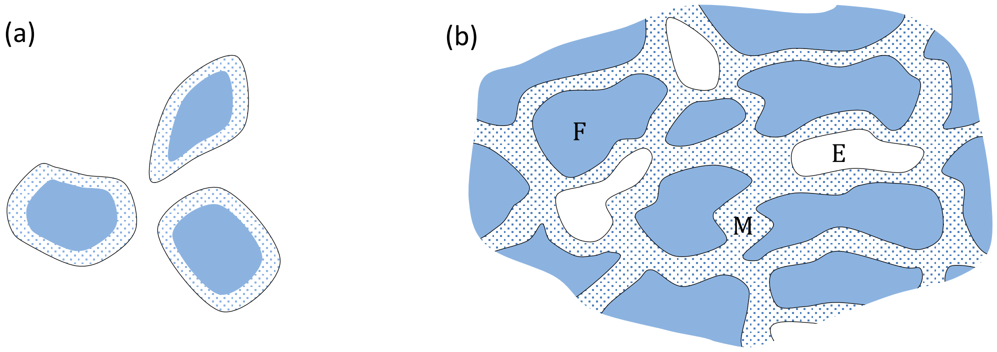

Figure 4.5. (a) The scenario of a network of completely isolated clusters. (b) The outermost edges of these clusters merge to form a percolation network of the metallic region. F, E, and M denote the full, empty and metallic regions respectively.

Fig.4.4(b) illustrates the top view of the resulting electron cluster where the dark area represents the incompressible electron fluid while the dotted region denotes the compressible metallic region. Everywhere else (white space) can be considered to contain an incompressible hole fluid. Fig.4.4(c) shows the corresponding density of states which is constant in both the incompressible electron and hole regions but varies within the metallic region between the bulk value and total depletion.

As the filling factor is increased, additional electrons will be added to the boundary of the electron cluster beginning with the lowest available states in the metallic region, growing the clusters until they begin to merge forming a percolating network of metallic regions as shown in Fig. 4.5. It clear that in case of isolated states (as shown in Fig.4.5(a)) the dissipative flow of electrons is not possible. At percolation however, when enough clusters have merge to form a path from one side of the system to the other, a finite amount of dissipative conduction through the metallic regions of the system becomes possible. This will be further discussed in the section on percolation below.

The above analysis is essentially a description of the formation of edge states [152] from the point of view of the non-linear screening of an external potential by the 2DES, as first considered by Beenakker [153] and Chang [150], and based on earlier work by Efros [146-148, 154] on the effect of Coulomb interaction on the 2DES. This was expanded on by Chklovskii, Shklovkii and Glazman [151] where these edge states were described as electrostatic channels consisting of alternating strips of compressible and impressible regions. Following these developments in the interaction of the 2DES, Copper and Chalker applied the influence of Coulomb interaction to the percolating network description of the QHE first proposed by Chalker and Coddington [155].

4.3. The percolation model

In the previous section, the nature of the density of the 2DES was discussed in terms of linear and non-linear screening. In the presence of long-range fluctuations from remote ions, the 2DES breaks up into clusters of electrons. Below we expand this view of the 2DES by considering the percolation network model which emphasises the nature of electron transport within the 2DES as the critical point at the centre of the LL is approached. Further, quantum tunnelling and inelastic scattering are introduced into the model to form a fuller picture of temperature/frequency dependent scaling of the QHTs.

4.3.1. Classical percolation

The study of percolation, which originated in the mathematical analysis of a fluid spreading randomly through a non-uniform medium [156], is applicable to a variety of physical phenomena and systems [157-161]. The problem can be defined as follows.

Imagine a large lattice in which each site can be in one of two states, occupied or empty. The occupation of sites occur in a random manner and is defined by a single parameter p, where p is the probability of a site being occupied and $(1-p)$ is the probability of a site being empty. p therefore represents the concentration of particles in the lattice. If $p=0$, all of the sites will be unoccupied but on the other hand if p is close to unity then almost all sites are occupied. As p increases the population of sites generally occur in a way which leads to the formation of clusters. These emerging clusters will continue to grow with increasing p with neighbouring clusters coalescing into larger clusters until at a critical value p_c an infinitely extending cluster is formed. This infinite cluster *percolates* through the lattice, connecting one edge of the lattice to the other in the same way water percolates through sand along an extending network of the fluid. Above the critical point p_c, only one such infinite cluster can exist [162]. The onset of an infinite cluster, i.e. the percolation threshold, is sharply defined such that for $p<p_c$ no percolation network exists but for $p>p_c$ one percolation network exists. In this sense percolation, which occurs at the critical point, is a phase transition and the behaviour of the system close to the phase transitions can be described in the usual way by critical exponents through a scaling theory [162]. The phase transition and the formation of the infinite cluster is characterised by a divergence of the typical cluster size as p_c is approached. A consequence of this critical phenomenon is the scaling relationship [162]

$$\xi_p \propto |p-p_c|^{-\nu_p}, \tag{4.1}$$

where ξ_p represents the typical cluster radius and ν_p is the critical exponent of the cluster correlation length ξ_p.

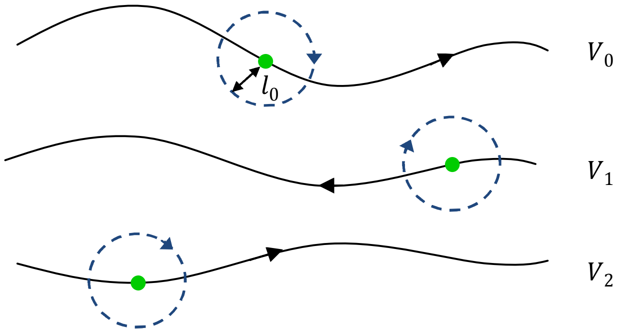

Figure 4.6. A diagram illustrating the dual nature of electron motion within a strong magnetic field which consists of an orbital motion of radius l_0 and slow drift of the guiding centres of long equipotential lines of contours.

It is obvious that there is a striking resemblance between the percolation problem and the localization problem of 2DESs. The connection between percolation theory and the localization-delocalization transitions in electron systems was first addressed by Ziman [163]. A quantitative semi-classical relationship between the two problems was verified for a 2DES in an applied magnetic field by Trugman [164]. The basic picture provided by the semi-classical analysis is as follows. In the presence of a strong magnetic field and a smooth random potential varying on a length scales larger than $l_0 = \sqrt{\hbar/eB}$, the solution of Schrödinger equation in a two-dimensional system produces eigenstates with invariant or constant potential energies $V(\boldsymbol{r})$. Electrons are therefore restricted to move along trajectories in the 2DES that maintain a constant potential [165]. The essential simplifying feature of this result is that electrons possess two uncorrelated components of motion. The first is an orbital motion of frequency $\omega_c = eB/m$ and radius l_0. The second takes the form of a slow drift of the guiding centres of these orbits along equipotential lines described by the background potential [54, 166] as shown in Fig. 4.6.

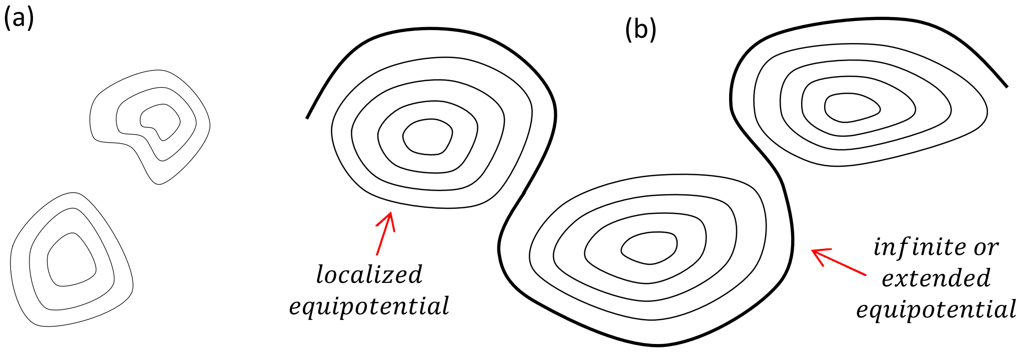

Figure 4.7. (a) An illustration of confining or localized contours. (b) A merger of contours forming an infinite or extended equipotential on the outmost edges of previously isolated contours.

It was shown that these equipotential lines form enclosed contours for all energies except the equipotential at the critical percolating energy E_c which coincides with the centre of a LL band [164]. As a result away from E_c (i.e. in the tail regions of LL band) the enclosing contours confine the movement of electrons to its cluster (as shown in Fig. 4.7(a)) where an electrons can only be displaced by drifting along its equipotential. Electrons are therefore effectively localized to a well-defined region within the 2DES. The microscopic formation of these clusters has already been discussed in detail in the previous section. The important contribution to this picture is the drift of electrons along equipotential lines within these clusters. As the centre of the LL band is approached the outmost equipotential of neighbouring clusters merge to form an ever extending path until at E_c a single infinite equipotential line moving across the entire system is formed as see in Fig. 4.7(b).

There is no dissipative conductivity through the system below the percolation threshold but at percolation a finite conductivity is achieved. The critical exponent from Eq. (4.1) has a value of $\nu_p = 4/3$ or 1.33 which is a well-known result for the solution of the percolation problem in two-dimensions [61, 162] and has been calculated exactly [167]. This result however, does not take into account quantum tunnelling and interference effects. The consequence of these effects on the percolation model is considered below.

4.3.2. The quantum correction to semi-classical percolation

The classical description of percolation is only valid for vanishingly small magnetic length l_0 since it assumes that there is no interference between equipotential lines. This assumption however breaks down as the percolation threshold or critical point is approached. Close to the centre of the LL band the outmost equipotential of neighbouring clusters approach each other and just before they coalesce, when the distance between them is less than l_0, quantum tunnelling between adjacent clusters is possible through minima in potential known as saddle points (see Fig. 4.8).

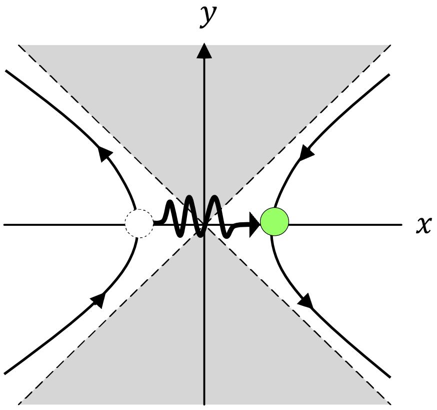

Figure 4.8. When two equipotential are within the magnetic length of each other a minimum in potential occurs known as a saddle point. Electrons are able to quantum tunnel from one electron cluster to another through these saddle points. The grey region represents areas of high potential.

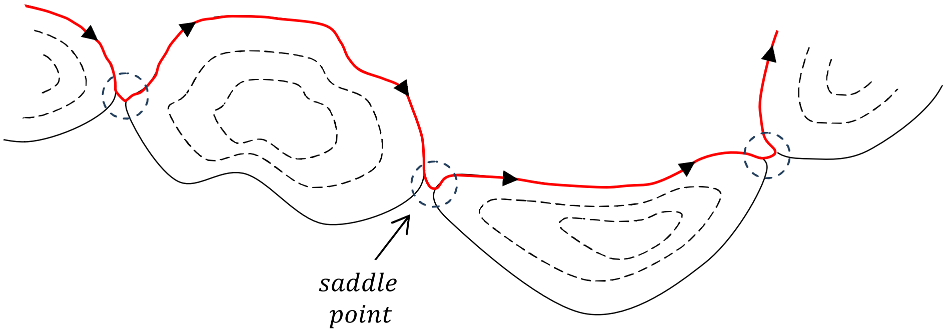

Figure 4.9. An illustration of the outmost equipotential of a group of clusters extended through saddle point tunnelling close to the percolation threshold.

Aided by these saddle points, it is possible for dissipative conductivity to be achieved before the percolation threshold is reached as depicted in Fig. 4.9. Electron transport from one side of the system to the other is possible through conducting networks of saddle points. In order to determine the localization length, this form of coherent transport has to be taken into account [168]. Using this network model Chalker and Coddington [71] were able to show that quantum tunnelling changes the critical exponent from it classical value of $\nu_p = 4/3$ to a value of $\nu = 7/3$ or 2.33 and this quantum critical value of the exponent coincides with the value expected in finite-size scaling discussed throughout this work. This result suggests that there is a strong link between saddle point tunnelling and the observation of quantum criticality of the scaling exponent. This argument has been supported by some authors [169] where through numerical analysis it has been shown that the inclusion of saddle point tunnelling distinguishes the two universality classes of quantum criticality ν of classical criticality ν_p. We develop this idea further to provide a qualitative interpretation of the results obtained in this work. It will be argued that the presence of quantum tunnelling is crucial to the experimental observation of quantum criticality in 2DES as expected in the finite-size scaling analysis of QHTs. A detailed treatment of the percolation model can be found in a recent report by Kramer *et al*. [61].

Finally, experimental evidence on nonlinear screening and the percolation through saddle point tunnel is briefly discussed. In recent times, advanced probing techniques have been developed that for first time allow a more precise and detailed description of electron transport in a 2DES to be studied. By performing scanning probe experiments on the surface of a 2DES in particular, the local electric potential at different locations of the 2DES surface can be determined, and an image formed of the charge distribution in the 2DES. These experiments, which have largely verified the percolation and non-linear screening description of the 2DES, include scanning tunnelling spectroscopy (STS) [170-172], photoluminescence [173], scanning force microscope (SFM) [174], atomic force microscope (AFM) [175] imaging, surface charge accumulation [176] imaging, and single-electron transistor spectroscopy [177].

The most remarkable demonstration of percolation and non-linear screen however is in a STS experiment reported by Hashimoto *et al*. [178] illustrating a QHT in real space of the $N = 0 \downarrow$ LL. Their main result is shown in Fig. 4.10. The local density of states of the 2DES is probed using point by point measurements of the local deferential conductivity dI/dV [179] through a stabilized tip. The map produced by the measurements illustrate the non-linear and screened disorder potential of density of states within the 2DES.

The bright areas in Fig. 4.10(a)-(g) represent areas of high electron concentration or clusters of incompressible electron fluid region while dark and empty regions represent areas of low electron concentration or incompressible hole regions.

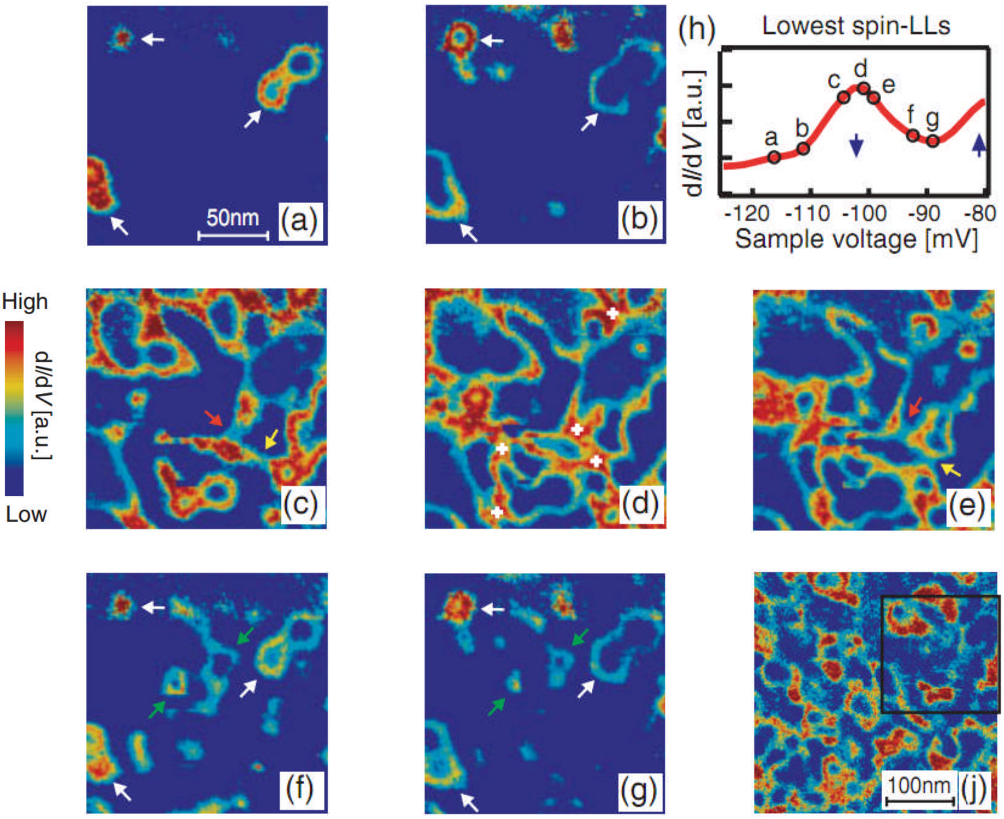

Figure 4.10. Taken from Hashimoto *et al* (2008). The local density of states is obtained by scanning the surface of a 2DES around the lowest spin down Landau level. (a)-(b) shows electron density in the localized regions on the low energy side of the Landau level, and (f) and (g) shows the corresponding picture on the high energy side of the Landau level. (c)-(e) shows electron density close to the percolation threshold. (h) indicates points on the Landau-level corresponding to (a)-(g). And (j) shows the density image for the entire sample, while the marked rectangle is the area shown for (a)-(g).

The compressible metallic regions can be seen around the edges of the electron clusters. Fig. 4.10(h) shows the spatially averaged dI/dV curve about the $N = 0\downarrow$ LL and is annotated with the locations of Figs. 4.10(a)-(g). As the critical point at the centre of the LL is approached the electron clusters grow in size (illustrated in Fig.4.10(a) and (b)) and merge until at the percolation threshold located at the centre of the LL an extended path forms seen in Fig.4.10(d). As the Fermi energy moves away from the critical energy the process is reversed and the clusters decrease in size, this is shown in Fig.4.10(f) and (g) by the green arrows which indicates shrinking features. It is noticed that identical features indicated by the white arrows in Figs. 4.10(a), (b) and 4.10(f), (g), appear on both sides of the LL, verifying the consistency of the localized regions in the tails of the LL.

Our main focus here is the QHT itself which occurs at the centre of the LL. As the percolation threshold is approached saddle points between adjacent clusters are observed. Examples of these quantum tunnelling points are indicated by the red and yellow arrows in Fig.4.10(c) and (e) where minima is potential between pairs of clusters was measured.

This remarkable collection of scanned images validates the key features of the percolation model and non-linear screening and crucially demonstrates how they describe QHTs.

4.3.3. Quantum correlation and coherence of 2DESs in the percolation model

A key feature in the percolation model is its emphasis on critical behaviour and linking this to a physical picture of randomly expanding clusters. In this section we define three key length scales that form the basis of the analysis of QHTs presented in the following sections. These length scales determine the correlation and coherence of electrons within the percolation model.

As presented in the foregoing description of the electrons clusters, electrons drift along equipotential lines which make up these clusters. At very high magnetic fields the width of these lines, which is determined by the magnetic length l_0, is vanishingly small such that neighbouring equipotential do not inference with each other. The equipotential lines can therefore be thought of as one-dimensional quantum wires each belonging to a discrete eigenstate of energy.

Electrons on the outmost equipotential of a cluster will undergo the maximum displacement within a given cluster. The localization length ξ of an electron, which is simply a measure of the displacement of an electron wavefunction in space, will therefore be limited to the typical size of an electron cluster within the system, ξ_p. From the classical description of percolation, as the critical point is approached ξ_p increases and as a result ξ also increases. However, as saddle points begin to form within the system there is a break between ξ and ξ_p since an extended quantum wire can be formed before two adjacent clusters have merged by the linking of the outmost equipotentials of the two clusters through a saddle point. The onset of saddle points allows a previously localized electron to escape its cluster by quantum tunnelling through a saddle point. In this case ξ will become greater than ξ_p. This split between the classical correlation length and the quantum correlation length will become important in the discussions of criticality given below. An electron drifting along an extended quantum wire will diffuse throughout the system from one cluster to another until it arrives into a cluster for which there exists no outgoing saddle point. As the percolation threshold is further approached it is obvious that the extended wire will eventually become an infinite equipotential connecting one side of the system to the other (typical of percolation systems discussed above).

Thus far the effect of temperature (or frequency) has not been considered. At non-zero temperatures a new length scale, the phase coherence length, is introduced into the problem. Until the introduction of temperature, an electron remains in its eigenstate of energy indefinitely (assuming negligible influence of other dephasing mechanisms). As the temperature is increased an electron-phonon collision will transfer an electron from its quantum wire to another and therefore change its eigenstate. An electron will therefore have a finite lifetime within a quantum wire corresponding to a phase coherence length L_φ. As long as L_φ of an electron is longer than the length of quantum wire (i.e. ξ) the effect of temperature is negligible but at high temperatures when $L_\varphi < \xi$, electron localization is of no practical importance since a phonon will cause a transition of an electron from one state to another states before the electron experiences any effect of localization. That is, an electron will be transferred from one quantum wire to another before it is able to fully explore its localized environment. The electron is therefore unaware of its localization and does not exhibit any localized behaviour. This argument, first present by Thouless [48] while considering transport in one-dimensional wires, illustrates the destruction of localization in the system. The system now takes up the characteristics of a bulk metal.

Phonon collisions, unlike saddle point tunnelling, are incoherent processes. At zero temperature therefore, an electron maintains coherence (i.e. remains in its quantum wire) over the length scale ξ but at finite temperature coherence is limited to L_φ. A decreasing L_φ reflects an increase in the inelastic scattering rate or relaxation mechanism and this is expected to occur with an increase in either temperature or frequency. The temperature dependent relaxation mechanism is discussed in section 2.4.1 while relaxation due to a high frequency applied electric field is discussed in section 3.1.2. The important point to note here is that after diffusing a length L_φ, a relaxation event occurs (either induced by temperature of frequency) which transitions an electron from one quantum wire to another.

4.4. Crossovers in criticality observed in the percolation model

Using the length scales that describe correlation and quantum coherence in the 2DES, ξ, ξ_p and L_φ, we discuss how competition between these relevant lengths bring about various crossovers which determine the nature of criticality of QHTs.

4.4.1. Phase coherence length dependent crossover

In this section we consider the effect of a varying L_φ on nature of the criticality of QHTs. In both temperature and frequency scaling, we recall that criticality was determined by measuring the FWHM width of the conductivity peak, through the expressions $\Delta B \sim T^{1/\nu z_T}$ and $\Delta B \sim f^{1/\nu z_\omega}$ (see Eq. (3.6) and Eq. (3.7)), where z_T is expected to be $z_T = 2/p$ (such that $\kappa = 1/\nu z_T$) and z_ω is predicted to be unity [6, 128]. The inconsistencies of the dynamic exponents z_T and z_ω have already been discussed in quite some detail in sections 2.5.2 and 3.1.3 respectively and will not be repeated here. However, given that it is expected that $z_T = z_\omega = 1$ [6], the controversy of the dynamical scaling exponent can, for the moment, be set aside by expressing the scaling functions as $\Delta B \sim T^{1/\nu}$ and $\Delta B \sim f^{1/\nu}$ where a universal quantum critical value of $\nu \sim 2.35$ is expected according to the scaling theory of QHTs [11]. The issue of the dynamic exponent in the context of the percolation theory will be dealt with in detail in section 4.5.1 below.

In Eqs. (3.4) and (3.5) from Chapter 3, T and f was related to L_φ where increasing either T or f causes a decrease in L_φ due to an increase in the rate of relaxation or inelastic scattering and this process in turn causes an increase in ΔB. The measurement of ΔB is determined from transport measurements at magnetic fields (or band of energies) close to the centre of the LL. To interpret these measurements in terms of the percolation model we therefore consider the nature of transport close to the percolation threshold.

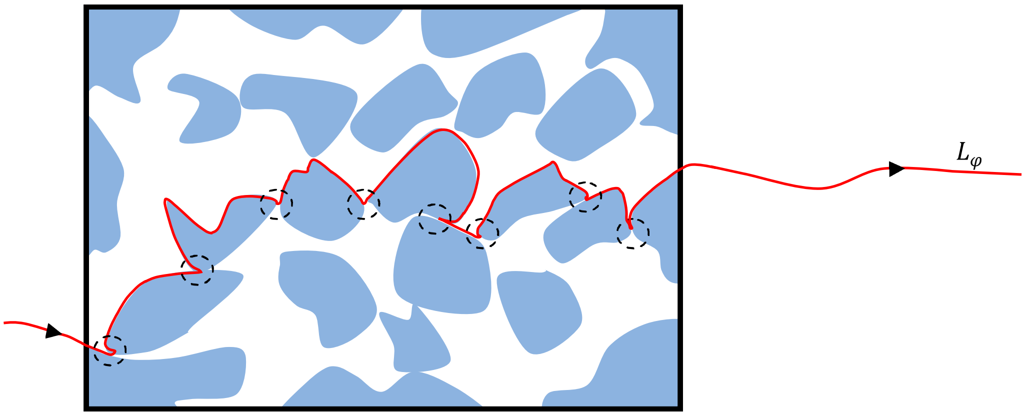

Figure 4.11. Close to the percolation threshold an extended wire is formed through a network of saddle points. At very low temperatures an electron drifting allow such an extended wire will be have phase coherence length which will be much longer than the sample size of the 2DES.

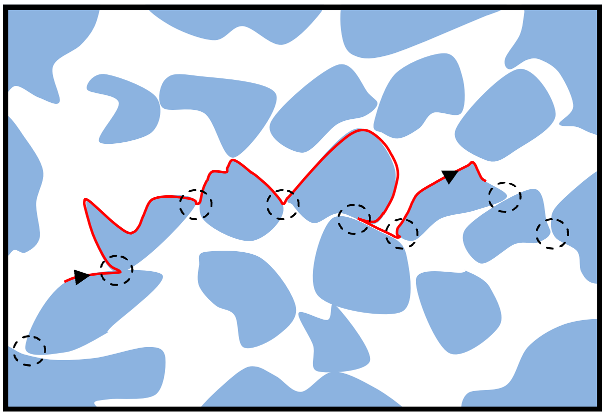

Figure 4.12. As the temperature is increased L_φ becomes smaller than the sample size such that an electron is scattered before it us able to diffuse through the entire length of the sample.

In such a scenario, at zero temperature, dissipative conductivity is solely achieved through electron transport along quantum wires extended via saddle point tunnelling. At finite but low temperatures (or frequency) and for any practical size of a 2DES, L_φ will be very large compared with the sample size L_{2D} and will theoretically be extended beyond the boundaries of the system. This is illustrated in the schematic of Fig. 4.11 which shows an example of a quantum wire extended via saddle points. The length of the wire, which (theoretically) extends beyond the boundaries of the system, represents $L_\varphi > L_{2D}$. An electron is able to drift from one side of the system to the other along the extended wire generating a finite amount of dissipative conductivity which results in a narrow width ΔB to be measured about the LL. It is important to note that the influence of temperature or frequency is negligible in this scenario since an electron, on average, is able to make it from one side of the system to the other before being scattered due to the relatively large value of L_φ.

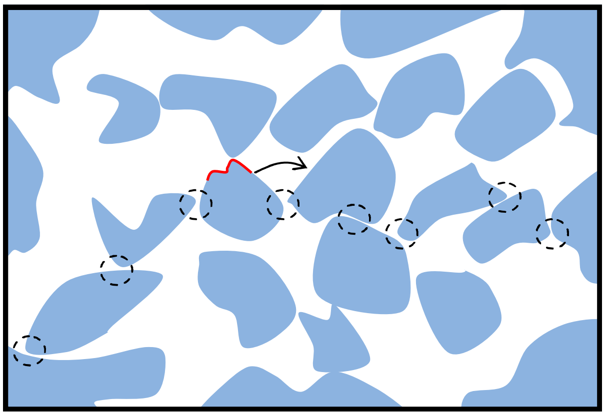

Figure 4.13. At very high temperatures when $L_{\varphi} < \xi_{p}$, an electron will be displaced through scattering before it is able to escape its cluster via a saddle point.

As the temperature or frequency is increased L_{φ} decreases but initially this will have no effect on dissipative conductivity (and as result ΔB) as long as the condition $L_{\varphi} > L_{2D}$ remains. ΔB therefore remains constant over this temperature/frequency range and this explains the saturated region at low values of temperature/frequency observed in many of the scaling results presented above. It should now be clear why the saturated region was attributed to finite-size effects.

Once $L_{\varphi} < L_{2D}$, conductivity will be influenced by scattering. In localized systems, scattering will aid conductivity by displacing electrons to clusters that would have been otherwise isolated and remote from the electron. Though quantum tunnelling remains dominate, conductivity no longer solely depends on the propagation of electrons along lengthy and interlinked networks of saddle points. Rather, electrons can be scattered to great distances in-between tunnelling events. The coexistence of tunnelling and scattering increases or enhances dissipative conductivity which will now increase with decreasing L_{φ}. ΔB in this regime therefore increases with temperature/frequency. This state of affairs is illustrated in the schematic of Fig. 4.12. It is important to note that QHTs in this regime are quantum critical according to the Chalker and Coddington criteria [61, 71, 169] since saddle point tunnelling is still present in the system. The critical exponent measured within this regime will therefore be $\nu \sim 2.35$ according to both scaling theory and the Chalker and Coddington quantum correction to classical percolation [71]. It is also noted that in this regime ξ is now limited by L_φ since an electron cannot be coherent beyond L_φ.

As L_φ is decreased further, the condition L_φ, $\xi < \xi_p$ will be reached. In other words, ξ will be smaller than the typical cluster size and on average an electron will be scattered before it is able to escape its cluster through a saddle point. Saddle point tunnelling will therefore cease to exist. This scenario is shown in Fig. 4.13. The absence of quantum tunnelling will reduce the system to a purely classical fluid in a random potential [162] exhibiting no quantum mechanically behaviour with respect to the percolation model. In this regime, quantum criticality is lost and the critical exponent measured for the range of temperatures/frequencies over which this condition exists will be that of the classical value of $\nu_p \sim 1.33$ [164].

The preceding analysis suggests that though quantum criticality exists in QHTs it can be hidden at high temperatures or frequencies where it is replaced by a classical critical transition. We therefore return to the long 2DES-CPW sample (investigated in Chapter 3) where the high resolution technique that was developed to measure the critical exponent may allow the experimental observation of this proposed crossover.

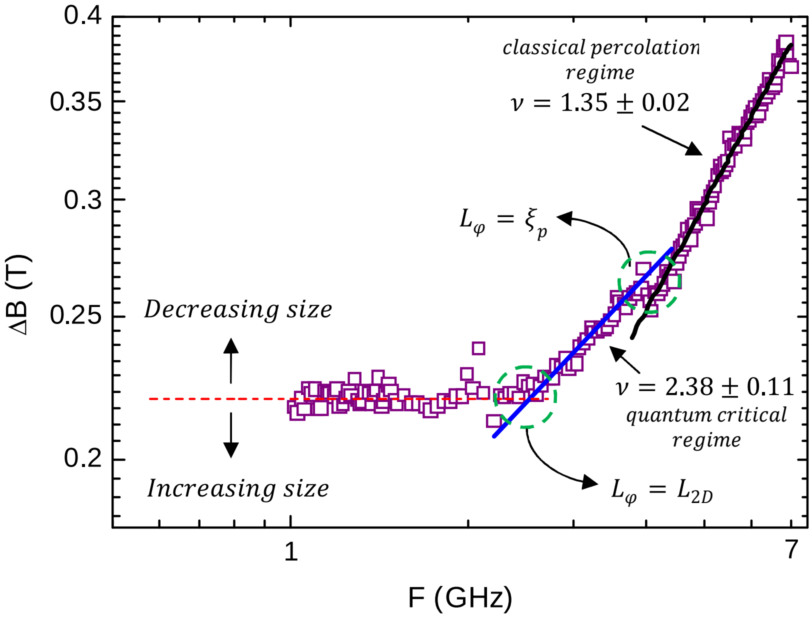

Figure 4.14. A high resolution frequency plot of the critical exponent reveals a quantum critical regime at lower frequency and a classical percolation regime at higher frequencies that correspond with their respective expected value of the critical exponent.

Since this transition is expected at low rather than higher frequencies, the frequency parameter is swept at a high resolution from the saturated region at $f = 0.1$ GHz to $f = 7$ GHz, which marks the onset of the first resonance feature (see Fig. 3.29(a)). The result from the determination of the critical exponent within this range and according to $\Delta B \sim f^{1/\nu}$ is shown in Fig. 4.14. Remarkable, varying L_φ at very small decrements reveals all three regimes discussed in the analysis above. The saturated regime, which has always been observed and attributed to the finite size of the sample L_{2D}, is found at lowest frequencies. As L_φ is gradually decreased, the $L_\varphi < L_{2D}$ regime in entered where the localization length exponent is determined to be $\nu = 2.38 \pm 0.11$ in accordance with quantum criticality. As L_φ is further decreased the classical regime, $L_\varphi < \xi_p$, is reached where exponent is measured as $\nu = 1.35 \pm 0.02$ and in good agreement with classical criticality.

The quantum critical regime therefore exists within the range $L_{2D} > L_{\varphi} > \xi_p$. Lack of consideration of the locations of the different regimes can lead the investigator to measure quantum criticality in the wrong region. In addition, not being able to distinguish between these regimes, which is very likely with a low resolution setup, will almost certainly cause one to fit a line across different regimes which should be considered separately. This perhaps explains why many reports, including some of the measurements presented in this thesis, fail to observe quantum criticality within 2DESs.

The chances of observing the quantum critical regime can be better enhanced by reaching the $L_{\varphi} = L_{2D}$ point sooner (in frequency) and/or delaying the arrival at the $L_{\varphi} = \xi_p$ point. In the case of the former, the duration (in frequency) of the saturated regime is determined by the size of the sample. A large sample size allows $L_{\varphi} = L_{2D}$ to occur at a much lower frequency, while a small sample size will push the $L_{\varphi} = L_{2D}$ point to a higher frequency, delaying the entrance into the quantum critical regime. As indicated by the annotations in Fig. 4.14, increasing the sample size lowers the saturation value of ΔB revealing more of the quantum critical regime whiles decreasing the sample size erodes the quantum critical regime. It is also obvious from Fig. 4.14 that at smaller sample sizes, L_{2D} becomes increasingly comparable to ξ_p such that quantum critical regime is barely observable. Though investigation on sample sizes have not been conducted in the work presented in this thesis, experimental investigations on the effect of sample size on conductivity have been reports by some authors [85, 87] where this correlation is very clearly observed verifying the present analysis.

In order to move the $L_\varphi = \xi_p$ point however, one needs to consider the influence of disorder within the system and this is discussed in the following section.

The crossover observed in Fig. 4.14 is the first such crossover ever reported in the literature for frequency scaling (published in Ref. [180]). A similar effect in the temperature dependence of QHT slope $d\rho_{xy}/dB$ however is suggested in a recent temperature dependent work by Li *et al*. [101].

4.4.2. Disorder dependent crossover

The impact of disorder on the nature of criticality presents yet another crossover. This is precisely the crossover observed in the combined results of Fig. 3.29 and Fig. 3.37 where by increasing the disorder within the system the nature of the critical exponent was changed from a classical like behaviour for a broad range of frequencies to a quantum critical behaviour for the same range of frequencies. Though the results presented in Chapter 3 describe a one-step change in disorder (see Table. 3.1), a more systematic investigation of disorder on criticality is presented in Ref [18] where the crossover is even clearer. Both results show that an increase disorder will bring about quantum criticality.

In terms of the percolation model, an increase in disorder, especially of the form introduced in the short-range 2DES-CPW, increases scattering within the vicinity of the 2DES. The introduction of static and randomly placed alloy impurities into the GaAs layer, within which the 2DES is formed, will increase large angle collision and it is intuitive that this will invariably produce clusters that are more fragmented.

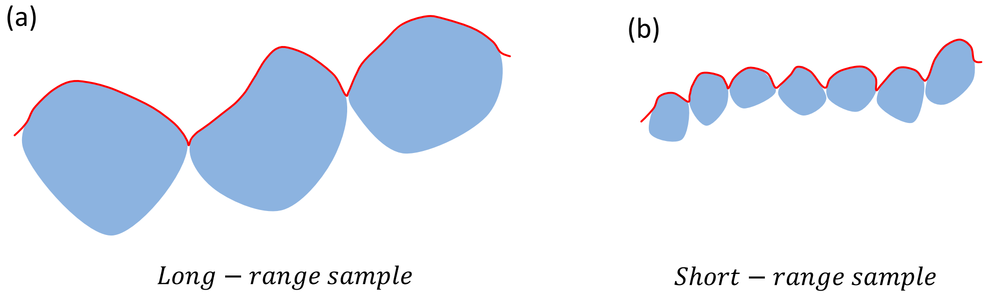

Figure 4.15. As L_φ decreases with increasing temperature or frequency, saddle point tunnelling will be cut of in the long-range sample before the short-range sample due to the comparatively different typical cluster sizes in the two types of samples.

As a result, clusters will be of smaller sizes than would otherwise occur if these large angle scattering events were not introduced. Increased disorder therefore means a decrease in ξ_p.

As discussed above, the elimination of saddle point tunnelling when $L_\varphi < \xi_p$ brings about classical criticality within a 2DES. A smaller value of ξ_p will therefore allow for a quantum critical regime to persist for a wider range of temperature/frequency than a large value of ξ_p. This is exactly the outcome observed in Chapter 3 where by increasing the disorder within a predominantly long-range system one arrives at system that appears to be quantum critical for a wide range of frequencies. Fig. 4.15 illustrates this effect showing two systems at the same temperature/frequency. As the temperature/frequency is increased, it is clear that the long-range system enters the $L_\varphi < \xi_p$ regime before the short-range system. The temperature/frequency will have to be significantly increased for L_φ to become smaller than ξ_p in the short-range system.

An increase in disorder in the plot shown in Fig. 4.14 can be explained as a significant movement of the $L_{\varphi} = \xi_p$ point to the left (towards higher frequencies). This explains the popular view that short-range systems such as InGaAs/InP systems in general are more suitable than long-range systems GaAs/AlGaAs system for the observation of quantum criticality [11, 82].

4.4.3. Field dependent crossover

In the discussion on the nature of criticality so far, we have only considered the scenario of a 2DES close to the percolation threshold. We now consider the nature of criticality as one moves away from critical point and into the tail regions of the LL band. In the classical view of percolation and according to $\xi_p \propto |E - E_c|^{-\nu_p}$, the typical cluster size decreases as the system moves away from the critical energy (see Fig. 4.1-4.3). At reduced cluster sizes, similar to the disorder argument presented above, quantum criticality will persist over a longer range of scaling parameter. A departure from the disorder argument however, is that there is a decrease in carrier density as the Fermi level moves away from the critical point, and as a result, there is a reduction in the availability of saddle points. This is illustrated in Fig. 4.1and Fig. 4.2, where it is noticed that the distance between adjacent clusters is greater in Fig. 4.1 than in Fig. 4.2, therefore saddle points are more likely to occur in the latter than the former. Nevertheless, an electron is still able to move from one side of the system to other, evident in the finite but vanishing amount of dissipative conductivity which exists in the tail regions of the LL band. This of course is possible due to variable range hopping (VRH) which is the dominant form of electron transport in this region (discussed in detail in section1.3.4 and 2.2.1).

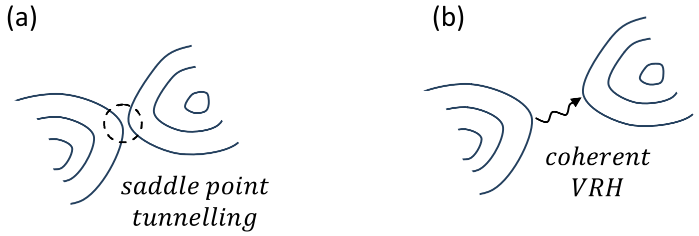

Figure 4.16. (a) Saddle point tunnelling close to the percolation threshold. (b) VRH becomes dominate as the Fermi energy moves away from the percolation threshold

Although the boundaries of electron clusters are increasing retreating from each other such that the occurrence of saddle points are increasingly rare, the increasing distance between the clusters is bridged by VRH (as shown in Fig. 4.16). VRH therefore, allows an electron to maintain coherence [181] beyond the borders of its cluster, similar to saddle point tunnelling. As discussed above, this is the requirement ($L_{\varphi} > \xi_p$) for the observation quantum critically, i.e. $\nu \sim 2.3$. For any value of $|E - E_c|$ however, at a high enough temperature/frequency the condition $L_{\varphi} > \xi_p$ can be broken, such that an electron is no longer able to quantum coherently escape its cluster. Beyond this point, VRH is destroyed and quantum transport is replaced by a classic activated-like transport. The transition between classical and quantum transport within the tail regions of the LL is discussed in detail by Shimshoni [181].

Owing to the fact that cluster sizes are smaller in the tail region of the LL than close to the centre, and the maintenance of the quantum critical condition of $L_{\varphi} > \xi_p$ through VRH, the quantum critical exponent is more easily observed in measurement taken within the tail regions of the LL than close to the centre. In other words, for any given temperature or frequency range, the condition $L_{\varphi} > \xi_p$, is more easily broken closer to the centre of the LL than further away since cluster size are large closer to the centre of the LL.

This explains the temperature dependent scaling results in Chapter 2 where within the same sample ν was consistently found to be universal at $\nu \sim 2.3$ when determined in the tail regions of the LL but non-universal and closer to the classical value when determined through κ which is dependent on electron transport close to the centre of the LL.

This crossover between the classical percolation and quantum criticality is illustrated in Fig. 4.17. The dashed lines in the figure denote the quantum-classical crossover in criticality. The vertical axis represents a decreasing L_{φ} with increasing temperature of frequency. The schematic shows that quantum criticality persists at all fields within the 2DES. At any finite field however, a sufficiently high temperature or frequency will cause the system to transition into a classic system which will yield classical characteristics for criticality. The extent to which this crossover is achieved depends on how far the system is from the critical point. Close to the critical point the crossover occurs at relatively low temperatures or frequencies, and far from the critical point the crossover occurs at relatively high temperatures or frequencies due to the dependence of clusters size on $|B - B_c|$.

The diagram present in Fig. 4.17 is a direct product of the results presented here on the dependencies of criticality and has not been derived from any previous work. However, independently a similar schematic has been predicted by Kapitulnik *et al*. [182] to explain superconductor-to-insulator transitions (SITs). In considering these SITs Kapitulnik *et al*. employs a percolation framework to explain the critical behaviour within these systems.

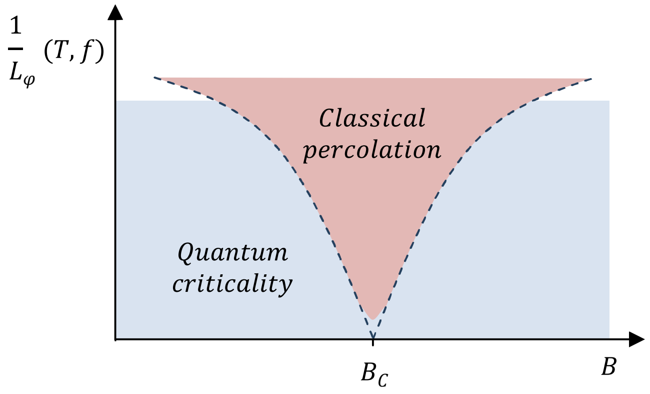

Figure 4.17. A representation of classical and quantum criticality with respect to $|B - B_c|$ and L_φ. Moving across the dashed line represents a crossover between the two regimes.

An adopted feature from this work in Fig. 4.17 regards the nature of criticality at the critical point B_c. Kapitulnik *et al*. argues that at a low enough temperature, any classical percolation approach must break down and therefore at very low temperatures a system at B_c is quantum critical and not classical and this is illustrated in Fig,. 4.17. The similarities between the Kapitulnik *et al*. result and that presented here is not surprising since unifying models bases on the percolation method have been developed [183] that successfully incorporated QHTs, classical percolation, superconductivity and metal-to-insulator transitions into a framework where each of the classes mentioned above represent different but related phases of a 2DES.

4.5. Implications of the quantum percolation model on scaling theory

From the percolation model of QHTs and the criticality of these transitions described above, we return to the finite-size scaling view of phase transition and suggest an interpretation based on the percolation analysis. We also discuss the implication of these results on the limits of the scaling theory regarding the QHE.

4.5.1. Finite-size scaling interpretation of the percolation result

Second order quantum phase transitions and how they relate to critical universal singularities were discussed in sections 1.3.2 and 3.1.1. In section 1.3.2 it was discussed that as the 2DES moves from the localized region and into the extended region a phase transition occurs. This phase transition is indicated by the divergence of an order parameter as the critical point between the two phases is approached. The order parameter, which represents the length over which the system maintains correlation, was identified in QHTs to be the localization length, $\xi \propto |E - E_c|^{-\nu}$ [6]. In the percolation model this corresponds to the typical size of the clusters or ξ_p since this is the length that defines the explorerable region of the electron, i.e., electrons are localized within ξ_p such that they are unaware of their environment beyond ξ_p. The cluster within which an electron finds itself therefore defines the extent of order experienced by the electron. The exception to this however concerns electrons that exist at the outmost edges of clusters. Electrons occupying these outmost equipotential states are able to explorer the system beyond individual clusters through saddle point tunnelling. According to Thouless [48], an electron must travel a distance comparable to its localization length before it can be influenced by localization effects simply because unless it has travelled such a distance, an electron cannot be aware of its localization. Relaxation mechanisms that occur on a length scale less than ξ_p therefore destroy localization. The outermost wavefunctions of electrons clusters therefore provide a measure of whether localization has been destroyed or not, and this indication is given through saddle point tunnelling. In so far as saddle point tunnelling persists, the coherence length of electron wavefunctions throughout the entire system (not just at the edge) must be larger than ξ_p and therefore even though a few carriers at edges of cluster are extended through saddle point tunnelling, majority of electrons are localized. In other words, the majority of electrons within the system will travel distances sufficient enough for localization effects to be felt. Under these conditions the critical phenomena as described by finite-size scaling of QHTs is valid. The absence of saddle point tunnelling however marks the point where all electrons within the system are unable to travel distances comparable to their cluster sizes and as a result, localization as required by finite-size scaling is destroyed.

In terms of the theory of critical phenomena, this can be understood as follows. In section 3.1.1 the concept of dynamic scaling was introduced where critical phenomena was described not just as a divergence of the spatial order but also a divergence of the temporal order. In other words, correlation must diverge both in space and in time. If correlation is space refers to ξ_p, correlation in time refers to the coherence time τ_φ or, as used above, the correlation length L_φ. It is only in the case of simultaneous divergence in both these parameters that criticality as defined by finite-size scaling (quantum criticality) applies [6, 9]. In the case of QHTs, L_φ must be equal to or greater than ξ_p as the critical point the centre of the LL is approached. This condition is easily met at low temperatures or frequencies where $L_\varphi > \xi_p$, however at higher temperatures or frequencies this condition is invalid therefore quantum criticality is lost. In short, for quantum criticality as defined by finite-size scaling to be experimentally observed, L_φ must stay head of ξ_p every step of the way as the critical point is approached to satisfy the condition of a simultaneous divergence in time and space.

According to this analysis the exact nature of the divergence of L_φ does not matter as long as $L_\varphi > \xi_p$, this may suggest a reason why criticality appears not to depend on the temperature scaling exponent p in the results presented in Chapter 2 and explain the fortuitous but incorrect assumption of $p = 2$ (see results on current scaling in section 2.4). We recall from the current scaling results in Chapter 2 that p depended on disorder or mobility. The relation between κ and ν may therefore simply the relation $\kappa = 1/\nu$, rather than $\kappa = p/2\nu$ with $p = 2$, where $L_\varphi \propto T^{-p/2}$.

The discussion above highlights the difficulties in the experimental observation of quantum criticality. Experimentally, inquiries of the critical nature of QHTs can only be made by varying L_φ. As has been presented in this thesis, this can be achieved using a number of phase breaking mechanisms (temperature, frequency or current scaling). In each case it is realised that the experimental range of the phase breaking mechanism may or may not vary L_φ across the crossover point discussed above. If the experimental range chosen is at very low temperatures or frequencies it is clear that there is a greater chance that L_φ will be varied within the quantum critical regime, ie, in the regime where $L_\varphi > \xi_p$. The value of the critical exponent determined within this experimental range will be expected to be in agreement with the quantum critical value of $\nu \approx 2.35$. On the other hand if the experimental range chosen is too high in temperature or frequency, it likely that the regime probed will be the classical percolation regime ($L_\varphi < \xi_p$) and the value of the critical exponents determined from such investigations will be closer to that of the classical value of criticality of $\nu \approx 1.35$ [164].

Investigations in criticality are further complicated if a low resolution of the varying scaling parameter (temperature or frequency) is used. In this case it is possible to go through the crossover point without experimentally observing it due to the low density of data points. One could erroneously fit a linear line across the two regimes such that the value of the critical exponent determined will be between the quantum and classical values, i.e. $1.35 < \nu < 2.35$. Without explicitly observing the crossover point, an experimental investigation of the critical nature of QHTs runs the risk of misinterpreting the value of the critical exponent. This is likely to be the reason why there are numerous inconsistencies and disputes between previous measurements of scaling exponent especially since most of these investigations have been low resolution temperature based measurements.

It is noted that the crossover observed in Fig. 4.14 was only possible due to the high resolution in the variation of the frequency parameter used and if one were reduce the density of data point in the plot the crossover point will be indistinguishable. It is therefore possible that the data present in Chapter 2 (Table 2.3 and Fig. 2.12) contains both the classical and quantum regimes but due to lack of resolution in data, the crossover point cannot be observed. This explains why the values in Table 2.3 are mostly found between $0.74 < \kappa < 0.42$, i.e. $1.35 < \nu < 2.35$ given that $\kappa = 1/\nu$.

4.5.2. The scaling limit of QHTs

We now discuss the possible limits of the scaling theory, this is directly linked to the persistence of the QHE since the scaling theory of the QHTs can be view as a shift from a quantum system towards a classical system in the high temperature or frequency limit.

In the work presented here the scaling theory has been verified for a temperature range up to about 1 K while frequency dependent scaling has been observed up to 30 GHz (see Fig. 3.23). The QHE itself has been experimentally observed at frequency as high as 35 GHz [140]. Temperature measurement of the QHE in a typical GaAs/AlGaAs systems on the other hand is only robust up to a few kelvin or the boiling point of liquid He [184]. It is clear that investigations on scaling provided a way to study the evolution from the quantum behaviour to the classical behaviour of 2DESs at high fields. It is simpler to discuss this in terms of the scaling of the slope between plateau-to-plateau transitions $d\rho_{xy}/dB \propto T^{-\kappa}$ rather than $\Delta B \propto T^{\kappa}$. We recall that the transition slope possess a similar scaling relationship and behaviour to that of the width of the LL peak (see section 1.4.3) with the exception of the critical scaling exponent possessing a negative sign. The advantage of considering $d\rho_{xy}/dB$ is that the classical limit of any sample can be obtained from the carrier concentration of the 2DES. In the classical Hall effect, which occurs at very high temperatures, ρ_{xy} is absent of plateaux and is simply a linear dependence in magnetic field with gradient $d\rho_{xy}/dB = 1/en_{2D}$. At the other extreme at very low temperatures, we have seen that scaling theory can be described using the percolation model. The two extremes are put together in Fig. 4.18. Due to the finite-size of any sample measured, a saturated regime is expected at the lowest temperatures. As the temperature is increased, the system enters into the quantum critical regime and then crosses over into the classical percolation regime. At the highest temperatures, which is the domain of the classical Hall effect, $d\rho_{xy}/dB$ is constant and independent of temperature. In between these two known areas is an unknown and unexplored region illustrated in Fig. 4.18.

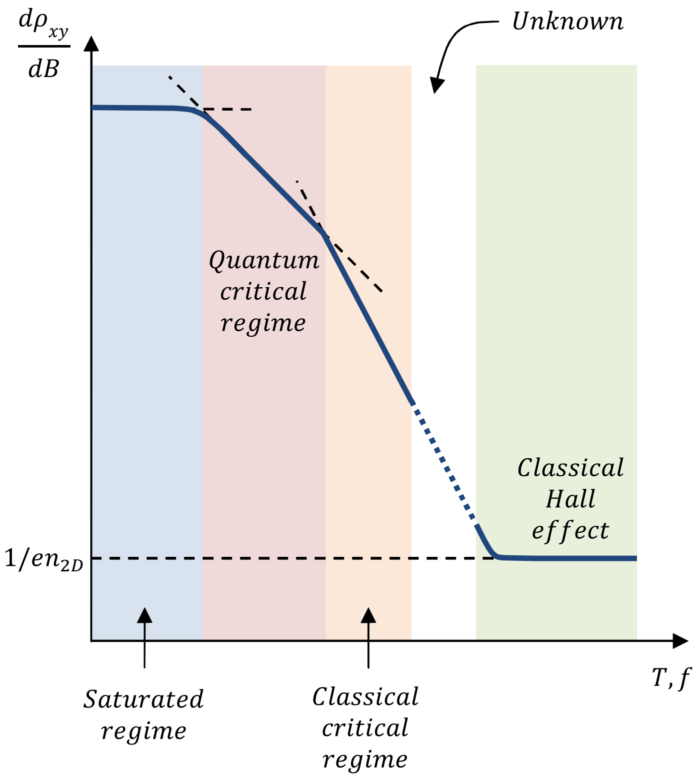

Figure 4.18. An illustrative plot combining all experimentally observable regions of the QHE determined from the results of the scaling of QHTs. The final evolution of the curve towards the classical Hall effect is still unknown.

It is unclear if the classical percolation regime extended all the way to the classical Hall regime or whether there exists any intermediate regimes. It of course makes no difference whether it is the temperature or the frequency that is being varied, therefore the same analysis can be applied to frequency scaling. A recent publication by Ikebe *et al.* [135] has reported observations of plateaux at terahertz frequencies using a Faraday rotation technique [185] to measure the Hall component of conductivity. This report provokes a few questions. The experiment performed is not at finite-frequency but rather the 2DES is probed by a band of frequencies with a terahertz bandwidth. Apart from the mention of the experiment being conducted in the terahertz regime the exact bandwidth is not stated. Though the nature of scaling is unclear when a 2DES is probed simultaneously by a band of frequencies, it is reasonable to assume that the highest frequency will determine L_{φ}. Given that the characteristics of the GaAs/AlGaAs sample used in the Ikebe *et al.* investigation ($n_{2D} = 2.7 \times 10^{11}\mathrm{cm}^{-2}$, $\mu = 1.4 \times 10^{5}\mathrm{cm}^{2}/\mathrm{Vs}$) are comparable to those reported on here, it is seems unlikely that the classical Hall limit will not be reached before the terahertz regime. At terahertz frequencies (just as at room temperatures) localization should be completely destroyed. The most conservative extrapolation of scaling results present in Chapter 3 suggests that all oscillations would be flattened out before the terahertz regime is reached, which is of two orders of magnitudes higher than the frequencies reported in Chapter 3.

The next chapter is devoted to investigating the final evolution of the scaling of QHTs towards the classical Hall regime. In order to shed light on the unexplored region shown in Fig. 4.18, scaling is attempted within the millimetre wave ranges covering a frequency range between 75 GHz and 150 GHz. The millimetre wave regime is precisely the region that sits between the gigahertz regime reported in Chapter 3 and the terahertz regime.

4.6. Conclusion

In this chapter, we have formulated the scaling problem in terms of a percolation model that seems to explain several observations made on the scaling of QHTs. We first discussed the microscopic view of a 2DES under a strong magnetic field and linked it to a classical percolation effect. The Chalker-Coddington quantum correction [71] was introduced to account for quantum effects.

The use of percolation-like models in describing the QHTs were among the earliest to be used to explain the phenomenon [54, 164, 165, 186-190] and has gained significant consideration since the development of the much celebrated Chalker-Coddington model. It has since been heavy supported by numerous experimental reports (see references in section 4.3.2). Though this work provides a qualitative description based on insights from the Chalker-Coddington model, many numerical [61, 74, 169, 183, 191, 192] and analytical works [193] exist in support of the model. The description presented here has focused on providing an understanding of experimental observations which hitherto have not been coherently explained.

Using the various crossover descriptions we have been able to answer the questions posed in the introduction. The key insight gained is that quantum criticality depends on the maintenance of the localization effect and this is only the case if an electron is able to coherently travel a distance greater than or comparable to the dimensions of its confinement. It is only then that an electron can experience the effects of localization. Relaxation mechanisms on length scales short than the cluster size will destroy localization.

A summary of this chapter has been published as Ref. [180].

5. Millimetre wave interaction of two-dimensional electron systems

5.1. Introduction

In this chapter an attempt is made to investigate QHTs in the millimetre wave frequency regime. In previous results presented in this thesis, scaling of QHTs was shown to exist at frequencies up to at least 30 GHz through the broadening of LL conductivity peak (see Fig. 3.23). This work (Chapter 3) constitutes the largest bandwidth over which QHTs have been studied. Single frequency measurements of the QHE however have been carried at 35 GHz [140], this stands as the highest frequency at which the QHE has been observed. Though the evidence of the QHE at terahertz frequencies was recently report [135], the theory following from the percolation model provided above strongly suggests that this is unlikely in a typical GaAs/GaAs heterostructure, in fact, the extrapolation of the data provided in this thesis does not support any quantum behaviour at frequencies close to or within the terahertz region. The compelling diagram presented in Fig. 4.18 shows that at sufficiently high frequencies (or temperature) the classical Hall regime should be established. The region between the upper microwave frequencies and moving towards the classical Hall regime however is completely unexplored by any previous experimental work and this is the region this chapter seeks to investigate.

The 2DES will be excited by frequencies between 75 GHz and 110 GHz. Unlike the guided wave setup used in Chapter 4, a free space system is adopted here. Using parabolic mirrors, the generated high frequency radiation was focus onto 2DES samples while is under a magnetic field and in a cryogenic environment. The frequency dependent response of the 2DES was collected and then detected using a superheterodyne detection technique.

5.2. Device and experimental technique

The device used in the millimetre wave measurements and the experimental setup is discussed below.

5.2.1. Device and sample characteristics

The devices used in following investigation consists of GaAs/AlGaAs samples with an etched 11 mm by 11 mm mesa and eight ohmic contacts distributed along the edges of the mesa (a schematic of the devices is shown in Fig. 5.1). The mesa is formed from chemically etching of the sample to a depth of about 200 nm and the Ohmic contacts, which are formed from a Au/Ge/Ni alloy, are processed in the usual way (see section 2.1.1 for further processing details). As with the 2DES-CPW device, the Ohmic contacts allow for the d.c. characterisation of the sample. The transmission nature of the free space setup only requires a clear and large surface area containing the 2DES on which the high frequency radiation can be focused. Similar to considerations made in the design of the 2DES-CPW device, the excitations of a large area of the 2DES should provide greater sensitivity and increased signal-to-noise ratio.

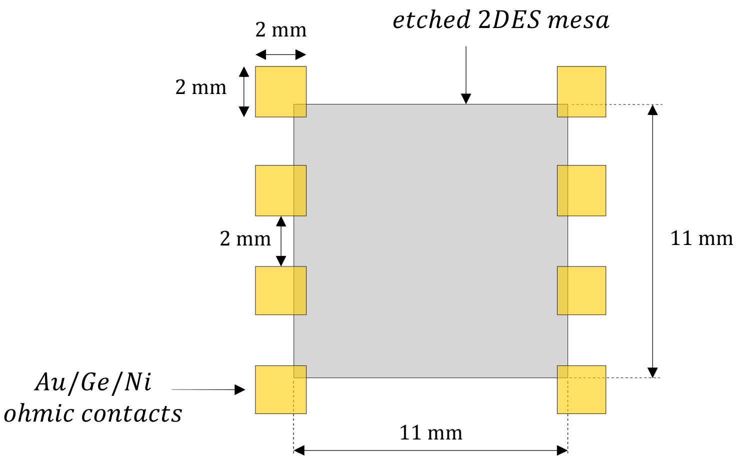

Figure 5.1. Diagram of devices used in millimetre wave experiment.

The size of the 2DES mesa is therefore chosen (11 mm x 11 mm) to maximize the excitable area of the 2DES given the minimum beam width of the focused radiation.

The sample used is characterized by a dark carrier concentration of $n = 2.26 \times 10^{11}$ cm^2 and mobility of $\mu = 1.01 \times 10^5$ cm^{2}V^{-1}s^{-1} determined at a temperature of 1.2 K. A d.c. plot of ρ_{xx} and ρ_{xy} measured using the Ohmic contacts is shown in Fig. 5.2.

5.2.2. Experimental setup

The 2DESs were inserted into an optical access cryostat with a base temperature of 1.2 K, and with a split-pair magnet allowing a magnetic field perpendicular to the sample to be applied. The transmission setup consisted of a millimetre wave source which generated a signal with a frequency between 75 GHz and 110 GHz.

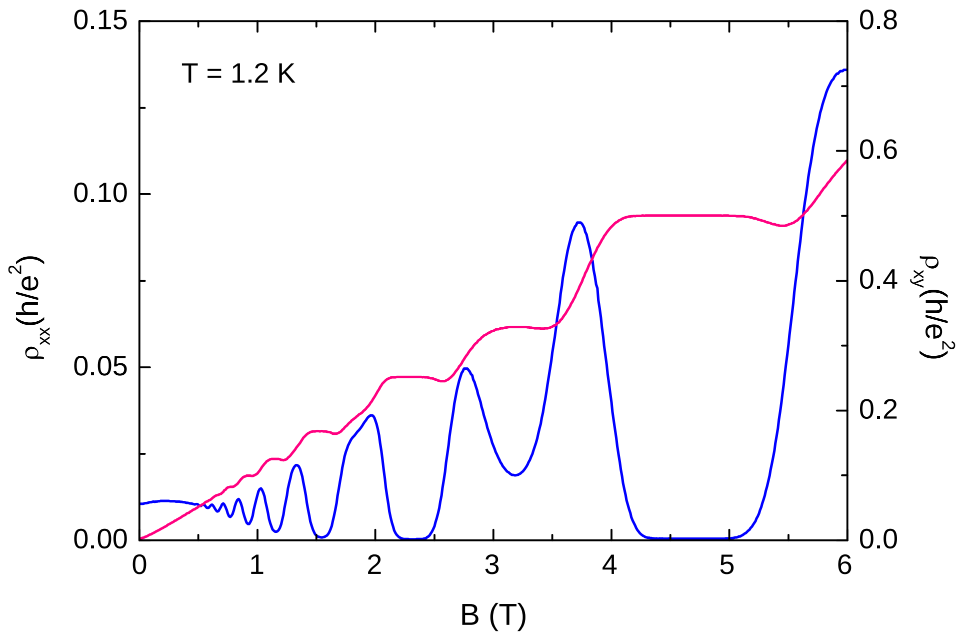

Figure 5.2. D.c. magnetotransport characteristics of millimetre wave sample taken at 1.2 K.

The path of the generated signal is directed by parabolic mirrors which focuses the signal on to the surface of the 2DES through an optical widow of the cryostat. The millimetre wave radiation then interacts with the 2DES as it is transmitted through the sample. The signal transmitted through the 2DES then exits the cryostat through another optical window and is directed into a receiver. A schematic of the setup is shown in Fig. 5.3.

The signal generation unit is made up of a MMW extender which is essentially a signal multiplier which multiplies the input signal by a factor of 6. The MMW extender is only operable within the range 75 GHz – 110 GHz.

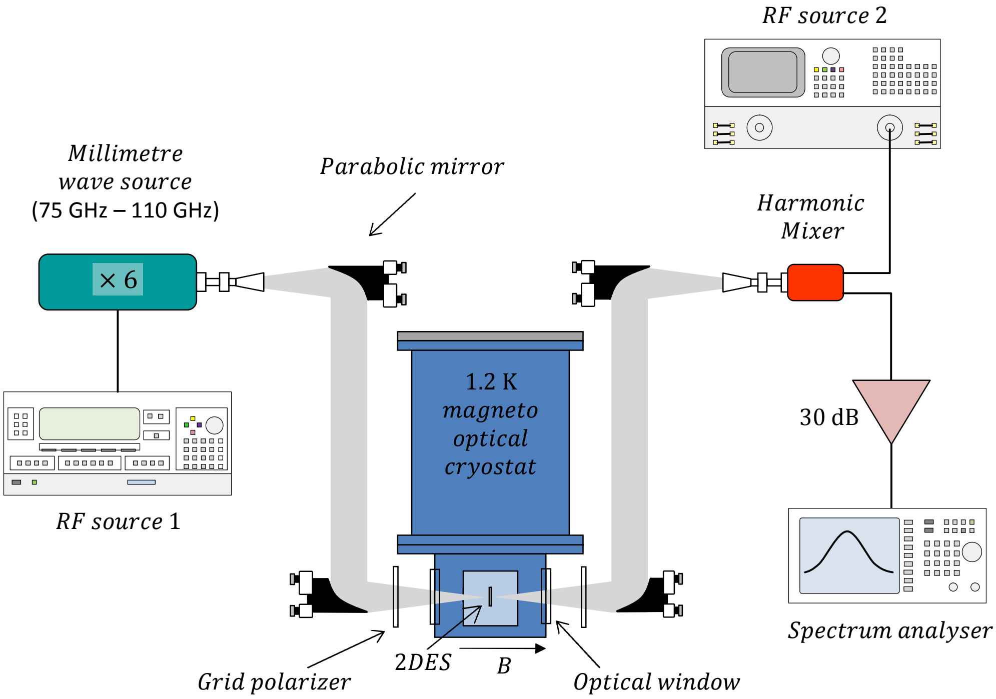

Figure 5.3. A schematic of the experimental setup showing the cryostat within which the sample is inserted, the signal generating unit and the signal detection unit.

The input to the MMW extender is supplied by an RF (radio frequency) source capable of generating frequencies within the required range of 12.5 GHz and 18.33 GHz (to access the operable bandwidth of the MMW source). Attached to the output of MMW extender is a horn antenna which emits the RF signal into free space.

The detection unit of the RF setup consisted of a harmonic mixer, an RF source, a 30 dB amplifier and a spectrum analyser. The harmonic mixer, which also operates within the range 75 GHz – 110 GHz, takes in two inputs, the MMW RF signal (from the output of the 2DES) and an RF source also known as the local oscillator or LO. The mixer produces a single output known as the intermediate frequency or IF. The aim of the detection unit is to receive and measure a signal that is within the MMW band.

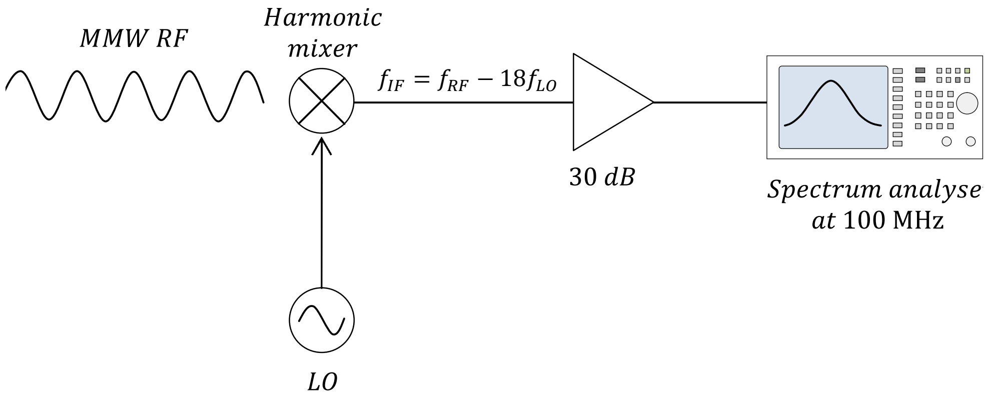

Figure 5.4. A schematic of the detection unit. The incoming MMW signal is downconverted by the mixer to an intermediate signal of lower frequency that can be easily measured by the spectrum analyser.

This is not a straightforward task since most spectrum analysers used in measuring RF signals operate up to a few gigahertz, and in particular, the spectrum analyser used in this setup is able to measure frequencies up to 3 GHz. The detection unit therefore uses a superheterodyne technique which downconverts the received MMW signal to 100 MHz, a frequency easily measured by the spectrum analyser. The mixer also contains a harmonic generator which produces harmonics of the LO. The mixer used in the setup is designed to select the 18th harmonic which is then mixer with the incoming MMW RF signal. The output signal of this frequency multiplication consists of the sum $f_{RF} + 18f_{LO}$ and the difference $f_{RF} - 18f_{LO}$. The frequency of the local oscillator can therefore be chosen such that the difference component of the output results in the desired intermediate frequency, $f_{IF} = f_{RF} - 18f_{LO}$. For the frequency band under consideration, the local oscillator was only required to be tuneable between approximately 4.2 GHz and 6.1 GHz. Due to the weak MMW RF signal received and the conversion loss of the mixer, the IF signal is amplified by a 30 dB amplifier and then sent to the spectrum analyser which is tuned to detect an IF signal at 100 MHz. The process is illustrated in Fig. 5.4.

The significant quantity of interest in the measurement setup is the magnitude of the received signal as measured by the spectrum analyser. At a certain MMW frequency, a magnitude measurement of the received signal can be taken at each magnetic field point to produce a magnetotransport measurement, and much like that presented in Chapter 3, the magnitude measured can then be related to the conductivity of the 2DES [134, 194].

Finally it is noted that the sample and the transmission path is shielded from unwanted external radiation and signal reflections through the use of anechoic absorbers. The widows of cryostat are also cover with black tape that is transparent to the MMW signal but opaque to visible light.

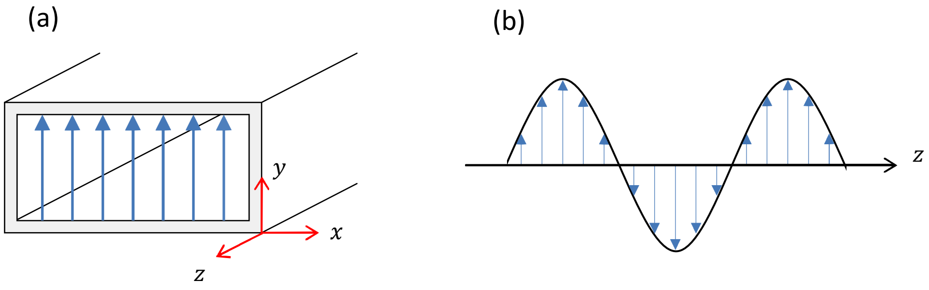

Figure 5.5. (a) An illustration of the TE_{10} mode in a rectangular waveguide where the direction of the electric field (represented by the arrows) is perpendicular to the direction of propagation, z. (b) A time varying view of the electromagnetic wave propagating along the z axis.

5.3. Transmission of an electromagnetic wave through a 2DES

The transmission configuration discussed in the experimental setup above is known as the Faraday geometry or configuration. This configuration is characterised by a transmission setup where the direction of the propagating electromagnetic wave is parallel to the magnetic field.

On the millimetre wave source, the emitting horn antenna is attached to a rectangular waveguide (see Fig. 5.3). The mode of propagation of the emitted electromagnetic wave is therefore a transverse electric TE_{10} mode [137]. In a TE mode, the electric field is perpendicular to the direction of propagation $E_z = 0$. The electric field pattern of a TE_{10} mode is illustrated in Fig. 5.5. As seen from Fig. 5.5(a), the TE_{10} mode excites an electric field in the direction of the shorter dimension of the rectangular waveguide while there is zero excitation in the direction of the longer dimension.

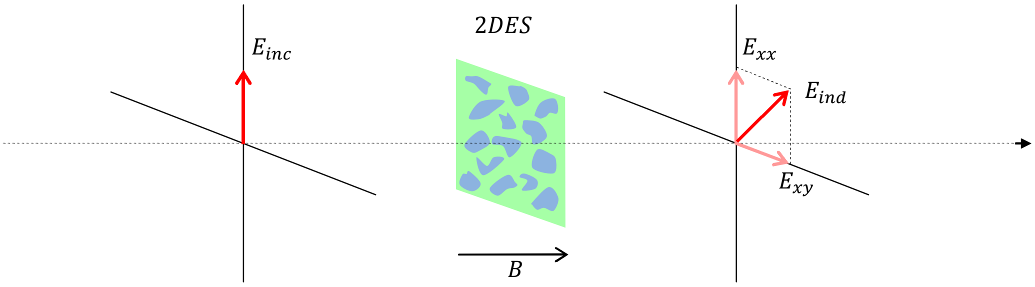

Figure 5.6. The incident electric E_{inc} excites electron transport within the 2DES under a magnetic field which in turn induces an electric field E_{ind}. The induced field is made up of electron transport due to diagonal conductivity along the incident electric field and Hall conductivity perpendicular to the incident field.

The wave emitted from the waveguide is transmitted through space and onto the surface of the 2DES. The electromagnetic wave incident on the surface of the 2DES induces electron transport in 2DES and in the presence of a magnetic field this produces Hall and diagonal conductivities within the system [195]. The propagation of an electromagnetic wave through a plasma of free carriers in the presence of a magnetic field has already been extensively studied [195, 196]. It can be shown that the electric field of the induced electric field corresponds to σ_{xx} and σ_{xy}, and is proportional to the intensity of the transmitted wave [195, 197]. Fig. 5.6 illustrates the transmission process. The incident electric field E_{inc} induces an electric field E_{ind} which contains the diagonal component of conductivity E_{xx} and Hall the component E_{xy} [134, 197].

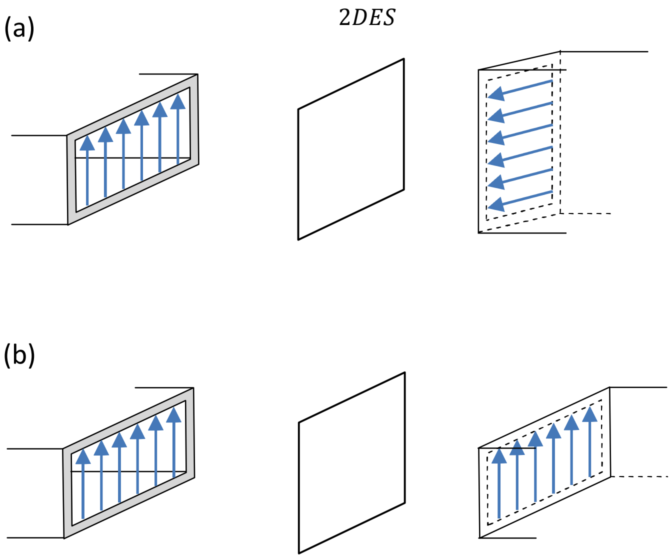

Figure 5.7. (a) An illustration of a crossed waveguide configuration which selects the Hall component of the induced wave. (b) A configuration that selects the diagonal conductivity component of the induced electric field.

The component of interest can be selected by considering the orientation of the receiving waveguide attached the detection unit (the harmonic mixer). A crossed waveguide configuration, shown in Fig. 5.7(a), will pick up the Hall component of the transmitted wave. As was previously mentioned, the mode permitted in a rectangular waveguide only allows electric fields varying along the shorter dimension of the waveguide therefore in the crossed configuration the diagonal conductivity component of the transmitted wave will be rejected while the Hall component is allowed to propagate. Likewise in Fig. 5.7(b), the Hall component will be rejected while the diagonal component is selected for transmission. This method of excitation and detection was first used by Kuchar *et al*. [134, 197] who employed this technique in measuring microwave induced conductivity in a 2DES.

The amplitude of the received wave is precisely measured by a spectrum analyser using the heterodyne detection technique described in the previous sections. It is therefore expected that the magnetic field dependence of the amplitude of the received wave will follow the outline of the magneto-transport QHE if it present in the 2DES.

5.4. Millimetre wave experimental results

We discuss results obtained from the millimetre wave setup below. Just as in Chapter 3, we focus on measuring the σ_{xx} and set the orientation of the receiving waveguide accordingly (as described in Fig. 5.7(b)). It should be noted that the measurements present below only investigate the QHE for a few frequencies spread across the accessible range of frequencies. Unlike Chapter 3, these measurements do not present a high resolution investigation. There are many difficulties in preserving the integrity of a free space system with a cryostat (undisturbed) for days at a time as required for such high resolution measurements (such as those presented in Chapter 3).

In obtaining the measurements, the magnetic field is initial set to the desired point, and a queued series of finite millimetre wave signals then transmitted through the free space system, via the cryostat, one at a time. The power of the transmitted signal is then measured at the receiver. The magnetic field is adjusted by a small increment and the process repeated for the next field point.

To begin, a reference of the magnetic field dependence of the transmitted signal and the free space setup is taken. In these reference measurements, the setup is just as described in Fig. 5.3 but without the 2DES sample in the cryostat.

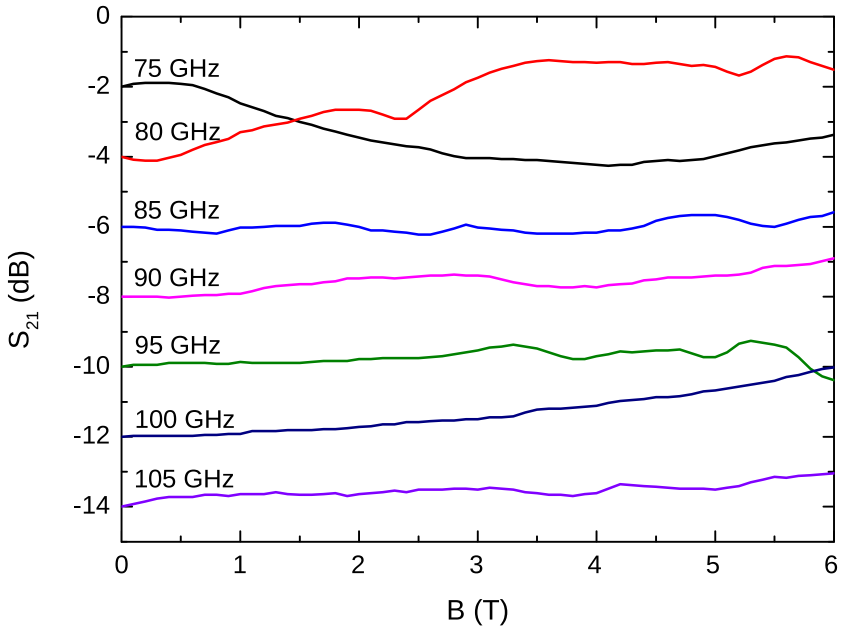

Figure 5.8. Reference measurements of the magnetic field dependence of the transmitted signal at various frequencies. These measurements are taken in the absence of a 2DES in path of the transmitted signal. The measurements have been offset in the y-axis for clarity.

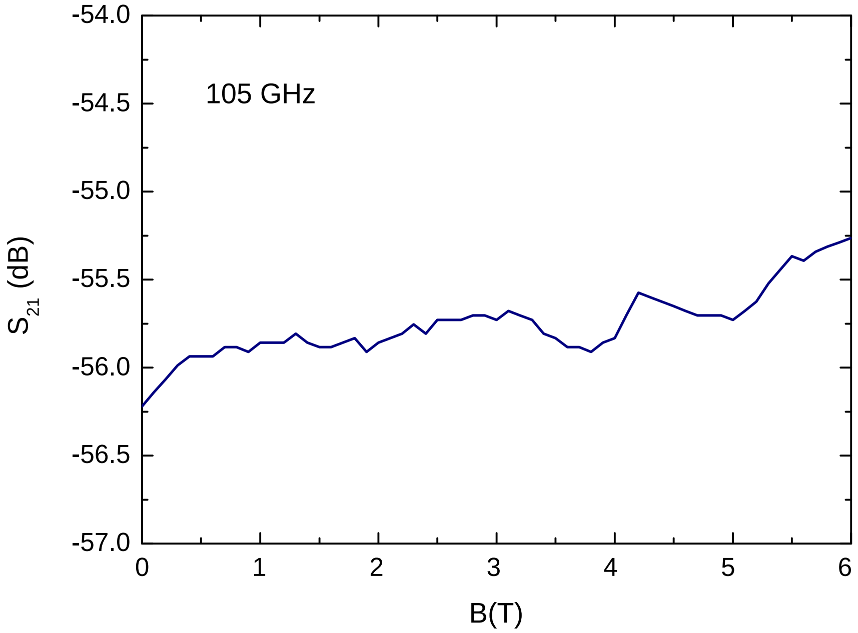

Figure 5.9. The field dependent reference measurement at 105 GHz.

Ideally, one would expect a constant dependence of the signal with magnetic field in the absence of the 2DES. The reference signal also provides information about the background noise at various frequencies. Fig. 5.8 shows the signal measured by the receiver at various frequencies within the investigated bandwidth. The plots have been offset on the y-axis to clearly and independent show the field dependence of each frequency, however, Fig. 5.9 shows the data of one of the frequencies. The noise floor of the system was determined to be ~100 dB. Any change in the signal above this level is easily detected by the setup. We also note that it is the relative change in power of the received signal as the magnetic field is swept that is of interest here and not the absolute value. The reference measurements for all frequencies investigate were well above the noise floor.

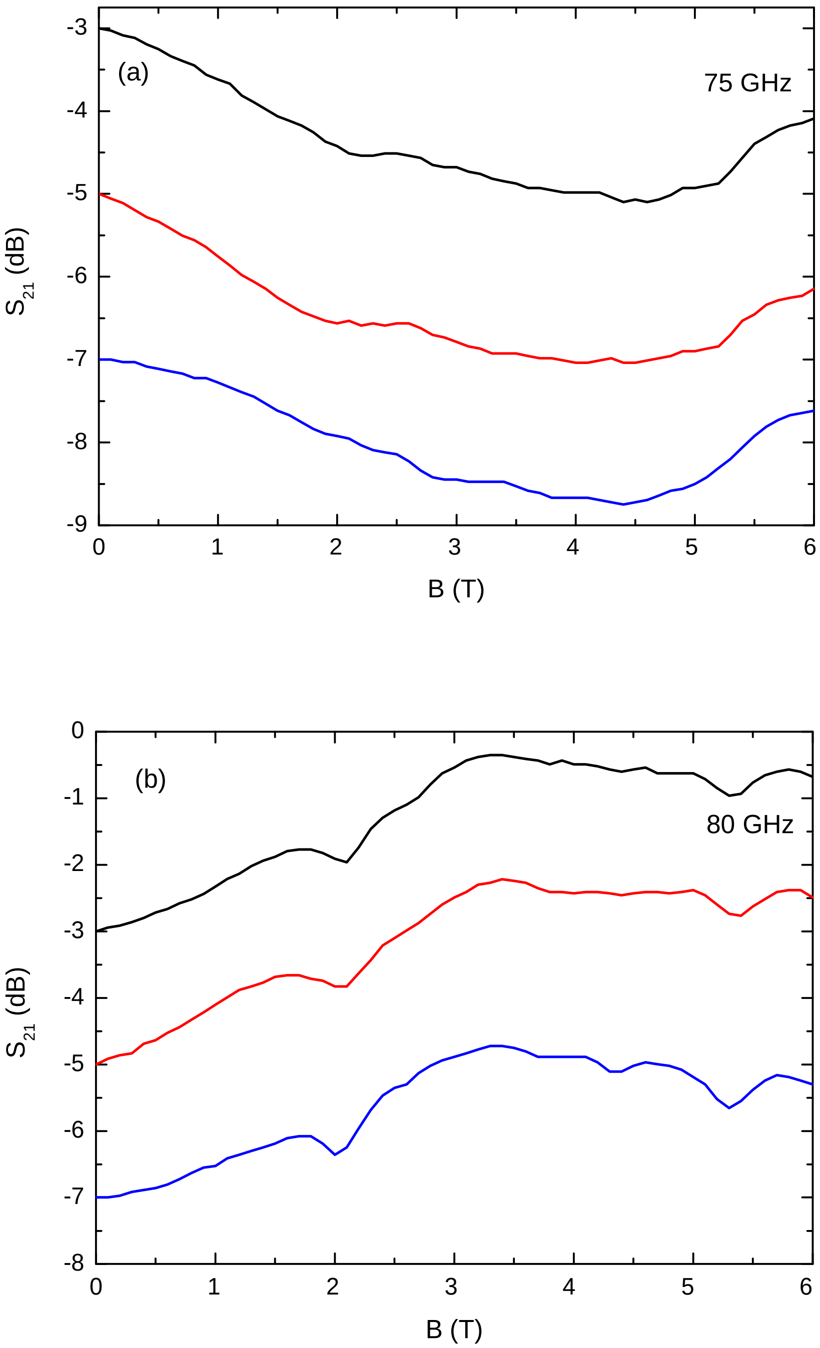

Figure 5.10. Two plots showing the repeatability of the magnetic noise for (a) 75 GHz and (b) 90 GHz. Measurements are taken at three different sweeps of the magnetic field. Every sweep shows the same features in the reference measurement.

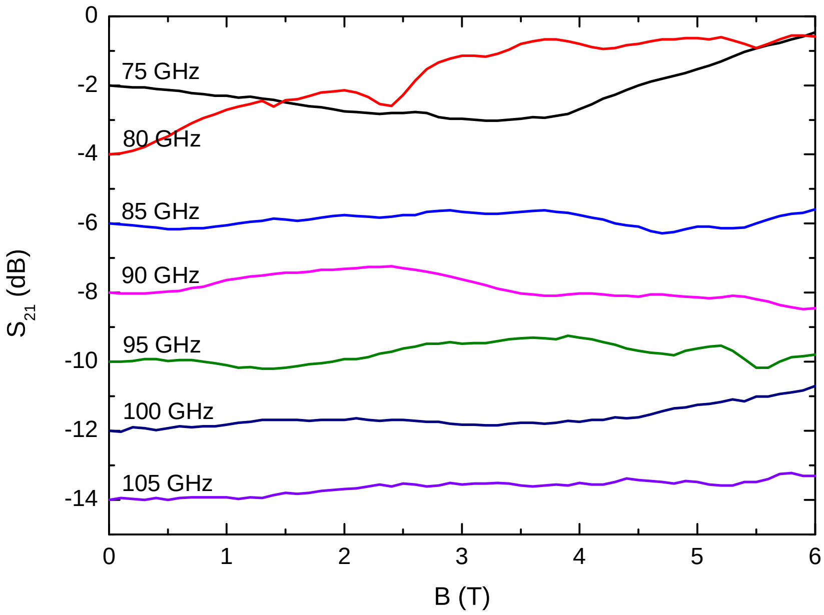

Figure 5.11. Fields dependent measurements of the transmitted signal with a 2DES at room temperature in its path.

From Fig. 5.8 and 5.9, one notices that the transmitted signal is fairly constant for most frequencies but some frequencies exhibit some amount of “magnetic” noise. The origin of this field dependent noise stems from the very slight mechanical movements of the parabolic mirrors used in the setup. These mirrors unfortunate contain tiny springs, used for positional adjustment, that appear to be influenced by stray magnetic fields from the cryostat. These springs cannot be done away with without great difficulty and sacrifice to signal strength. However, the magnetic noise is repeatable and can therefore be subtracted or accounted for. The effect of the noise on results is therefore greatly reduced (less than 0.5 dB). Fig. 5.10 shows the repeatability of the noise for two of the worst affected frequencies, where three separate measurements show the same features. It is noted that the features change when the parabolic mirrors are mechanical disturbed (for example, unscrewing and re-screwing them), confirming that these features are a consequence of the effect of a strong magnetic field on the parabolic mirrors. For a consistent set of measurements, the setup remains untouched once fitted.

Another set of measurements are taken with the sample inserted into the cryostat and in the path of the transmitted signal but 2DES is kept at room temperature. The results are shown in Fig. 5.11. It is observed that the plots are similar to that those shown in Fi.g 5.8 where there was no 2DES. This verifies that the 2DES is not active at room temperatures.

As the temperature is cooled however, the effect of the QHE should be significant in the field dependent measurements if localization has not been destroyed at millimetre wave frequencies. Since σ_{xx} is being probed in this setup, if the QHE is present, one should notice oscillation in the transmitted signal that correspond to the location of the LL peaks seen in Fig. 5.2 (as was observed in Chapter 3 for microwave frequencies).

Fig. 5.12 shows the results obtain at 1.2 K. Fig. 5.12(a) shows the field dependent measurement at 90 GHz. The signal absorption due to the cyclotron resonance of the 2DES is observed in the plot. For a frequency f, the resonance is expected at the field $B = 2\pi f m^*/e$, where m^* is the effect mass of an electron in GaAs and e is the charge of an electron. At 90 GHz, the cyclotron resonance should occur at $B = 0.215\text{T}$ when the effect mass is taken to be $m^* = 0.067m_0$. This is good agreement with Fig. 5.12(a). It should be noted however that the magnetic field is swept at intervals of 0.05 T and therefore the location of the absorption can only be accurate to within this value. The measurements for other frequencies are shown in Fig. 5.12(b) where the cyclotron resonance is observed for all frequencies.

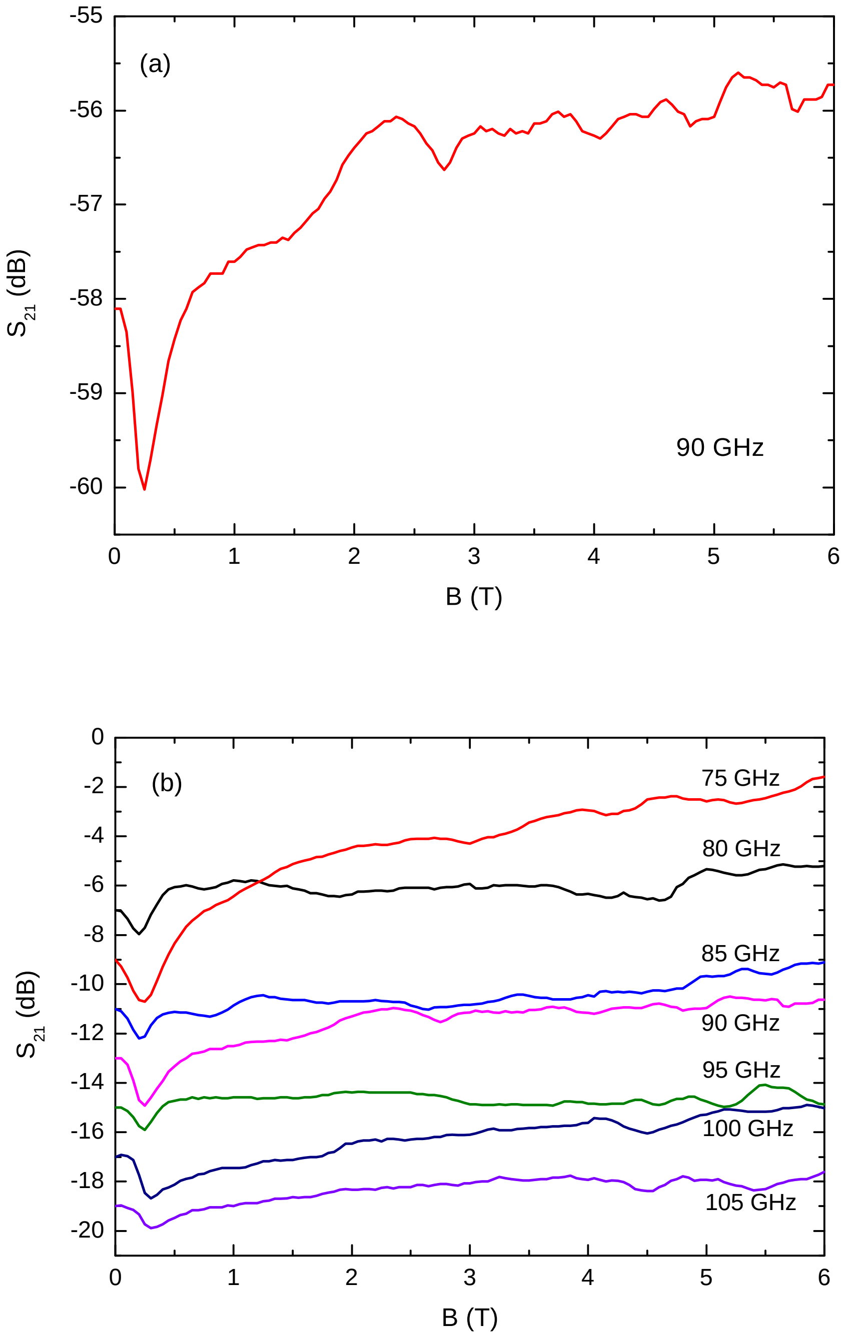

Figure 5.12. Measurements of the transmitted signal taken at 1.2 K for (a) 90 GHz and (b) the frequency range investigated. A cyclotron absorption dip can be observed at all frequencies but there is no observed evidence of the QHE, even at high magnetic fields.

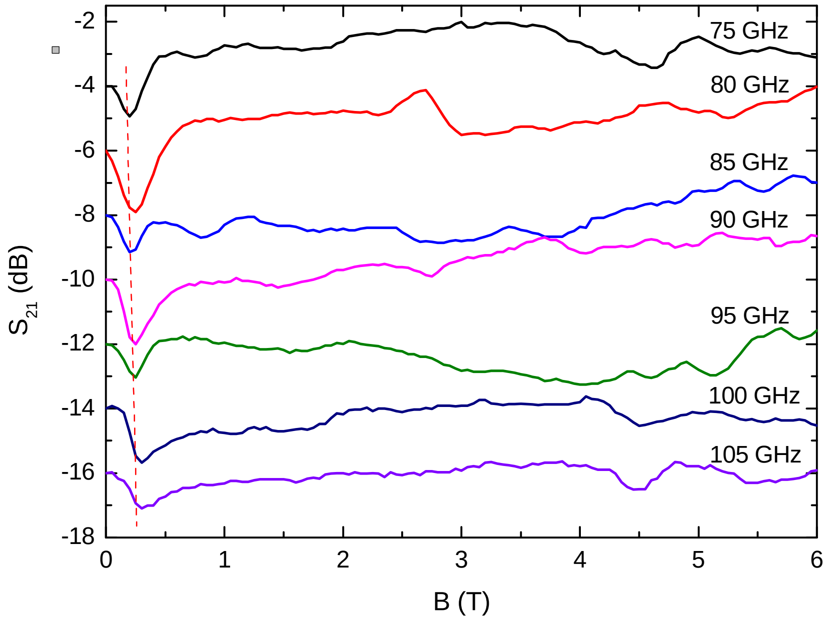

Figure 5.13. The field dependence of the transmitted signal after the background and mechanical noise has been subtracted. The dashed line should the expected location of the cyclotron resonance abortion. There is still no evidence of the QHE in these measurements.

The observation of the cyclotron resonance provides evidence of the interaction of the 2DES with the probing signal and confirms that the system is sensitive enough to detect magnetic field dependent quantum effects within the 2DES. Crucially, however, there is no evidence of any features of the QHE, even at very high fields. Fig. 5.13 shows the results obtained when the background and mechanical noise have been subtracted from the measurements taken. The dashed line in Fig. 5.13 denotes the expected location of the cyclotron absorption dips in the transmitted signal. It is estimated that sensitivity of the system is within about 0.5 dB or ~10% of the power loss. Even so, the results clearly show that the system is sensitive enough to observe the cyclotron resonance. The lack of any QHE features therefore confirms the discussion on the limit of the scaling theory of the QHE discussed in section 4.5.2. At millimetre wave frequencies and above, one expects localization to be completely destroyed and thus one does not expect to observe any feature of the QHE.

Finally, the effect of an increase in carrier concentration is presented in Fig. 5.14, where two measurements are taken, one under illumination and the other in the dark. The increase in carrier concentration has no effect on the observation of the feature of the QHE at high fields but we observe greater absorption of the transmitted signal by the cyclotron resonance of the 2DES due to an increased number of electrons interacting with the transmitted signal.

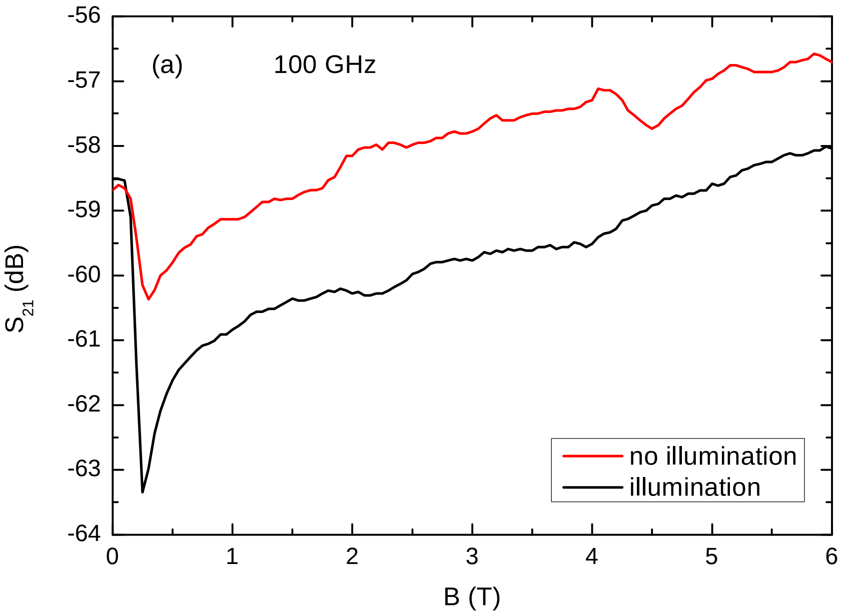

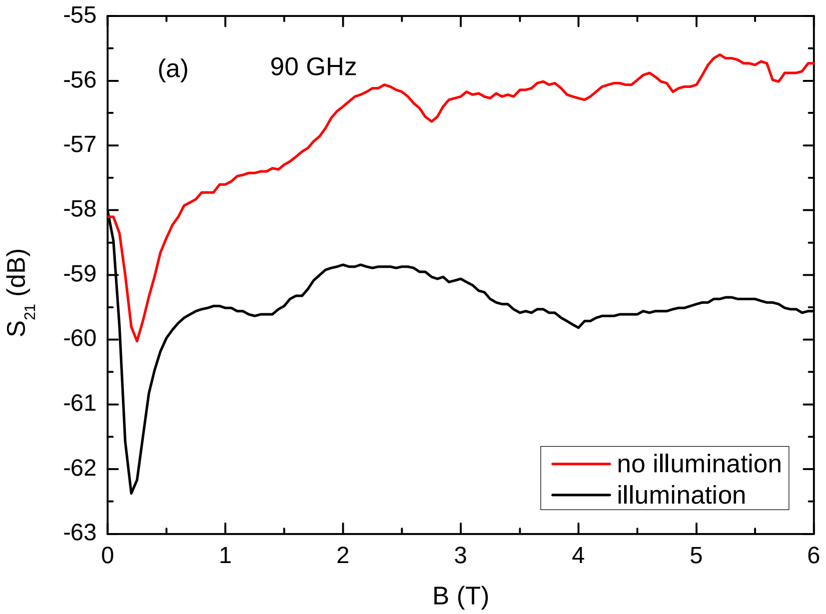

Figure 5.14. Measurements of the transmitted signal taken under illumination and in the dark at two frequencies.

5.5. Discussion and conclusion

In this chapter we have investigated the existence of the QHE at millimetre wave frequencies where a free space setup was used to probe the 2DES. Through a series of measurements, interaction between the 2DES and the transmitted electromagnetic signal is observed. The QHE, on the other hand, is not observed within the measurements taken. This strongly suggests that the QHE cannot be maintained at millimetre wave frequency just as one would expect a breakdown of the QHE at room temperature. Any possible observation of the QHE at terahertz frequencies, as suggested by some studies [135], is therefore unlikely. The results presented in Chapter 3 measures the QHE up to 30 GHz. It is observed from this data (shown in Fig. 3.32) that as the frequency of interaction increases, the broadening of LL peaks worsens. This is due to the increased scattering rate implied by a reducing phase coherence length as the frequency is increased (see sections 1.4.3 and 3.1.1). The increased scattering rate smears out the well-defined energy levels or LLs that exist at $T, f = 0$, reverting transport within the 2DES to that observed in the classical Hall effect. The limit of the QHE was also probed by Kuchar *et al*. [134, 197] where at 33 GHz it was also clear that the QHE could not survive an increase in frequency of an order of magnitude.

All three investigates discussed in this section, Chapter 4 (up to 30 GHz), Kuchar *et al*. [134, 197] (33 GHz) and Ikebe *et al.* [135] (terahertz regime), used GaAs/AlGaAs heterostructures samples of comparable characteristics. Even though the probing method is slightly different in each of these three cases, the underlining physic should produce the same (consistent) result in these investigate. The study of the scaling of QHTs discussed in previous chapters, as a by-product, have made easier to understand the limits of the QHE. The most transparent analysis lies in the scaling theory of the slope of plateau-to-plateau transitions (of the Hall resistance) presented in section 4.5.2. Scaling can be observed in the gradual decreasing of the slope plateau-to-plateau transitions as the temperature or frequency is increased. In this analysis, two limits or extremes are evident; the absolute zero temperature limit and the classical limit. The absolute zero temperature limit produces a transition slope with a gradient tending to infinity (for systems of very large sizes). On the other hand, we know that in the classical limit (where no quantum phenomena can be maintained) the slope is simply the gradient of classical Hall resistance which has the precise value of $1/en_{2D}$. As one increases the temperature or the frequency of the applied electric field, the gradient of the slope gradually changes from infinity to $1/en_{2D}$, where at $1/en_{2D}$ the classical limit, at room temperature for example, is reached. This process is determined by the scattering mechanism being controlled by the temperature or frequency. Therefore if one wish to observe the QHE at higher and higher temperatures and frequencies, one has to produce samples with a lower $1/en_{2D}$ value, in other words, one has to increase the carrier concentration. Consequently, according to the scaling analysis, increasing the carrier concentration will push the classical limit to higher temperature or frequencies. This seemingly simple remedy however produces a challenging experimental difficulty. At higher carrier concentrations, the LLs of the QHE are pushed to higher magnetic fields since an increase in n_{2D} increase the energy spacing between LLs or the cyclotron gap $\hbar\omega$. These higher field LLs can only be reached at great (technological) expense. Another challenge is faced when one realises that the carrier concentrations required for the QHE to be observed at higher temperatures or frequencies is beyond the single subband capacity of a typical GaAs heterostructure.

These two difficulties were solved in a recent investigation [198] where the QHE was observed at room temperature and at the extraordinarily high field of 45 T using a graphene sample. Graphene devices allow for very high carrier concentrations within a single subband. The high magnetic field on the other hand was achieved using a 45 T hybrid magnet.

In practical terms, the analysis of the scaling theory of QHTs reveals what one must do in order to experimentally observe the QHE effect, and this requires the manipulation of the magnetic field and the carrier concentration. In theory however, the process of scaling, discussed throughout this thesis, is simply the varying of the phase coherence length or the scattering parameter. If the energy separation between LLs can be sufficiently increased, then a higher activation energy will be required to scatter electrons from one LL band to other and therefore at greater energy gaps these discrete quantum states can be distinguishable and maintained at room temperature. The energy separation is achieved through the magnetic field and the carrier concentration since the degeneracy of each LL is field dependent. It is also noted that a large electron lifetime (in other words, a high mobility) produces narrower disorder broadening of LLs and therefore assists in distinguishing between adjacent LLs at high temperatures.

The conclusion of the above analysis is that is a typical GaAs heterostructure, the required energy separation cannot be achieved at room temperatures or frequencies at or beyond the millimetre wave regime, without the aid of very high fields and carrier concentration. Therefore for the typical samples used here (and the other investigation referred to above), one would not expect to observed the QHE in the millimetre wave or terahertz regime.

6. Summary and conclusion

This thesis investigates the nature of the critical phenomena associated with QHTs which occur between plateau-to-plateau transitions in the QHE in 2DESs. Theoretically, it has been suggested that these QHTs, which are expected to be quantum phase transitions, exhibits certain universal behaviours that can be observed by investigating the charge transport of 2DESs.

Previous experimental studies of on the nature and universality of QHTs have produced results that are both contradictory to the expected theoretical behaviour and inconsistent among experimental results. At the heart of the dispute is the universality of the critical exponents associated with QHTs, which according to critical phenomena theory, should be universal constants which are independent of the specific microscopic details of the 2DES under investigation.

This thesis independently investigates all three proposed critical exponents, ν, κ, and p, in order to reveal the nature of their universality. The critical exponents are suggested to be related through the relation $\kappa = p/2\nu$. The exponents are studied using a finite-size scaling analysis.

In Chapter 2, using experimental techniques based on the variation of various temperatures associated with the 2DES, it is observed that the exponents ν is universal within all samples studied, however, the exponents κ and p were not found to be universal across all sample investigated. The value of κ tended to be higher than expected and the exponent p exhibited dependence on the mobility of the sample, the opposite of the nature of universality which is precisely the independence of critical exponents on the microscopic details of the 2DES. An argument is present in Chapter 2 to support the disorder dependence of p which is unsurprising if one considers the dephasing mechanisms within the 2DES.

In Chapter 3, a high resolution frequency based technique is used to further the investigations in the critical nature of QHTs. In this chapter, the scaling analysis is studies by varying the frequency of the applied electric field driving electron transport within the 2DES. In addition, the influence of disorder on the nature of QHTs is studied. It has previously been suggested that by increasing the disorder within a 2DES the nature of criticality approaches the expected universal behaviour. This was confirmed by the results presented in this chapter. It was found that increasing the disorder within the 2DES yields a universal exponent while a less disordered system produces a critical value inconsistent with theoretical predictions.

In Chapter 4, the vast collection of results including the peculiar features observed in the results present in the two preceding chapters are explained using an intuitive and transparent quantum percolation model which had previously been used in explain certain features attributed to the QHE in 2DESs. This chapter attempts to explain why the exponent ν is consistently measured to be universal within the tail regions a LL band but the measured value of κ within the same sample and LL does not exhibit the universal behaviour. It also explains the reason and nature of the influence of disorder on the nature of criticality. It explains the dependence of p on disorder and finally it also suggests why the observation of the quantum criticality, as expected by theoretical predictions, is so difficult to observe experimentally. Underpinning these explanations is the competition between three key length scales, the localization length ξ, the typical cluster size of electrons within a 2DES ξ_p and the phase coherence length L_φ. Crossovers between these length scales define transitions between the universal and the non-universal behaviour of QHTs in 2DESs. Varying the temperature or frequency of the applied electric field of the 2DES changes L_{φ}. The expected universal quantum critical behaviour persists as long as $L_{\varphi} > \xi_{p}$, on the other hand a classical critical behaviour is observed when $L_{\varphi} < \xi_{p}$. Mistakes in the experimental observation of the universal (quantum critical) behaviour occur when the investigator does not consider the distinction between these two regimes.

An interesting question arises from the analysis of the scaling theory of QHTs. What defines the limit of the observation of the QHE and how high in frequency (or temperature) can the QHE be observed? This is investigated in Chapter 5 using a millimetre wave free space transmission setup (between 75 GHz to 110 GHz). Just as in temperature, one anticipates the existence an upper limit to the frequency at which the QHE can be observed but a recent result suggested that the QHE can be observed within the terahertz regime (0.3 to 3 THz). The millimetre wave results however did not find any evidence of the QHE at such high frequencies. It is suggested that at such high frequencies the separation between LLs are smeared out (as expected for high temperatures).

The work presented in this thesis deals with some novel areas not previous investigated in scaling theory of QHTs. These investigations are the first to independently study all scaling exponents related to QHTs in a single work and on the same sample. Though such a study is required in order to coherently explain the disagreements between scaling exponents, it had hitherto not be investigated.

The result on the frequency based measurements presented here is the largest bandwidth of frequencies over which the scaling theory has been observed and investigated (between 100 MHz and 30 GHz).

The high resolution of the results present in Chapter 3 is also the most detailed work published in literature, with a resolution of an order of magnitude higher than the next detailed investigation.

The investigation of a short-range disordered system using a high frequency electromagnetic wave is the first ever presented in the literature.

The experimental observation of the frequency dependent crossover in criticality in a 2DES presented in Chapter 4 is first to be published in the literature.

And finally, the results in Chapter 5 are the first attempts to probe the millimetre wave regime for the observation of the QHE.

References

[1] E. Hall, On a new action of the magnet on electric currents, American Journal of Mathematics, 2 (1879) 287-292.

[2] K.v. Klitzing, G. Dorda, M. Pepper, New Method for High-Accuracy Determination of the Fine-Structure Constant Based on Quantized Hall Resistance, Physical Review Letters, 45 (1980) 494-497.

[3] R.B. Laughlin, Quantized Hall conductivity in two dimensions, Physical Review B, 23 (1981) 5632.

[4] H. Aoki, T. Ando, Effect of localization on the hall conductivity in the two-dimensional system in strong magnetic fields, Solid State Commun., 38 (1981) 1079.

[5] B.I. Halperin, Quantized Hall conductance, current-carrying edge states, and the existence of extended states in a two-dimensional disordered potential, Physical Review B, 25 (1982) 2185.

[6] S.L. Sondhi, S.M. Girvin, J.P. Carini, D. Shahar, Continuous quantum phase transitions, Reviews of Modern Physics, 69 (1997) 315.

[7] M.E. Fisher, The theory of equilibrium critical phenomena, Reports on Progress in Physics, 30 (1967) 615.

[8] B.I. Halperin, P.C. Hohenberg, Scaling Laws for Dynamic Critical Phenomena, Physical Review, 177 (1969) 952-971.

[9] P.C. Hohenberg, B.I. Halperin, Theory of dynamic critical phenomena, Reviews of Modern Physics, 49 (1977) 435-479.

[10] P. Heller, Experimental investigations of critical phenomena, Reports on Progress in Physics, 30 (1967) 731.

[11] B. Huckestein, Scaling theory of the integer quantum Hall effect, Reviews of Modern Physics, 67 (1995) 357.

[12] H.P. Wei, D.C. Tsui, M.A. Paalanen, A.M.M. Pruisken, Experiments on Delocalization and University in the Integral Quantum Hall Effect, Physical Review Letters, 61 (1988) 1294.

[13] L.W. Engel, D. Shahar, Ç. Kurdak, D.C. Tsui, Microwave frequency dependence of integer quantum Hall effect: Evidence for finite-frequency scaling, Physical Review Letters, 71 (1993) 2638.

[14] H.P. Wei, L.W. Engel, D.C. Tsui, Current scaling in the integer quantum Hall effect, Physical Review B, 50 (1994) 14609.

[15] S. Koch, R.J. Haug, K.v. Klitzing, K. Ploog, Experiments on scaling in Al_{x}Ga_{1-x}As/GaAs heterostructures under quantum Hall conditions, Physical Review B, 43 (1991) 6828.

[16] N.Q. Balaban, U. Meirav, I. Bar-Joseph, Absence of Scaling in the Integer Quantum Hall Effect, Physical Review Letters, 81 (1998) 4967.

[17] S. Koch, R.J. Haug, K.v. Klitzing, K. Ploog, Experimental studies of the localization transition in the quantum Hall regime, Physical Review B, 46 (1992) 1596.

[18] W. Li, G.A. Csathy, D.C. Tsui, L.N. Pfeiffer, K.W. West, Scaling and Universality of Integer Quantum Hall Plateau-to-Plateau Transitions, Physical Review Letters, 94 (2005) 206807.

[19] W. Shockley, G.L. Pearson, Modulation of Conductance of Thin Films of Semi-Conductors by Surface Charges, Physical Review, 74 (1948) 232-233.

[20] T. Ando, A.B. Fowler, F. Stern, Electronic properties of two-dimensional systems, Reviews of Modern Physics, 54 (1982) 437.

[21] F.F. Fang, A.B. Fowler, A. Hartstein, Effective mass and collision time of (100) Si surface electrons, Physical Review B, 16 (1977) 4446-4454.

[22] F. Stern, W.E. Howard, Properties of Semiconductor Surface Inversion Layers in the Electric Quantum Limit, Physical Review, 163 (1967) 816-835.

[23] H.L. Stormer, R. Dingle, A.C. Gossard, W. Wiegmann, Inst. Conf. Ser. London, 43 (1978).

[24] D.G. Schlom, L.N. Pfeiffer, Oxide electronics: Upward mobility rocks!, Nature materials, 9 (2010) 881-883.

[25] L.N. Pfeiffer, The road to carrier mobilities at 100M, EP2DS-19 Conf., Tallahassee, Florida, USA, (2011).

[26] J.P. Harrang, R.J. Higgins, R.K. Goodall, P.R. Jay, M. Laviron, P. Delescluse, Quantum and classical mobility determination of the dominant scattering mechanism in the two-dimensional electron gas of an AlGaAs/GaAs heterojunction, Physical Review B, 32 (1985) 8126-8135.

[27] C. Kittel, Introduction to solid state physics, Wiley, New York, (1996).

[28] O. Madelung, Introduction to solid-state theory, Springer, 1995.

[29] P.W. Anderson, Absence of diffusion in certain random lattices, Physical Review, 109 (1958) 1492-1505.

[30] B. Kramer, A. MacKinnon, Localization: theory and experiment, Reports on Progress in Physics, 56 (1993) 1469.

[31] N.F. Mott, Electrons in disordered structures, Advances in Physics, 16 (1967) 49.

[32] M.H. Cohen, H. Fritzsche, S.R. Ovshinsky, Simple Band Model for Amorphous Semiconducting Alloys, Physical Review Letters, 22 (1969) 1065.

[33] N.F. Mott, E.A. Davis, Electronic processes in non-crystalline materials, Clarendon Press Oxford, 1971.

[34] N.F. Mott, Metal-Insulator Transition, Reviews of Modern Physics, 40 (1968) 677.

[35] P. Drude, Zur Elektronentheorie der Metalle, Annalen der Physik, 306 (1900) 566-613.

[36] B. Shklovskii, A. Efros, Electronic properties of doped semiconductors, Moscow Izdatel Nauka, (1979).

[37] A.F. Ioffe, A.R. Regel, Prog. Semicond., 4 (1960) 237.

[38] N.F. Mott, Electronics and Structural Properties of Amorphous Semiconductors, edited by P. G. Le Comber and J. Mort (Academic, London), (1973) p. 1.

[39] A. Miller, E. Abrahams, Impurity Conduction at Low Concentrations, Physical Review, 120 (1960) 745-755.

[40] V. Ambegaokar, B.I. Halperin, J.S. Langer, Hopping Conductivity in Disordered Systems, Physical Review B, 4 (1971) 2612.

[41] E.N. Economou, M.H. Cohen, Existence of Mobility Edges in Anderson's Model for Random Lattices, Physical Review B, 5 (1972) 2931.

[42] N.F. Mott, Conduction in glasses containing transition metal ions, Journal of Non-Crystalline Solids, 1 (1968) 1-17.

[43] G.J. Dolan, D.D. Osheroff, Nonmetallic Conduction in Thin Metal Films at Low Temperatures, Physical Review Letters, 43 (1979) 721-724.

[44] P.A. Lee, A.D. Stone, H. Fukuyama, Universal conductance fluctuations in metals: Effects of finite temperature, interactions, and magnetic field, Physical Review B, 35 (1987) 1039-1070.

[45] S.V. Kravchenko, G.V. Kravchenko, J.E. Furneaux, V.M. Pudalov, M. D'Iorio, Possible metal-insulator transition at B=0 in two dimensions, Physical Review B, 50 (1994) 8039-8042.

[46] E. Abrahams, P.W. Anderson, D.C. Licciardello, T.V. Ramakrishnan, Scaling Theory of Localization: Absence of Quantum Diffusion in Two Dimensions, Physical Review Letters, 42 (1979) 673.

[47] D. Thouless, Electrons in disordered systems and the theory of localization, Physics Reports, 13 (1974) 93-142.

[48] D.J. Thouless, Maximum Metallic Resistance in Thin Wires, Physical Review Letters, 39 (1977) 1167.

[49] P.W. Anderson, P.A. Lee, The Thouless Conjecture for a One-Dimensional Chain, Progress of Theoretical Physics Supplement, 69 (1980) 212.

[50] P.A. Lee, T.V. Ramakrishnan, Disordered electronic systems, Reviews of Modern Physics, 57 (1985) 287-337.

[51] N. Mott, W. Twose, The theory of impurity conduction, Advances in Physics, 10 (1961) 107-163.

[52] T. Ando, Y. Matsumoto, Y. Uemura, Theory of Hall effect in a two-dimensional electron system, Journal of the Physical Society of Japan, 39 (1975) 279-288.

[53] S.V. Iordansky, On the conductivity of two dimensional electrons in a strong magnetic field, Solid State Communications, 43 (1982) 1-3.

[54] R.E. Prange, R. Joynt, Conduction in a strong field in two dimensions: The quantum Hall effect, Physical Review B, 25 (1982) 2943.

[55] Y. Huo, R.N. Bhatt, Current carrying states in the lowest Landau level, Physical Review Letters, 68 (1992) 1375.

[56] B. Huckestein, B. Kramer, One-parameter scaling in the lowest Landau band: Precise determination of the critical behavior of the localization length, Physical Review Letters, 64 (1990) 1437.

[57] H. Aoki, T. Ando, Critical localization in two-dimensional Landau quantization, Physical Review Letters, 54 (1985) 831.

[58] T. Ando, H. Aoki, Finite-size scaling study of localization in Landau levels, Journal of the Physical Society of Japan, 54 (1985) 2238.

[59] L.P. Kadanoff, W. GÃ–Tze, D. Hamblen, R. Hecht, E.A.S. Lewis, V.V. Palciauskas, M. Rayl, J. Swift, D. Aspnes, J. Kane, Static Phenomena Near Critical Points: Theory and Experiment, Reviews of Modern Physics, 39 (1967) 395-431.

[60] M.E. Fisher, Quantum Corrections to Critical-Point Behavior, Physical Review Letters, 16 (1966) 11-14.

[61] B. Kramer, T. Ohtsuki, S. Kettemann, Random network models and quantum phase transitions in two dimensions, Physics Reports, 417 (2005) 211-342.

[62] Y. Ono, Energy dependence of localization length of two-dimensional electron system moving in a random potential under strong magnetic fields, Journal of the Physical Society of Japan, 51 (1982) 2055-2056.

[63] L. Schweitzer, B. Kramer, A. MacKinnon, Magnetic field and electron states in two-dimensional disordered systems, Journal of Physics C: Solid State Physics, 17 (1984) 4111-4125.

[64] H. Aoki, T. Ando, Critical localization in two-dimensional Landau quantization, Physical Review Letters, 54 (1985) 831-834.

[65] T. Ando, H. Aoki, Finite-size scaling study of localization in Landau levels, Journal of the Physical Society of Japan, 54 (1985) 2238-2249.

[66] B. Miek, Europhys. Lett., 13 (1990) 453.

[67] B. Huckestein, Scaling and universality in the integer quantum Hall effect, EPL (Europhysics Letters), 20 (1992) 451.

[68] C.B. Hanna, D.P. Arovas, K. Mullen, S.M. Girvin, Effect of spin degeneracy on scaling in the quantum Hall regime, Physical Review B, 52 (1995) 5221-5232.

[69] E.S. SÃ¸rensen, A.H. MacDonald, Integer quantum Hall effect in double-layer systems, Physical Review B - Condensed Matter and Materials Physics, 54 (1996) 10675-10687.

[70] Y. Ono, T. Ohtsuki, B. Kramer, Scaling Behavior of Level Statistics in Quantum Hall Regime, Journal of the Physical Society of Japan, 65 (1996) 1734-1743.

[71] J. Chalker, P. Coddington, Percolation, quantum tunnelling and the integer Hall effect, Journal of Physics C: Solid State Physics, 21 (1988) 2665.

[72] D.-H. Lee, Z. Wang, S. Kivelson, Quantum percolation and plateau transitions in the quantum Hall effect, Physical Review Letters, 70 (1993) 4130.

[73] A.G. Galstyan, M.E. Raikh, Localization and conductance fluctuations in the integer quantum Hall effect: Real-space renormalization-group approach, Physical Review B - Condensed Matter and Materials Physics, 56 (1997) 1422-1429.

[74] P. Cain, R.A. Römer, M. Schreiber, M.E. Raikh, Integer quantum Hall transition in the presence of a long-range-correlated quenched disorder, Physical Review B, 64 (2001) 235326.

[75] P. Cain, R.A. RÃ¶mer, M.E. Raikh, Renormalization group approach to energy level statistics at the integer quantum Hall transition, Physical Review B, 67 (2003) 075307.

[76] R.A. Römer, P. Cain, Adv. Solid State Phys., 43 (2003) 235.

[77] J. Kondev, J.B. Marston, Supersymmetry and localization in the quantum hall effect, Nuclear Physics B, 497 (1997) 639-657.

[78] D.H. Lee, Z. Wang, Transitions between Hall plateaux and the dimerization transition of a Hubbard chain, Philosophical Magazine Letters, 73 (1996) 145-152.

[79] A.M.M. Pruisken, Universal Singularities in the Integral Quantum Hall Effect, Physical Review Letters, 61 (1988) 1297.

[80] D. Liu, S. Das Sarma, Universal scaling of strong-field localization in an integer quantum Hall liquid, Physical Review B, 49 (1994) 2677.

[81] B.L. Altshuler, et al., Effects of electron-electron collisions with small energy transfers on quantum localisation, Journal of Physics C: Solid State Physics, 15 (1982) 7367.

[82] H.P. Wei, S.Y. Lin, D.C. Tsui, A.M.M. Pruisken, Effect of long-range potential fluctuations on scaling in the integer quantum Hall effect, Physical Review B, 45 (1992) 3926.

[83] J. Wakabayashi, M. Yamane, S. Kawaji, Experiments on the Critical Exponent of Localization in Landau Subbands with the Landau Quantum Numbers 0 and 1 in Si-MOS Inversion Layers, J. Phys. Soc. Japan, 58 (1989) 1903.

[84] V.T. Dolgopolov, A.A. Shaskin, B.K. Medvedev, V.G. Mokerov, Sov. Phys. JETP, 72 (1991) 113.

[85] S. Koch, R.J. Haug, K.v. Klitzing, K. Ploog, Size-dependent analysis of the metal-insulator transition in the integral quantum Hall effect, Physical Review Letters, 67 (1991) 883.

[86] F. Hohls, U. Zeitler, R.J. Haug, Hopping Conductivity in the Quantum Hall Effect: Revival of Universal Scaling, Physical Review Letters, 88 (2002) 036802.

[87] W. Li, C.L. Vicente, J.S. Xia, W. Pan, D.C. Tsui, L.N. Pfeiffer, K.W. West, Scaling in Plateau-to-Plateau Transition: A Direct Connection of Quantum Hall Systems with the Anderson Localization Model, Physical Review Letters, 102 (2009) 216801.

[88] A.B. Fowler, A. Hartstein, R.A. Webb, Conductance in Restricted-Dimensionality Accumulation Layers, Physical Review Letters, 48 (1982) 196-199.

[89] S. Washburn, R.A. Webb, Aharonov-Bohm effect in normal metal quantum coherence and transport, Advances in Physics, 35 (1986) 375-422.

[90] J.-L. Pichard, M. Sanquer, Quantum conductance fluctuations and maximum entropy ensembles for the transfer matrix, Physica A: Statistical Mechanics and its Applications, 167 (1990) 66-92.

[91] F. Kuchar, R. Meisels, K. Dybko, B. Kramer, DC-and AC-scaling of the integer quantum Hall effect in the presence of interactions, EPL (Europhysics Letters), 49 (2000) 480.

[92] P.T. Coleridge, R. Stoner, R. Fletcher, Low-field transport coefficients in GaAs/Ga_{1-x}Al_{x}As heterostructures, Physical Review B, 39 (1989) 1120-1124.

[93] P.T. Coleridge, Small-angle scattering in two-dimensional electron gases, Physical Review B, 44 (1991) 3793-3801.

[94] T. Ando, Theory of Quantum Transport in a Two-Dimensional Electron System under Magnetic Fields. IV. Oscillatory Conductivity, J. Phys. Soc. Japan, 37 (1974).

[95] M.A. Paalanen, D.C. Tsui, J.C.M. Hwang, Parabolic Magnetoresistance from the Interaction Effect in a Two-Dimensional Electron Gas, Physical Review Letters, 51 (1983) 2226-2229.

[96] A. Efros, B. Shklovskii, Coulomb gap and low temperature conductivity of disordered systems, Journal of Physics C: Solid State Physics, 8 (1975) L49.

[97] A. Briggs, Y. Guldner, J.P. Vieren, M. Voos, J.P. Hirtz, M. Razeghi, Low-temperature investigations of the quantum Hall effect in InxGa1-xAs-InP heterojunctions, Physical Review B, 27 (1983) 6549.

[98] F.W. Van Keuls, X.L. Hu, H.W. Jiang, A.J. Dahm, Screening of the Coulomb interaction in two-dimensional variable-range hopping, Physical Review B, 56 (1997) 1161.

[99] S. Koch, R.J. Haug, K.v. Klitzing, K. Ploog, Variable range hopping transport in the tails of the conductivity peaks between quantum Hall plateaus, Semiconductor science and technology, 10 (1995) 209.

[100] M. Furlan, Electronic transport and the localization length in the quantum Hall effect, Physical Review B, 57 (1998) 14818.

[101] W. Li, J.S. Xia, C. Vicente, N.S. Sullivan, W. Pan, D.C. Tsui, L.N. Pfeiffer, K.W. West, Crossover from the nonuniversal scaling regime to the universal scaling regime in quantum Hall plateau transitions, Physical Review B, 81 (2010) 033305.

[102] D.G. Polyakov, B.I. Shklovskii, Conductivity-peak broadening in the quantum Hall regime, Physical Review B, 48 (1993) 11167.

[103] H.W. Jiang, C.E. Johnson, K.L. Wang, S.T. Hannahs, Observation of magnetic-field-induced delocalization: Transition from Anderson insulator to quantum Hall conductor, Physical Review Letters, 71 (1993) 1439.

[104] C.P. Umbach, S. Washburn, R.B. Laibowitz, R.A. Webb, Magnetoresistance of small, quasi-one-dimensional, normal-metal rings and lines, Physical Review B, 30 (1984) 4048-4051.

[105] E. Abrahams, P.W. Anderson, P.A. Lee, T.V. Ramakrishnan, Quasiparticle lifetime in disordered two-dimensional metals, Physical Review B, 24 (1981) 6783.

[106] B.L. Altshuler, A.G. Aronov, D.E. Khmelnitsky, Effects of electron-electron collisions with small energy transfers on quantum localisation, Journal of Physics C: Solid State Physics, 15 (1982) 7367.

[107] P.W. Anderson, E. Abrahams, T.V. Ramakrishnan, Possible Explanation of Nonlinear Conductivity in Thin-Film Metal Wires, Physical Review Letters, 43 (1979) 718.

[108] G.J. Dolan, D.D. Osheroff, Nonmetallic Conduction in Thin Metal Films at Low Temperatures, Physical Review Letters, 43 (1979) 721.

[109] J.J. Lin, J.P. Bird, Recent experimental studies of electron dephasing in metal and semiconductor mesoscopic structures, Journal of Physics: Condensed Matter, 14 (2002) R501.

[110] G.F. Giuliani, J.J. Quinn, Lifetime of a quasiparticle in a two-dimensional electron gas, Physical Review B, 26 (1982) 4421-4428.

[111] H. Fukuyama, E. Abrahams, Inelastic scattering time in two-dimensional disordered metals, Physical Review B, 27 (1983) 5976-5980.

[112] A. Yacoby, U. Sivan, C.P. Umbach, J.M. Hong, Interference and dephasing by electron-electron interaction on length scales shorter than the elastic mean free path, Physical Review Letters, 66 (1991) 1938-1941.

[113] T. Brandes, Inelastic scattering, multifractality, and scaling in the integer quantum Hall effect, Physical Review B, 52 (1995) 8391-8399.

[114] T. Brandes, L. Schweitzer, B. Kramer, Multifractal wave functions and inelastic scattering in the integer quantum Hall effect, Physical Review Letters, 72 (1994) 3582-3585.

[115] T. Brandes, L. Schweitzer, B. Kramer, Temperature-dependent broadening of Ï xx-peaks and inelastic scattering in the integer quantum Hall effect, Physica B: Condensed Matter, 216 (1996) 369-371.

[116] E. Chow, H.P. Wei, Experiments on inelastic scattering in the integer quantum Hall effect, Physical Review B, 52 (1995) 13749-13752.

[117] E. Chow, H.P. Wei, S.M. Girvin, M. Shayegan, Phonon Emission from a 2D Electron Gas: Evidence of Transition to the Hydrodynamic Regime, Physical Review Letters, 77 (1996) 1143-1146.

[118] D.G. Polyakov, B.I. Shklovskii, Variable range hopping as the mechanism of the conductivity peak broadening in the quantum Hall regime, Physical Review Letters, 70 (1993) 3796.

[119] N.A. Dodoo-Amoo, K. Saeed, S.P. Khanna, L. Li, E.H. Linfield, A.G. Davies, J.E. Cunningham, Experimental studies on the non-universality of scaling exponents in quantum Hall transitions, Unpublished.

[120] N.A. Dodoo-Amoo, K. Saeed, J.E. Cunningham, L.H. Li, S.P. Khanna, E.H. Linfield, A.G. Davies, Scaling behaviour of interger quantum Hall effect in GaAs/AlGaAs heterostructures, Proceedings of the Conf. on UK Semiconductors, (2011).

[121] B. Shapiro, E. Abrahams, Scaling for the frequency-dependent conductivity in disordered electronic systems, Physical Review B, 24 (1981) 4889-4891.

[122] M. Pollak, T.H. Geballe, Low-Frequency Conductivity Due to Hopping Processes in Silicon, Physical Review, 122 (1961) 1742-1753.

[123] A.R. Long, Frequency-dependent loss in amorphous semiconductors, Advances in Physics, 31 (1982).

[124] M. Pollak, H.A. Pohl, Dielectric dispersion in some polymers and polyelectrolytes: A model, The Journal of Chemical Physics, 63 (1975) 2980-2987.

[125] J.C. Dyre, T.B. SchrÃ¸der, Universality of ac conduction in disordered solids, Reviews of Modern Physics, 72 (2000) 873-892.

[126] A.G. Hunt, Ac hopping conduction: Perspective from percolation theory, Philosophical Magazine Part B, 81 (2001) 875-913.

[127] J.T. Chalker, G.J. Daniell, Scaling, Diffusion, and the Integer Quantized Hall Effect, Physical Review Letters, 61 (1988) 593-596.

[128] B. Huckestein, M. Backhaus, Integer Quantum Hall Effect of Interacting Electrons: Dynamical Scaling and Critical Conductivity, Physical Review Letters, 82 (1999) 5100.

[129] D.-H. Lee, Z. Wang, Effects of Electron-Electron Interactions on the Integer Quantum Hall Transitions, Physical Review Letters, 76 (1996) 4014.

[130] Z. Wang, S. Xiong, Electron-electron interactions, quantum Coulomb gap, and dynamical scaling near integer quantum Hall transitions, Physical Review B, 65 (2002) 195316.

[131] Z. Wang, M.P.A. Fisher, S.M. Girvin, J.T. Chalker, Short-range interactions and scaling near integer quantum Hall transitions, Physical Review B, 61 (2000) 8326.

[132] F. Hohls, U. Zeitler, R.J. Haug, R. Meisels, K. Dybko, F. Kuchar, Dynamical Scaling of the Quantum Hall Plateau Transition, Physical Review Letters, 89 (2002) 276801.

[133] F. Hohls, U. Zeitler, R.J. Haug, High Frequency Conductivity in the Quantum Hall Regime, Physical Review Letters, 86 (2001) 5124.

[134] F. Kuchar, R. Meisels, G. Weimann, W. Schlapp, Microwave Hall conductivity of the two-dimensional electron gas in GaAs-AlxGa1-xAs, Physical Review B, 33 (1986) 2965.

[135] Y. Ikebe, T. Morimoto, R. Masutomi, T. Okamoto, H. Aoki, R. Shimano, Optical Hall Effect in the Integer Quantum Hall Regime, Physical Review Letters, 104 (2010) 256802.

[136] C.P. Wen, Coplanar waveguide: A surface strip transmission line suitable for nonreciprocal gyromagnetic device applications, Microwave Theory and Techniques, IEEE Transactions on, 17 (1969) 1087-1090.

[137] D.M. Pozar, Microwave engineering 3rd, Danvers, MA: Wiley, (2005).

[138] H. Aoki, Quantised Hall effect, Reports on Progress in Physics, 50 (1987) 655.

[139] F. Wegner, Exact density of states for lowest Landau level in white noise potential superfield representation for interacting systems, Z. Physik B - Condensed Matter, 51 (1983) 279-285.

[140] R. Meisels, F. Kuchar, W. Belitsch, G. Hein, K. Pierz, High-frequency conductivity experiments on the integer quantum Hall effect at the limits of universality, Physica B: Condensed Matter, 256–258 (1998) 74-77.

[141] W. Li, G.A. Csathy, D.C. Tsui, L.N. Pfeiffer, K.W. West, Direct observation of alloy scattering of two-dimensional electrons in Al[sub x]Ga[sub 1 - x]As, Applied Physics Letters, 83 (2003) 2832-2834.

[142] K. Saeed, N.A. Dodoo-Amoo, L.H. Li, S.P. Khanna, E.H. Linfield, A.G. Davies, J.E. Cunningham, Impact of disorder on frequency scaling in the integer quantum Hall effect, Physical Review B, 84 (2011) 155324.

[143] N.A. Dodoo-Amoo, K. Saeed, J.E. Cunningham, L.H. Li, S.P. Khanna, E.H. Linfield, A.G. Davies, Role of short-range interactions on frequency scaling of the integer quantum Hall effect, Proceedings of the 19th Int. Conf. on Electron Properties of Two-Dimensional Systems, (2011).

[144] C. Jiang, D.C. Tsui, G. Weimann, Threshold transport of high-mobility two-dimensional electron gas in GaAs/AlGaAs heterostructures, Applied Physics Letters, 53 (1988) 1533-1535.

[145] J.A. Nixon, J.H. Davies, Potential fluctuations in heterostructure devices, Physical Review B, 41 (1990) 7929.

[146] A.L. Efros, Density of states of 2D electron gas and width of the plateau of IQHE, Solid State Communications, 65 (1988) 1281-1284.

[147] A.L. Efros, Non-linear screening and the background density of 2DEG states in magnetic field, Solid State Communications, 67 (1988) 1019-1022.

[148] A.L. Efros, Metal-non-metal transition in heterostructures with thick spacer layers, Solid State Communications, 70 (1989) 253-256.

[149] D.B. Chklovskii, P.A. Lee, Transport properties between quantum Hall plateaus, Physical Review B, 48 (1993) 18060-18078.

[150] A.M. Chang, A unified transport theory for the integral and fractional quantum hall effects: Phase boundaries, edge currents, and transmission/reflection probabilities, Solid State Communications, 74 (1990) 871-876.

[151] D.B. Chklovskii, B.I. Shklovskii, L.I. Glazman, Electrostatics of edge channels, Physical Review B, 46 (1992) 4026-4034.

[152] R. Haug, Edge-state transport and its experimental consequences in high magnetic fields, Semiconductor science and technology, 8 (1993) 131.

[153] C.W.J. Beenakker, Edge channels for the fractional quantum Hall effect, Physical Review Letters, 64 (1990) 216-219.

[154] A.L. Efros, F.G. Pikus, V.G. Burnett, Density of states of a two-dimensional electron gas in a long-range random potential, Physical Review B, 47 (1993) 2233-2243.

[155] N.R. Cooper, J.T. Chalker, Coulomb interactions and the integer quantum Hall effect: Screening and transport, Physical Review B, 48 (1993) 4530-4544.

[156] S.R. Broadbent, J.M. Hammersley, Percolation processes I. Crystals and mazes, in: Proceedings of the Cambridge philosophical society, 1957, pp. 629-641.

[157] M.F. Sykes, J.W. Essam, Critical Percolation Probabilities by Series Methods, Physical Review, 133 (1964) A310-A315.

[158] M.F. Sykes, J.W. Essam, Exact Critical Percolation Probabilities for Site and Bond Problems in Two Dimensions, Journal of Mathematical Physics, 5 (1964) 1117-1127.

[159] H.L. Frisch, J.M. Hammersley, D.J.A. Welsh, Monte Carlo Estimates of Percolation Probabilities for Various Lattices, Physical Review, 126 (1962) 949-951.

[160] V.A. Vyssotsky, S.B. Gordon, H.L. Frisch, J.M. Hammersley, Critical Percolation Probabilities (Bond Problem), Physical Review, 123 (1961) 1566-1567.

[161] C. Domb, M.F. Sykes, Cluster Size in Random Mixtures and Percolation Processes, Physical Review, 122 (1961) 77-78.

[162] D. Stauffer, Scaling theory of percolation clusters, Physics Reports, 54 (1979) 1-74.

[163] J. Ziman, The localization of electrons in ordered and disordered systems I. Percolation of classical particles, Journal of Physics C: Solid State Physics, 1 (1968) 1532.

[164] S.A. Trugman, Localization, percolation, and the quantum Hall effect, Physical Review B, 27 (1983) 7539.

[165] R. Joynt, R.E. Prange, Conditions for the quantum Hall effect, Physical Review B, 29 (1984) 3303-3317.

[166] T. Ando, Electron localization in a two-dimensional system in strong magnetic fields. II: Long-range scatterers and response functions, J. Phys. Soc. Jpn, 53 (1984) 3101-3111.

[167] H. Saleur, B. Duplantier, Exact Determination of the Percolation Hull Exponent in Two Dimensions, Physical Review Letters, 58 (1987) 2325-2328.

[168] G.V. Mil'nikov, I.M. Sokolov, JETP Lett., 48 (1988).

[169] Y. Dubi, Y. Meir, Y. Avishai, Quantum Hall criticality, superconductor-insulator transition, and quantum percolation, Physical Review B, 71 (2005) 125311.

[170] S. Perraud, K. Kanisawa, Z.-Z. Wang, T. Fujisawa, Imaging the percolation of localized states in a multisubband two-dimensional electronic system subject to a disorder potential, Physical Review B, 76 (2007) 195333.

[171] J. Wiebe, C. Meyer, J. Klijn, M. Morgenstern, R. Wiesendanger, From quantized states to percolation: Scanning tunneling spectroscopy of a strongly disordered two-dimensional electron system, Physical Review B, 68 (2003) 041402.

[172] M. Morgenstern, J. Klijn, C. Meyer, R. Wiesendanger, Real-Space Observation of Drift States in a Two-Dimensional Electron System at High Magnetic Fields, Physical Review Letters, 90 (2003) 056804.

[173] G. Eytan, Y. Yayon, M. Rappaport, H. Shtrikman, I. Bar-Joseph, Near-Field Spectroscopy of a Gated Electron Gas: A Direct Evidence for Electron Localization, Physical Review Letters, 81 (1998) 1666.

[174] F. Dahlem, E. Ahlswede, J. Weis, K. v. Klitzing, Cryogenic scanning force microscopy of quantum Hall samples: Adiabatic transport originating in anisotropic depletion at contact interfaces, Physical Review B, 82 (2010) 121305.

[175] A. Baumgartner, T. Ihn, K. Ensslin, K. Maranowski, A.C. Gossard, Quantum Hall effect transition in scanning gate experiments, Physical Review B, 76 (2007) 085316.

[176] S.H. Tessmer, P.I. Glicofridis, R.C. Ashoori, L.S. Levitov, M.R. Melloch, Subsurface charge accumulation imaging of a quantum Hall liquid, Nature, 392 (1998) 51-54.

[177] N.B. Zhitenev, T.A. Fulton, A. Yacoby, H.F. Hess, L.N. Pfeiffer, K.W. West, Imaging of localized electronic states in the quantum Hall regime, Nature, 404 (2000) 473-476.

[178] K. Hashimoto, C. Sohrmann, J. Wiebe, T. Inaoka, F. Meier, Y. Hirayama, R.A. Romer, R. Wiesendanger, M. Morgenstern, Quantum Hall Transition in Real Space: From Localized to Extended States, Physical Review Letters, 101 (2008) 256802.

[179] M. Morgenstern, J. Klijn, C. Meyer, M. Getzlaff, R. Adelung, R.A. Römer, K. Rossnagel, L. Kipp, M. Skibowski, R. Wiesendanger, Direct Comparison between Potential Landscape and Local Density of States in a Disordered Two-Dimensional Electron System, Physical Review Letters, 89 (2002) 136806.

[180] N.A. Dodoo-Amoo, K. Saeed, S.P. Khanna, L. Li, E.H. Linfield, A.G. Davies, J.E. Cunningham, The quantum percolation model of the scaling theory of the quantum Hall effect: a unifying model for plateau-to-plateau transitions., J. Phys. conf. series (Unpublished), (2013).

[181] E. Shimshoni, Classical versus quantum transport near quantum Hall transitions, Physical Review B, 60 (1999) 10691-10694.

[182] A. Kapitulnik, N. Mason, S.A. Kivelson, S. Chakravarty, Effects of dissipation on quantum phase transitions, Physical Review B, 63 (2001) 125322.

[183] Y. Dubi, Y. Meir, Y. Avishai, Unifying Model for Several Classes of Two-Dimensional Phase Transition, Physical Review Letters, 94 (2005) 156406.

[184] S.D. Sarma, A. Pinczuk, Perspectives in quantum Hall effects, Wiley-VCH, 2008.

[185] Y. Ikebe, R. Shimano, Characterization of doped silicon in low carrier density region by terahertz frequency Faraday effect, Applied Physics Letters, 92 (2008) 012111-012113.

[186] R.F. Kazarinov, S. Luryi, Quantum percolation and quantization of Hall resistance in two-dimensional electron gas, Physical Review B, 25 (1982) 7626-7630.

[187] S.A. Trugman, S. Doniach, Vortex dynamics in inhomogeneous superconducting films, Physical Review B, 26 (1982) 3682-3697.

[188] H.A. Fertig, Semiclassical description of a two-dimensional electron in a strong magnetic field and an external potential, Physical Review B, 38 (1988) 996-1015.

[189] B. Shapiro, Dissipative transport in transition regions between quantum Hall plateaus, Physical Review B, 33 (1986) 8447-8457.

[190] S. Luryi, R.F. Kazarinov, Theory of quantized Hall effect at low temperatures, Physical Review B, 27 (1983) 1386-1389.

[191] A.G. Galstyan, M.E. Raikh, Localization and conductance fluctuations in the integer quantum Hall effect: Real-space renormalization-group approach, Physical Review B, 56 (1997) 1422-1429.

[192] Y. Meir, Percolation-Type Description of the Metal-Insulator Transition in Two Dimensions, Physical Review Letters, 83 (1999) 3506.

[193] E. Bettelheim, I.A. Gruzberg, A.W.W. Ludwig, Quantum Hall transitions: An exact theory based on conformal restriction, Physical Review B, 86 (2012) 165324.

[194] F. Kuchar, R. Meisels, K. Lim, P. Pichler, G. Weimann, W. Schlapp, Hall Conductivity at Microwave and Submillimeter Frequencies in the Quantum Hall Effect Regime, Physica Scripta, 1987 (2007) 79.

[195] E.D. Palik, J.K. Furdyna, Infrared and microwave magnetoplasma effects in semiconductors, Reports on Progress in Physics, 33 (1970) 1193.

[196] J.K. Furdyna, Helicons, Magnetoplasma Edge, and Faraday Rotation in Solid State Plasmas at Microwave Frequencies, Appl. Opt., 6 (1967) 675-684.

[197] F. Kuchar, R. Meisels, K.Y. Lim, P. Pichler, G. Weimann, W. Schlapp, Hall Conductivity at Microwave and Submillimeter Frequencies in the Quantum Hall Effect Regime, Physica Scripta, 1987 (1987) 79.

[198] K.S. Novoselov, Z. Jiang, Y. Zhang, S.V. Morozov, H.L. Stormer, U. Zeitler, J.C. Maan, G.S. Boebinger, P. Kim, A.K. Geim, Room-Temperature Quantum Hall Effect in Graphene, Science, 315 (2007) 1379-1379.